University of Oxford

Department of Engineering Science

Nanoscale Engineering of Guest@Host Metal-Organic Framework Materials for Optoelectronic Properties

Abhijeet Kishor Chaudhari
St Catherine's College
July 2017

A dissertation submitted for the degree of Doctor of Philosophy

Declaration

This dissertation is submitted for the degree of Doctor of Philosophy in the University of Oxford, United Kingdom. The research work described throughout this dissertation was carried out by the author in the period from February 2014 to June 2017, under the guidance of Prof. Jin-Chong Tan in the Department of Engineering Science at the University of Oxford.

To the best of my knowledge, the work described in this dissertation is original, except where due reference has been made of the work(s) of others, and nothing has been included that is the outcome of work done in collaboration of others, except where specifically noted. No part of this dissertation, or any similar to it, has been, or is currently being submitted for any degree at this or any other university. This dissertation is less than 45,000 words in length.

Abhijeet Kishor Chaudhari

Oxford, U.K.

July 2017

Abstract

This thesis describes the nano-engineering of self-assembly processes, to accomplish nanoscale metal-organic framework (MOF) systems potentially useful for optoelectronic applications. The well-known fact underlying the large crystal size formation of common MOF compounds has been re-investigated here, not only to minimise the prolonged synthesis time but also to yield facile deposition in uniform thin film formats. This thesis presents the innovative concept of high concentration reaction (HCR) and its utility for making nano MOFs. Surprisingly, this method resulted in formation of a new kind of gel-like soft materials, for which I coined the term — supraMOFs — meaning supramolecular MOF hybrid materials.

A detailed study of supraMOFs focussing on their constituent nano MOF elements, stimuli-responsive behaviours, and sol-gel conversion phenomena have been systematically performed. Akin to low molecular weight gels (LMWG), mechanical properties of supraMOFs displaying storage modulus (*G*') > loss modulus (*G*") have been confirmed by rheological experiments. The use of sol-gel MOF system to attain a uniform MOF film, has been demonstrated through an example of HKUST-1 thin coating of ~10 nm roughness and ~1 μm thickness.

The HCR concept was further extended to develop advanced functional nano MOF systems, where one-step rapid synthesis of fluorescent MOF nanosheets has been accomplished. The old but effective concept of functionalisation of MOFs using porous coordination space and external guest species was implemented here, but with a twist. Particularly, the challenge of caging larger sized guest species into smaller pore apertures of MOFs, in parallel to controlling material growth in the nanoscale regime were solved by adopting the HCR approach. Furthermore, this thesis has demonstrated new interesting possibilities employing fluorescent nano MOF system to engineer smart sensors for detecting volatile organic compounds (VOCs), and mechanical stresses *via* a mechanochromic luminescent MOF nanoplate system.

Acknowledgments

My special thanks go to my DPhil supervisor, Prof. Jin-Chong Tan, who is the sole reason behind my DPhil journey at the University of Oxford. He helped me at every stage, right from joining DPhil at Oxford till the end of the course. His friendly behaviour and encouraging comments about my work kept me optimistic, energetic and enthusiastic all the time. His endless efforts in making my research presentable in high impact factor journals are unquestionably admirable. I am extremely thankful to him for his constant support, encouragement, inspiration and positive criticisms.

I am truly grateful to Samsung Electronics Ltd. and Samsung Advanced Institute of Technology (SAIT), Seoul, South Korea for providing the research funding to support my DPhil studies at Oxford. Special thanks goes to Hajin Kim and Intaek Han from SAIT, who constantly appreciated my work and supported my ideas and thoughts on research deliverables. I express my deepest gratitude to Samsung team for not just the financial support but also for making fruitful research collaboration, which definitely made my research life more rewarding in Oxford.

I would like to thank Linacre College and St Catherine's College for making my outside-lab-life easier by providing me with comfortable accommodation within walking distance from the lab. I would like to express my gratitude to St Catherine's College for selecting me as a graduate scholar of the college and awarding me the Great Eastern Scholarship for two consecutive years. As a strong link between student and his academic progress, I give my special thanks to Linacre college, St Catherine's College and advisor from both the colleges, namely Prof. Samar Khatiwala and Prof. Peter Ireland. I am thankful to the Department of Engineering Science and St Catherine's College for providing conference grants and indirectly supporting me throughout my DPhil course. I am also thankful to several people from the Department,

particularly the safety officer, chemical waste officer, and people from the stores, who did their bit indirectly for my research work.

I am grateful to Research Complex at Harwell (RCaH) for allowing me to use their research facilities. I must mention the constant help from Iain Walmsley of RCaH. Dr. Gavin Stenning and Dr. Marek Jura of R-53, Rutherford Appleton Laboratory, are key people, who played important roles by providing continuous access to the powder X-ray diffractometer used heavily in my research. My special thanks go to Dr. Svemir Rudic from ISIS, Harwell, who has been a good friend and mentor rather than just a senior scientist and our collaborator. I would also like to add my thanks to Dr, James Taylor of the Hydrogen Lab, RAL and Dr. Kalin Dragnevski of LIMA, Department of Engineering Science, Oxford for instrument access.

Finally, I would also like to thank my lab colleagues Matthew, Mahdi, Zhixin, Yueting, Irina, Kirill, and office colleagues Xuegang, Heather, Arun, Rangarajan, Rudolpho for their friendly company in lab and office.

I dedicate my thesis to my mother and sisters, without whom nothing would have ever happened.

Table of Contents

Nomenclature

Acronym	Full term
Å	Angstrom
ad	Adenine
ACQ	Aggregation caused quenching
ACN	Acetonitrile
A	Amperes
AlQ	Al-tris-(8-hydroxyquinoline)
AFM	Atomic force microscopy
AM-FM	Amplitude modulation (AM) and frequency modulation (FM)
bpy	Bipyridine
BTC	1,3,5-Benzenetricarboxylic acid
BTB	4,4',4''-Benzene-1,3,5-triyl-tribenzoic acid
BDC	1,4 -Benzene dicarboxylic acid/Terephthalic acid
Bu	Butyl
BPDC	4,4'- Biphenyl dicarboxylic acid
cc	Cubic centimetre
CAT	Crystal-to-amorphous transformation
CCT	Crystal-to-crystal transformation
ca	Chloranilic acid
cm	Centimeter
°C	Degree celcius
CIE	Commission internationale de l'éclairage/International Commission on Illumination
2D	Two dimensional
3D	Three dimensional
DFT	Density functional theory
DSS	Dynamic strain sweep
DMF	*N, N*-Dimethylformamide
dto	Dithiooxalic acid
dpyg	1,2-Dipyridylglycol
DMASM	4-[p-(dimethylamino)styryl]-1-methylpyridinium
DMSO	Dimethyl sulfoxide

DCM	Dichloromethane
DRS	Diffuse reflectance spectra
DEF	*N*, *N*-Diethylformamide
DMA	*N*, *N*-Dimethylacetamide
dnp	Double numeric with polarisation basis set
EtOH, ETH	Ethanol
eV	Electron volts
E	Young's modulus
E_g	Energy gap
FT-IR	Fourier transform infra-red
FETs	Field-effect transistors
GPa	Gigapascal
G'	Storage modulus
G"	Loss modulus
GST	Germanium Antimony Telluride
GGA	Generalized-gradient approximation
Gaq_3	Ga-tris-(8-hydroxyquinoline)
γ	Shear strain
HKUST-1	Hong Kong University of Science and Technology-1
HCR	High concentration reaction
H_2adp	Adipic acid
8HQ	8-Hydroxyquinoline
HOMO	Highest occupied molecular orbital
h	Hour
Im	Imidazole
ITO	Indium Tin Oxide
IRMOF	Isoreticular metal-organic framework
I	Current
Inq3	In-tris-(8-hydroxyquinoline)
IPA	Isopropanol/2-Propanol
kPa	Kilopascal
kHz	Kilohertz
kV	Kilovolts
KM	Kubelka-Munk

LUMO	Lowest unoccupied molecular orbital
LEDs	Light emitting diodes
LMWG	Low-molecular-weight gels
LaB_6	Lanthanumhexaboride
MOF	Metal-organic framework
MeOH, MEH	Methanol
Me	Methyl
MPa	Megapascal
mIm	2-Methylimidazole
$MeNH_2$	Methyl ammonium
m	Meter
mW	Milliwatts
min	Minutes
mmol	Millimoles
mL	Millilitre
MOGs	Metal-organic gels
nm	Nanometer
Nd-YAG	Neodymium-doped yttrium aluminium garnet
NMOF	Nano metal-organic framework
ndc	2, 6-Naphthalene dicarboxylic acid
NPs	Nanoparticles
N	Newton
OLEDs	Organic light emitting diodes
OX-1	Oxford University-1 material
ox	Oxalate
PCPs	Porous coordination polymers
PW	Perdew and Wang
PXRD	Powder X-ray diffraction
PVDs	Photovoltaic devices
pzdc	Pyrazine-2,3-dicarboxylate
pydca	Pyridine-2,4-dicarboxylate
pyz	Pyrazine
QD	Quantum dots
QDIPs	Quantum dot infrared photodetectors

QDSCs	Quantum dot solar cells
QDSLDs	Quantum dot super luminescent diodes
QY	Quantum yield
R_{wp}	Weighted R-factor
RT	Room temperature
rpm	Revolutions per minute
SupraMOF	Supramolecular metal-organic framework hybrid assembly
S	Siemens
SC-SC	Single crystal-single crystal
salphdc	*N,N*'-Phenylenebis (salicylideneimine) dicarboxylic acid
SBU	Secondary building unit
SAMs	Self-assembled monolayers
s	Second
SEM	Scanning electron microscopy
τ	Shear stress
TPP	Two photon-pumped
TEM	Transmission electron microscopy
tan δ	Loss tangent
TGA	Thermal gravimetric analysis
TFT	Thin film transistor
TFA	Triflic acid
Tz	1H-1,2,4-Trizole
$ThSi_2$	Thorium silicide
THF	Tetrahydrofuran
TCB	1,3,5 -Tricyanobenzene
TDAN	Triethylenediamine
TEB	1,3,5-Tris-(4-ethynylbenzonitrile)benzene
tpp	4,4',4'',4'''-Tetracyanotetraphenylmethane
mm	Millimetre
UV	Ultra violet
UMCs	Unsaturated metal centres
µL	Microlitre
VE	Viscoelastic
V	Volts

VOCs	Volatile organic compounds
W	Watt
ZnQ	Zn-(bis-8-hydroxyquinoline)
ZIF-8	Zeolitic imidazolate framework-8

Chapter One

Introduction

Metal-Organic Frameworks (MOFs)[1-3] are hybrid (inorganic-organic) materials comprising 3-D extended architectures, constructed from repeating symmetric units through the self-assembly of molecular building blocks. By virtue of the designable potential of MOFs, researchers could fabricate novel materials to target applications such as gas separation/storage, fuel cells, optical sensors, porous magnets, chiral separation/catalysis, photo-catalysis, molecular sieving, semiconducting devices etc.[3-9] MOFs are generally obtained as a single-crystal material, whereby the synthetic conditions used strongly affect the physico-chemical properties of the resultant compounds. For instance, literature on MOF materials shows drastic changes in crystalline structures, particle size and mode of coordination (ultimately determining the topological features of the end products) by varying temperature, pressure, solvent, and pH conditions. Despite being a single crystalline material, some novel materials based on MOFs have emerged in the last few years. For example, polymer blends or quantum dot (QD) doped MOF composites have been reported with enhanced mechanical and optical properties for improved performance as hosts for gas separations/storage or catalytic/magnetic/optical applications.[10-14] Recently, MOFs in the form of thin films have been explored with electronic applications in mind.[15] Nonetheless, there are a few limiting parameters of existing methods associated with MOF hybrid materials in relation to their optoelectronic properties and device fabrication, some of them are listed below:

a) Conventional methods for synthesising pure MOF compounds typically require prolonged (few days to 1 week) hydrothermal or solvothermal reactions comprising organic linkers and metal ion solutions.[16]

b) Nanoscale MOFs have shown improved properties over bulk amount of large particle size MOFs.[17-20] However, state-of-the-art hydrothermal reactions do not allow precise control over exact MOF particle size at the nanoscale, thereby producing a larger distribution of (less desirable) micron-sized particles instead.

c) Manufacturing MOFs in the form of thin films involves the use of costly self-assembled monolayers (SAMs), this strategy also does not allow fabrication over large surface areas.[21] Due to random and large size crystal growth of MOF compounds, they are difficult to fabricate in thin-film form needed for device fabrication and thus limiting the use of material for large-area industrial applications and real-world commercialisation.

d) The majority of MOF materials are poor electrical conductors with large band gaps. Two important aspects, namely MOF polycrystalline boundaries and localised charge in the framework (poor electron delocalisation) are reasons for weak charge transport in MOFs, resulting in semiconductors or insulators.[22]

e) Guest encapsulation and infiltration in MOF is challenging when the size of the pore aperture is relatively smaller than that of the guest, although they possess generally larger internal voids (e.g. ZIF-8 - internal void dimension: >11Å, entry pore aperture size: <3.4Å). Therefore most of the research in this field is concentrated on small guest encapsulation with only a few exception linked to large guest encapsulation studies.[23-24]

f) Luminescent MOFs do not show intense emission properties unless they are made from rare-earth metal ions or long chain conjugated organic linkers.[25-26]

Keeping above constraints in mind and aiming at nano scale engineering of MOF with tuneable opto-electonic behaviour, I have developed innovative methods using supramolecular chemistry and self-assembly concepts. Supramolecular science[27] has triggered a new wave of discoveries of next-generation functional materials, especially stimuli-responsive soft matter,[28] which could afford multiple functions applicable to emergent technologies. It is envisioned that the unique combination of self-organised supramolecular systems,[29] self-healing[30] and thermo-reversibility,[31] and on-demand sol-gel transformation[32] makes stimuli-responsive materials not only extremely versatile, but also straightforward to process into novel multifunctional devices.[33] Yet, the precise control over its microstructural alignment and detailed understanding of complex organisation, constituting a self-assembly,[27] remain some of the biggest challenges facing supramolecular materials science today. One of the best examples featuring self-organisation of lamellar hierarchical growth lies in the naturally occurring protein assembly, known as collagen,[34] whose highly-aligned fibrous microstructure not only dictates its bio-mechanical stability, but also underpins numerous bio-stimuli functions.[35] To this end, exploration of synthetic routes mimicking the self-directed molecular assemblies evidenced in nature has attracted considerable interests, further broadening the scope of applications linked to novel functional materials and soft matter. For example, oriented growth of supramolecular assemblies allows switchable or tuneable material properties, which have utility in emerging areas ranging from microfluidics and molecular filtration, to nanowires and microelectronics devices.[36] Recent studies have also focused on the co-operative effects arising from nanoparticle-polymer pairs (or block-copolymers), to create energetically favourable multi-component systems, incorporating complex patterned growth of bespoke nanomaterials.[37-38]

This thesis starts with an introduction about each chapter covering brief description of the overall work, then extending to the literature review in Chapter 2 describing discovery of self-assembled hybrid porous materials, i.e. metal-organic frameworks, their growth, uses and efforts taken to advance the field towards optoelectronic area including a survey on other contemporary optoelectronic materials and their fundamental properties. Chapter 3 covers materials synthesis, techniques used for characterisation of samples and theoretical methods used for electronic and structural properties elucidation.

In Chapter 4, a rare example of a supramolecular soft hybrid material — featuring gel fibre networks coexisting with nanoparticles of the iconic MOF, designated as “HKUST 1” has been described with synthesis and detailed characterisation; remarkably nanocrystals of HKUST-1 was synergistically formed *in situ*, as an integral part of the 3-D hierarchical self-assembly process. Interestingly, the new system of hybrid materials elucidated in this study bridges the gap and connects the growing field of MOFs with the vibrant field of supramolecular gels and functional soft matter. Chapter 4 provides the first definitive study of the little explored new class of hybrid materials — integrating the fascinating concepts of “MOFs” and “supramolecular gels”-for which I coined the term “SupraMOFs”. Hierarchical micro-architecture demonstrated by the MOF-based supramolecular hybrid gel assemblies are substantially different and unique compared with recent reports on “MOF aerogels”, “MOF xerogels” and “metal-organic gels (MOGs)” found in the literature.

Another emerging field of Metal-Organic Frameworks (MOFs) is MOF-based optoelectronics, and guest-induced tuneable physico-chemical properties in MOFs, which are gaining enormous interest among researchers to explore innovative applications associated with it. Chapter 5 describes the discovery of a rare example

of host-guest nanoconfinement phenomenon, enabled by *in situ* encapsulation within the periodic nanocages of ZIF-8 (i.e. an archetypal MOF with a pore size ~1 nm). The concept of '*in situ* encapsulation' applied to MOFs has been proposed with structural and chemical properties by supporting the demonstration of its efficacy to afford facile nanoconfinement of a bulky luminous ZnQ molecule [Zn-(bis-8-hydroxyquinoline)-monomeric metal complex] to create optically-active nanocrystals. Significantly, using the *in situ* methodology I show that not only it is possible to alleviate the difficulty faced by conventional *ex situ* methods (e.g. ion exchange) in which the narrow nanopore windows of ZIF-8 preventing infiltration of bigger guest molecules, but also this approach yields high-purity encapsulated crystals very rapidly (i.e. ~minutes vs. hours/days). Resultant Guest@Host hybrid nanomaterials (ZnQ@ZIF-8) exhibit tunable photophysical characteristics, which can be correlated to the host-guest electronic pathways arising from its donor-acceptor energy transfer mechanism. The extensive host-guest intermolecular interactions caused by spatial confinement of ZnQ in nanocages (of ZIF-8) led to a strong red-shifted emission spectra evidenced in the encapsulated hybrid. This translates into a warmer color rendering useful for certain lighting applications. Another striking result concerns the major improvement observed in the photophysical stability of the luminescent guest species upon its encapsulation within the ZIF-8 pores. Results described in Chapter 5 suggests that, the nanoscale cavity of MOF could act as a protective vessel to shield light-sensitive fluorophores and dye molecules against rapid photochemical decomposition.

Focussing on similar area of MOF for sensors and optoelectronics, my research was expanded to obtain an unconventional two-dimensional (2D) metal-organic framework (MOF), which can be imparted with tuneable optoelectronic and photo-chemical properties, of potential utility for disruptive chemical sensors and lighting.

Whilst 3D MOFs are much recognised for their enormous physical and chemical versatilities, their lower dimensionality cousins — assuming the shape of “2D nanosheets” — are not well represented in the MOF literature today. And, to the best of our knowledge, yet to be accomplished are: porous 2D nanosheets incorporating a 3D MOF structure, augmented with tuneable “guest-induced emergent properties”. This is because of the limitations imposed by existing MOF synthetic pathways, which do not easily yield thin foils of 2D functionalised materials constituting an extended 3D framework architecture. In Chapter 6, description about possibilities to solve the aforementioned challenge using a straightforward strategy can be found. In this chapter, I have demonstrated a very fast and highly versatile supramolecular synthetic approach (materials reaction time < 1 min), allowing one-pot preparation of functionalised 2D nanosheet structures (i.e. Guest@MOF system), all achieved at room temperature. Detailed findings revolve around the *in situ* nanoscale confinement of bulky light-emitting “guest” molecules inside the pores of the “host” MOF nanosheet material, resulting in intriguing optoelectronic characteristics. Light has been shed on the intriguing host-guest coupling interactions by means of vibrational spectroscopy, in conjunction with enhancements in quantum yield and lifetimes to understand the underpinning physico-chemical mechanisms. The new Guest@MOF nanosheets show an extraordinary propensity for detection of a broad range of harmful volatile organic compounds (VOCs). This is possible thanks to the intimate nature of host-guest coupling arising from MOF nanoconfinement effects, implicating substantial optochemical perturbations (e.g. emission blue/red shifts, intensity modification, luminescence quenching). Crucially, the role of the “caging environmental effect” provided by the MOF nanosheet host was confirmed by the fact that, unconfined emissive guest molecules do not exhibit any sensing capability. Interestingly using a

small quantity of functionalised Guest@MOF nanosheets, our simple proof-of-concept chemical sensor accomplished a reversible detection of a low level of acetone, and further demonstrated the device is swiftly regenerated (~seconds). The concept itself is a reflection of one of the many possible examples, illustrating the considerable promise for engineering real-world applications — opened up by the new versatile concept of "Guest@MOF 2D nanosheets", which has been achieved through rapid supramolecular nanomaterial assembly at ambient conditions.

Under the same umbrella of optoelectronics, mechanochromic luminescent materials are worthwhile to study due to their smart and luminescent response against external pressure. Mechanochromic luminescent materials changes emission behaviour when subject to mechanical forces or when put under pressure, therefore they can exhibit switchable optical properties desirable for photonics-based sensing and tunable optoelectronic applications. Chapter 7 is focused on the study of a previously unreported "mechanochromic luminescent" MOF material termed: "Perylene@ZIF-8" (*i.e.* Guest@MOF host), nano-engineered from the host-guest confinement methodology. A detailed demonstration of a straightforward self-assembly strategy performed at ambient conditions to accomplish rapid fabrication of functionalised Guest@MOF nanoplates, constructed from highly-emissive Perylene "guest" molecules confined within the porous sodalite cages of the ZIF-8 "host" framework has been described in this chapter. This new nanoplate material displays reversible luminescent properties observable by naked eye, switching between the blue ⇌ green emissions (subject to photoexcitation) under a moderate level of pressure (~tens of MPa). Chiefly, the major discovery lies in the spatial isolation of the photoemissive guests afforded by the extended periodicity of the MOF host, due to which I have observed the unique "solution-like" optical properties even in the solid-

state condition. Utilising diffuse reflectance spectroscopy, I show that there are intimate host-guest interactions causing substantial modifications in the electronic structures, which has been confirmed *via* band gap calculations giving insights into the underpinning photophysical phenomena. When exceeding a high pressure of ~1.5 GPa the nanoplates become amorphised, the resulting material still retains its mechanochromic luminescent behaviour thus presenting an attractive pathway for engineering functional amorphous nanocomposites. To the best of our knowledge, this discovery presents the first example of a mechanochromic luminescent MOF system achieved through the host-guest nanoconfinement strategy. Previous examples in the literature on mechanochromic luminescent MOFs have only concerned the emission attributed to the coordinating linkers; here emission behaviour originated from a spatially confined guest which can be modulated by imposing a pressure onto the MOF host. This new paradigm based on the concept of Guest@MOF assembly is versatile and could be extended to many different combinations of guest emitters and host structures.

Chapter 8 is focussed on the use of high concentration reaction approach to synthesise other SupraMOF systems, which can exhibit smart material response like sol-gel phase transitions by the virtue of external stimuli. Detailed description in this chapter includes the exciting discovery of a mechano-stimulus responsive supramolecular gel material constructed using the same chemical constituents to that of ZIF-8. This is the first example of a ZIF-type gel material.

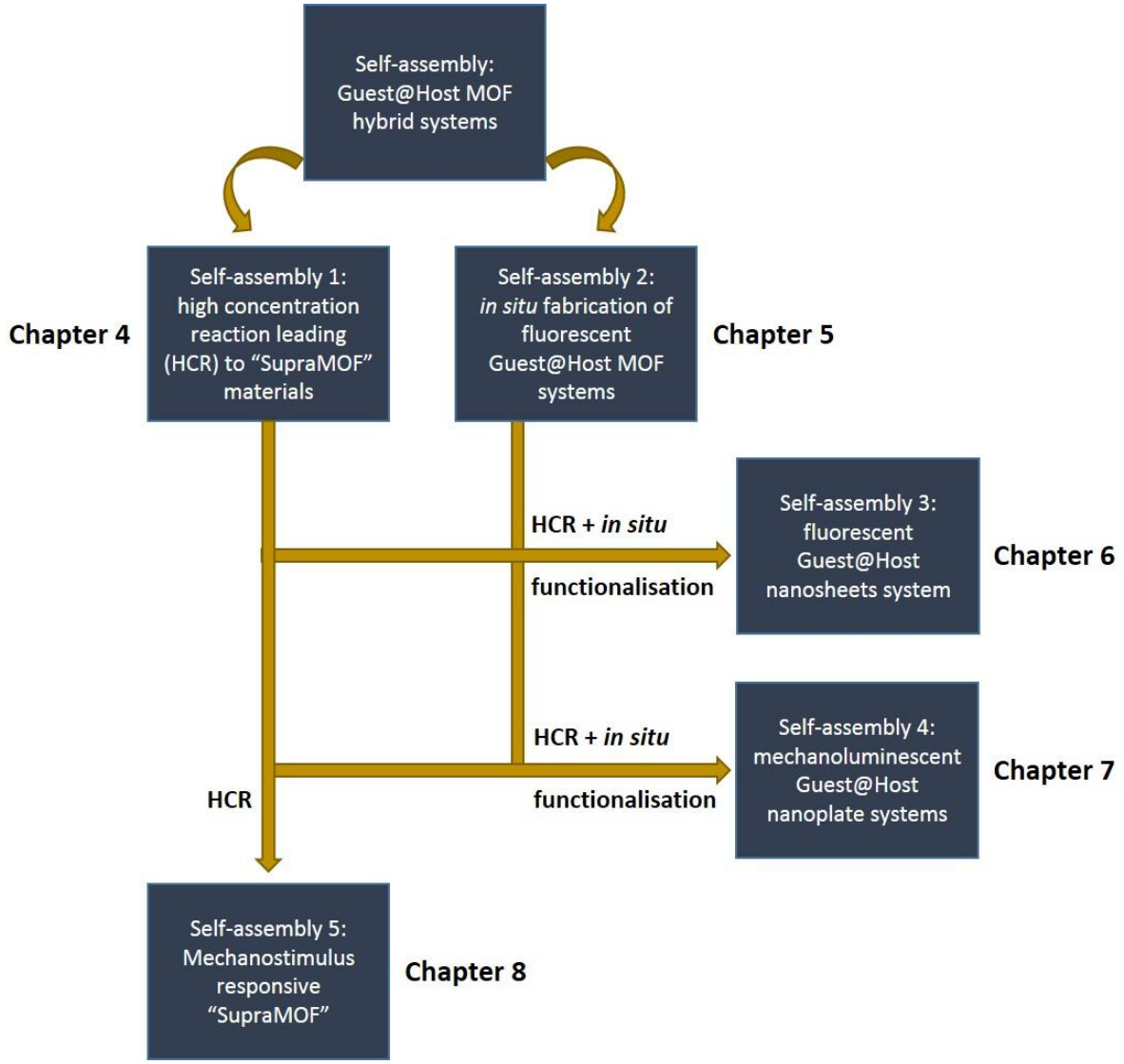

Figure 1.1 Flow chart summarising the scope of the original research work described in current thesis.

Chapter 9 is the concluding chapter, in which all major findings have been summarised and promising future research avenues are also presented. Figure 1.1 presents the complete picture of the original research described in this thesis.

Chapter Two

Literature Review

2.1 MOFs: Concept, Discovery and Progress

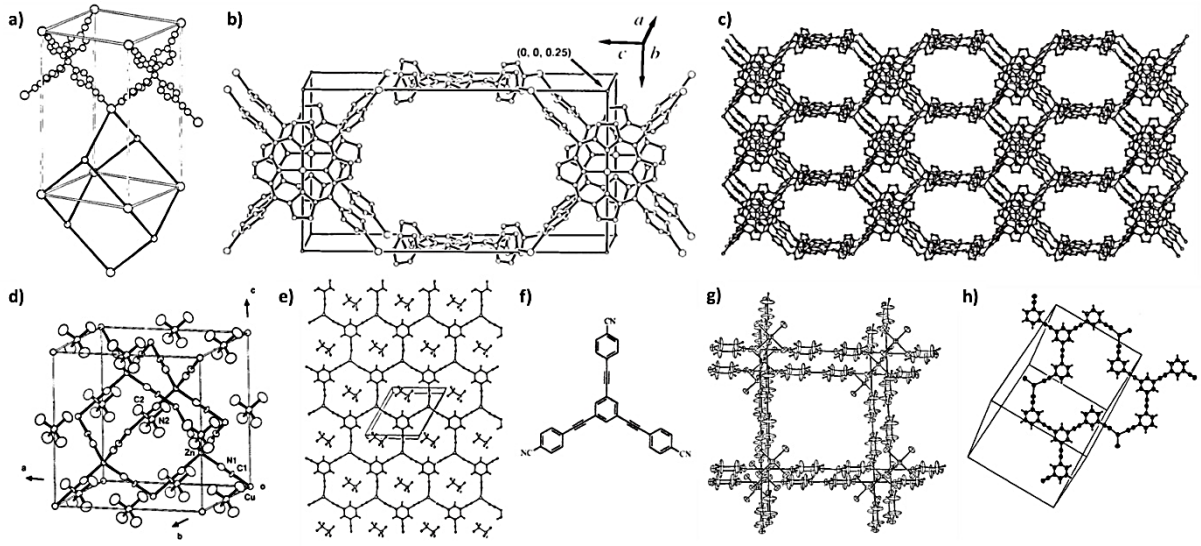

Figure 2.1 a) Structure of $Cu^{I}[C(C_6H_4{\cdot}CN)_4]$, large circles indicate Cu atoms), [1] b) unit cell structure of $[Cu^{II}(tpp)Cu^{I}]$, c) packing diagram of {$[Cu^{II}(tpp)Cu^{I}]$ showing porous channels along the *a*-axis, [1] d) unit cell of $[N(CH_3)_4][CuZn(CN)_4]$, [39] e) crystal structure of $[Ag(TCB)(CF_3SO_3)]$ along the *c*-axis, [40] f) organic linker TEB for making $[Ag(TEB)(CF_3SO_3)]$, g) structure of $Zn(4,4'\text{-bpy})_2]SiF_6$ along the *ab* plane, [41] h) structure of $[Ag^{I}(CF_3SO_3)]{\cdot}2C_6H_6$.

The idea of continuous network formation of metal and organic constituents was first envisioned by Robson and Hoskins in 1989.[1] Robson *et al.* expressed the thought of possible joining of tetrahedral and octahedral metal cores *via* organic bridging joints for the generation of well-ordered cavities in their report published in February 1989. With detailed structural study of $[Cu^{(I)}$-4,4',4",4"'-Tetracyanotetraphenylmethane$].BF_4$, Robson explained the possibility of making thermally stable, highly porous, solvent accessibly/exchangeable, ion accessible/exchangeable infinite ordered arrays of metal-organic compounds (Figure 2.1a-c). In his first reported compound, BF_4^- ion was

found to occupy pores of framework, which he successfully exchanged with other anions like $[PF_6]^-$. He showed ion exchange ability of the framework with the help of FT-IR vibrational spectroscopy. In July of the same year (1989), Robson came up with Zn(II) and Cd(II) based hetero-metallic framework compounds containing Cu(I) as another metal centre and showed the effect on the framework porosity that avoids interpenetration due to two metal centred coordination (Figure 2.1d).[39] Potential in metal-organic frameworks (MOFs) for multifunctional applications was realised from this report, which was further exemplified by other pioneering researchers of the field. Robson's efforts were mainly dedicated to the crystal engineering of framework materials with exotic properties like anion exchange, solvent exchange, non-interpenetration of framework, large porous channels etc.[42] Later Stephen Lee and co-workers from University of Michigan introduced a new dimension of inorganic-organic coordination networks by explaining interesting auxetic behaviour (negative Poisson's ratio) and negative coefficients of thermal expansion (NTE) of $[Ag(TEB)(CF_3SO_3)]$ framework structure (TEB: Figure 2.1f), which possessed features like honeycomb AlB_2 and hinge $ThSi_2$ type phases having internal pore dimensions of 15 Å (Figure 2.1e).[40] Surprisingly, they found that occluded C_6H_6 molecules in the pore could be exchanged by C_6D_6 without framework collapse. The same group later reported another Ag(I) based 2D framework material $[Ag(1)(CF_3SO_3)].2C_6H_6$ with high thermal stability up to 200 °C (Figure 2.1h). After a few reports of ionic framework compounds, the first neutral coordination network $[Zn(4,4'bpy)_2SiF_6]$ was reported by Subramanian *et al.* (Figure 2.1g).[41] $[Zn(4,4'bpy)_2SiF_6]$ found to constitute large square shaped hydrophobic channels of 11.39×11.39 Å^2 (8×8 Å^2 effective pore size) and SiF_6 as a coordinating organic linker instead of charge balancing anion.

As the field started to grow with slowly increasing number of framework compounds till 1995,[40] Omar Yaghi then professor at Arizona State University published similar example of framework compounds and coined the term 'metal-organic framework'[2] which was previously termed by other researchers as: coordination polymers, coordination networks, molecular building blocks, network structures, infinite polymeric frameworks etc. Today they are widely accepted by the name 'metal-organic frameworks' (MOFs) or by the other name- 'porous coordination polymers' (PCPs), a term coined by Prof. Susumu Kitagawa from Kyoto University, who is one of the pioneers and great contributors of the field. In his report, Omar Yaghi described a thermally stable (up to 350 °C) [$CoC_6H_6(COOH_{1/3})_3(NC_5H_5)_2.2/3NC_5H_5$] framework compound made from Co(II) and 1,3,5-benzenetricarboxylic acid (BTC).[2]

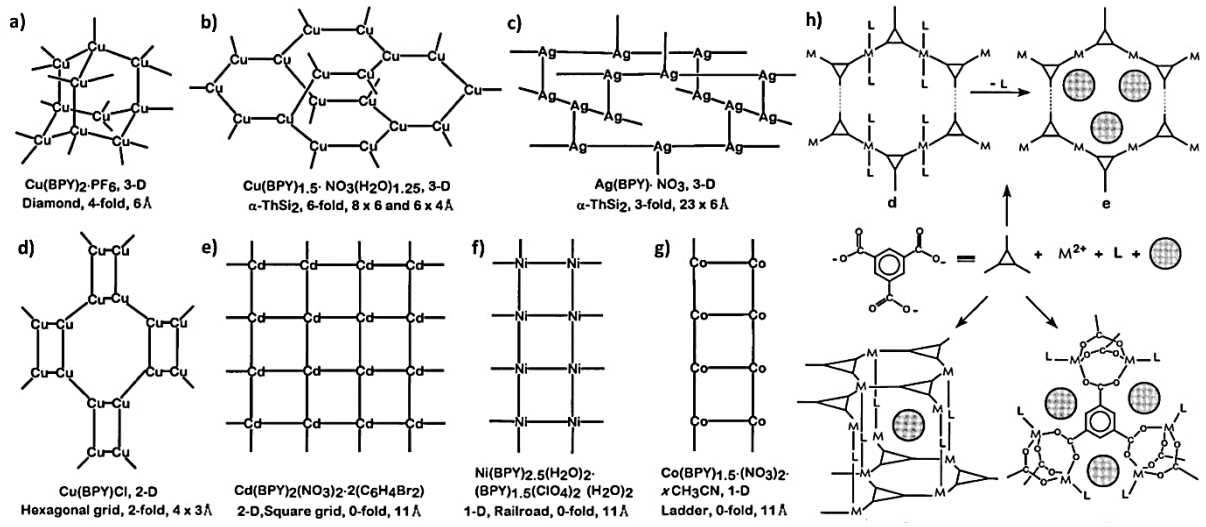

Figure 2.2 a) to g) M-bpy extended networks, line represents bpy (except vertical lines in c and horizontal lines in d), formula, type, pore dimension, interpenetration are mentioned beneath each structure; h) scheme representing different structural features originated from M-BTC motif combined with other organic linkers.[43]

Three years later in 1998, an extended review article was published by Yaghi and co-workers, in which the fundamental concepts, and strategies for making a variety of MOF compounds, including metal sulphides, M-4,4'-bpy ionic frameworks, neutral

frameworks from carboxylates, π-stacked frameworks, etc. had been covered (Figure 2.2.).[43] In this review several aspects of MOFs had been discussed concerning host-guest chemistry mainly ion exchange capability of frameworks (NMe_4^+ replacement by Cu^{2+}, Ni^{2+}, Zn^{2+}, Hg^{2+}, Cd^{2+}), high thermal stability of materials (up to 500 °C for Mn-Ge-S framework) and diamondoid topology.

2.2 High Surface Area MOFs for Gas Sorption

MOFs have been highly explored to date for their ability to store gas molecules. In 2001, Banglin Chen *et al.* reported the $[Cu_3(BTB)_2(H_2O)DMF_9(H_2O)_2]$ (MOF14) framework (Figure 2.3a,b) containing interwoven networks and pore dimension of 16.4 Å with capacity to store >400 mg/g of N_2 and >700 mg/g of Ar at 1 atm (Figure 2.3c).[44]

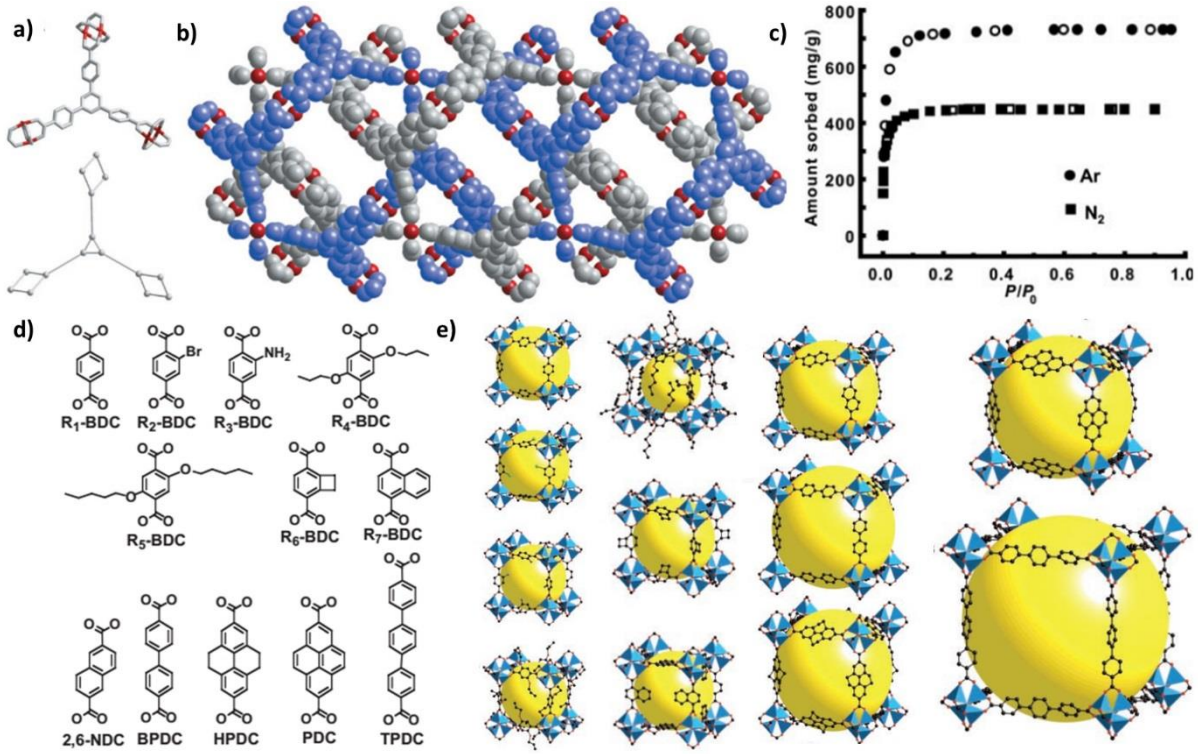

Figure 2.3 a) Structure of $[Cu_3(BTB)_2(H2O)_3]\cdot 9DMF\cdot 2H_2O$;[44] b) packing structure of $[Cu_3(BTB)_2(H2O)_3]\cdot 9DMF\cdot 2H_2O$ showing two interwoven networks in grey and blue colour for carbons; c) gas uptake by $[Cu_3(BTB)_2(H2O)_3]\cdot 9DMF\cdot 2H_2O$; d) a series of organic linkers used to synthesise e) different isoreticular MOF structures having different pore metrics.[45]

They reported the Langmuir surface area of 1502 m^2/g for the framework from gas uptake measurements. The same framework also revealed type-I sorption characteristics of CH_4 gas and for solvent vapours like CH_2Cl_2, CCl_4, C_6H_6, C_6H_{12}, and m-Xylene without any hysteresis. After realising gas storage capacity of MOFs, Eddaoudi *et al.* designed several MOFs for studying gas uptake and separation using MOFs.[45] In his report, a variety of organic linkages based on biphenyl, tetrahydropyrene, pyrene and terphenyl moieties were used (Figure 2.3d) to construct small to large pore sizes in the yielded framework compounds (Figure 2.3e). Their attempts resulted in the 16 highly crystalline materials with pore dimensions ranging from 3.8 Å to 28.8 Å, open space up to 91.1% and 240 cc/g uptake of CH_4 by one of the frameworks. Systematic characterisation of this MOF series showed promising strategy for synthesising new frameworks and their valuable gas storage capacities. Another systematic synthesis of 25 MOFs out of 9600 micro reactions was reported by Banerjee *et al.*, which contained Zn(II) and Co(II) metal centres with tetrahedral coordination environments in all the MOFs.[46]

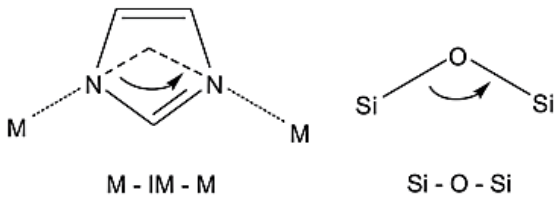

Figure 2.4 Bond angle similarity between imidazole (Im) based frameworks and zeolites as shown in the figure above.[47]

Yaghi and co-workers pointed out the similarities between Zeolites and a group of MOFs by comparing the Si-O-Si angle of Zeolites and M-N(linker)-N(linker)-M in MOFs (Figure 2.4).[47] The term 'zeolitic imidazolate frameworks' (ZIFs) was introduced for such MOF compounds, made from imidazole and its derivative based organic linkers.

Importantly, similar frameworks were reported by other researchers[37, 48] before actual report of Yaghi and co-workers in 2006. However, Yaghi is the first person to name them ZIFs and explore their porous properties in detail. ZIFs exhibited high surface areas, high gas uptake and high thermal stability. ZIF-8 is one of the ZIF compounds explored from many dimensions by researchers for its interesting structural features and ease of synthesis.

2.3 Functional MOFs or PCPs

One of the pioneers of the field, Prof. Susumu Kitagawa from Kyoto University, used the term porous coordination polymers (PCPs) instead of MOF since the term 'coordination polymers' was in the use from the early 1960s. A review article published by Prof. Kitagawa in 2004 addressed multi-dimensional properties of PCPs (MOFs).[3] the role of different organic linkers, types of linkers, contribution of different coordination numbers of metal centres, use of spectator guest species in PCP synthesis are key points discussed thoroughly in this review. Detailed understanding of the field and new concepts of PCPs were realised from this review article. Unlike previous reports on MOFs, Prof. Kitagawa sheds light on PCPs for their potential use as smart stimuli-responsive materials.

2.3.1 Construction of Functional PCPs/MOFs

Use of the Ag(I) or Cu(I) ions for making different coordination environments from different organic linkers, reaction conditions, solvents, pH, counter ions can be understood from the review article.[3] Importantly, it further pinpoints generation of unsaturated open metal sites, especially in lanthanide based ordered array of PCPs with the help of coordinated labile solvent molecules, which can be removed without framework collapse. Such unsaturated metal centres (UMCs) are very important for

use in chemical adsorption, heterogeneous catalysis or for sensing purposes. Since transition metal ions can form different coordination environments, a variety of shapes can be achieved in PCPs generated from linear, T or Y-shaped, tetrahedral, square-planar, square-pyramidal, trigonal-bipyramidal, octahedral, trigonal-prismatic, pentagonal-bipyramidal coordination geometries (Figure 2.5).[3]

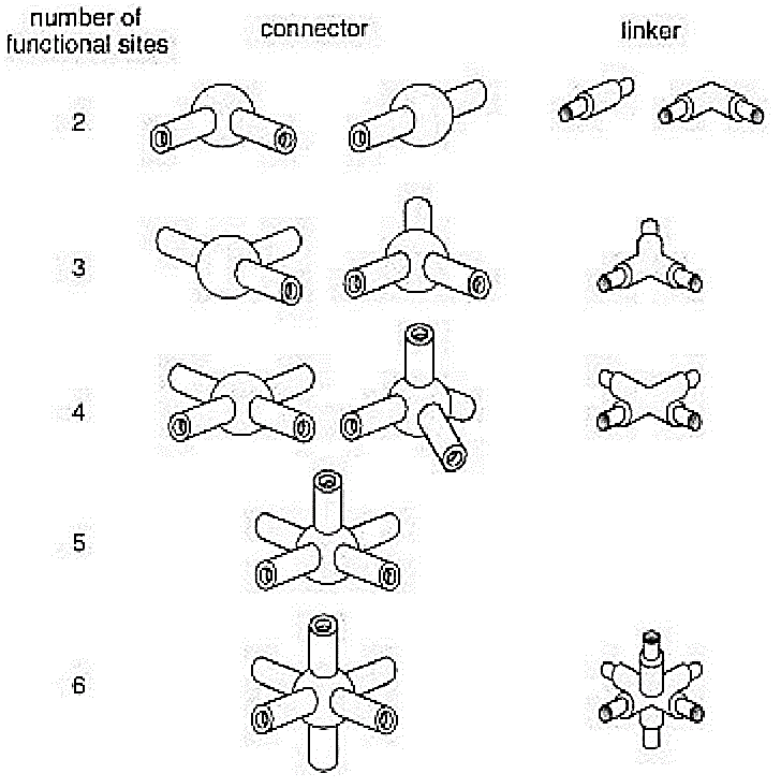

Figure 2.5 PCP components described by Kitagawa *et al.*[3]

To simplify the complexity in the way network forms, the term 'secondary building unit' (SBU) meaning metal clusters from one or more metal centres and organic linkers was introduced to classify topologies of different frameworks. To date, there are a wide range of topologies/nets reported in the literature for MOF/PCP materials.[49] Depending on the type of linkers and SBUs, different directionality in the framework can be attained such as the helical arrangements of channels to generate homo chiral frameworks. Such materials can be made purely from non-chiral constituents and

potentially useful for enantio-separations or asymmetric heterogeneous catalysis. Creation of continuous 1D chains of ionic species inside PCP channels *via* hydrogen bonding have a huge potential for facile proton conduction in solid state under various conditions of temperature and humidity.

Back in 2004, Kitagawa *et al.* describe the use of different anions like ClO_4^-, BF_4^-, NO_3^-, NCS^-, PF_6^-, NO_2^-, SiF_6^{2-}, CN^-, $CF_3SO_3^-$, SO_4^{2-}, N_3^-, Cl^-, F^-, I^- in addition to the organic linkers, and metal ions to neutralise the overall charge of the framework and ordered spatial arrangement of hydrogen bonded network of ions (Figure 2.6). Today, several PCPs/MOFs can be found in the literature, which exhibit high proton conduction due to trapped ionic species to facilitate ionic hoping in the porous channels. Many efforts were taken to avoid interpenetration in the framework, but Kitagawa and co-workers showed the advantages of interpenetrated frameworks in terms of high stability and dynamic response to the gas adsorption with hysteretic behaviour. Interpenetrated PCP like [Cu(1,4-BDC)(4,4'-bpy)$_{0.5}$] is an example of highly stable and dynamic adsorbent material. One of the important strategies to design functional PCPs/MOF reported is the use of metalo-ligand[50-51] as a linker for building continuous networks (Figure 2.7). Several advantages were realised from the use of metallo-ligands mainly i) functional porosity from functional linker, ii) adjustable coordination environment of metalo-ligand, iii) generation of Lewis acidic site, and iv) linking of framework through different connecting directions. $RuCl_2(pyz)_4$, $[Cr/Fe/Ru(ox_3)]^{3-}$, $[Cr(dto)_3]^{3-}$ are some of the instances of metalo-ligands, which assembled together *via* the additional metal centres and form 2D/3D arrays.[52-54]

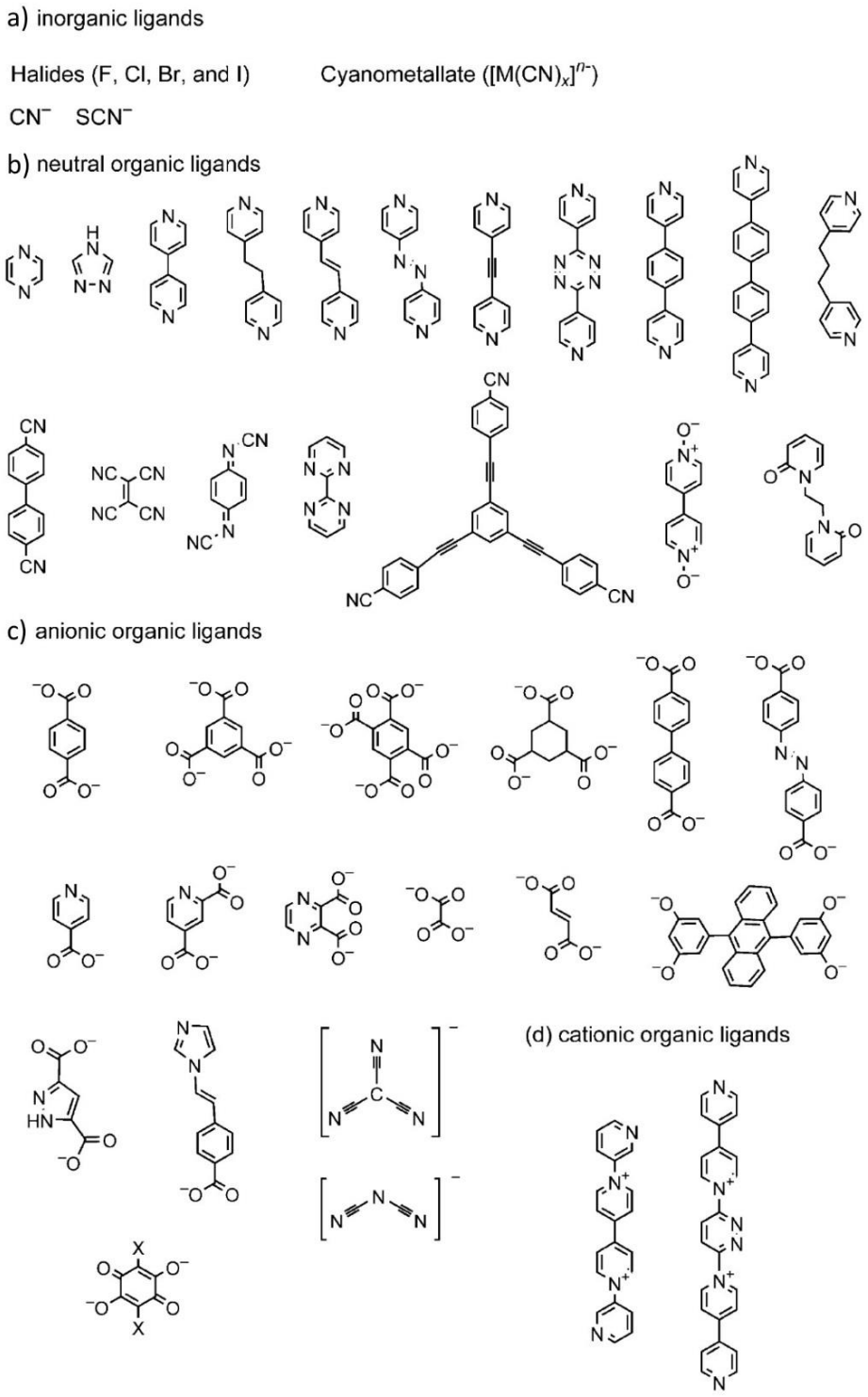

Figure 2.6 Different types of organic linkers to build PCPs that leads to different types of materials with adjustable pore metrics.[3]

Metallo-ligand can play very important role in generating UMCs and serve as orderly arranged reaction vessels for catalysis or site specific binders for foreign guest species. In [ZnCu(2,4-pydca)2(H_2O)$_3$(DMF)].DMF, Zn(II) are the centres of framework serve as connectors of metalo-ligand and Cu(II) centres are from metalo-ligand which possess UMCs available for guest coordination.[55] Interestingly metalo-ligands were found to provide robustness to the structure and generation of large coordination voids in the framework. PCP [$Zn_3Cu_2(OH)_2(salphdc)_2$]2DMF synthesised from metalo-ligand containing Cu(II) centres and simple Schiff base organic ligands found to generate large voids of 14 × 14 Å in the network joined by Zn(II) centres (Figure 2.7b).[56] Researchers also made analogous material by replacing Cu(II) by Co(II) with similar crystal lattice parameters.

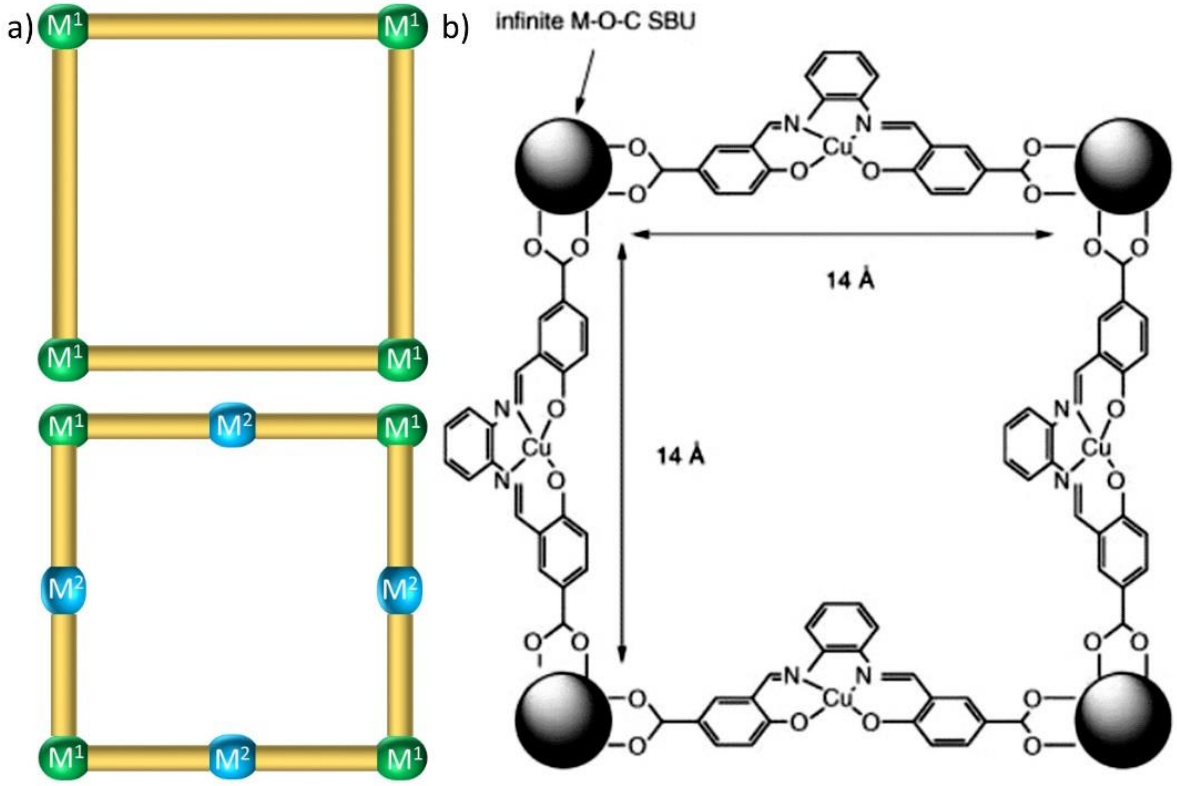

Figure 2.7 a) Sketch explaining possible generation of UMCs using metalo-ligand in PCP synthesis against pure organic linkers, M^1 (green) are metal centres constructing MOF and M^2 (blue) from metalo-ligand[50-51] b) an example of PCP [ZnCu(2,4-pydca)$_2$(H_2O)$_3$(DMF)].DMF with Cu UMCs.[56]

2.3.2 Classification of Functional PCPs/MOFs

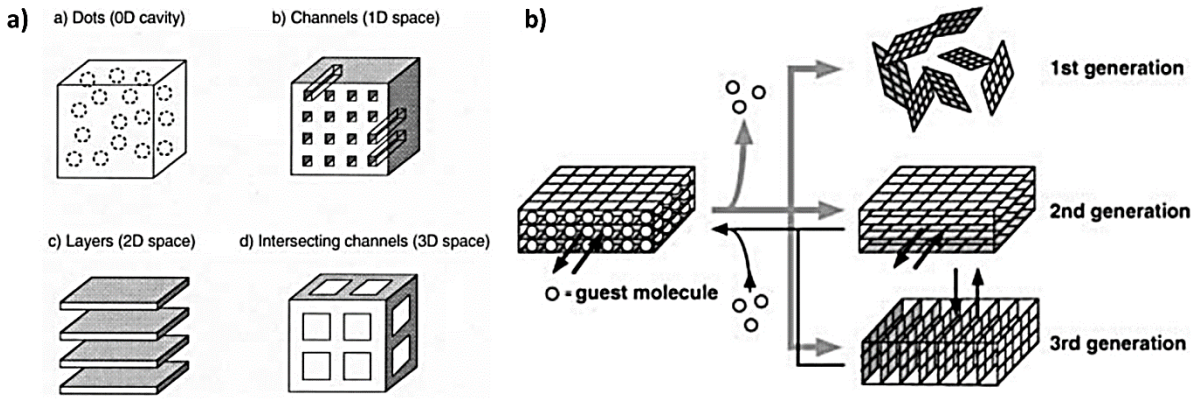

Figure 2.8 Pore type based classification of porous materials, b) different generations of porous materials.[3]

Based on porosity, porous structures can be subdivided into four categories *viz*. A) dot structures with 0D cavities; B) Channel structures with 1D space; C) layered structures with 2D space; and D) intersecting channel materials with 3D space (Figure 2.8a).[3] And based on the guest response to the framework structure upon its removal and re-inclusion, materials can be categorised into: 1st, 2nd and 3rd generation materials (Figure 2.8b). 1st generation PCPs collapse upon removal of trapped guest species, 2nd generation stays intact without change in the framework dimensions, however 3rd generation are multifunctional PCPs which sustain upon removal of guest species, but at the same time will change the structural features upon re-inclusion of foreign guest species. Because of such structural changes in the framework, PCPs/MOFs with such properties are called dynamic or flexible frameworks. Such dynamic systems were found to behave in an interesting fashion and offered various smart applications in selective molecular storage, solid state sensors *via* solid state structural changes, etc.[6] Molecular weak interaction sites within framework towards guest species are important factors playing a vital role in achieving smart 3rd generation materials. In some cases weak interactions are the main reason for keeping frameworks intact. For example, in

the case of compound $Cu(ca)(ROH)_2$ different layers are separated (8.45 Å Cu to Cu distance of alternate layers) by the hydrogen bonded guest species hold together by the (ca) and ROH linkers (Figure 2.9),[57] where the removal of trapped species by heating collapses the framework structure.

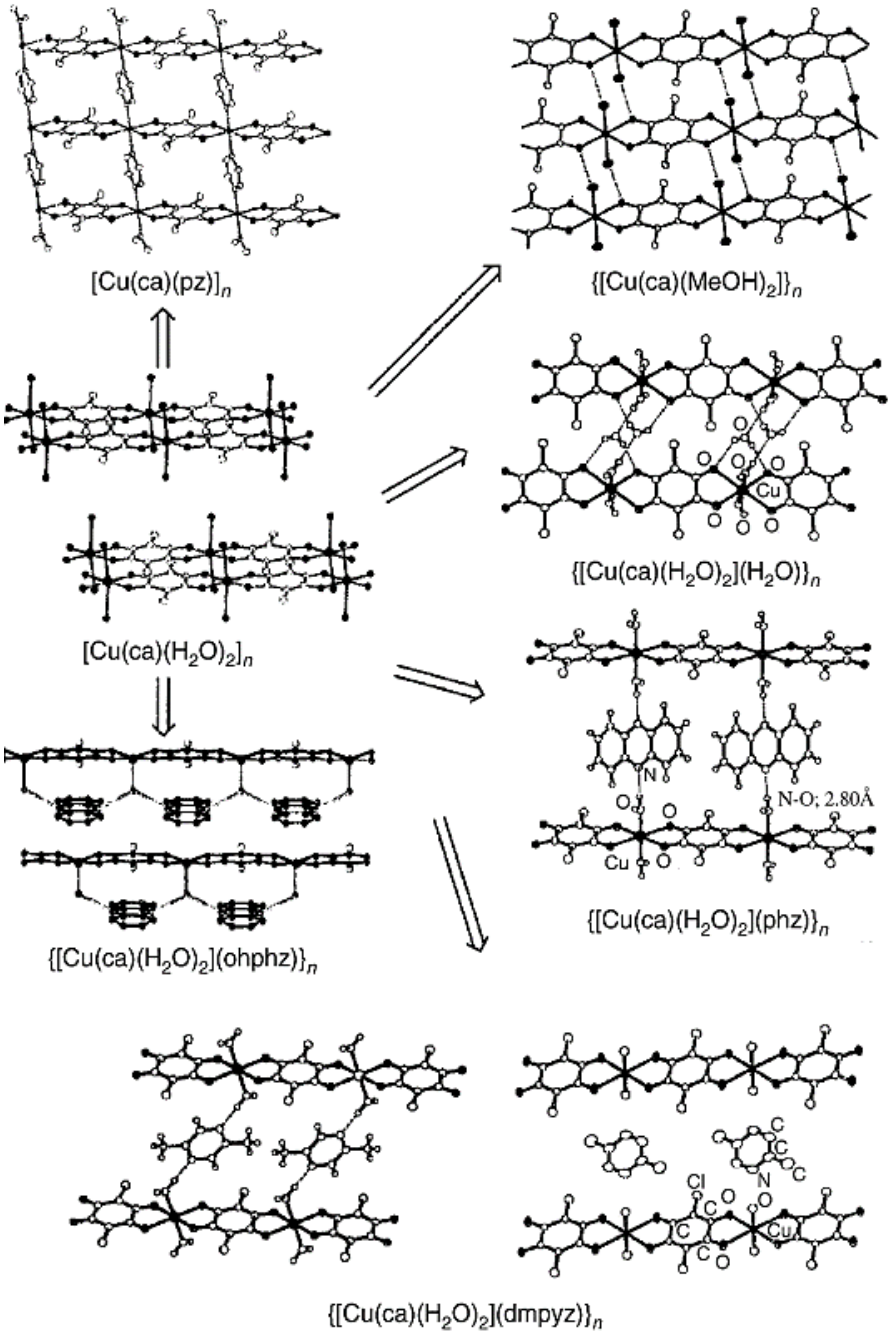

Figure 2.9 Guest-induced dynamic structural response of $Cu(ca)(H_2O)_2$.[57]

However, some stacked layered structures exhibit dynamic response without underpinning structural collapse. Layered compound $Cu(ca)(H_2O)_2 \cdot phz$ containing aromatic stacks of phz molecules shows the separation distance of 8.45 Å between layers, which can be expanded up to 11.0 Å stabilised by π-π interactions and hydrogen bonding.

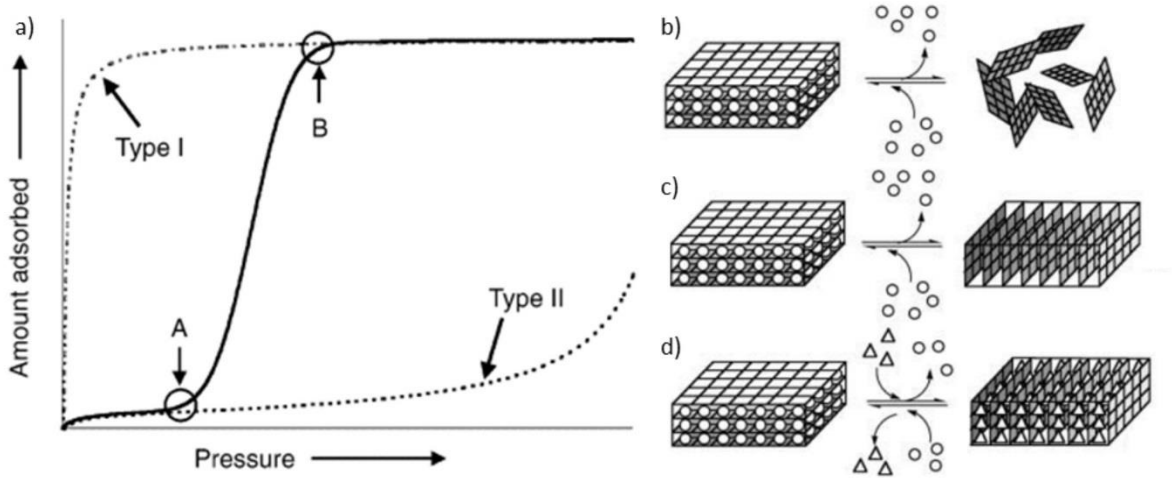

Figure 2.10 a) Smart sorption isotherm observed in the case of flexible PCP material that tend to show structural changes during sorption measurements, guest induced transformations shown in b-d, b) represents crystal-to-amorphous transformation (CAT, 3rd I), c) tyep 1 crystal-to-crystal transformation (CCT, 3rd II-1), d) tyep 2 crystal-to-crystal transformation (CCT, 3rd II-2)[3]

Dynamic framework systems always exhibit interesting sorption properties. Gate opening behaviour (due to structural transition) with combination of type I, II, II sorption isotherm can be seen in such materials (Figure 2.10a).[3] Such effects mainly occurred from making and/or breaking of the weak interactions of frameworks. Based on the guest responses to the dynamic frameworks, further classification was introduced by Kitagawa and co-workers. Frameworks with guest induced crystal to amorphous phase are called type 3rd-I (CAT: crystal to amorphous transformation) and crystal to crystal change called type 3rd-II (CCT: crystal to crystal transformation) frameworks (Figure 2.10b-d).

2.3.3 Structural Dynamics in PCPs/MOFs

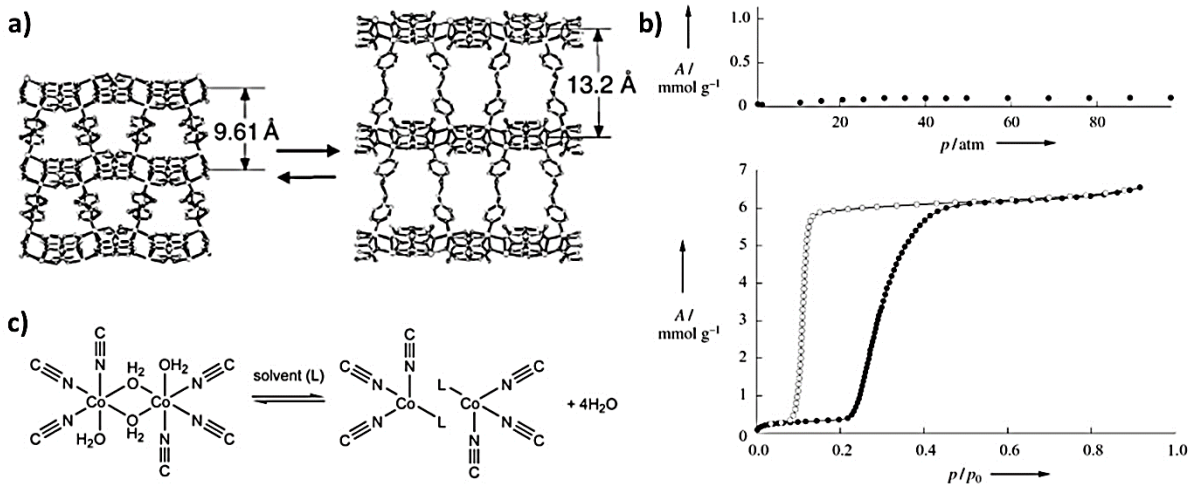

Figure 2.11 a) Reversible solid–state crystal structure change in the case of [Cu_2(pzdc)(dpyg)],[58] b) negligible gas uptake (top) but dynamic methanol sorption behaviour (bottom) of [Cu_2(pzdc)(dpyg)], c) bond cleavage assisted structural change observed in cobalt based PCP.[59]

Kitagawa *et al.* expressed their idea of flexibility against robustness and bistability against single stability in their review article.[3] Smart structural changes due to guest activities are not very common in the case of materials. PCPs/MOFs show bistable feature originated from weakly interacting species like labile solvents namely H_2O, alcohols, ketones, ethers, aromatic/aliphatic small molecules, etc. 3D pillar layered structure [Cu_2(pzdc)(dpyg)]·8H_2O exhibit interesting structural transformation by adsorption and desorption of H_2O, MeOH molecules (Figure 2.11a).[58] Detailed study using synchrotron powder X-ray diffraction revealed 27.9% of cell contraction and layer separation from 9.6 Å to 13.2 Å upon adsorption-desorption process. Interestingly, N_2 and CH_4 were not adsorbed by the framework, unlike H_2O or MeOH (Figure 2.11b). Structural changes in the framework were found to occur near the Cu(II) centres, where carboxylate bond breaks and reforms with transformation of the whole network from 3D to becoming 2D interpenetrating. Jahn-Teller distortion is one

of the main reasons for structural changes at Cu(II) site, where axial bond elongation could happen. Very weakly interacting solvents like diethyl ether showed structural changes in Co(II) based frameworks $[Co_2(H_2O)_4][Re_6O_8(CN_6)]\cdot 10H_2O$ and $[Co(H_2O)_3]_4[Co_2(H_2O)_4][Re_6O_8(CN)_6]\cdot 44H_2O$.[59] Bond making and breaking of Co-$O_{(ether)}$ cause the structural change and indirectly affects compound colour (Figure 2.11c). Reversible colour change occurs in visible light from orange to dark blue-violet upon evaporation of diethyl ether and re-inclusion of ether into the structure. Today, several examples can be found in literature about guest induced expansion-contraction of crystal cells, sliding of 2D layers, open-close forms of interpenetrated networks.[60-64]

2.3.4 Dynamics in MOFs/PCPs for Gas Sorption

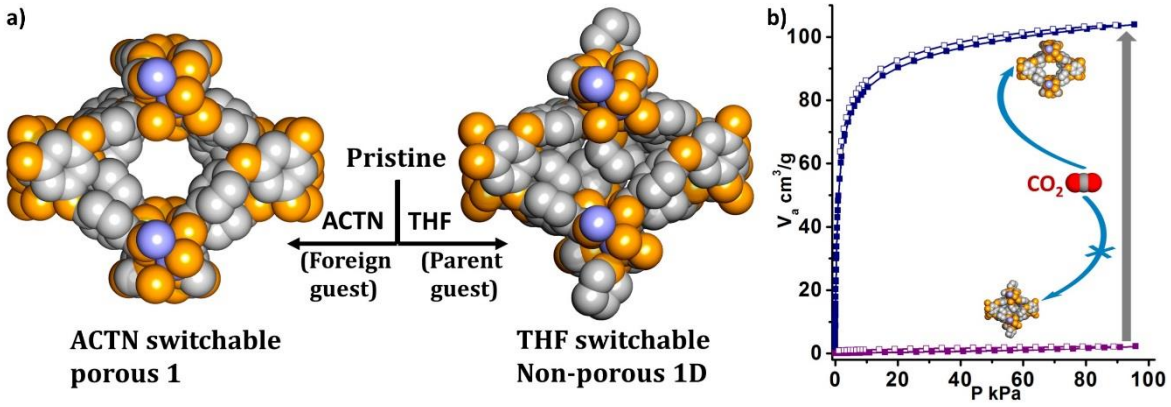

Figure 2.12 a) Guest assisted dynamic structural transformation that causes closing and opening of pores in $[Cd_{1.5}(L)(H_2O)]\cdot G$, b) pore opening and closing evidenced from dramatic change in sorption amount of CO_2.[65]

A notable example of guest–induced locking and opening of framework porosities can be found in Cd(II) based PCP reported by Chaudhari *et al.*(Figure 2.12).[65] Intentional design of flexible organic linker bearing 'O' atom as an aromatic ring connector and a

framework $[Cd_{1.5}(L)(H_2O)]\cdot G$ made with same linker having coordinated water to the Cd centre was found to play a vital role in achieving several guest stimuli triggered single crystal-to-single crystal (SC-SC) transformations in the material. Initial coordinated water upon keeping crystals at RT out of mother liquor solution can be replaced by THF guests residing inside the voids. This alters the cell dimensions and causes locking of the pores. However, opening of framework porosity without occluding guests and coordinated H_2O or THF molecules successfully attained *via* guest replacement step before taking crystals to RT using labile acetone solvent.

Interestingly coordinated THF does not get detached from the Cd centre by heating the crystals, but acetone substituted structure serves the purpose and generates UMC at Cd centre. Other guest like 1-Butanol also coordinates to Cd(II) UMC and supports the breathing behaviour of pores. This framework locking and unlocking phenomenon was strongly evidenced from the CO_2 uptake in two different phases obtained by SC-SC transformations. An example of such SBU with flexibility in the linker as well as in the coordination environment would be very promising in terms of designing sensors for incoming guest species. Another noteworthy example of flexible PCP for smart molecular uptake is $Zn_2(BDC)_2(TDAN)$.[66] This compound was reported by Yanai *et al.* with detailed explanation of its ability to host external UV–sensitive guest Azobenzene (AB). Reversible configuration changes in molecule AB from cis to trans triggered by UV irradiation and heating allows the tuning of the pore dimensions in the PCP after inclusion of AB inside the pores (Figure 2.13a). This dynamical behaviour of pores were claimed and understood by investigating the sorption amounts of framework with and without UV irradiation and PXRD structural changes due to UV-heating processes (Figure 2.13b, c). PXRD pattern shows changes in the structure due to the inclusion of AB, which further alters the structure

upon UV irradiation and heating at 120 °C. From sorption studies, it was evidenced that uptake increases by almost 8.3 times upon UV irradiation with 45 ml/g of N_2 compared with <10 ml/g uptake for non UV-irradiated PCP.

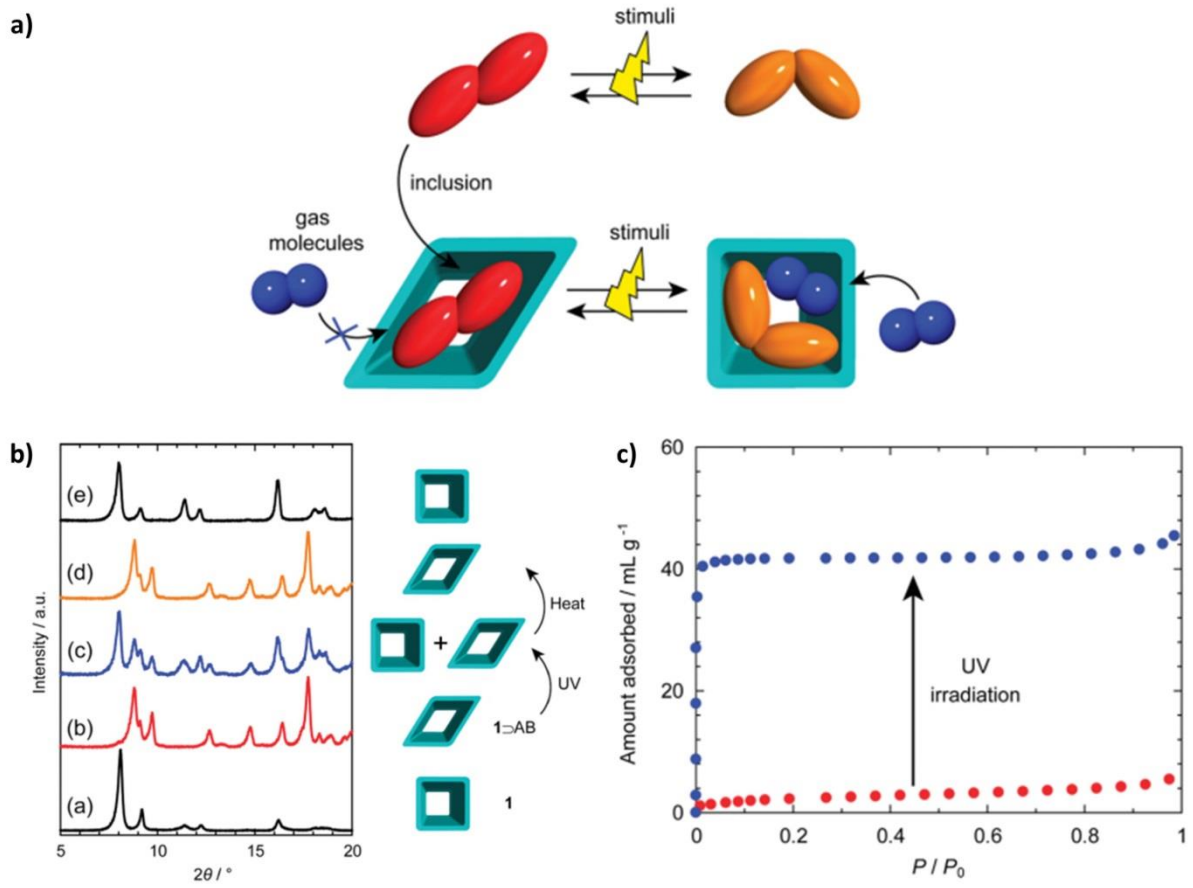

Figure 2.13 a) Schematic representation of guest assisted structural changes of porous channel in $Zn_2(BDC)_2(TDAN)$, which were used as a way to switch from porous to non-porous form of PCP, b) PXRD structural changes showing effect of UV and heat on PCP, c) using smart response of PCP, porosity was enhanced by many folds evidenced from sorption isotherm shown in Figure.[66]

2.3.5 Functional PCPs/MOFs for Proton Conduction

PCPs/MOFs offer continuous 1D/2D channels with a tuneable internal environment of weakly interacting guest species, which can be exchanged with other guests. Researchers have shown that channels of PCPs/MOFs are useful for conduction of protons. Facile proton mobility at higher temperatures (~120 °C) in materials is the

prerequisite for their use in fuel cells. Therefore, for fuel cell technology, material should withstand such high temperatures with simultaneous facile proton conduction. Kitagawa and co-workers used the channels of PCPs/MOFs to accommodate heterocyclic imidazole molecules, which possess ability to make strong hydrogen bonding (Figure 2.14a-c).[67]

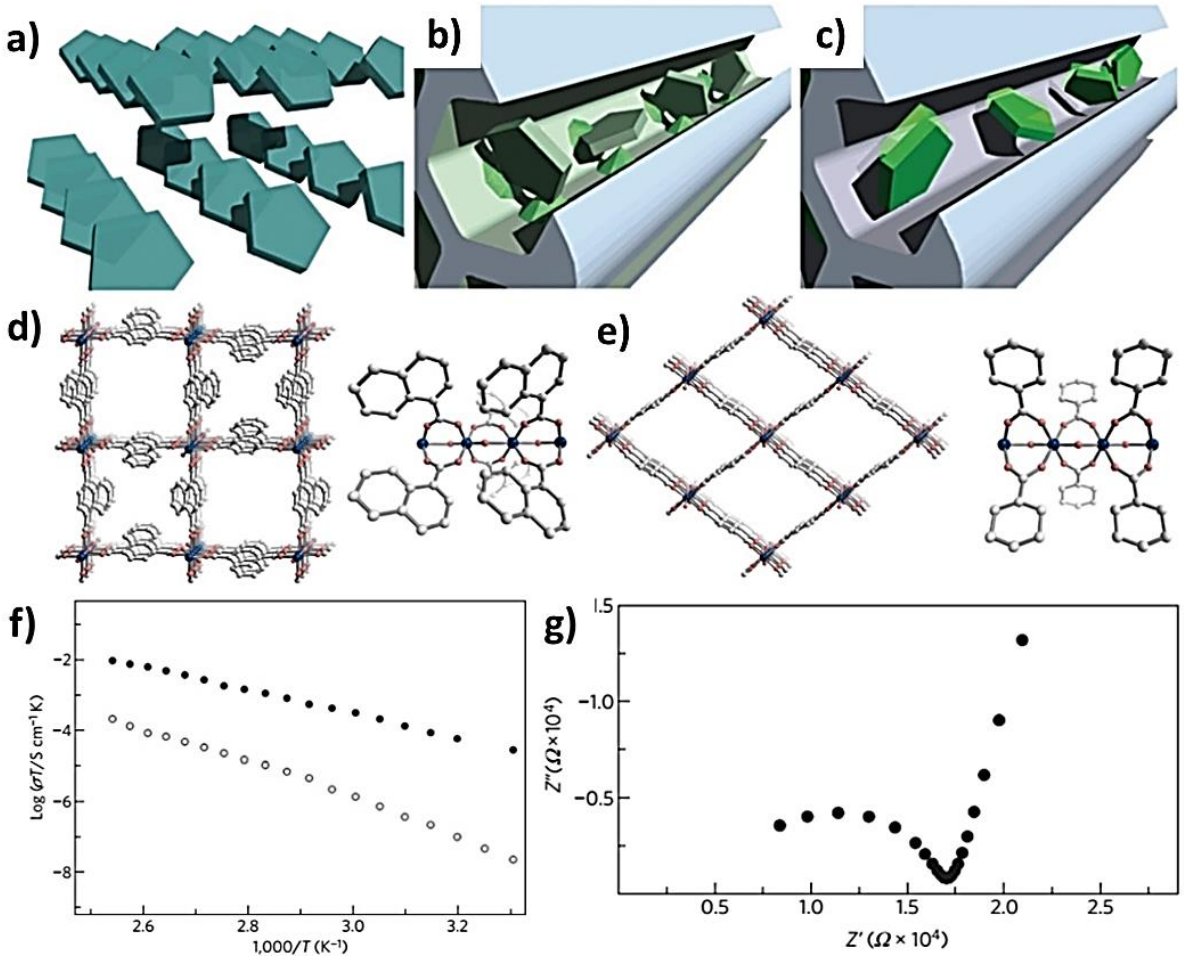

Figure 2.14 a) Schematic showing closely packed imidazole molecules in its pure form, b) strongly–interacting imidazole molecules with internal walls of PCP by weak molecular interactions, c) weakly–bound imidazole allowing more facile mobility of proton in porous channels of PCP, d) packing structure (left) and basic unit (right) of Al(OH)(1,4-ndc), e) packing structure (left) and basic unit (right) of Al(OH)(1,4-bdc), f) proton conduction of Al(OH)(1,4-ndc)⊃Im, (solid circles) and Al(OH)(1,4-bdc)⊃Im, (open circle), g) Nyquist plot of Al(OH)(1,4-ndc)⊃Im.[67]

High proton conduction was explored by tuning the hydrogen bonding interactions of imidazole guest with the help of bi-porous channels of Al(OH)(1,4-ndc) and porous channels of Al(OH)(1,4-bdc) (Figure 2.14d,e). It was shown that only imidazole molecules on their own aggregates in a dense spatial arrangement due to the strong hydrogen bonding and reduces proton mobility (Figure 2.14a). However, their well-ordered spatial arrangement in PCPs allows variable interaction based on channel size, interacting sites of pore in PCPs etc. (Figure 2.14b, c). A significant increase of proton conduction from host-guest interactions was evidenced from their measurements. Guest free Al(OH)(1,4-ndc), and Al(OH)(1,4-ndc)⊃Imidazole exhibit 10^{-13} S/cm and 5.5 × 10^{-8} S/cm conductivity, respectively.

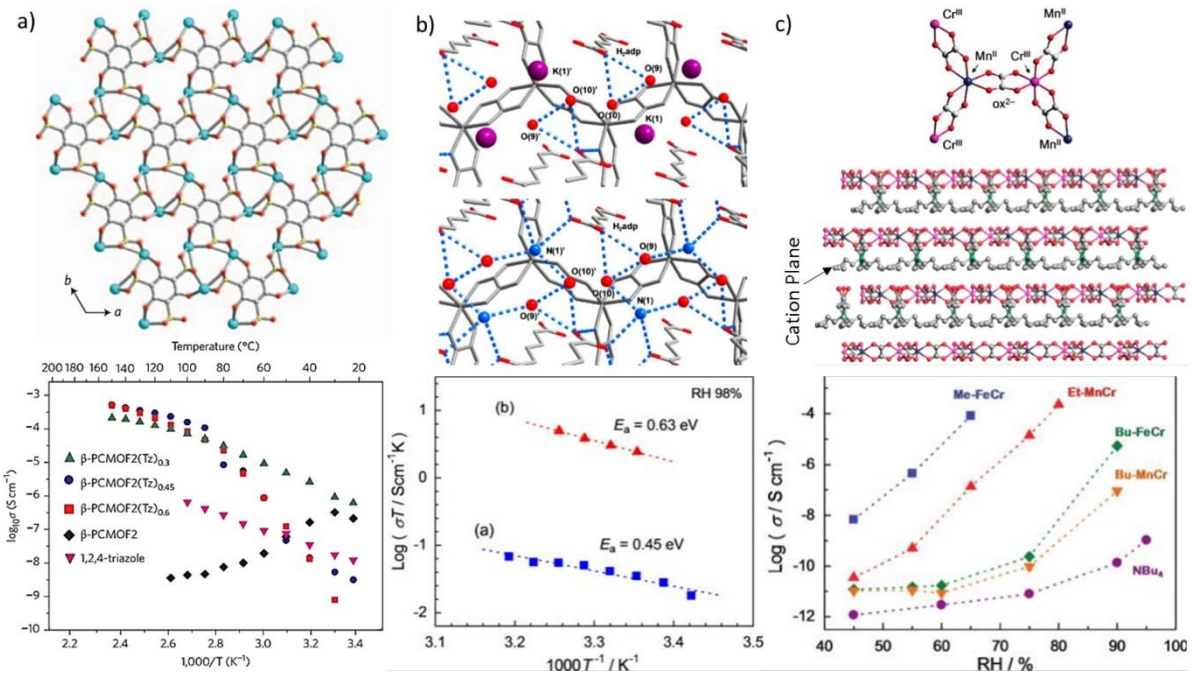

Figure 2.15 a) Structure (top) of β-PCMOF2 (S: yellow, Na: cyan, C: grey, O: red) and its proton conduction behaviour at different temperatures (bottom),[68] b) structure of $K_2(H_2adp)[Zn_2(ox)_3]\cdot 3H_2O$ (top) and $(NH_4)_2(H_2adp)[Zn_2(ox)_3]\cdot 3H_2O$ (middle), (K: pink, N: blue); bottom graphs shows proton conduction of $K_2(H_2adp)[Zn_2(ox)_3]\cdot 3H_2O$ (blue squares) and $(NH_4)_2(H_2adp)[Zn_2(ox)_3]\cdot 3H_2O$ (red circles);[69] c) structure of Bu-MnCr and its packing showing the plane of cationic species present between planes of oxalate framework (top), variation of proton conduction with the change in structural unit of cationic plane (bottom).[70]

Temperature rise also improves conduction from 5.5×10^{-8} S/cm to 2.2×10^{-5} S/cm at 120 °C.The difference in the imidazole mobility for proton hopping in its pure form, in Al(OH)(1,4-ndc) and in Al(OH)(1,4-bdc) was clearly observed from their conductivity values and from ^{2}H solid state NMR spectroscopy. From ^{2}H solid state spectra, peak splitting at lower temperatures and sharpening of peak at high temperatures with single peak profile in the case of Al(OH)(1,4-ndc)⊃Im (deuterated) revealed the directional activity of occluded guest Imidazole molecules with rise in temperature for facile proton conduction. Later Prof. Shimizu reported example of MOF called β-PCMOF2 made from Na(I) and 2,4,6-trihydroxy-1,3,5-benzenetrisulfonate, which exhibits high proton conduction at high temperatures (~150 °C) (Figure 2.15a).[68] In this case also, the advantage of N-heterocycles for hopping of protons was utilised inside the 3D porous chemically active scaffold of β-PCMOF2. Since MOF constructed from the linker constituting sulfonate donor group, framework channels decorated with hydrogen bond donating SO_2 and OH groups in addition to the externally added heterocyclic guest species. The importance of guest species was realised from the decrease in proton conduction above 70 °C in the case of non-guest containing framework and increase in conduction up to 5 X 10^{-4} S/cm at 150 °C for 1H-1,2,4-trizole (Tz) loaded β-PCMOF2. Loss of proton due to dehydration upon heating and eventual decrease in proton conduction was intentionally avoided using Tz guest insertion into the channels of β-PCMOF2, which can serve as a source of protons to hop in the hydrogen bonded network within the channel. Considering potential in MOFs for H^{+} conductions, several other frameworks were reported by MOF researchers, with major contribution from Prof. Hiroshi Kitagawa from Kyoto University. H. Kitagawa and co-workers have developed MOF systems with deliberately introduced different guests inside channels by ionic exchange, and

monitored high proton mobility.[69-70] They proved the importance of hydrogen bonding inside MOF channels for proton hopping by cation substitution using cations which can either promote or inhibit hydrogen bonding. In specific, oxalate–based framework $[Zn_2(ox)_3]\cdot H_2adp\cdot 2NH_4\cdot 3H_2O$ containing hydrogen bonded ammonium (NH_4) cations was successfully transformed into framework containing non-hydrogen bonded K^+ cation of formula $[Zn_2(ox)_3]\cdot H_2adp\cdot 2K\cdot 3H_2O$ without losing crystallinity of the framework (Figure 2.15b).[69] It was found that $[Zn_2(ox)_3]\cdot H_2adp\cdot 2K\cdot 3H_2O$ exhibited lower proton conductivity of 1.2×10^{-4} S/cm at 25°C and 98% RH compared to the 0.8 X 10^{-2} S/cm exhibited by $[Zn_2(ox)_3]\cdot H_2adp\cdot 2NH_4\cdot 3H_2O$ at the same conditions. The decrease in proton conductivity and single crystal structural features were direct evidences for proving the fact of hydrogen bonding role in conducting the protons. The same research group explored the effect of hydrophilicity in altering the proton conduction. MOF with same organic linkers but with hetero metal centres were designed possessing charge neutralising cations. A series of frameworks of common formula $[NR_3(CH_2COOH)]\ [M\cdot Cr(ox)_3]$, (where R = Methyl, Ethyl, Butyl and M= Fe, Mn) were made to check the effects on proton conduction (Figure 2.15c).[70] Sandwich layers of cations NR_3, offer the tuning of hydrophilicity of the framework channels. Among all frameworks, $[NMe_3(CH_2COOH)]\ [Fe\cdot Cr(ox)_3]$ has the highest hydrophilicity due to methyl group in cation and presence of Fe which allows high sorption of water molecules inside the framework promoting high proton conduction. Figure 2.15c shows the trend observed in conductivity with variable %RH, which reveals the order of framework hydrophilicity.

A noteworthy report based on proton conductivity triggered by solvent guests was documented by Joseph Hupp and co-workers (Figure 2.16).[71] In their study, one of the most studied MOF called HKUST-1 bearing easily achievable UMCs at Cu(II)

sites was used to attain variable and promising proton conduction. UMC sites were used to coordinate water molecules and then different solvent species with varying degree of interaction with H_2O were introduced into the porous channels of HKUST-1 to modify proton conduction of the pristine framework (Figure 2.16a). Water coordination to Cu(II) UMCs or other solvent coordination and occlusion were monitored using H^1 NMR study. It was found that coordination of other non-protonic solvent at Cu(II) reduces the conduction as other solvents without proton do not help in proton Grotthuss-type hopping mechanism. Moreover, other protonic solvent coordination like MeOH or EtOH with lower acidity compared to H_2O exhibit lower proton conductivity as H_2O possesses almost 30 times higher acidity (pK_a = 14.0) to that of methanol (pK_a = 15.5) and 32.5 times higher to that of ethanol (pK_a = 15.9).

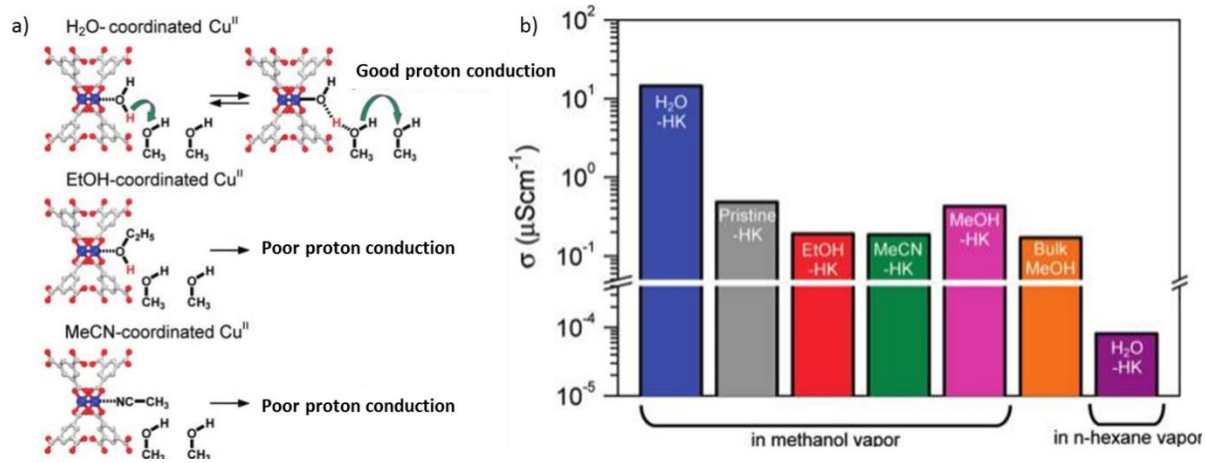

Figure 2.16 a) Representation of variation in proton conduction response observed by replacement of coordinating and interacting solvents, b) bar chart that compares the observed proton conduction in HKUST-1 by switching coordinating solvent and the guest solvent.[71]

Therefore, water coordination to UMCs plays a significant role and among occluded guests methanol helps in extracting proton from coordinated water and its further conduction in HKUST-1 channels. Comparison of the conductivities of different guest

vapours were performed using an exposure of H_2O coordinated HKUST-1 to the vapours of methanol, ethanol, acetonitrile and hexane. It was found that hexane exposure lowers the conductivity compared to the higher conductivity for ethanol exposed framework, and the highest was observed from methanol exposed framework (Figure 2.16b).

2.3.6 MOF based gel materials

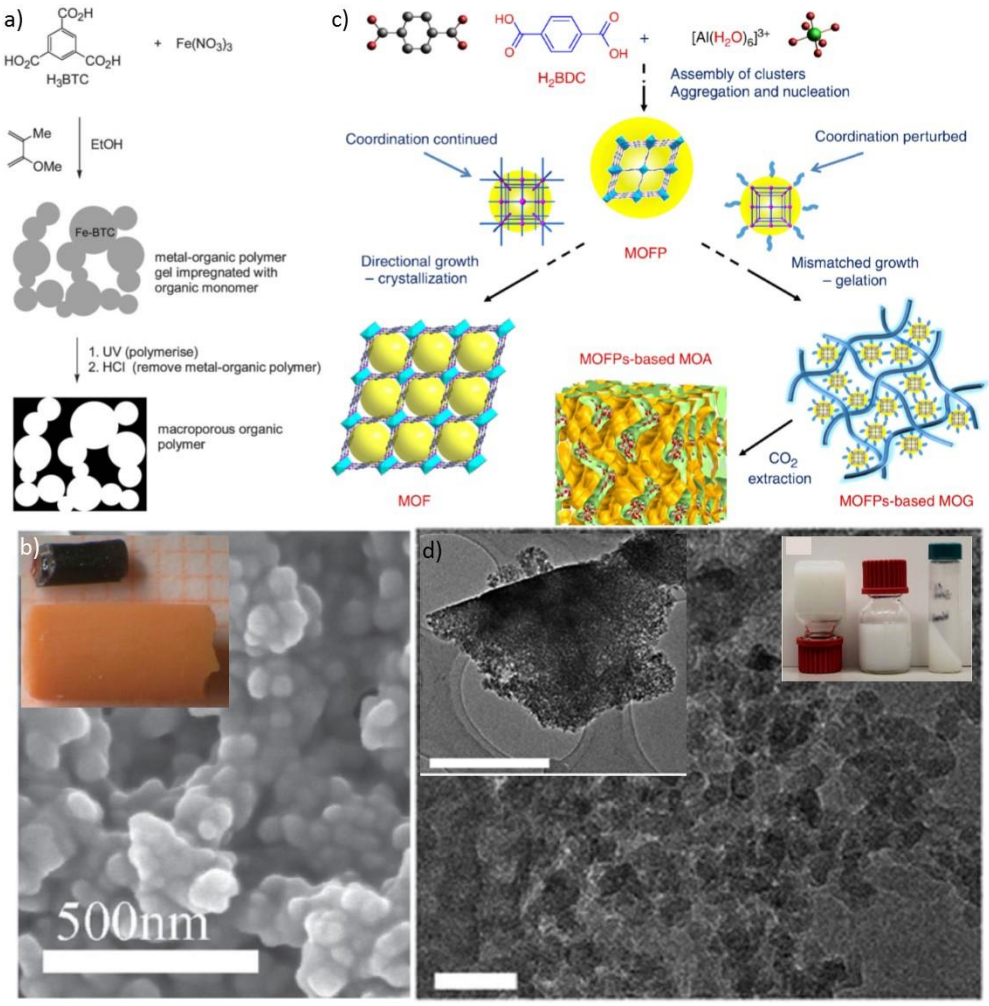

Figure 2.17 MOF based gel materials a) Fe-BTC based gel material used as scaffold for UV assisted polymerisation[72] b) SEM image of Fe-BTC based metal-organic gel showing MOF particles aggregated together, inset: xerogel (black) and wet monolithic gel (brown),[73] c) scheme showing formation of MOF based gels from Al(III) and BDC system,[74] d) recent report on MOF based gel using UiO-66 MOF components ($ZrOCl_2$ and BDC), figure shows fine constituents of gels observed under TEM, inset: larger picture seen under TEM and other inset shows successful gelation evidenced by tube inversion method.[75]

Like conventional low molecular weight gel materials, some MOF systems tend to form gels upon aggregation of MOF particles. Early report in 2005 by Stuart James and co-workers documented the formation of gel material from $Fe(NO_3)_3.9H_2O$ and 1,3,5-Benzenetricarboxylic acid.[72] In their report, it is described that cross linking between metal ions and organic linkers lead to coordination polymerisation, which generates coordination polymer particles. Coordination polymer particles further cross link to each other leaving macroscopic spaces behind for solvent molecules to trap. Entire process then results into the hybrid gel material. Interestingly, same gelation also occurred in presence of other organic polymer precursors, which allowed polymerisation process to happen in presence of gel material (Figure 2.17a). Such example of scaffolding for polymerisation using metal organic gels was claimed to be the first example by the authors. Later, similar Fe-BTC based gel material was reported by Martin Lohe *et al*. in 2009.[73] The detail study of gel composition, monolithic aerogel formation (Figure 2.17b inset), and porosity estimation by N_2 sorption had been carried out by Martin Lohe *et al*. Their results from SEM (Figure 2.17b) and elemental analysis directly showed the evidence of MOF particle formation with the formula $Fe^{(III)}{}_3O(C_6H_3(COO)_3)_2NO_3$ matching exactly with the MIL-100(Fe) compound. In 2013, Li *et al*. reported series of Al(III) containing MOF based gel materials (Figure 2.17c).[74] Their report describes the use of rigid linker and Al(III) for creating light weight metal organic aerogels. Synthetic mechanism and possible route for the formation of metal-organic framework and metal-organic framework particle assisted gel network were clearly depicted/described in their report. Furthermore, this report sheds light on the transition in structure of gel material to that of aerogel and, comparison of dry gel powder pattern with the simulated PXRD pattern of MIL-53(Al) structure. Li *et al*. explored the surface area, pore volume, gas (N_2, CO_2, H_2) and vapour (benzene, n-

hexane, methanol) sorption properties of several combinations of Al(III):BTC and BDC based gel materials, to show the significance of MOF aerogel material over pure MOF compounds. Moreover, dye separation study was also conducted in their study explaining efficiency for liquid state dye molecular separation from water in comparison with the conventional polymer membranes (Polydimethylsiloxane). Recently this year, Bart Bueken *et al*. documented series of Zr^{4+} containing MOF based gel materials involving gel material of UiO-66-X (X :H, NH_2, NO_2, $(OH)_2$), UiO-67, MOF-801, MOF-808 and NU-1000 (Figure 2.17d).[75] With careful air and supercritical CO_2 drying, they derived high surface area xerogels and aerogels displaying as high as 1459 m^2/g (number denotes BET surface area for UiO-66 based xerogel) surface area. In their report, aspects like shaping of MOF gels, fabrication of optically transparent xerogels using solvent and heat treatment, and creation of mesoporous MOF gel spheres using oil-drop granulation method are discussed in detail. Similar high surface area MOF (ZIF-8) based monolithic material derived from sol-gel approach was reported back in 2015 by Tian Tian *et al*.,[76] which is now commercial product sold under the start-up company named 'Immaterial' which is based in Cambridge. Interestingly, monolithic material made from ZIF-8 nanoparticles showed 3 times higher volumetric surface area compared to the conventional ZIF-8 powder samples. According to the report, monolithic material exhibited higher densities with respect to much lower density of ZIF-8 powder samples. From above examples, it is clear that MOF based gel materials are slowly growing in numbers with more promising porosity and monolithic physical form, which is suitable for industrial processing and applications.

2.4 Optoelectronic Materials

2.4.1 Background

Material science has seen overwhelming growth in the field with its great significance to human lives, dated way back to 29,000 BC as a source to construct pottery to today's smart and advanced world of materials to design highly advanced devices and tools. Material science has given us the life of comfort through technology developed tools like smartphones, batteries, watches, computers, biomedical devices etc. Most of the electronic or smart appliances composed of materials of various types including smart glasses, phase change chalcogenides, conducting carbons, polymeric assemblies, quantum dots, organic molecules, metal-complexes, oxides, etc. Among all these materials, the most common factor is that they respond to electrical energy and/or they change their behaviour upon interacting with light and thus useful for designing a device, sensor or emitter. Some of the important examples are discussed below to highlight the progress in optoelectronic materials science.

2.4.1.1 Chalcogenides

Chalcogenide is the general term used to describe heteroatom compounds containing chalcogen anion and electropositive atom, e.g. sulphides, selenides, tellurides. Chalcogenides is one of the most explored class of materials for optoelectronic applications. The most common examples of chalcogenides are ZnS, CdS (monochalcogenides); WSe_2, $TiSe_2$ (Dichalcogenides); MoS_3 (Trichalcogenides), VS_4 (Tetrachalcogenides) etc. Interesting aspect of chalcogenides is that they show reversible structural changes from amorphous to crystalline and allow us to tune various properties like optical, electrical, thermal, etc. Structural change behaviour in chalcogenides were recently adopted in an innovative manner by Prof. Bhaskaran and co-workers from the University of Oxford. They developed simple devices from thin

layers of GST ($Ge_2Sb_2Te_5$) of a few nm thickness (~7 nm) with the aim of flexible electronics in mind (Figure 2.18).[77] GSTs were previously used for rewritable optical data storage technologies, and non-volatile phase change memories. Recent work published in Nature by Bhaskaran *et al.*[77] demonstrates the significance of combining optical and electronic behaviour of GSTs.

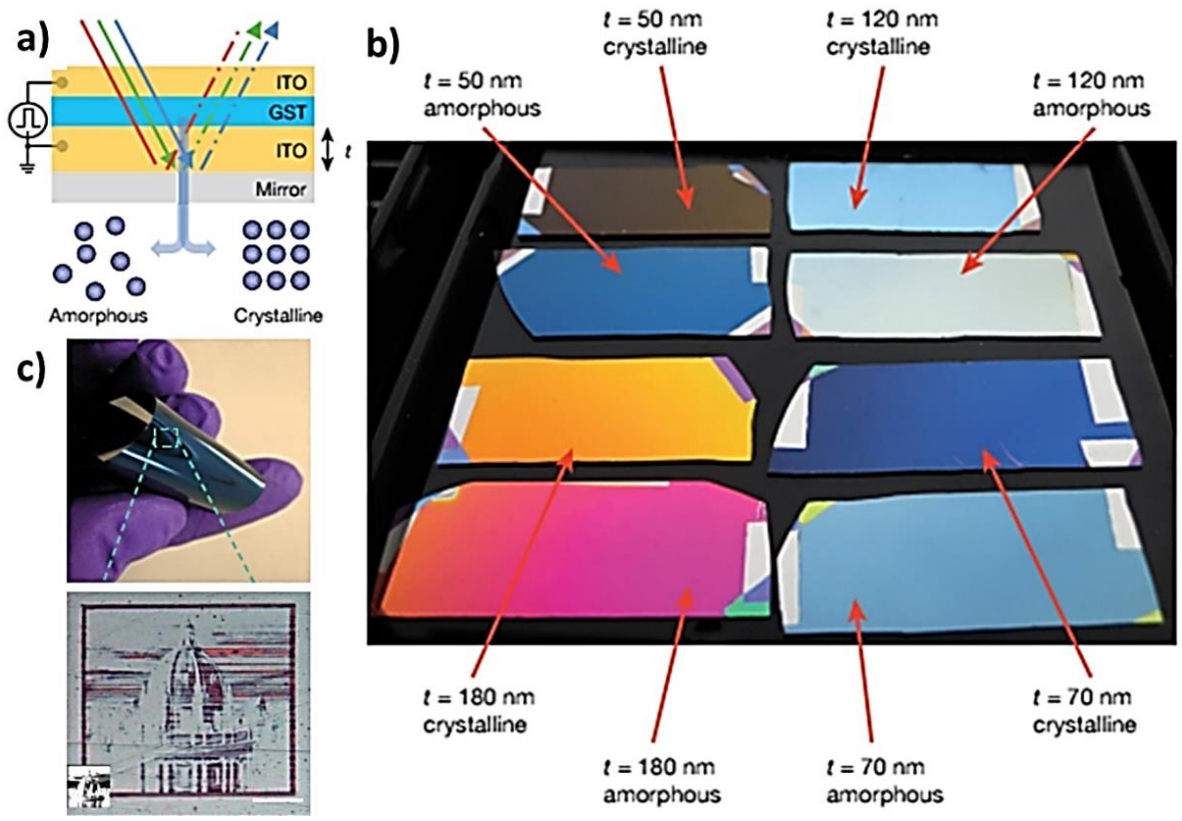

Figure 2.18 a) A concept of GST based device for optoelectronic application, b) smart response in the form of colour change of 10s nm-thick layer GST device with different thickness of ITO as indicated in a, c) a flexible device having nanoscale imprints printed electronically.[77]

They showed that the variation in thickness of the ITO layer in device with a constant GST thickness allows the tuning of the reflected optical colour in the visible range (Figure 2.18a, b). They reported the possible use of newly developed devices in ultrafast solid–state displays with pixels in the nanometer range, smart glasses, smart lenses, artificial retinal tools, etc. As GST exhibits amorphous phase in R.T. and

crystalline phase at ~220 °C, the device shows the change in colour upon heating at ~220 °C. Devices with different thicknesses of bottom ITO electrode varies in colour at RT and high temperatures. Furthermore, they demonstrated the strategy for developing flexible microdevices by printing nm level designs electronically and by following the same ITO thickness formula (Figure 2.18c). As GST also shows the structural transition by application of an external voltage, such devices could be very promising in the optoelectronic field.

2.4.1.2 Supramolecular Assemblies

2.4.1.2.1 Molecular Cages

Cage assemblies are purely organic based or hybrid metal-organic containing molecular assemblies having void spaces within. Such assemblies interact weakly with each other in solution state or in an aggregated form in solid state and form supramolecular network. Such cages are useful to derive controlled optoelectronic properties. A notable recent example of such cage assembly is platinum (II) based tetraphenylethylene containing molecular cage assembly reported by Prof. Peter Stang and co-workers (Figure 2.19).[78] The advantage of emissive properties of tetraphenylethelene organic moiety and its changing optical behaviour upon phenyl ring rotation and ethylenic bond twist was utilised to design smart emissive metalacages using Pt(II) metal centre.

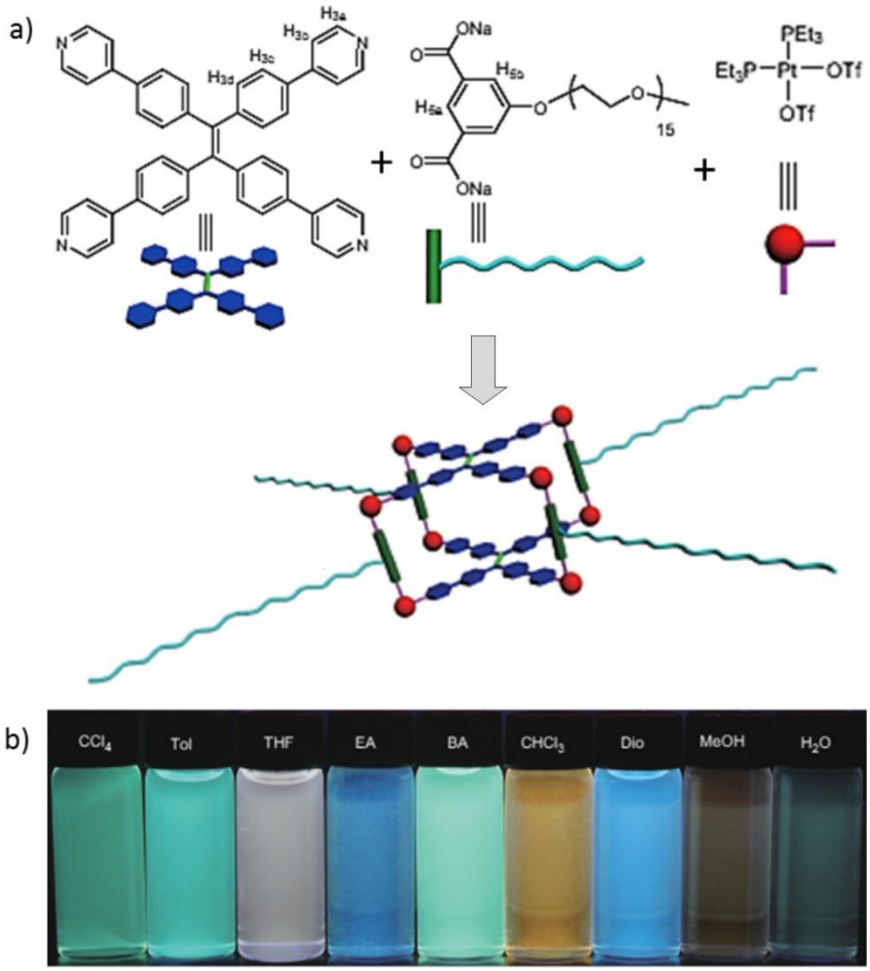

Figure 2.19 a) Scheme represents the synthesis of metallacages from aromatic organic ligand and Pt based salt, b) tuneable emission of metallacages from blue to dark orange in different solvents.[78]

Metallacage shown in Figure 2.19a is an example with interesting emission behaviour drastically different from the emission of pure organic moiety which generally show aggregated induced quenching. While light emission which is in general difficult to attain was obtained by metallacage upon making solution in THF solvent. Different solutions made using various solvents emitted light of wide spectra comprising light blue, intense blue, light green, yellow, pink, brown etc. (Figure 2.19b). Such behaviour with changing emission by solvent interactions are useful as sensors for detecting volatile organic solvents or small organic molecules. Demonstration of

ester compound detection was also documented in the same report using metallacage. Nonpolar or polar interactions, π-π interactions, H-bonding are the key parameters that determine assembly behaviour by separating the cages from each other or putting them close enough for aggregation to derive switchable emission. The same report also mentioned the problems in MOF compounds, which show solubility problems and difficulty of attaining the switchable emission in the solution state.

2.4.1.2.2 π-Gelators

π-Gelators are soft molecular gels derived from gelators possessing aromatic π-units containing fused naphthalene, anthracene, pyrene moieties or conjugated systems.[79] π-molecular systems are particularly interesting for their interesting electronic properties like luminescence, charge transfer, electrical conduction etc. Such properties allowed researchers to use them in making LEDs, FETs and PVDs. π-molecular systems offer easy processing methods for thin film device fabrication and thus allow switching of electronic properties based on the aggregation of molecules. Organogels containing π-gelators have also been used in photovoltaic applications such as fabrication of dye sensitised solar cells, thin film solar cells in the form of gelled electrolytes. Organogel electrolyte provides better contact between active materials for improving the performance of the device. Anodic photocurrent generation from organo gel films of thiophene based π-gelators, PBI based gels, or photocurrent generation from hybrids made from π-gelators in conjunction with C60 derivatised acid are notable examples of π-gelators for optoelectronics. Apart from PVDs, π-gelators also found extensive use in sensing and imaging as they are effective fluorescent molecular systems.

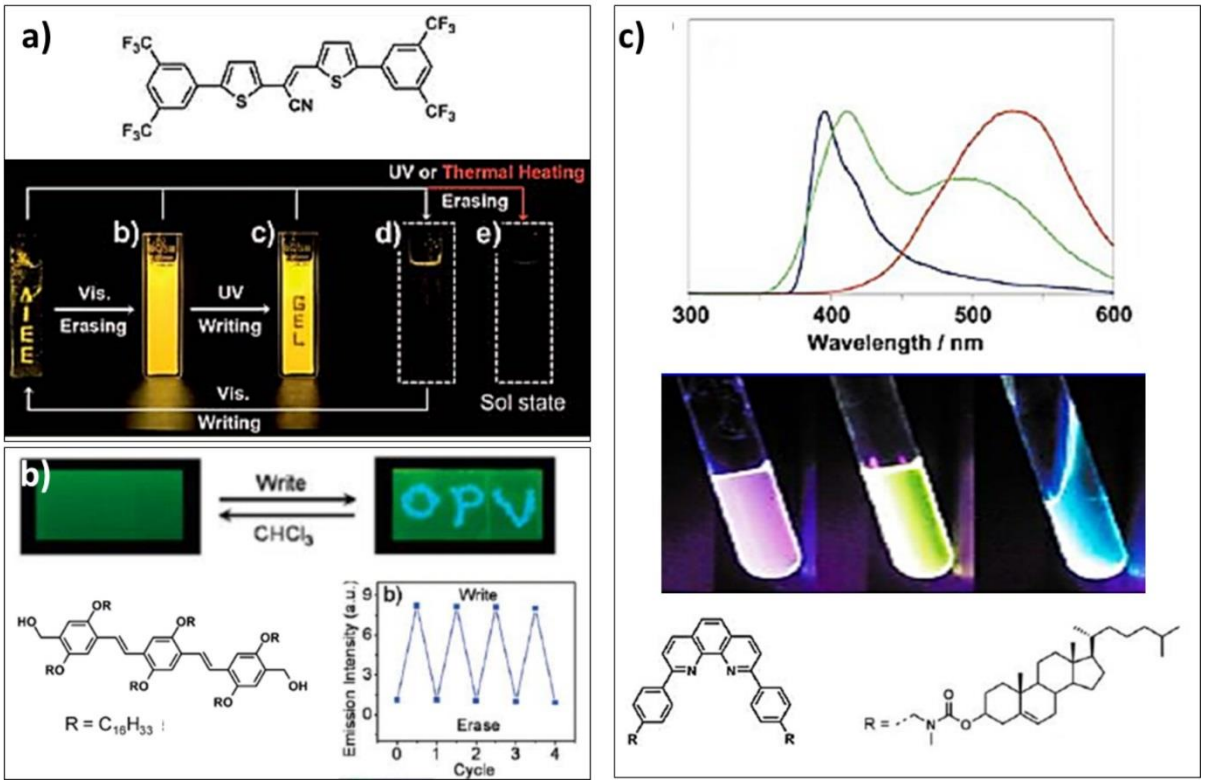

Figure 2.20 Thiophene derivative π-gelator molecule for making gel composite that displays luminescence derived write and erase activity by the virtue of UV or Visible light or thermal heating,[80] b) Oligo p-phenylvinylene derivative based gel for $CHCl_3$ sensitive emission to further utilise in overwrite-erase optoelectronic applications,[81] c) phenanthroline derivate based gel exhibits dramatic emission switch as a result of addition of triflic acid and gel to sol conversion by heat treatment; blue emission observed in sol state at 90 °C while green emission after addition of TFA, pink emission is the pristine emission of the gel.[82]

Interestingly, π-molecular systems exhibit tuneable optical properties when they gelate. Additionally, use of changes in the chemical surroundings of π-gelators offer their use for sensing a variety of molecular based materials or analytes like acids, explosive, volatile organic compounds, enantiomers etc. Extra advantage of phase conversion of organo-gels from gel to sol assisted by changes in molecular assembly can be utilised in reversible tuning of fluorescent properties. For example, oligo p-phenylvinylene derivative based gel with green emission coverts into the phase with blue emissive behaviour due to disintegration of assembly at high temperatures

(Figure 2.20b).[81] Blue emission again reverts back to green emission upon exposure of film material to chloroform. Such molecular changes have found important uses as molecular switch or to create rewritable-erasable fluorescent images. A similar application can be achieved using light sensitive Thiophene-based organo-gels, which become non-fluorescent when exposed to UV or by heating the gel that in turn reverts to emissive phase upon exposing to the visible light (Figure 2.20a).[80] Some organo gels could show a drastic change in emission just by minute changes in the chemical structure like proton transfer in presence of proton acceptors or proton donors. Phenanthroline derivate based organogel is an example of such phenomenon, it shows purple to green emission change when subjected to the molar concentration of trifluoroacetic acid and upon disintegrating the gel by heating at 90 °C, it further changes emission to blue (Figure 2.20c).[82]

2.4.1.3 Quantum Dots

Quantum dots are tiny semiconductor particles of few nanometre size which emit light of different wavelength based on the size of particles upon applying electric field, and thus extremely useful for the fabrication of LED devices or smart displays, etc. Several examples can be found in literature on tuning of the emission properties from lower wavelengths of blue light to higher wavelength of red light. Well known example of QDs are CdSe, CdTe nanoparticles, which are straightforward to synthesise and allow tuning of core–shell composition for further tuning of material emission, and electrical conducting properties. Since the sizes of such particles are in nanometre range, fabrication of thin film uniform displays is the easiest task for optoelectronics, which also make possible design of flexible displays. In the last two decades, flexible display technology has been revolutionised with the help of QD based materials. QDs generally exhibit high quantum yields and high thermal stabilities compared to other

organic molecules or dyes. Figure 2.21a, b show the emission of CdSe QDs of different sizes.[83] As the size of the nanoparticles increases, emission shits to higher wavelengths and reduces the band gap values. Average size of 4.8 nm for red emitting QDs can be seen from TEM image. With different size of QDs, LED that emits different colour of light can be fabricated (Figure 2.21c).

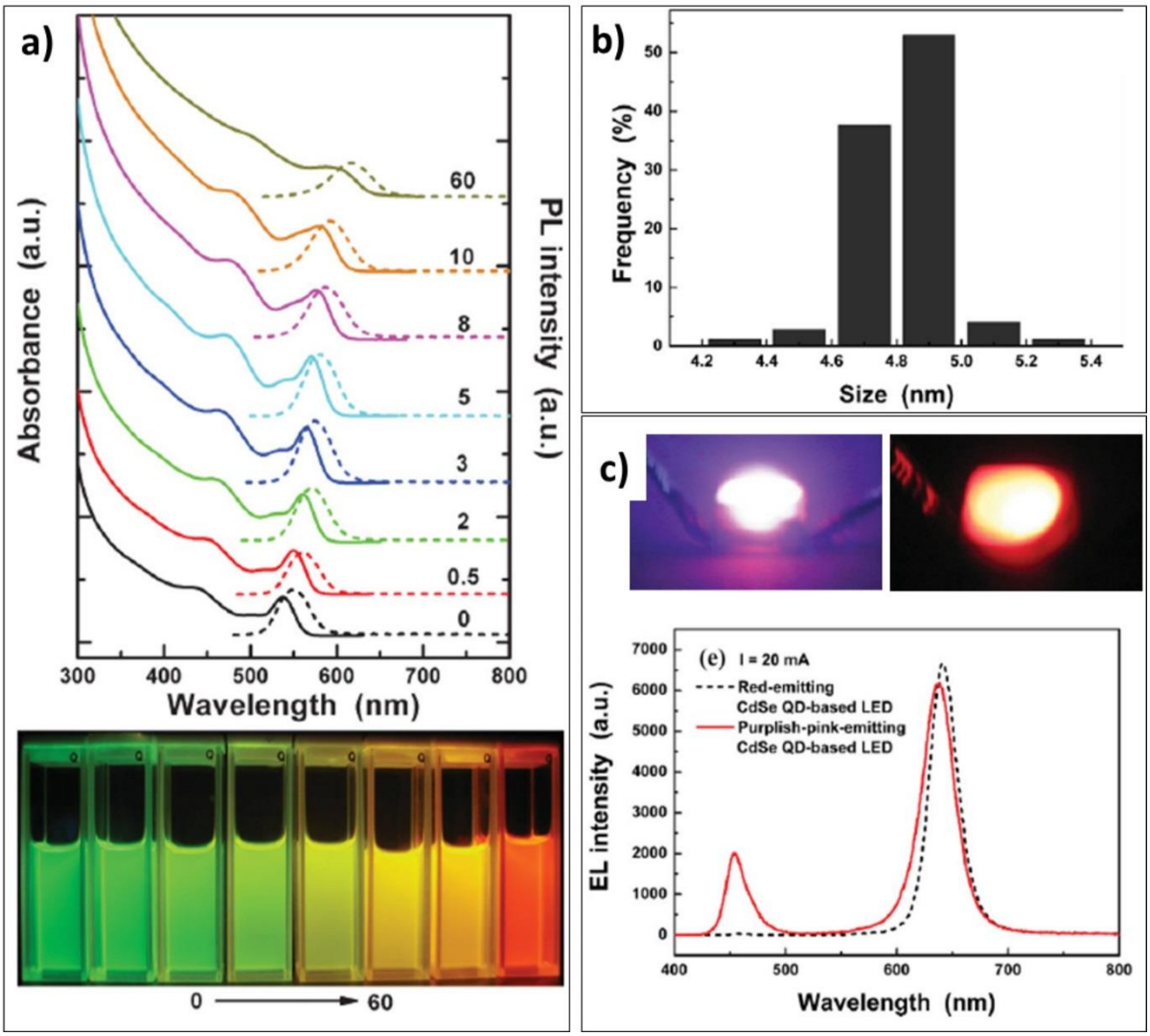

Figure 2.21 a) Spectra (top) and emission picture (bottom) of CdSe quantum dots with different particle sizes (number to the right of each spectrum indicates time in minutes), b) size of red emitting QD particles determined from dynamic light scattering experiment, c) two different particle size QD based purple and red LEDs, spectra at bottom for respective LEDs.[83]

Possibilities of structural tuning further allowed improvement of optoelectronic properties of QDs, which enable the development of quantum dot infrared photodetectors (QDIPs), quantum dot solar cells (QDSCs), quantum dot super luminescent diodes (QDSLDs) and quantum dot amplifiers.

2.4.1.4 Polymer Assemblies

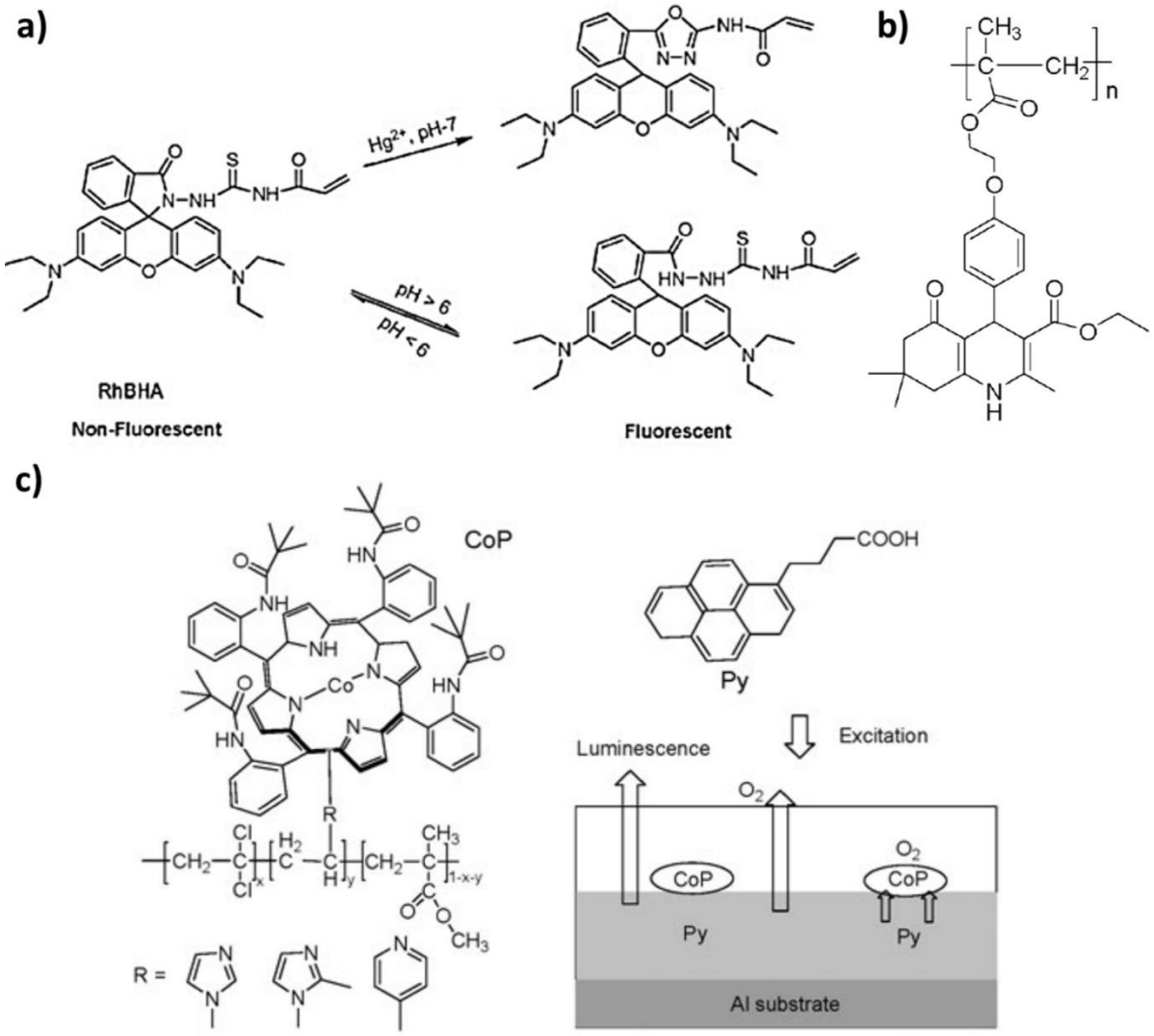

Figure 2.22 a) Rhodamine derivative moiety present in poly(ethylene oxide)-b-poly(N-isopropylacrylamide-co-RhBHA) that senses Hg^{2+} as a result of spirolactum to ring open process accompanied by no fluorescence to fluorescence,[84] b) Fe^{3+} sensing polymer based on quinolone derivative as a side chain and methacrylate moiety as backbone,[85] c) a polymer based on cobalt containing porphyrin as a side chain molecule (left) used in double layer device (right) in which bottom layer made from pyrene derivative and top layer from polymer matrix for luminescence based oxygen sensing application.[86]

Polymer based assemblies offer many advantages over small organic molecules as a single polymer chain could possess multiple recognition sites for specific analyte interactions, different pendant like functional side groups for optimising properties like molecular packing, stability of overall polymer etc. Depending on side pendants, both the electronic and optical properties can be modified. Additionally, entire polymer solubility can be upgraded based on such side pendants, which could allow an entire matrix to solubilise even in water for real world applications like sensing or element recognition application, for instance Hg^{2+} sensing from contaminated natural water sources (Figure 2.22a).[84] Due to continuous uniformity in backbone chemistry of polymers, they generally exhibit intense optoelectronic properties. Flexibility In polymer side chain chemistry allows the easy processing of material for large area thin film coatings, free standing films, etc. An example of polymer reported by Lu *et al.* specifically recognises Fe^{3+} metal cations amongst other metallic cations Zn^{2+}, Ni^{2+}, Cu^{2+}, CO^{2+} by showing quenching in fluorescence upon binding of particularly Fe^{3+} (Figure 2.22b).[85] Fluorescence was attained in the polymer by selection of quinoline derivative as a monomer for co-polymerisation with the soft methacrylate segment. Another example of smart double layered fluorescent polymer based on pyrene backbone and Co-porphyrin moiety was utilised as oxygen sensor at atmospheric pressure (Figure 2.22c).[86] Double layer polymer containing a layer of pyrene and another layer of Co-porphyrin act as luminescence quenching centre and oxygen binding sites respectively. Terpolymers shown in Figure 2.22c served as O_2 sensors at practical pressures of O_2 in the atmosphere in the range 10-21 kPa.

2.4.1.5 Metal Oxides

Some of the outstanding challenges of optoelectronic field including low carrier mobility, optical opacity, poor current carrying capacity and mechanical flexibility of

devices have been overcome to a greater extent by the introduction of metal-oxide materials in the field. After the discovery of metal-oxide materials, the conventional hydrogenated semiconducting silicon based thin film transistors (TFTs) used for device fabrication as a display backplane were replaced by metal oxide materials having much better carrier mobility, optical transparency, mechanical stress tolerance, compatibility with other materials. SnO_2 was the first metal oxide reported in 1964 for making TFT. Later, the field developed with a number of other polycrystalline materials like In_2O_3, and ZnO documented in the literature. Furthermore, many other metal oxide materials were used commercially as useful transparent TFTs including tin-doped indium oxide, In-Ga-Zn mixed metal oxide etc.

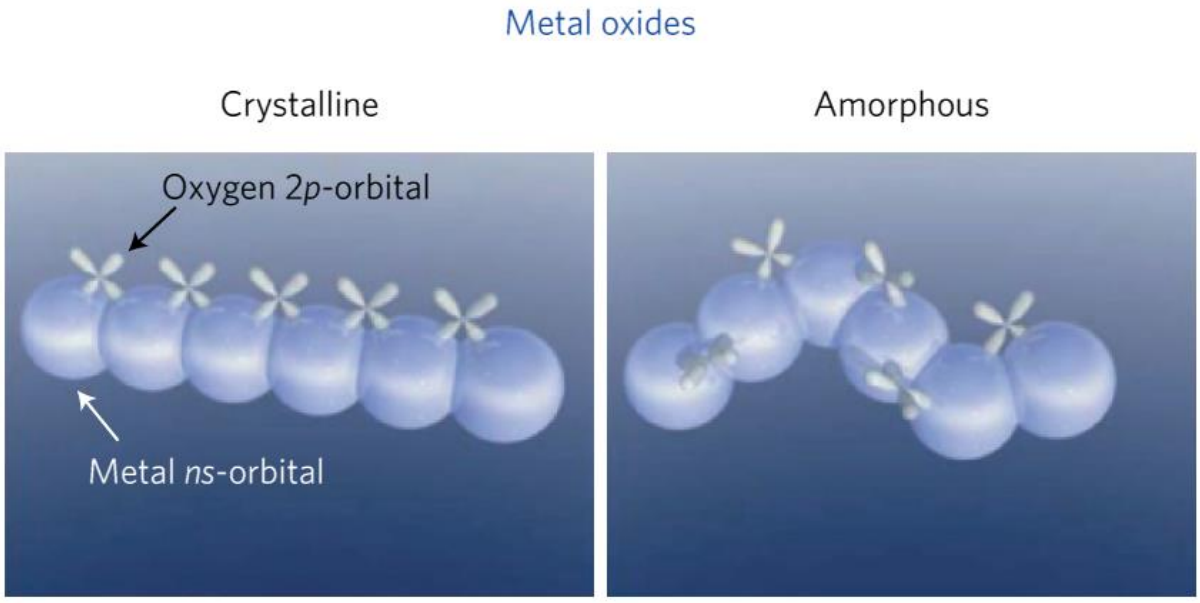

Figure 2.23 Representation of orbitals that contributes to the conduction band in amorphous and crystalline oxide materials.[87]

Most interestingly, the crystalline or amorphous phases of metal oxides do not get modified drastically in terms of their electronic properties unlike other types of optoelectronic materials.[87] As the valence band in metal oxide comprises 2p anti–

bonding O orbital and the conduction band comprises spherical ns orbital of metal bonding states, lattice distortion of crystalline material to cause phase change from amorphisation does not affect the spherical metal s orbitals, thus keeping the electronic properties intact (Figure 2.23). Moreover, addition of dopants into a metal oxide allows change in band gap values of the entire thin layer transparent oxide coatings for example In_2O_3 band gap (3.7 eV) can be modified by doping it with Al (band gap of InAlO = 3.8 eV). Transparent conducting ITO was extensively used in fabrication of a variety of optoelectronic devices like solar cells, LEDs, photovoltaic devices, etc. due to its excellent optical transparency (optical band gap of 4 eV), minimum toxicity, ease in uniform large area film deposition on glass or plastics and low sheet resistance of 10 Ω/m^2.

2.4.1.6 Metal-Complexes

First optoelectronic device based on metal complexes was reported in 1948.[88] Metal complexes are basically the combinations of the advantages of two main components, metal ions and organic molecules. The metal centres provide different coordination sites to design complexes of different sizes shape and geometries. Redox states of metal centres and their electronic delocalisation of energy states offer differentiating optoelectronic properties when combined with charge carrying organic molecules. Alq_3 based thin film light–emitting diode is the first example of metal complex derived device which was first reported by Tang and Van Slyke of Kodak Company in late 1980s.[88] Use of metal complexes for fabrication of OLEDs later revolutionised the world of optoelectronics and witnessed several materials based on a variety of metal-complexes made from metal centres mainly Zn^{2+}, Al^{3+}, Ir^{3+} etc. The progress of metal-complex use in optoelectronics can be seen from the Figure 2.24.

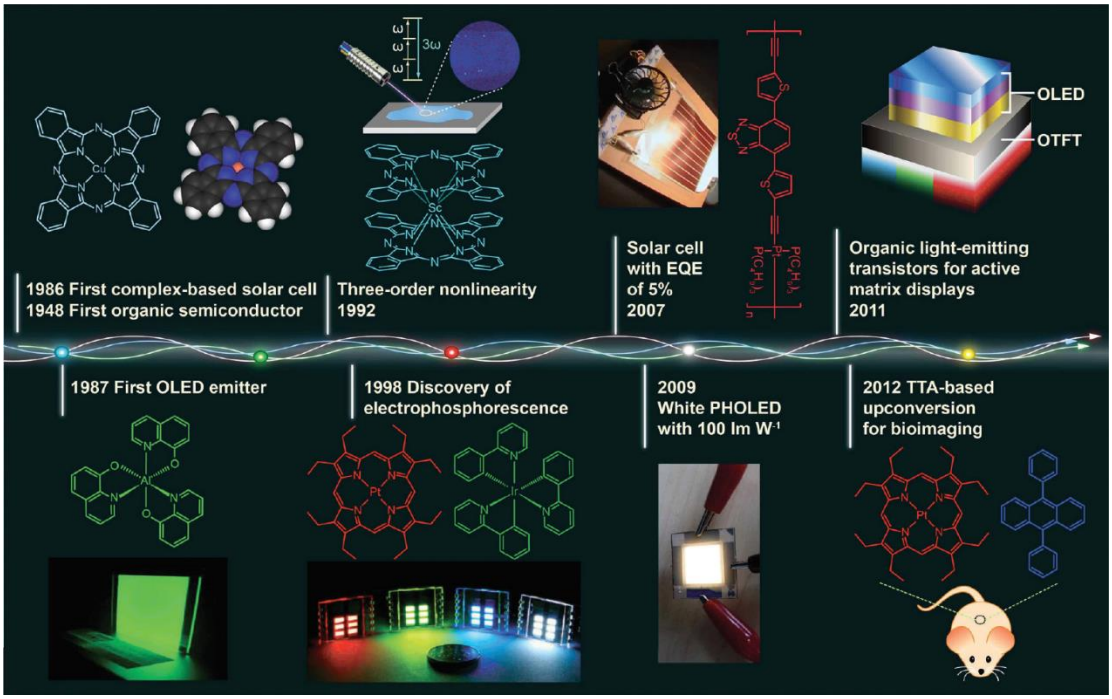

Figure 2.24 Important milestones in the growth of optoelectronic devices purely based on metal-complexes.[88]

Since molecular rigidity reduces the non-radiative transitions by minimising vibrations and ultimately avoids intersystem crossing to triplet state and collision heat loss, complexation of organic molecules to metal centres improves optical properties by rigidifying them and by allowing charge injection and transportation. Example of Zn(II) based metal complexes demonstrates such tuneable optical properties. By varying R group in metal complex, emission can be shifted from blue to green as energy states can be changed by effects of organic donating–accepting groups.

2.4.2 Importance of Material Morphology in Optoelectronics

Material morphology is one of the vital parameters in optoelectronics, which contributes largely to resultant variations in properties like absorption, emission, electrical conduction, etc. Mainly morphological control of material in nano regime offers highly improved optoelectronic properties compared to bulk size or large size

morphologies. The field of optoelectronic benefits from the rising era of materials with 2D layered morphologies or structure. The main advantage of 2D morphologies is that they are easy to process for flexible device fabrication, allowing interactions between layers of materials, to yield enhanced light matter interactions and photon absorption. Several examples of 2D materials can be found in literature, which have proven better optoelectronic characteristics compared to their bulk or 3D counterpart like atomically thin heterostructures of chalcogenides, atomically thin graphene layer, thin 2D van der Waal's layered materials etc.[89-93]

2.4.3 Why MOFs for Optoelectronics?

From above discussion of optoelectronic materials, it is quite clear that materials having structural dynamics with phase change properties or metal-organic interactions or having voids in the form of cages or ordered structure or metal hetero atom clusters display significant optoelectronic behaviour. The MOF field has witnessed thousands of examples until today with control on almost all aspects of framework, including pore symmetry, pore dimensions, pore stability, pore flexibility, metal centres, metal coordination number, redox states, heterometal centres, mixed organic linkers, electron donating or withdrawing atoms, charge balancing ions, guest assisted phase changes, flexible SBU assisted framework dynamics, linker exchange, metal exchange, ion exchange, thermal phase change, pressure induced framework breathing etc. Therefore, MOF materials are the most promising candidates for advancing the field of optoelectronics to the new higher level of smart technology.

2.5 Nano MOFs: Concept, Design and Synthesis

Well documented significance of material particle size at nanoscale points to the need for designing the MOF particles in nanometre scale for better performance of material

and device development. Conventional synthesis of MOFs mainly consists of the use of hydrothermal or solvothermal reactions, which mostly yields rather large size crystals in micrometre range. There are several advantages of large crystals in determining structural transitions using single crystal diffraction or to study single crystal structure properties for gaining in-depth understanding. However, the biggest disadvantage of large size crystals is difficulty in making thin film devices or uniform coatings. Therefore, it is essential to derive nanometre size MOF particles or ordered large scale deposition of MOF ordered structures. Maspoch and co-workers documented several reports from literature that demonstrated strategies for making nano scale MOFs.[94] Two main documented methods of nano MOF synthesis are i) emulsion mediated or template supported self-assembly formation of MOFs, and ii) controlled growth and harvest of nanoscale MOF once they formed (Figure 2.25a). In the emulsion method, small droplets stabilised by surfactant molecules served as reaction sites for MOF formation; since droplet sizes are smaller, they allow the control over the crystal size in nano regime. Templates have been used in the form of small molecules, solvent molecules or polymeric scaffolds to develop nano scale MOFs.

On the other hand, second method involves the synthesis of self-assembled MOF system using controlled reaction conditions like solvent, temperature, light or microwave radiation, ultra sonication etc. to limit the crystal growth at the nanoscale and then to harvest immediately upon formation. There are several demonstrations available in the literature focussing on the miniaturisation of MOF morphology using above mentioned factors. Microwave synthesis is one such strategy that has been explored to make nanoscale MOFs like IRMOF-1, 2, 3.[94]

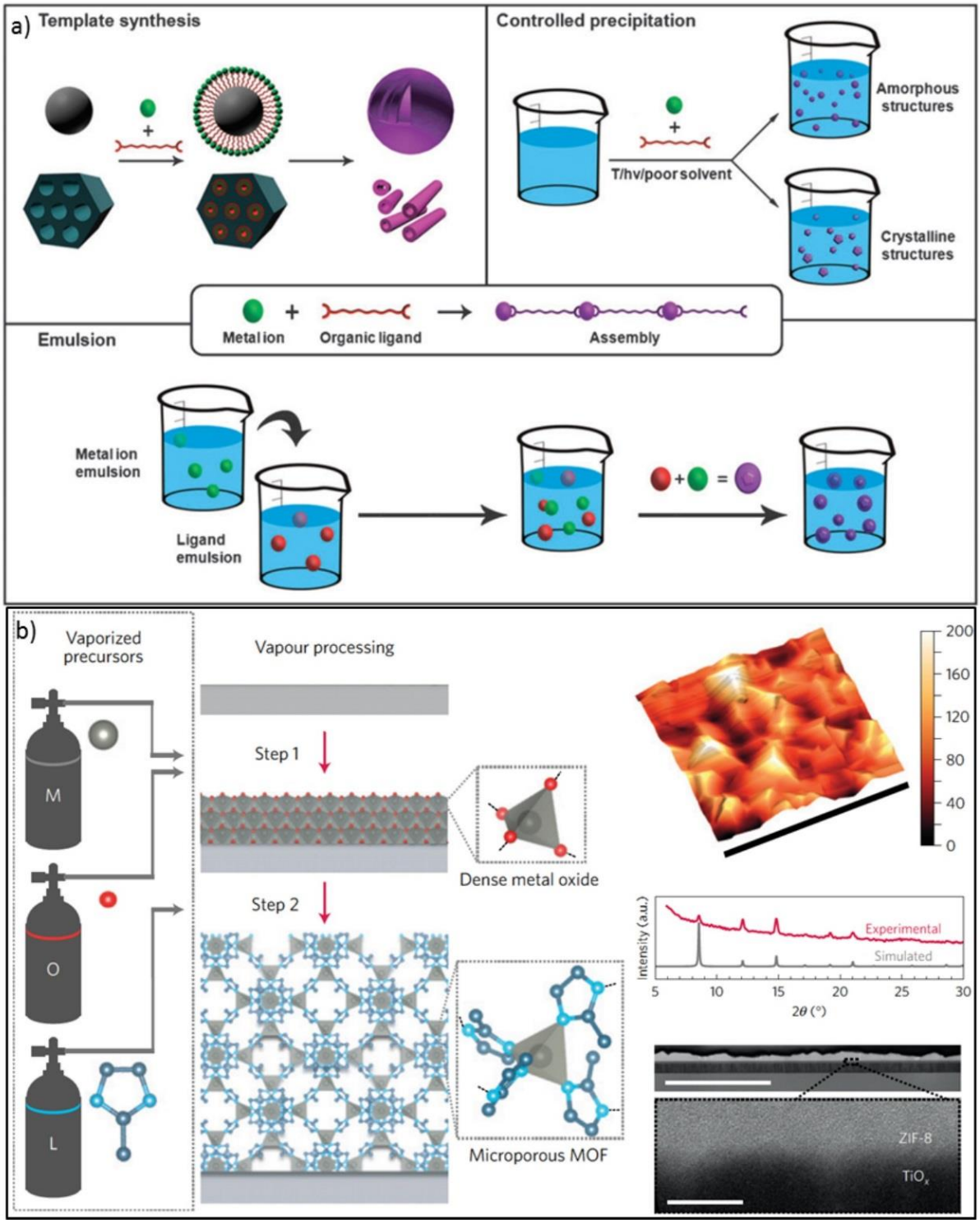

Figure 2.25 a) Different synthetic routes to yield nanoscale MOFs,[94] b) newly developed method of vapour deposition technique for fabrication of nm-thick coatings of ZIF-8 compound, supported by atomic force microscopy (scale in nm), PXRD and scanning electron microscopy experiments.[95]

The use of synthetic strategies for making nanoscale MOFs and their advanced applications have been targeted and accomplished to a certain extent in the realm of MOF materials. Some of them worth mentioning are the nano drug delivery molecular system using porous spaces of MOFs, catalysis, contrast agents, optical properties, sensors etc. As nano MOFs are controlled morphologies of porous molecular systems, they offer the advantages of integration into smart devices for achieving promising results in the above mentioned applications. Particularly 2D morphologies found to play significant role in terms of making thin layer coatings either through layer-by-layer deposition or by casting method, or by solvothermal method. Very recently, a novel method was developed by Ameloot and co-workers that defined and demonstrated a way to build highly controlled uniform thin films of MOFs using vapour deposition method (Figure 2.25b).[95] Vapour deposition method is a well-known concept for materials researchers as it has been used to develop several conducting, semi conducting devices, solar cells based on metal oxides/chalcogenides/perovskites etc. However, their work showing a very promising discovery of ZIF-8 thin film fabrication using vapour deposition method is a highly positive sign for the MOF field for taking a big leap towards real world applications.

2.6 Potential Applications of MOFs in Optoelectronics to Date

Rapid progress in the research of MOF field expanded applications of MOFs in technologically advanced applications like microelectronics, sensing, optics, lighting etc.[5, 15] There are various ways adopted by MOF researchers to fabricate functional MOFs useful for optoelectronic purpose.

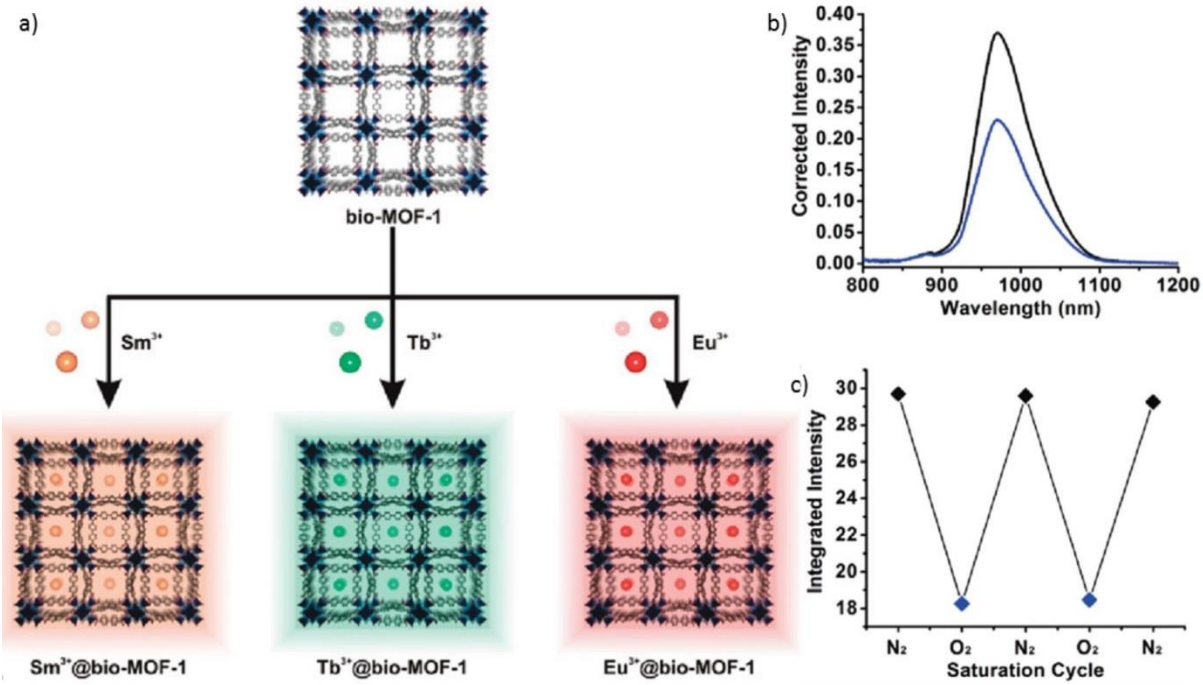

Figure 2.26 a) bio-MOF-1 transformation into functionalised bio-MOF-1 by cation exchange route using lanthanide cations, b) decrease in emission of Yb^{3+}@bio-MOF-1 upon subjecting to the oxygen at ambient pressure, c) consecutive cycles with maintained emission recovery by exposing material to nitrogen gas.[38]

One such route is to use ionic MOF bearing either cation or anion in their voids for charge neutralisation and later with post-modification replace the occluded ions with functional ions. Rosi and co-workers reported the first bio-MOF compound based on amino acid and Zn^{2+} cation. Among bio-MOF series, bio-MOF-1 i.e. $[Zn_8(ad)_4(BPDC)_6O]\cdot 2MeNH_2\cdot 8DMF\cdot 11H_2O$ was utilised for sensitisation of lanthanide cations and their use as NIR emitting material (Figure 2.26a).[38] Lanthanide cations offer tuning of the emission properties over a broad range of the spectrum, however their diminishing optical properties in water limits use in aqueous medium. Moreover lanthanide based complexes face solubility problems in water and hence lanthanide emission properties for bio-medical imaging sensing could not be achieved. Since bio-MOF-1 possesses large cavities with 1D elongated porous channel exhibiting total surface area of ~1700 m^2/g, it serves as large host of functional cationic guests like

lanthanide cations. An idea put forth by researchers in this case is the replacement of pre-existing dimethylammonium cations inside porous channels by lanthanide cations. Rigidified by an organic bridge of BPDC organic linker gives high thermal stability to the MOF which adds plus point for achieving stable optoelectronic material. The successful cation replacement was achieved in this case and compounds with occluded Tb^{3+}, Eu^{3+} and Yb^{3+} were characterised in detail. All samples shown crystalline nature evidenced from PXRD even after soaking into the water. Each sample also exhibited sensitisation in organic solvents with enhanced emission properties. Surprisingly emission of lanthanide cations was found intact in water medium as well, which otherwise quench easily. Use of NIR emitting bio-MOF encapsulated with Yb^{3+} was demonstrated by showing changes in the emission behaviour of compound in solid state upon exposure to the oxygen gas at ambient pressure (Figure 2.26b). A signal reduction to 40% was observed on exposing compound to O_2, however the signal of emission was found to recover with inert nitrogen gas (Figure 2.26c).

Host-guest strategy has always proved its significance for functionalising composite material or to tune already existent inherent host framework properties. Using the same bio-MOF-1 compound, another research group from Zhejiang University demonstrated two photons pumped lasing.[10] In their report, pyridinium hemicyanine dye: 4-[p-(dimethylamino)styryl]-1-methylpyridinium (DMASM) was used as a guest material to functionalise the bio-MOF-1 crystals and generate guest loaded MOF i.e. DMASM@bio-MOF-1 (Figure 2.27a). From the realisation of the importance of two-photon excited fluorescence and two photon-pumped (TPP) lasing for applications like optical data storage, biological imaging etc., Yu *et al.* used a dye molecule with known TPP lasing behaviour, i.e. pyridinium hemicyanine cationic dye.

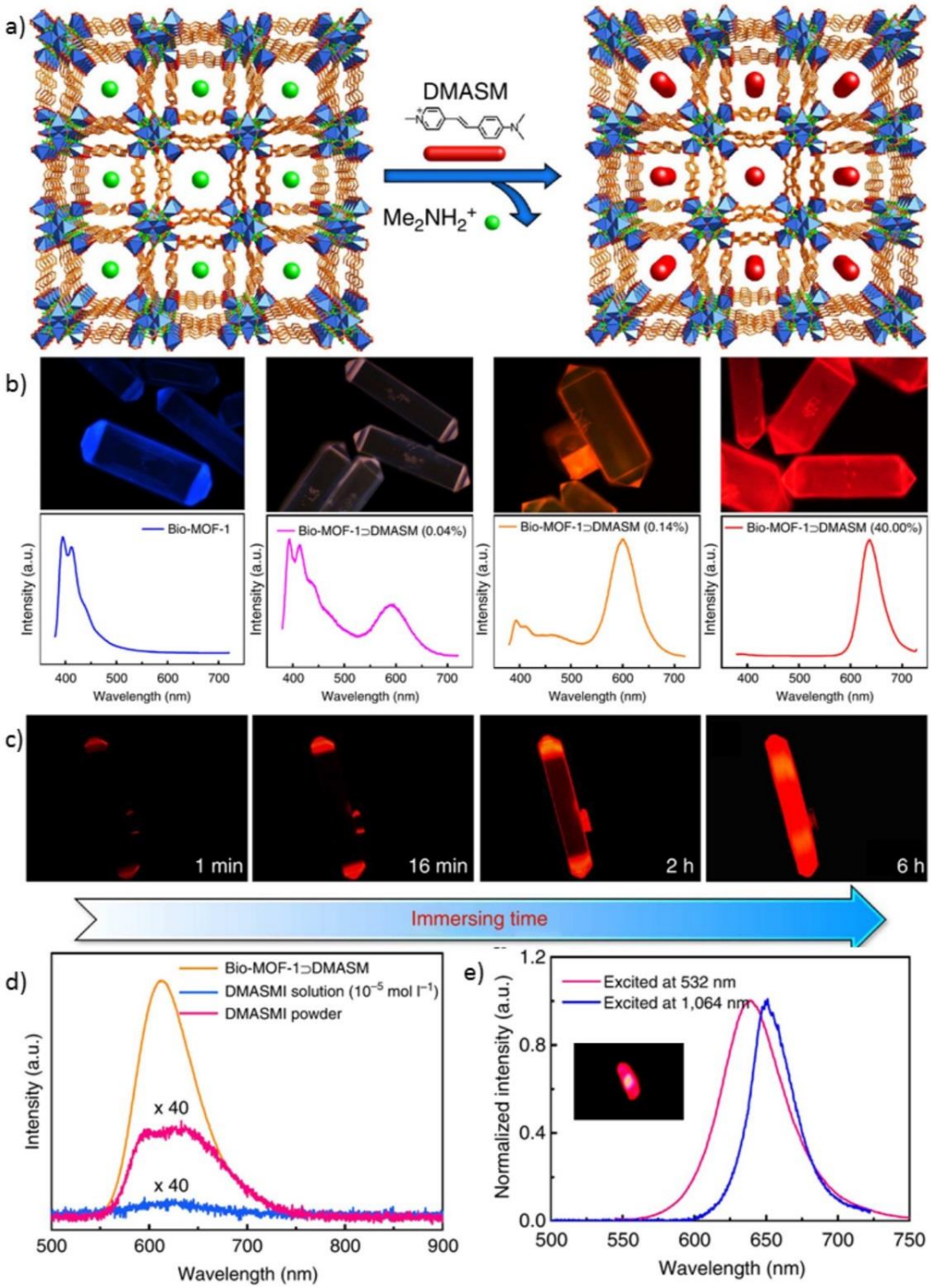

Figure 2.27 a) bio-MOF-1 Functionalisation using external cationic dye DMASM, b) change in the emission of bio-MOF crystal as cationic dye enters into the pores in different concentration, c) *in situ* tracking of dramatic entry of red emitting dye into the pores of bio-MOF-1 with the help of confocal microscopy, d) emission enhancement of DMASM on confinement compared to its pure form in solid state and solution state, e) emission behaviour of DMASM@bio-MOF-1 at two different excitation wavelengths, inset picture is the red light generated from DMASM@bio-MOF-1 by exciting it at 1064 nm using Nd-YAG laser.[10]

Although such molecules display ideal TPP behaviour in solution state, in solid state they have been observed to exhibit aggregation caused quenching (ACQ) and thus minimises their use in solid state devices. Here, bio-MOF-1 has been used as a medium to sort out dye molecules in a spatially ordered manner, avoiding ACQ. This is the first report that documents interesting cation exchange phenomenon by external cationic dye with the help of dramatic changes in the emission of a single crystal of bio-MOF-1. Slow entry of the dye into bio-MOF-1 *via* 1D porous channels, replacing dimethylammonium cation was monitored using confocal microscopy. Figure 2.27c shows direct evidential changes in emission of different regions of crystal especially with low amount loading edges were found to emit higher intensity red light and with higher loading of cationic dye, all regions of the crystal were found to show uniform red emission throughout. Light has also been shed on host emission with low loading of dye, then slow dominance of red emission from dye, causing host→guest charge transfer, explained on the basis of emission profiles that exhibit red shift (Figure 2.27b). The first achievement of this study was the high fold improvement in the emission intensity of guest dye, which otherwise found weakly emissive in solution form or in solid form in its pure form (Figure 2.27d). The numbers presented in the report were surprising; the study showed that DMF solution of dye exhibit 0.45% quantum yield and in solid state it exhibits 1.48%. However, the dye in a confined state within the bio-MOF-1, quantum yield achieved was 25.87%. These are the evidences that points to the minimisation of intermolecular interactions, significantly reducing the ACQ effect. Another noteworthy phenomenon attained from this host-guest couple was the two photon excited emission. It was found that emission observed at 637 nm when excited at 532 nm was red shifted by 15 nm under the excitation wavelength of

1064 nm (Figure 2.27e). Red shift occurred along with the change in full width at half maximum from 50 to 33 nm.

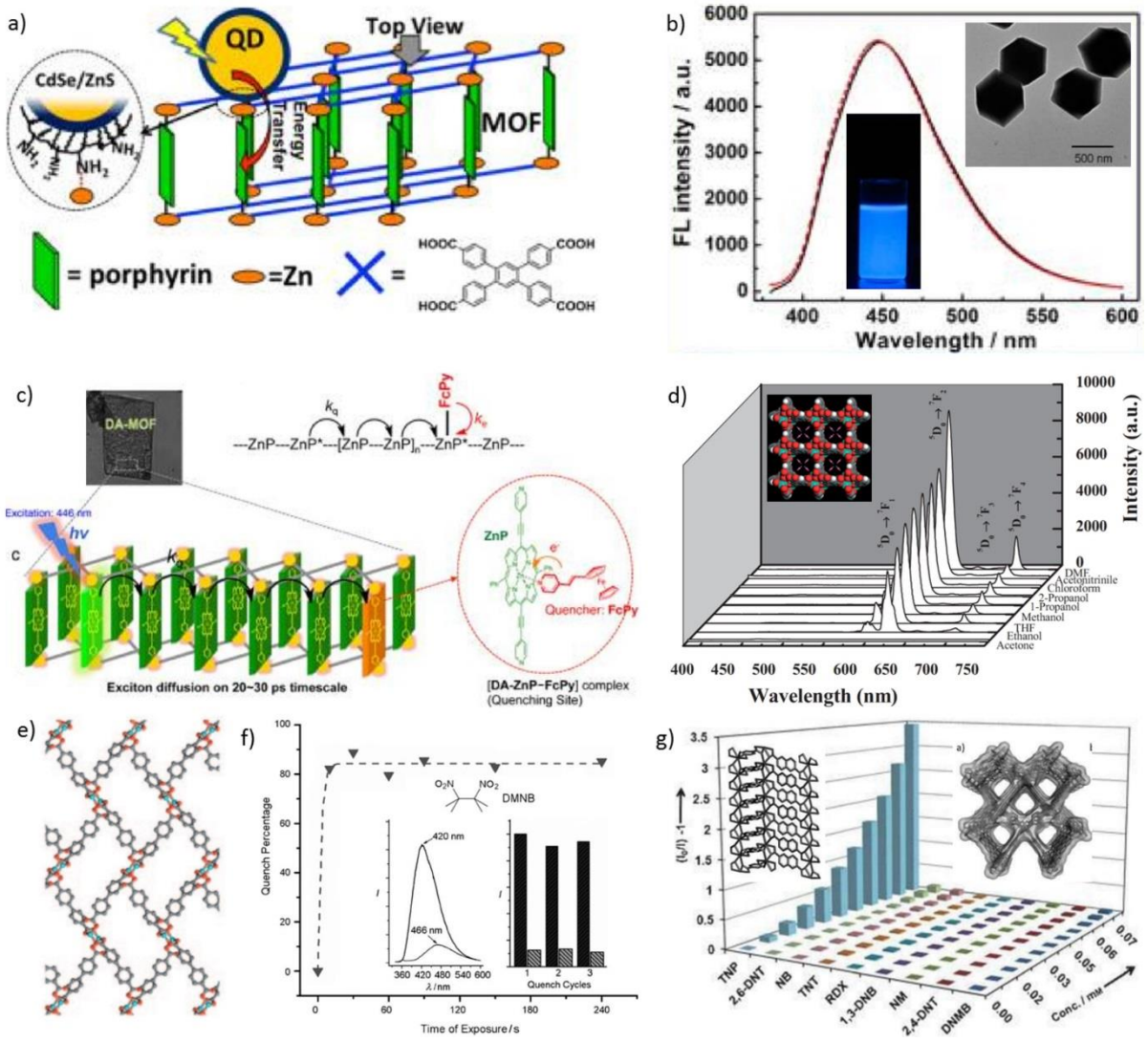

Figure 2.28 a) Scheme representing QD sensitisation of MOF for light harvesting,[96] b) carbon QD functionalised ZIF-8 material with blue emission, inset shows TEM images of material,[97] c) scheme that shows porphyrin based MOF compound for light harvesting,[98] d) emission based small molecule sensing using lanthanide metal centre MOF shown inset,[99] e) 3D luminescent MOF for solid state nitro-group containing explosive sensing f) from the effect of luminescence quenching upon exposure to vapours of explosive powders,[100] f) bar diagram showing selective TNP explosive sensing using naphthalene based luminescent 3D MOF compound (inset).[101]

It was claimed that re-absorption process occurs due to high concentration of dye content within the bio-MOF-1 that affects the emission in the process. Two

photons pumped lasing was generated by pumping centre of the DMASM@bio-MOF-1 crystal using Nd-YAG laser at 1064 nm. Light output was collected using fibre optic spectrometer and turned out that red light of 50 µm spot size can be generated.

The MOF field has made the greatest progress over the last two decades, aiming at applications in sensing, optics, electronic and multifunctional devices. Apart from above mentioned examples of MOF for optoelectronics, another few important ones worth to mention include : quantum dot assisted light harvesting MOF reported by Hupp and co-workers (Figure 2.28a);[96] fluorescent carbon quantum dot functionalised ZIF-8 for sensing applications reported by Chen and co-workers (Figure 2.28b);[97] light harvesting from porphyrin based MOF reported again by Hupp and co-workers (Figure 2.28c);[98] luminescent lanthanide based MOF for sensing small molecule species reported by Banglin Chen *et al.* (Figure 2.28d);[99] and MOF luminescence quenching based selective explosive detection by Li *et al.* (Figure 2.28e,f)[100] and Ghosh *et al.* (Figure 2.28g).[101]

More recently, new approaches have been adopted by researchers to develop nano scale MOF materials to fabricate thin film devices for advanced optoelectronic applications. More efforts are taken in the direction of improving electronic and optoelectronic properties. Huge contribution has been made in this area by Mark Allendorf and co-workers, demonstrating the achievable MOF properties, particularly band gap engineering, electrical conduction, luminescence properties, thermo-elctronic behaviour, photovoltaic response etc. Review paper published by Allendorf and co-workers in 2009 documented the progress till then about the optical properties of MOF, in which different concepts of charge transport in MOFs, emission possibilities *via* metal cores or ligand based or guest oriented are discussed in detail accompanying literature reports.[102] Very recently, an updated roadmap was published

by Ameloot and co-workers, which gives a clear picture of MOF progress in the microelectronics, sensing, and optoelectronic sector.[15] Important topics including fundamental properties required in MOF for optoelectronic devices, charge transport mechanism, energy harvesting, light emitting devices, magnetic and dielectric properties, microfabrication processes, and several MOF based devices reported in literatures have been covered in this 2017 review article.

Chapter Three

Materials Synthesis and Characterisation

3.1 Synthesis Methods

3.1.1 Synthesis of HKUST-1 Based SupraMOFs

1,3,5-benzenetricarboxylic (BTC) acid (2 mmol) was dissolved in 1 mL of the respective solvents, and then triethylamine (6 mmol) was added in order to achieve complete soluble ligand in the solvent. This solution was sonicated for 5 minutes prior to reaction with the copper nitrate solution, which was prepared in a corresponding 1 mL solvent by taking 3 mmol of $Cu(NO_3)_2$ and dissolving further with sonication for 1~2 minutes. Solution of copper nitrate was then added to 1,3,5-benzenetricarboxylic acid with vigorous shaking for a few seconds, the mixture was then left undisturbed till it showed gel-like behaviour as confirmed by the tube inversion method (Figure 3.1).

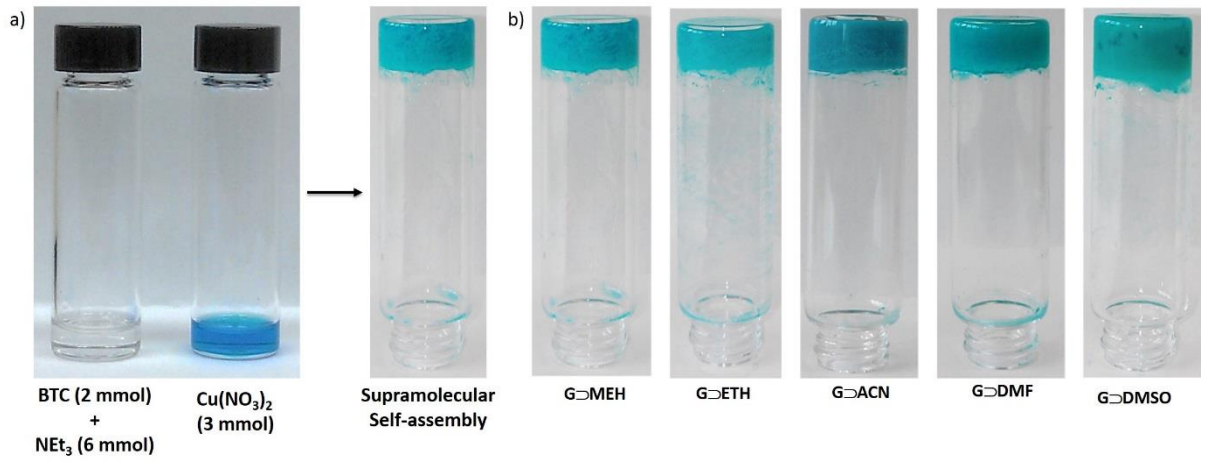

Figure 3.1 a) Scheme showing synthesis of the HKUST-1-based supramolecular hybrid self-assembly (reactants were solubilised in 1 mL of DMF), b) gel (G) samples synthesised by using different solvents (MEH: methanol, ETH: ethanol, ACN: acetonitrile, DMF: *N,N*-dimethylformamide, DMSO: dimethyl sulfoxide)

3.1.2 Thin Film Fabrication Using HKUST-1 Nanoparticles Harvested From SupraMOF Gel Materials

Hybrid gel materials obtained from the aforementioned synthesis were used as precursors for fabricating MOF thin films. Each material was washed three times using 20 mL of methanol and then centrifuged to collect the NMOF particles. Suspension remained at the bottom of centrifuge tube was collected and later used to deposit thin films of MOF onto glass substrates *via* the doctor blade technique (Figure 3.2), with varying gap size set between the tip of the blade and surface of the glass substrate [from a few microns (4 μm), up to 10s of microns (50 μm)]. The same NMOF suspension has also been successfully used for dip coating and spin coating methods [step wise: (i) 500 rpm for 50 s, (ii) 800 rpm for 50 s, (iii) 1000 rpm for 20 s].

Figure 3.2 MOF thin films with increasing thickness, from left to right ca. 1, 2, 5 10 μm, obtained from sol-gel method of G⊃DMSO and deposited *via* doctor-blade technique. Film thicknesses were characterised by Alicona infinite focus microscopy using a 3D non-contact optical profilometer.

3.1.3 Synthesis of Host-Guest Znq@ZIF-8 Material

The hybrid host-guest material was synthesised employing combination reaction IV in Table 3.1, where ZnQ was obtained from a concentration ratio of 0.5 : 1 mmol (Zn^{2+}: 8HQ). Initially, ZnQ was synthesised by mixing Zn^{2+} and 8HQ in 25 mL of methanol.

In another flask, 4 : 16 mmol of Zn^{2+} : mIm was added in 25 mL of methanol. This solution was kept stirring for 5 minutes and after that ZnQ solution was added slowly. After vigorous stirring, the temperature was raised to 80 °C. Yellow colloidal nanocrystals started to appear at this stage and the yielded product can be further maximised by adding an excess amount of both Zn^{2+} and mIm in 1 : 4 mmol ratio.

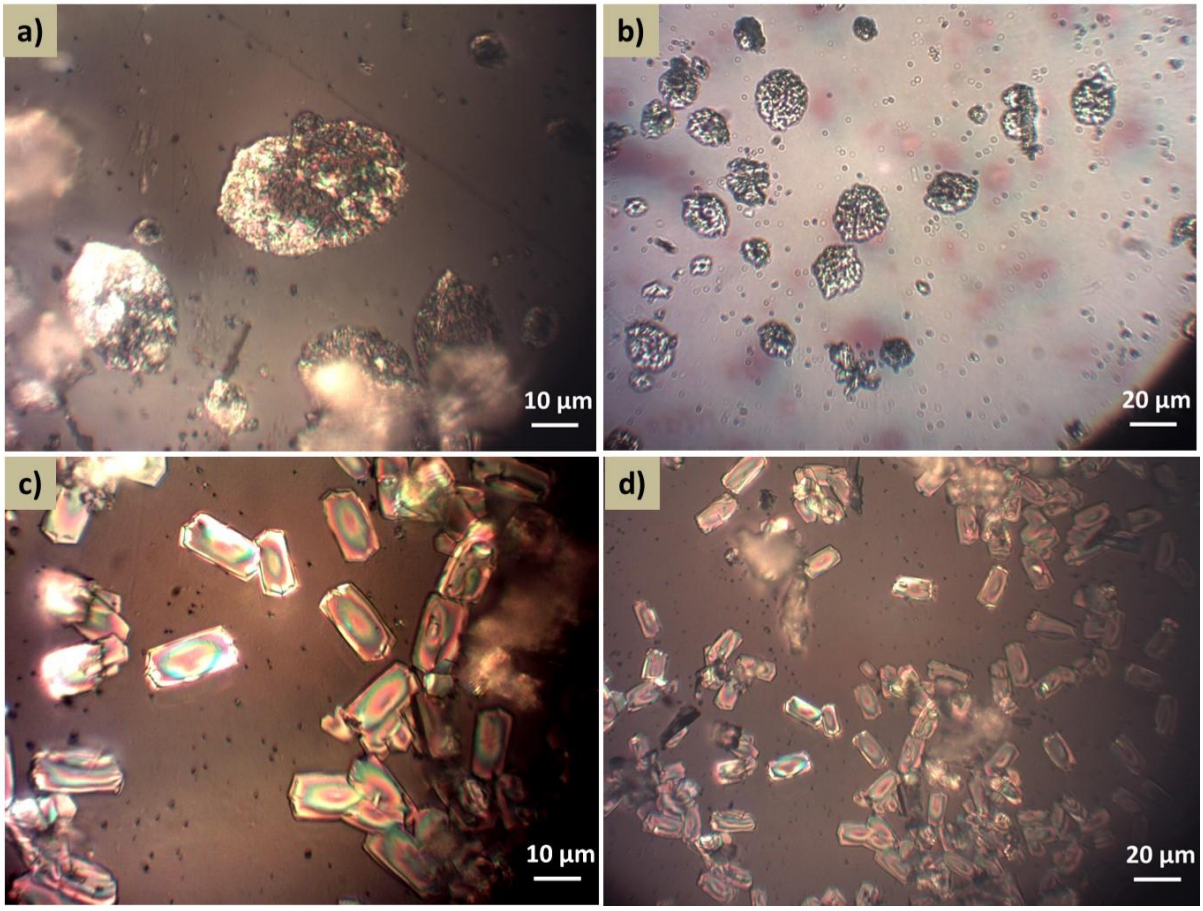

Figure 3.3 Optical images of a mixture of crystals obtained in the (sub-optimal) reactions I and II. (a-b) show partially-formed ZnQ hexagonal crystals whose crystal faces are decorated by small crystallites of other unknown side-products. (c-d) show hexagonal microplates of ZnQ complex obtained in the product mixture, which correspond to the 2-D hexagonal crystal morphology[103] identified in an isolated synthesis to yield phase pure ZnQ.

The synthesis took ~10 minutes. The crystalline product was washed thoroughly (4 cycles) using copious amount of methanol and acetone to remove excess ZnQ compound and residual soluble products. The final product was separated by centrifugation at 8000 rpm.

$$Zn^{2+} + 8HQ = ZnQ \quad (1)$$

$$ZnQ + Zn^{2+} + mIm = ZnQ@ZIF\text{-}8 \quad (2)$$

Table 3.1. Solution-based chemical reactions designated as I to IV, conducted at 80 °C using different combinations of starting reactant concentrations in 25 ml of methanol (concentrations are mentioned in mmol).

Reaction no.	ZnQ guest		ZIF-8 host		Products
	Zn^{2+}	8HQ	Zn^{2+}	mIm	
I	3	6	4	16	Impure product mixtures (Figure 3.3)
II	2	4	4	16	Impure product mixtures (Figure 3.3)
III	1	2	4	16	No crystallisation
IV	0.5	1	4	16	Phase pure nanocrystals (Figure 3.4)

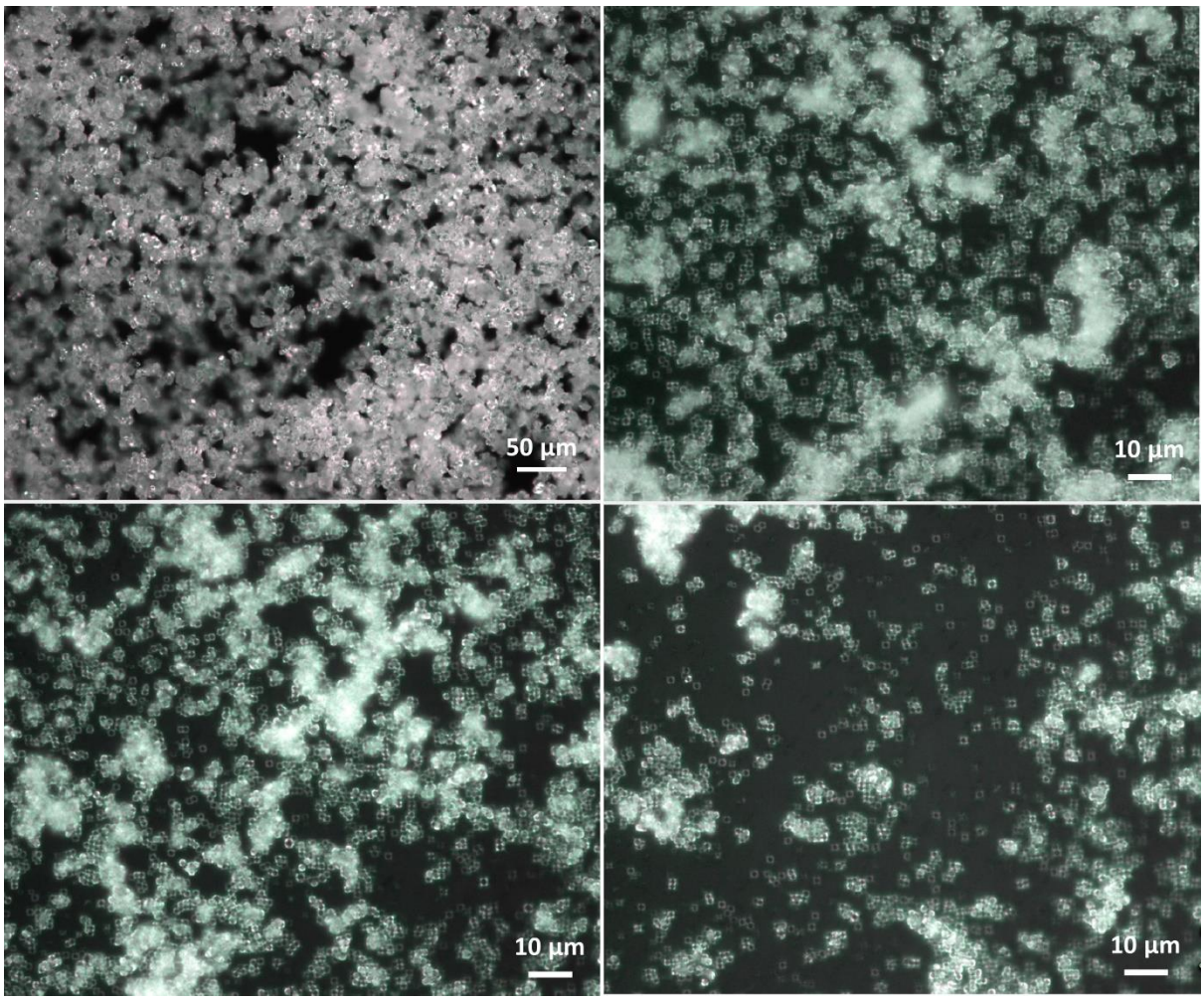

Figure 3.4 Optical microscopy images of ZnQ@ZIF-8 hybrid host-guest compound obtained from the (optimal) reaction IV, yielding a phase pure product exhibiting uniform crystal size.

3.1.4 Synthesis of Porous OX-1 2D Nanosheets as Host Framework Material

2 mL *N,N*-dimethylformamide (DMF) clear solution of $Zn(NO_3)_2$ (1.5 mmol, termed Solution A) was combined with 3 mL clear solution of 1,4-benzenedicarboxylic acid (3 mmol, BDC) plus triethylamine (NEt_3^+) (6 mmol) (termed Solution B). A fibrous gel-like supramolecular material formed immediately upon combining solutions A and B (Figure 3.5). The gel phase is disordered, comprising both crystalline (2D nanosheets) and non-crystalline materials in addition to excess amounts of reactants and guest molecules. The nanosheet rich fibers were washed twice with copious amounts of polar solvents: first using DMF followed by methanol and acetone, and with simultaneous sonication (10 minutes per solvent, then centrifugation). This washing procedure quickly breaks down the supramolecular fibres to release the 2D nanosheets (insoluble), and at the same time removing externally adhered guest species (not in MOF pores) and excess reactants.

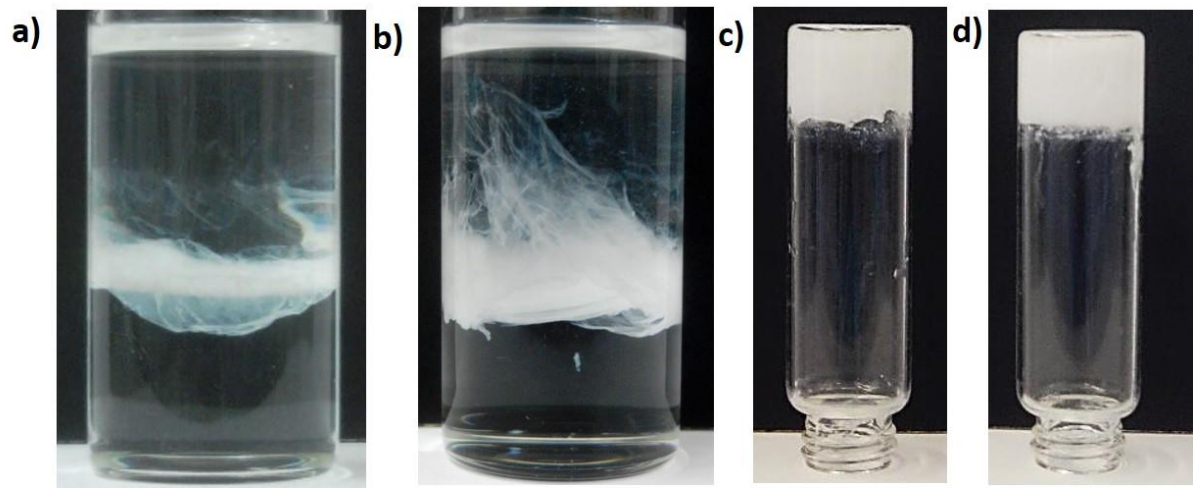

Figure 3.5 a) and b) Supramolecular synthesis of OX-1 nanosheets showing stepwise development of fibrous soft matter at the interface of two reactants, c) and d) forming a bulk of hybrid gel material confirmed by vial inversion test.

Finally, nanosheets harvested can be separated by centrifugation (8000 rpm) and subject to vacuum drying at 110 °C for 4 hours. The isolated nanosheets are highly

crystalline MOF material: $(HNEt_3)_2[Zn_3BDC_4]\cdot DMF$, designated as the "OX-1" nanosheets.

3.1.5 Synthesis of Functionalised MOF Nanosheets: ZnQ_{DMF}@OX-1 and ZnQ_{DMA}@OX-1

Preparation of functionalised MOF nanosheet materials (Guest@OX-1) involves a simple additional step of *in situ* mixing of *N,N*-Dimethylformamide (as clear solution) containing guest species e.g. ZnQ/AlQ/Naphthalene/Anthracene/Fluorescein into Solution B. This facile high-concentration reaction (HCR) method is shown in Figure 3.6. To ensure that luminescent guests are not left adhered to the MOF surface, the product was washed thoroughly twice using solvents that will solubilise the guest species (first using DMF, followed by methanol and acetone). Note that the washing step is carried out with simultaneous sonication (10 minutes per solvent, then centrifugation) to further expedite the removal of external guest species.

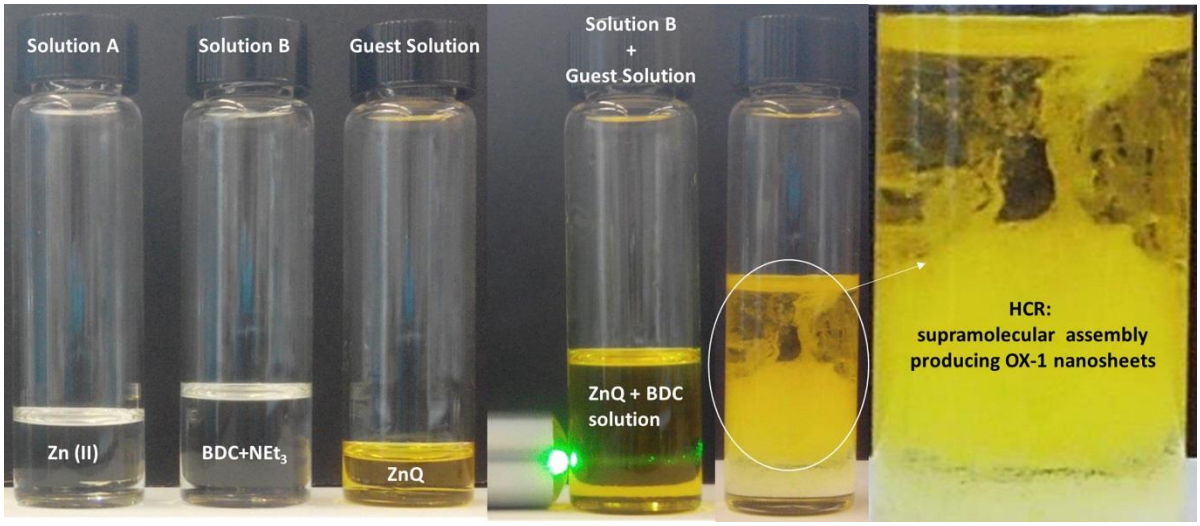

Figure 3.6 Clear solutions of Zn(II) in DMF (2 mL solution A), BDC linker plus NEt_3^+ in DMF (3 mL solution B), and ZnQ guest solution (1 mL). Image on the far right shows the high-concentration reaction (HCR) when combining the A + B + ZnQ guest solutions, producing instantaneous supramolecular assembly containing OX-1 nanosheet materials.

Mixture of solvents (Benzene: DMF = 1:2) was used for Anthracene or Naphthalene guest solution, and the same solvent mixture was used for washing the product material to remove excess reactants.

3.1.5.1 Preparation of Different "Guest Solutions" For Functionalisation of the OX-1 Host

a) ZnQ: ZnQ was synthesised in 1 mL of DMF by reacting 1:2 molar ratio of Zn(II), (0.5 mmol) and 8-Hydroxyquinoline (8HQ), (1.0 mmol).
b) AlQ: AlQ was synthesised in a similar manner to that of ZnQ except by taking 1:3 molar ratio of Al(III), (0.5 mmol) and 8HQ (1.5 mmol).
c) Naphthalene: 0.5 mmol of Naphthalene was dissolved in 1.5 mL of Benzene and then it was mixed with 1.5 mmol solution of Zn(II) in 3 mL of DMF prior to the reaction with BDC linker solution.
d) Anthracene: 0.5 mmol of Anthracene was dissolved in 2 mL of Benzene and then mixed with Zn(II) solution in 3 mL of DMF and sonicated further to prepare a clear solution.
e) Fluorescein: 0.1 mmol of Fluorescein was dissolved in 1 mL of DMF and mixed with Zn(II) solution before reaction with the BDC linker.

Table 3.2. Systematic set of reactions to show that it is possible to control the loading of guest species confined within the OX-1 nanosheet host framework. Changes in the absorption behaviour of the different products as a function of guest loading are plotted in Figure 3.7 below.

Reaction	ZnQ (Guest Concentration)		Zn-BDC (OX-1 Concentration)	
	Zn(II)	8HQ	Zn(II)	BDC^{2-}
1	0.1 mmol	0.2 mmol	1.5 mmol	3.0 mmol
2	0.3 mmol	0.6 mmol	1.5 mmol	3.0 mmol
3	0.5 mmol	1.0 mmol	1.5 mmol	3.0 mmol
4	1.0 mmol	2.0 mmol	1.5 mmol	3.0 mmol

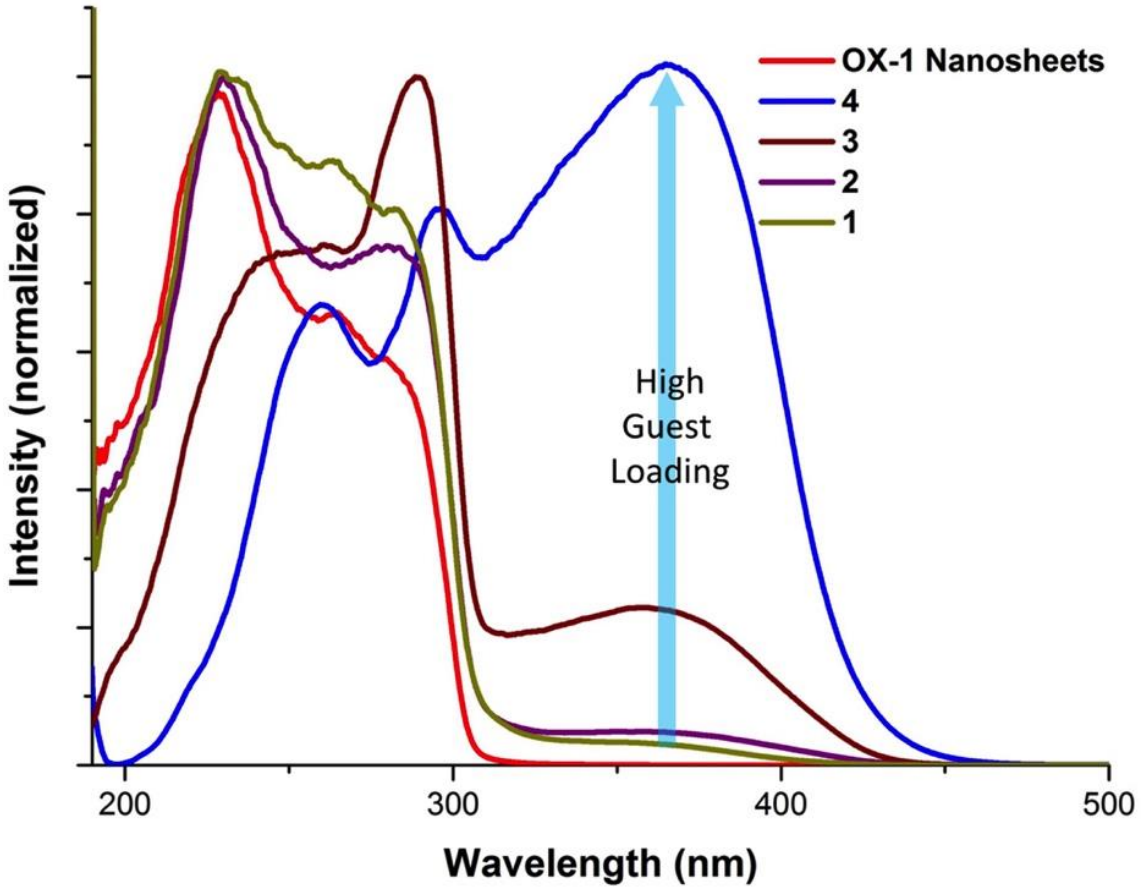

Figure 3.7 Controlled experiment with loading of various amounts of ZnQ guest emitters in OX-1 nanosheet host material (table above). Notice how the absorption spectra being modified significantly with higher guest concentration loading, signifying a stronger host-guest coupling effect.

3.1.6 Synthesis of ZIF-8 SupraMOF Gel Material

12.0 mmol of 2-methylimidazole was dissolved and deprotonated in 3 mL of DMF, followed by addition of 12.0 mmol of trimethylamine (NEt_3). Another solution was prepared by dissolving 3.0 mmol of $Zn(NO_3)_2$ solution in another 3 mL of DMF. The former solution was then combined with the latter solution, they immediately reacted to form a fibrous architecture in solution phase. This solution containing fibrous product was then sonicated for 5 seconds which yielded a uniform and stable supraMOF gel material.

3.1.7 Synthesis of Lower-Symmetry ZIF-8 Nanoplates Extracted from SupraMOF Gel

The supraMOF gel material was disintegrated by adding 50 mL of additional DMF and then sonicated for 10 minutes. It produced a solution containing the dispersed white particles of ZIF-8 nanoplates. This colloidal suspension was centrifuged at 8000 rpm for 5 minutes, to isolate a white compound at the bottom of the tube. This precipitated product was then washed thoroughly using 50 mL of methanol twice and 50 mL of acetone later. At each washing step, compound in centrifuge tube was sonicated for 10 minutes before centrifuging. After washing, the compound was dried under vacuum at 110 °C. This final drying step will transform the powder precipitate by reconstituting the ZIF-8 nanoplates into a monolith.

3.1.7.1 Synthesis of Conventional ZIF-8

2-methylimidazole (12.0 mmol) and $Zn(NO_3)_2$ (3.0 mmol) were dissolved together in 50 mL of methanol and stirred till white product precipitates at room temperature. The

obtained product was thoroughly washed with plenty of methanol, centrifuged, and finally dried under vacuum at 100 °C.

3.1.8 Synthesis of Perylene@ZIF-8 Nanoplates and Monoliths

Three clear solutions were prepared in three different glass vials namely: 1) 6.0 mmol of $Zn(NO_3)_2$ solution in 15 mL of DMF, 2) 0.2 mmol of Perylene in 18 mL of Dichloromethane (DCM), and, 3) 15 ml DMF solution of 24.0 mmol of 2-methylimidazole (mIm) deprotonated using 24.0 mmol of Triethylamine (NEt_3) (named as solution A). Zn^{2+} solution and Perylene solutions were mixed together (to form solution B), which was then combined with solution A. Instantaneous product formation was observed upon the mixing of solutions A and B, yielding a light-yellow coloured compound (Figure 3.8). 50 mL of DCM was added into the Erlenmeyer flask containing the product and sonicated for 10 minutes, then the product was separated by centrifugation at 8000 rpm for 5 minutes.

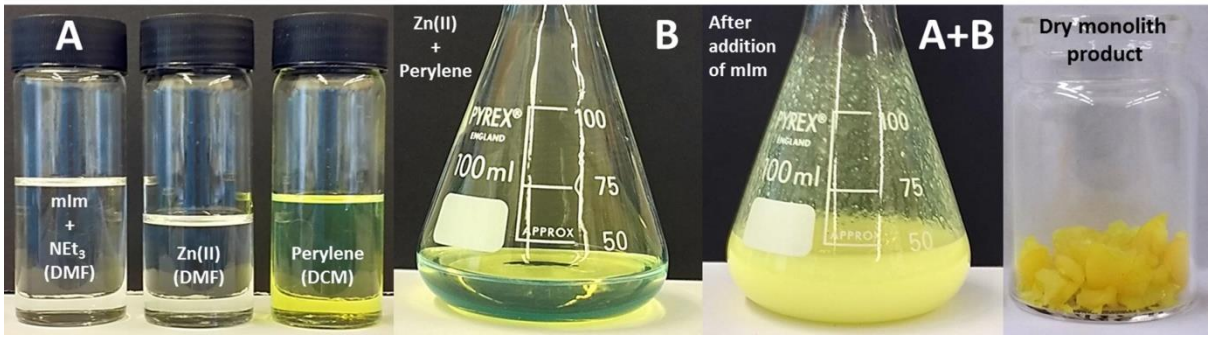

Figure 3.8 Photographs depicting the synthesis protocol of the Perylene@ZIF-8 compound. Upon mixing the clear solutions A and B, a rapid reaction was observed leading to the formation of a light-yellow coloured product.

To make sure that the obtained product (i.e. Perylene@ZIF-8) was free from any surface adhered Perylene, the centrifuged product was further washed twice with 50 mL of DCM, each time accompanied by vigorous sonication (10 min) during the

washing steps. After washing the sample with DCM, it was further washed with 50 mL of methanol (to make sure product is free from unreacted 2-methylimidazole) and then finally with 50 mL of acetone, accompanied by a 10 min vigorous sonication at each washing stage. The washed sample isolated by centrifuge was dried at 90 °C under vacuum for 6 hours. Drying of sample resulted in a darker-yellow coloured monolithic material containing Perylene@ZIF-8 (Figure 3.8).

3.2 Materials Characterisation

3.2.1 Rheological Measurements on Gel–Like SupraMOF Materials

Rheological measurements were performed on HKUST-1 based supraMOF using the Physica MCR-301 (Anton Paar) rheometer equipped with a temperature controlled basal plate (Figure 3.9). Parallel plate configuration was used for all studies by keeping a 1 mm gap distance between the basal and the top plates. A constant shear stress of 10 Pa was applied for creep and stress recovery tests. Rheological measurements on the ZIF-8 nanoplates based supraMOF gel sample were performed using a 2-mm gap between the basal and the top plates.

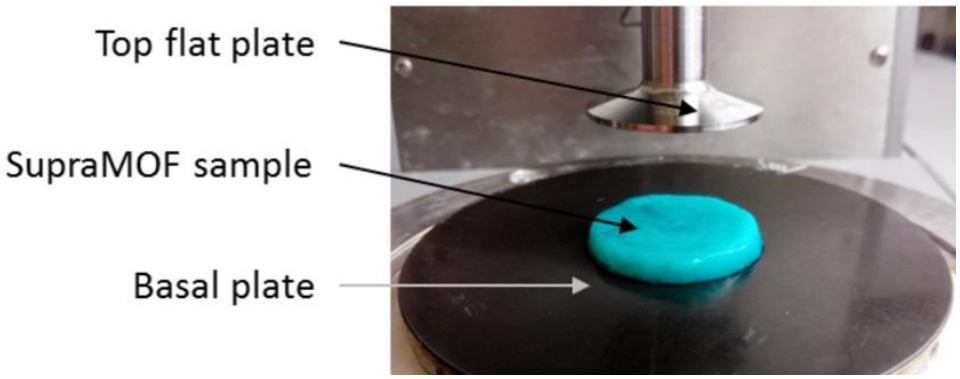

Figure 3.9 Photograph showing HKUST-1 supraMOF on basal plate of the rheometer, it also shows top flat plate used for measurements.

3.2.2 Microscopic Studies

3.2.2.1 Sample Texture, Thin Film Topography Using Optical Microscopy

Alicona Optical Profilometer Theory: Alicona Profilemeter is based on focus variation microscopy in which one can measure the surface texture by calculating roughness of a specimen (Figure 3.10). Profilometer creates 3D surface images, that contain colour and topographical information. The information further gets used for analysis of surface roughness parameters. The focus variation of an optic provides multiple images at different vertical distances (Figure 3.10 (right) inset). With the help of optical sharpness and focus one can obtain a full high-resolution 3D surface image.

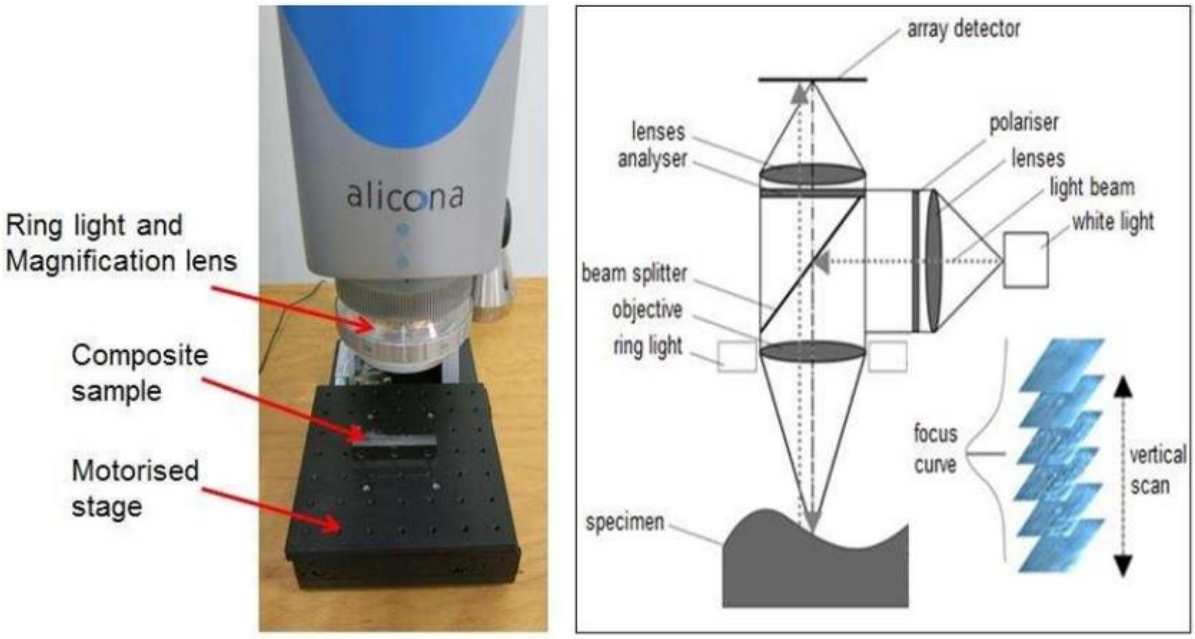

Figure 3.10 Image showing various parts of Alicona instrument (left) and its internal components (right) highlighting the working principle behind instrument.

For understanding fibrous texture and morphological nature of gel samples, reactants were coated on top of each other using doctor blade coater and then left for drying at R.T. (Figure 3.11). Optical images and surface height topography of MOF thin films were characterised using infinite focus microscopy, IFM (Alicona Infinite Focus 3D

Profilometer). Thin film thickness was characterised by scratching thin film to the hard glass surface and then measuring the depth of scratch using the non-contact optical profilometer (see Figure 3.12 for details).

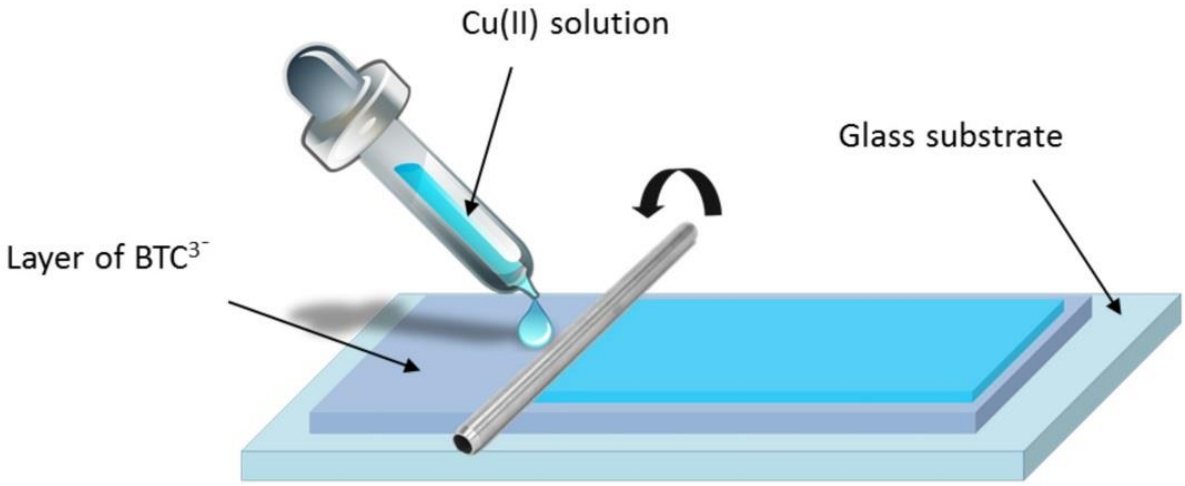

Figure 3.11 Schematic representation for making a thin coated sample on glass substrate to study the material topography.

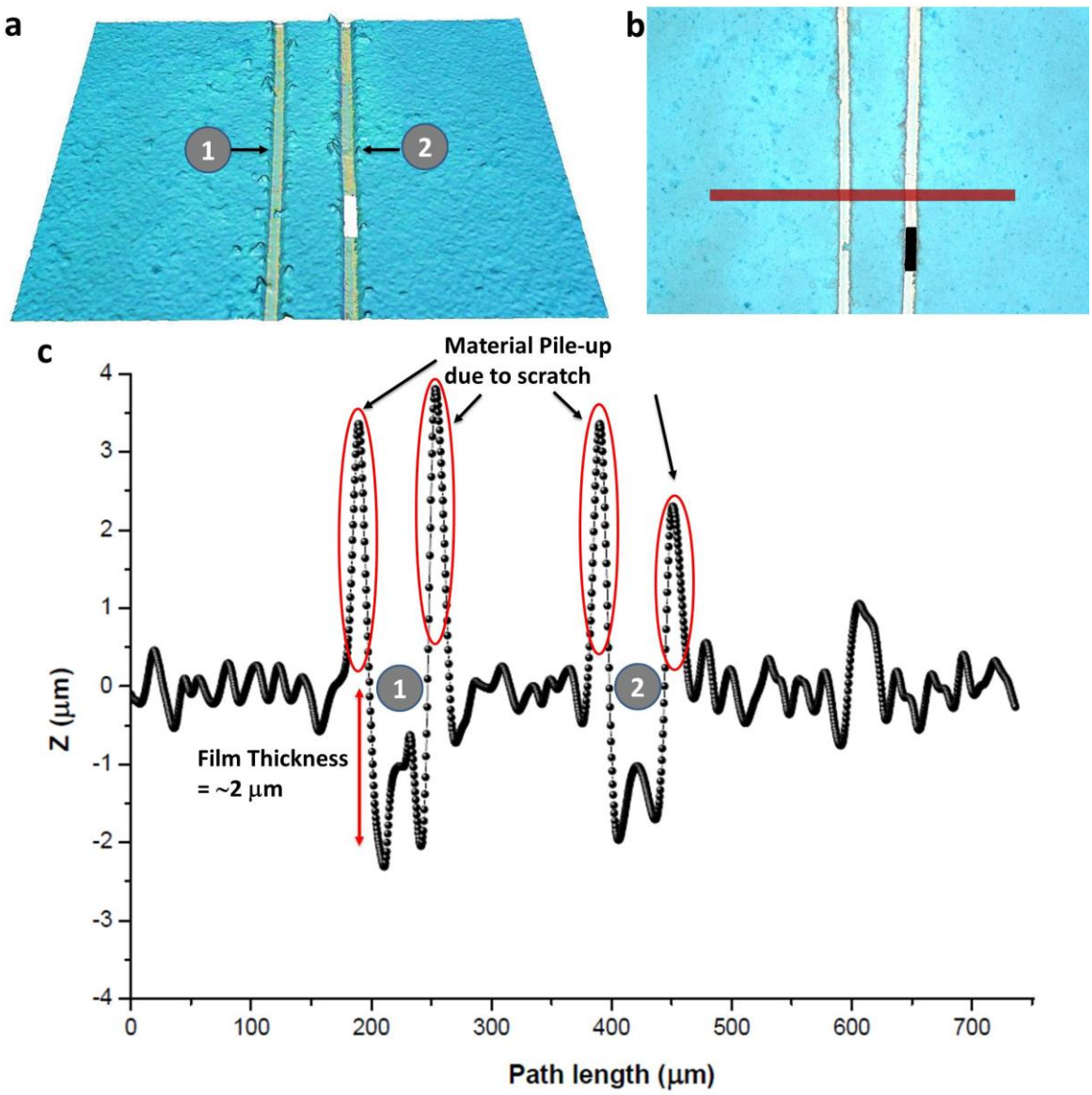

Figure 3.12 Example of thin film thickness measurement method involving optical imaging of the material through the scratches made on film surface: (a) 3D optical colour image determined *via* non-contact profilometer (Infinite Focus Alicona), and (b) 2D image of the sample with two different scratches imaged in a single scan showing (c) film thickness of ~2 μm. Film obtained from the sol of G⊃MEH.

3.2.2.2 Atomic Force Microscopy (AFM)

AFM theory: AFM is a popular technique to study surface texture and morphology. It involves scanning a sharp tip situated at the end of a flexible cantilever that moves across a sample surface (Figure 3.13). The tips typically have an end radius of 2 to 20 nm, depending on tip type. The forces generated between the tip and sample surface

results in the deflection of a cantilever. The interaction between sample surface and tip involve mechanical contact forces, van der Waal's forces, capillary forces, chemical bonding, electrostatic forces, and magnetic forces. The deflection of a cantilever is monitored by a laser beam falling on the back of the cantilever. The two most commonly used modes of operation are contact mode AFM and tapping mode AFM, which can be conducted in air or liquid environments. In the contact mode, sample scanning is performed while monitoring the change in cantilever deflection with the split photodiode detector. On the other hand, the tapping mode involves oscillations of cantilever at its resonance frequency (typically~300 kHz). The electrostatic forces increase when tip gets close to the sample surface, therefore the amplitude of the oscillation decreases. The laser deflection method is used to detect the amplitude of cantilever oscillation. Similar to the contact mode, feedback loop maintains a constant oscillation amplitude by moving the scanner vertically at every x,y data point. Recording this movement forms the topographical image.

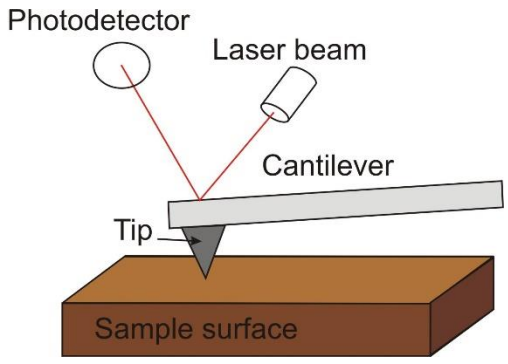

Figure 3.13 A schematic illustration showing basic components of AFM.

Sample preparation: samples were prepared in a similar way they were prepared for doing optical microscopy, i.e. by drop coating onto glass piece and then dried at R.T. AFM height topography and AM-FM tapping mode imaging were carried out using the Asylum Research MFP-3D AFM in air. Silicon AFM probe (Tap300-G, Budget Sensor)

with resonant frequency of 300 kHz and a force constant of 40 N/m mounted on the AM-FM cantilever holder was used for nanomechanical characterisation; the tip calibration was performed using a standard sample of Matrimid®5218 with an established Youn*G*'s modulus (*E* = 4 GPa). Veeco Dimension 3100, under the standard tapping mode and a silicon tip was used for AFM imaging of Perylene@ZIF-8, and ZIF-8 derived from supraMOF samples.

3.2.2.3 Scanning Electron Microscopy (SEM) and Sample Preparation

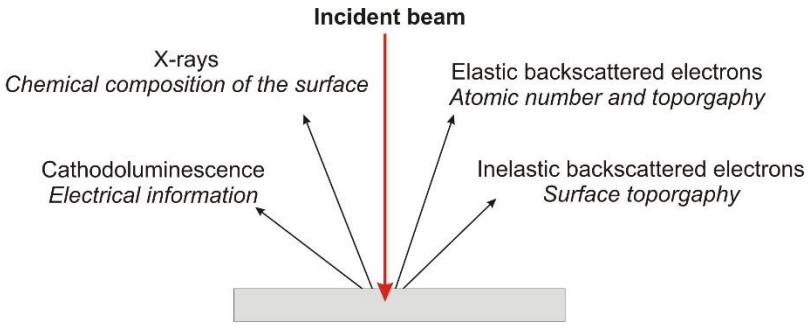

Figure 3.14 SEM uses inelastic backscattering for recording surface topography of sample. Above diagram shows different effects of electron beam interaction with sample and the further use of interacted beam for detailed study of sample.

SEM theory: SEM provides surface topography along with information about other surface characteristics such as chemical composition, electrical conductivity etc. The data get generated from the reflection of accelerated electron beams by sample surface. When electrons hit the sample surface, they lose their energy by repetitive random scattering and adsorption in an outer layer into the depth varying from 100 nm to 5 microns. A resultant interaction between electron beam and the surface provides signals. The signals mainly originate from secondary or inelastic scattered electrons (Figure 3.14). Secondary electrons are ejected from the k-orbitals of atoms within the surface layer of thickness about a few nanometers. Secondary backscattered electrons provide the most common signal to investigate surface topography with

lateral resolution up to 0.4 - 0.7 nm. The SEM image formed is the result of the intensity of the secondary electron emission from the sample at each x,y data point during the scanning of the surface.

Sample preparation: gel specimens were coated with a thin layer of gold for 30 seconds using the SC7620 Polaron sputter coater (Quorum Technologies) before examination under the SEM. Similarly, nanoparticles and nanosheet or nanoplate MOF samples were drop coated using dilute dispersion in methanol onto the small piece of glass and then dried by leaving them at R.T. for an hour before gold sputtering. Scanning electron microscopy was performed on gold coated gel and nanoscale MOF samples using the Carl Zeiss EVO LS15 environmental electron microscope set up.

3.2.2.4 Transmission Electron Microscopy (TEM)

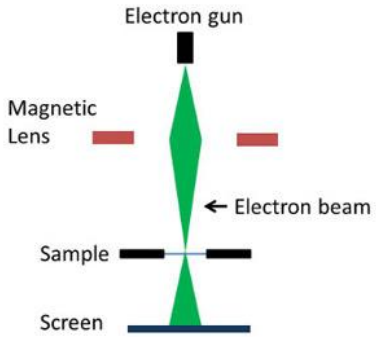

Figure 3.15 Above diagram is a sketch showing basic components of TEM instrument.

TEM theory: In TEM, the source of illumination is a beam of electrons of very short wavelength, generated using a tungsten filament placed at the top of a cylindrical column of about 2 m high. The entire optical system of TEM is enclosed under vacuum. Magnetic coils present along the column at specific intervals are used for focussing the electron beam. In short, TEM involves a high voltage beam of electron emitted by a cathode and formed by magnetic lenses, which later transmit through the thin sample to create the sample image (Figure 3.15). The beam of electron that has been partially

transmitted through the very thin specimen carries information about the structure of the specimen. The spatial variation in this information gets magnified by a series of magnetic lenses until it is recorded by hitting a fluorescent screen, photographic plate, or light sensitive sensor like CCD (charge-coupled device) camera. The image detected by the CCD can be displayed in real time on a monitor or computer.

Sample preparation: for performing transmission electron microscopy, very dilute solutions of thoroughly washed wet nanoscale compounds were used. Dilute sample dispersion in methanol were subjected to sonication for a minimum of15 minutes before drop coating them on holey carbon coated copper grids (300 mesh, Agar scientific). Sample on copper grid was dried by leaving it at R.T. for an hour prior to TEM imaging. TEM images were acquired using the JEOL JEM-2100 LaB6 transmission electron microscope at 200 kV.

3.2.3 Spectroscopic Studies

3.2.3.1 Raman Spectroscopy

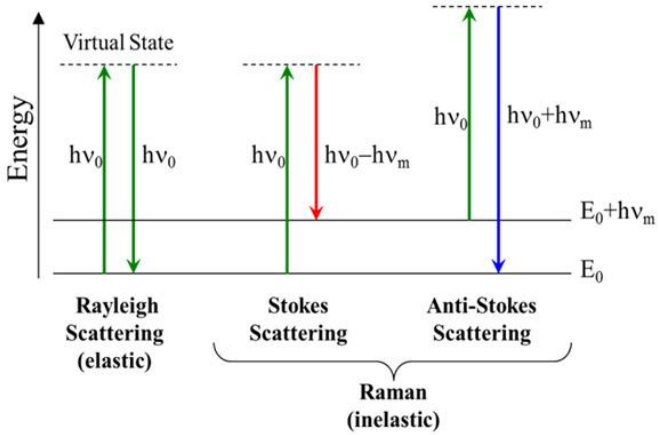

Figure 3.16 Above illustration shows difference between the Rayleigh scattering and the Raman scattering.

Raman spectroscopy theory: Raman spectroscopy is based on Raman Effect, which is a frequency shift of a small fraction of scattered radiation, different from a frequency

of monochromatic incident radiation. Raman spectra obtained from the inelastic scattering of incident radiation through its interaction with vibrating molecules (Figure 3.16). It investigates the information about the molecular vibrations. When a monochromatic radiation strikes at sample, it scatters in all directions after its interaction with sample molecules. Much of this scattered radiation has a frequency which is equal to frequency of incident radiation and constitutes Rayleigh scattering. Only a small fraction of scattered radiation has a frequency different from frequency of incident radiation and constitutes Raman scattering. When the frequency of incident radiation is higher than frequency of scattered radiation, Stokes lines appear in Raman spectrum. But when the frequency of incident radiation is lower than frequency of scattered radiation, anti-Stokes lines appear in Raman spectrum. Stokes shifted Raman bands involve the transitions from lower to higher energy vibrational levels and therefore, Stokes bands are more intense than anti-Stokes bands and hence are measured in conventional Raman spectroscopy while anti-Stokes bands are measured with fluorescing samples because fluorescence causes interference with Stokes bands. A change in polarizability during molecular vibration is a pre-requisite condition to obtain Raman spectrum of sample.

Sample preparation: Raman spectroscopy on the ZnQ@ZIF-8 sample was performed by dispersing some crystalline powder of sample on glass slide and then imaged under the Bruker Senterra dispersive Raman microscope equipped with 532 nm, 633 nm and 785 nm lasers. Sample was tested by using various laser powers from 5 mW to 50 mW and then spectra were recorded using the 532 nm laser. For other samples including OX-1 framework, functionalised OX-1 frameworks ground powder samples were used to monitor Raman spectra using MultiRAM FT-Raman Spectrometer (Bruker) equipped with a 532 nm laser.

3.2.3.2 Infrared (IR) Absorption Spectroscopy

IR theory: Infrared spectroscopy is a technique based on the vibrations of the atoms of a molecule. An infrared spectrum is commonly obtained by passing infrared radiation through a sample and determining what fraction of the incident radiation is absorbed at a particular energy. The energy at which any peak in an absorption spectrum appears corresponds to the frequency of a vibration of a part of a sample molecule. An FTIR spectrometer works by taking a small quantity of sample and introducing it to the infrared cell, where it is subjected to an infrared light source, which is scanned from 4000 cm^{-1} to around 600 cm^{-1}. The intensity of light transmitted through the sample is measured at each wavenumber allowing the amount of light absorbed by the sample to be determined as the difference between the intensity of light before and after the sample cell. This is known is the infrared spectrum of the sample. In the infrared region of the spectrum, the resonance frequencies of a molecule are due to the presence of molecular functional groups specific to the molecule.

Sample preparation: Infrared absorption spectroscopy was performed using the Bruker Vertex 80V FTIR interferometer on dry solid powder.

3.2.3.3 UV-Visible Spectroscopy

UV-Vis theory: Ultraviolet and visible radiation interacts with material to cause electronic transitions (promotion of electrons from the ground state to a high energy state). The ultraviolet region covers the wavelength region of 190-380 nm, the visible region fall between 380-750 nm. The following electronic transitions could occur in UV-Vis range: a) π-π^* b) n-π^* c) σ-σ^* d) n-σ^*. The σ to σ^* transition requires an absorption of a photon with a wavelength which does not fall in the UV-vis range. Thus, only π to π^* and n to π^* transitions occur in the UV-vis region are observed.

Sample preparation: solid–state diffuse reflectance spectra (DRS) were recorded on a UV-2600 Shimadzu spectrophotometer using a standard sample holder.

3.2.3.4 Fluorescence Emission Spectroscopy

Fluorescence spectroscopy theory: Upon absorption of light, molecules get excited to higher energy excited state levels. Molecular excitation process allows molecules to reach any of the vibrational sub-levels associated with each electronic state. Having absorbed energy and reached one of the higher vibrational levels of an excited state, the molecule rapidly loses its excess of vibrational energy by collision and falls to the lowest vibrational level of the excited state. In addition, almost all molecules occupying an electronic state higher than the second undergo internal conversion process and travel from the lowest vibrational level of the upper state to the higher vibrational level of a lower excited state which has the same energy. From there the molecules again lose energy until the lowest vibrational level of the first excited state is reached. From this level, the molecule can return to any of the vibrational levels of the ground state, emitting its energy in the form of fluorescence (Figure 3.17). Since the emission of fluorescence always takes place from the lowest vibrational level of the first excited state, the shape of the emission spectrum is always the same, despite changing the wavelength of exciting light.

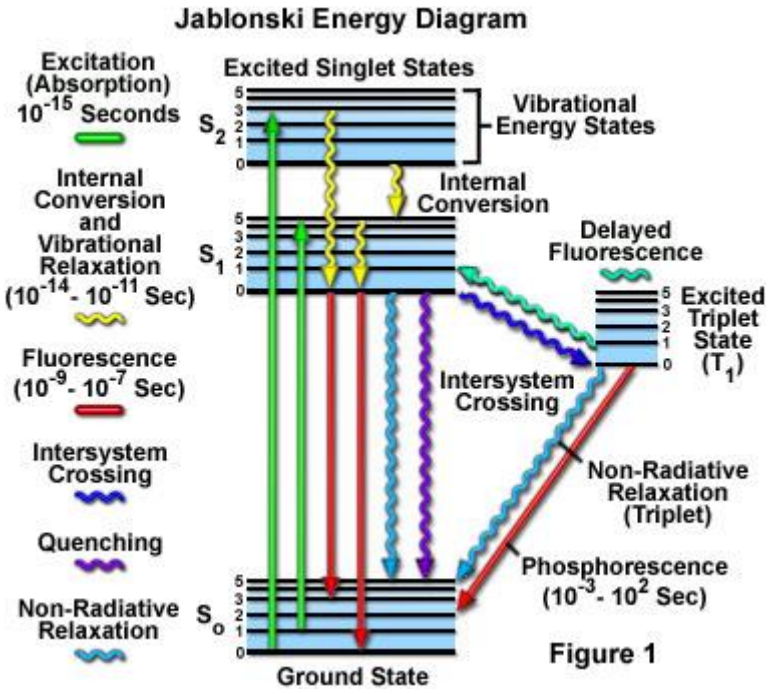

Figure 3.17 Above image is a Jablonski diagram explaining the electronic states of a molecule and the transitions between them.

Sample preparation: solid–state emission spectra of ZnQ@ZIF-8, ZnQ and ZIF-8 samples were measured using the Horiba FluoroMax spectrofluorometer at a fixed slit width of 5 nm and a constant excitation wavelength of 350 nm. Emission spectra for samples of ZnQ_{DMF}@OX-1, ZnQ_{DMA}@OX-1, dispersion of ZnQ_{DMF}@OX-1 in different solvents and Perylene@ZIF-8 were recorded using the UPRtek MK350N+ photospectrometer, together with the CIE chromaticity. Quantum yield and fluorescence lifetime measurements were performed on the Hamamatsu Quantaurus-QY Absolute PL quantum yield spectrometer (C11347) and Quantaurus-Tau fluorescence lifetime spectrometer (C11367), respectively. Diluted nanosheet dispersions in respective solvents were used for fluorescence QY and lifetime measurements.

3.2.4 Other Material Characterisation

3.2.4.1 Powder X-ray Diffraction (PXRD)

Theory: X-ray diffraction is a common material characterisation method for the study of crystal structures and atomic spacing. The basis of X-ray diffraction is a constructive interference between monochromatic X-rays and a crystalline sample. X-rays are generated by a cathode ray tube, filtered to obtain monochromatic radiation, collimated to concentrate, and focussed to the sample. A constructive interference gets generated when X-rays interact with the sample and satisfies Bragg's Law i.e. $n\lambda=2d \sin \theta$. Bragg's law is the direct relation between the wavelength of electromagnetic radiation and the diffraction angle and the lattice spacing in a crystalline sample. Diffracted X-rays can be detected further by the detector for evaluation of the sample structures, purity, and/or phase change. In powder X-ray diffraction (PXRD), the random orientations of the powdered sample allow the diffraction from all directions of the lattice, when sample gets scanned for a particular range of 2θ angles. By converting diffraction peaks to d-spacings, compound identification can be achieved as every compound reflects unique d-spacings. PXRD is widely used for the identification of unknown crystalline materials (minerals, inorganic compounds, hybrid materials).

Pawley Refinement in Material Studio: Pawley refinement is a refinement procedure for obtaining the best possible unit cell from diffraction data, starting with a suggested unit cell.[104] In the Reflex module of Materials Studio, Pawley refinement is one of the four methods of powder pattern refinement. It enables user to refine crystal structures against experimental powder diffraction data by decreasing the weighted R-factor, R_{wp}. In Pawley refinement R_{wp} is decreased regardless of the molecular structure present inside the unit cell. A wide range of parameters can be refined using the

Pawley method, encompassing a choice of peak profile and asymmetry functions, crystallite size, lattice strain, lattice constants, integrated Bragg intensities, and background coefficients. The peak fitting process involves two steps. Optimisation of integrated intensities and background coefficients is the first step, while other parameters are fixed. In the second step, the peak shape, cell parameters and zero-point shift parameters are optimized for fixed values of intensities and background coefficients. The two step refinement process can be further continued until it reaches the convergence.

PXRD on samples: For powder X-ray diffraction, samples were prepared by drying them in vacuum oven and then ground to fine powders using mortar and pestle. Ground powders were subjected to X-ray diffraction using the Rigaku Smart Lab diffractometer with Cu Kα source (1.541 Å) and Miniflex Rigaku bench–top X-ray diffractometer. Diffraction data were collected from 2° to 30° of Bragg diffraction 2θ angle, at the rate of 1°/min with 0.01° step size.

3.2.4.2 Particle Size Determination

ZIF-8, ZnQ@ZIF-8 particle sizes were determined using dynamic light scattering (DLS) measurements. Dilute dispersions of samples measured using the Malvern Zetasizer Nano ZS ZEN3600 set up.

3.2.4.3 Thermal Gravimetric Analysis (TGA)

Theory: Thermal gravimetric analysis (TGA) is the material characterisation technique for powder samples, which allows the study of sample composition and its behaviour with temperature rise. TGA measures the amount of weight change of a material, as a function of increasing temperature in an atmosphere of nitrogen, helium, air, other gas, or in a vacuum. TGA provides information regarding phase transitions, absorption and desorption, chemisorption, thermal decomposition, and solid-gas reactions (e.g.,

oxidation or reduction). The amount of sample required for the analysis can vary between 1 mg to 150 mg. This technique is sensitive enough to detect weight change of as small as 0.01 mg of weight. It helps to determine temperature and the weight change of decomposition reactions, which allows quantitative composition analysis. This helps in determining water content or the residual solvents in a material. TGA can also give information about the purity of samples like mineral, inorganic compound, or organic material.

Sample preparation for TGA: powdered samples free from solvent molecules by drying in vacuum and high temperature were sealed in glass vials and then used for recording thermal gravimetric data. It was recorded using the TA Instrument Q50 at a heating rate of 20 °C min^{-1} from 30-700 °C under dry nitrogen.

3.2.4.4 Electrical Conductivity Measurement of SupraMOF Containing HKUST-1 Nanoparticles

Theory: Electronic versus ionic conductivity: Electrical conductivity indicates the ability of material to conduct an electric current. Electrical conductivity generally observed in metals. The atoms of metals normally possess one to three electrons in their outer shells. In a solid-state condition, freely bound electrons n outer electronic shell can move from atom to atom. When a charge is applied to one side of a lump of metal its electrons move easily in response, away if it is negative and towards if it is positive. One can make a wire out of the metal and apply a steady supply of electrons at one end and get a current through the wire. On the other hand, ionic conductivity occurs in solutions of various salts (also in melted salts.) When an ionic compound (salt) is formed the electrons from the metallic atoms are captured by the atoms of the non metal. For instance in sodium chloride, the sodium atoms give up their single outer electron becoming positive sodium ions and the chlorine atoms capture those

electrons becoming negative chlorine ions. In the solid state the positive and negative ions are held together by their opposite charges in a rigid lattice. In the liquid state (solution or melted) the ions move around freely. If positive and negative electrodes are inserted into an ionic liquid the positive ions will migrate towards the negative pole and the negative ions will move towards the positive pole. At the negative pole, positive ions capture electrons. At the positive pole negative ions give up their extra electrons. Each ion is changed chemically in some way. The movement of charged ions in the liquid is ionic conduction.

Alternating current (AC) versus direct current (DC) measurement: There are two techniques used to measure electrical conductivity.

i) AC conductivity measurement: this technique is used to identify good ionic conductors. Complex impedance, admittance, permittivity and modulus, are the four basic functions to analyse the ac data.

ii) DC conductivity measurements: this technique is used to identify good ionic as well as electronic conductors. The contribution of ionic or electronic components to the

conductivity depends on the temperature range.

Frequency dependence of ac conductivity: there are three mechanisms of charge transport that can contribute to a direct current in amorphous semiconductors. They all can contribute to the ac conductivity as follows. (a) Transport by carriers excited to the extended states; (b) Transport by carriers excited into the localized states at the edges of the valence or conduction band and (c) If energy density of states is finite, hopping transport occurs by electrons with energies near the Fermi level.

In AC electrical conductivity measurement, electric conductivity originates because of applied potential dependent of time. The potential is of oscillatory type with sinusoidal

wave from, here the classical parameter electric resistance is termed as impedance. Thus, impedance is the analogue term for electric resistance in an alternating current. The potential oscillates between +V and -V magnitude. Here, the impedance is a complex number, in which the imaginary part provides information about the magnitude of signal loss, with relation to previous potential magnitude applied by an equipment. The magnitude loss of original signal investigated as a function of frequency gives the impedance spectroscopy. During the experiment, the electric potential is constant and with small intensity, the frequency is continuously changed. The electric conductivity called dc does not depend on the time, this conductivity is the classical term determined by Ohm's law V=RI.

Sample preparation and conductivity measurement of gel samples: electrical conductivity of gel samples were measured using the Keithley 2614B sourcemeter and a custom designed conductivity cell lined with aluminium electrodes spaced at 1 cm apart. The conductivity of the visco-elastic solid was measured from a thin layer of VE⊃ACN material sandwiched between a pair of flat aluminium electrodes.

3.2.5 Theoretical Calculations

3.2.5.1 Molecular Orbital Energy Calculations

Highest occupied molecular orbital (HOMO) and lowest unoccupied molecular orbital (LUMO) energy levels for both species (i.e. ZIF-8 and ZnQ) were calculated considering 1×1×1 unit cell and a single molecule respectively, using the DMol3 density functional theory (DFT)[105] code implemented in Accelrys Material Studio. The generalised-gradient approximation (GGA) exchange-correlation functional by Perdew and Wang (PW91)[106] was adopted to determine the HOMO-LUMO band gaps. A 1×1×1 unit cell was considered for calculating the energy levels of the (vacant) ZIF-8

framework and the isolated Perylene molecule in the case of Perylene@ZIF-8. To model the guest@host assembly containing a confined Perylene guest molecule, the Perylene molecule was docked into the void of the ZIF-8 (host) framework and geometrically optimised using the Forcite module. The band gap of the optimised guest@host structure was then calculated using DMol3. The calculation parameters used are listed in the Appendix provided at the end of the thesis (Table A6).

3.2.5.2 Geometry Optimisation and Band Gap Calculations

Geometrical optimisation was performed using the Forcite module implemented in Materials Studio v.8. For the OX-1 host framework structure, molecular cluster comprising a single pore was taken into consideration by using the 1×2×1 super cell, to calculate the plausible guest geometry as a result of host confinement effects.

Chapter Four

New Class of Materials: ‘‘SupraMOFs’’

4.1 Background

4.1.1 Supramolecular Chemistry

The chemistry beyond the molecule, known as ‘supramolecular chemistry’[107-108] has witnessed a rapid growth over the past two decades.[36, 109-111] Notably, the traditional candidates in the field of supramolecular science, featuring the self-assembly of small molecules comprising purely organic compounds have been superseded by exotic and very diverse families of hybrid (organic-inorganic) molecular assemblies and composite systems.[112-115] Self-assembly methodologies that yield functional gel materials have attracted significant interest owing to their potential applications in medicine,[32, 116] energy,[117-118] and environmental sustainability.[119] Within this broad class of soft matter, metal-containing gel materials termed ‘metallogels’[120-122] could offer additional controls for tuning the structural and physico-chemical properties for many targeted applications.[123-125] Metal-containing metallo-gelators studied to date can basically be divided into two main categories: (a) solvent immobilisation attributed to metal-coordination effects,[126] and (b) solvent immobilisation conferred by metal complex species used in constructing metallogels.[112, 122] Recently, researchers have also focused on metal-organic gels (MOGs),[127-131] which generally contain continuous chains of alternating metal and organic molecules to enable the immobilisation of solvents.[132-133]

4.1.2 Whats is SupraMOF

Innovative implementation of the basic principle of continuous chain formation of metal-organic building blocks has opened the door to the recent development of *smart* supramolecular gels,[75, 134-135] containing porous 3D scaffolding of metal-organic frameworks (MOFs).[1-3, 136] I termed these materials — 'supraMOF', as derived from supramolecular gel self-assemblies coexisting with in-situ generated MOF entities. Literature on MOF compounds has proliferated to cover a very wide and diverse spectrum of applications.[5, 11, 137-139] Despite their vast potential utilities, MOF science in combination with self-assembled supramolecular materials is, hitherto, a largely unexplored research topic. One exciting possibility is to yield 'smart' supramolecular materials[134-135] by leveraging the tuneability of MOF compounds, to attain stimuli-responsive behaviours towards: magnetism, light, sound waves, mechanical stresses, temperature, electricity, etc. Moreover, sol-gel systems will offer new possibilities for facile processing and affordable deposition of functional films towards engineering of sensors, actuators and microelectronic devices.[4, 15, 140] In this study, I present a rare type of supramolecular hybrid material built from self-organisation of nano-metal-organic framework (NMOF) particles, which are accommodated within highly-aligned fibre network scaffolding. Metal-organic framework (MOF)[99, 136, 138, 141] is a rapidly expanding class of crystalline nanoporous materials, whose three-dimensional (3D) framework consists of ordered units of metal ions or clusters bridged by organic linkages. MOFs offer rich chemical functionalities combined with vast structural versatility.[140, 142] The high uniformity and 3D microporous architecture of MOF crystals could provide

the unique platform for symbiotic effects, yielding orthogonal interactions[143-144] central to achieve supramolecular self-assembly.

4.2 SupraMOF Materials Containing HKUST-1

The microporous material designated as HKUST-1,[145] represents one of the most intensely studied MOFs today due to its wide-ranging potential applications. Typically, it can be obtained *via* solvothermal reactions between Cu(II) and BTC^{3-} (1,3,5-benzene tricarboxylic acid), yielding crystalline HKUST-1 [$Cu_3(BTC)_2$], as the most thermodynamically favourable product.[146] In fact, HKUST-1 is renowned for its ease of synthesis using different solvents, temperatures, or bases,[147-150] in addition to membranes, hollow capsules and superstructures derived from it.[151-152] Herein I demonstrate that, by employing a high concentration of standard reactants of HKUST-1 in a relatively small quantity of solvents, yields previously unreported gel-like hybrid materials that exhibit counterintuitive chemico-physical properties.

4.3 High Concentration Reaction (HCR) Approach for Synthesis

In the present work, I discovered that room-temperature reaction between $Cu(NO_3)_2$ solution and deprotonated BTC, using triethylamine base (NEt_3) yields facile formation of an unconventional gel-like supramolecular self-assembly. Interestingly, the aforementioned reactions can be accomplished in both polar-protic and -aprotic solvents, resulting in an entirely new system of MOF-based supramolecular hybrid materials, which I termed: G⊃ACN, G⊃DMF, G⊃DMSO, G⊃ETH and G⊃MEH (where G denotes gel obtained using solvent ACN: acetonitrile, DMF: N, N-dimethyl formamide, DMSO: dimethyl sulfoxide, ETH: ethanol, MEH: methanol). The formation

mechanism was investigated utilising different solvents, which allowed us to study the rich morphological and structural diversity of these novel hybrid materials. I found that the use of different solvents yields hybrid materials that exhibit distinct structural, mechanical, chemical and electrical properties. Noteworthy, sol-gel transitions occur only in the case of G⊃DMSO, while viscoelastic phase conversion (from soft to rigid network) is evident only in G⊃ACN. Moreover, detailed characterisation of physico-mechanical properties has enabled us to pinpoint structural dependencies of uncommon functions. The above mentioned are key highlights of the current study which are explored in detail herein.

4.4 Smart Behaviour of SupraMOFs: Stimuli Response

4.4.1 Sol-Gel Transition

Application of DMSO as a solvent for making solutions of $Cu(NO_3)_2$ and BTC produces a hybrid gel compound featuring unique properties, as depicted in Figure 4.1 Although the reaction of BTC and Cu(II) in DMSO solvent has previously been reported,[153] in proposed approach, the addition of triethylamine (NEt_3) triggers an unexpected auxiliary effect leading to the formation of a new supramolecular material. Remarkably, this hybrid gel compound, G⊃DMSO, exhibits multiple responses against thermal, mechanical and chemical stimuli (Figure 4.1a). First, it was found that subsequent alternate additions of 1molar equivalent of BTC and/or 1.5 equivalent of Cu(II) solution cause the hybrid assembly to undergo a rapid phase transformation, i.e. switching from gel to sol, and *vice versa*. This observation confirms that the hybrid gel can be broken down by dissolution, but subsequently re-assembled upon the addition of cationic Cu(II) or anionic BTC^{3-}, such that chemical triggering accounts for the

reversible nature of sol-gel transformation observed. Nevertheless, as this process is repeated with successive cycles of additions of BTC and/or Cu(II) solutions, an increasingly longer time was required to recover the gel form.

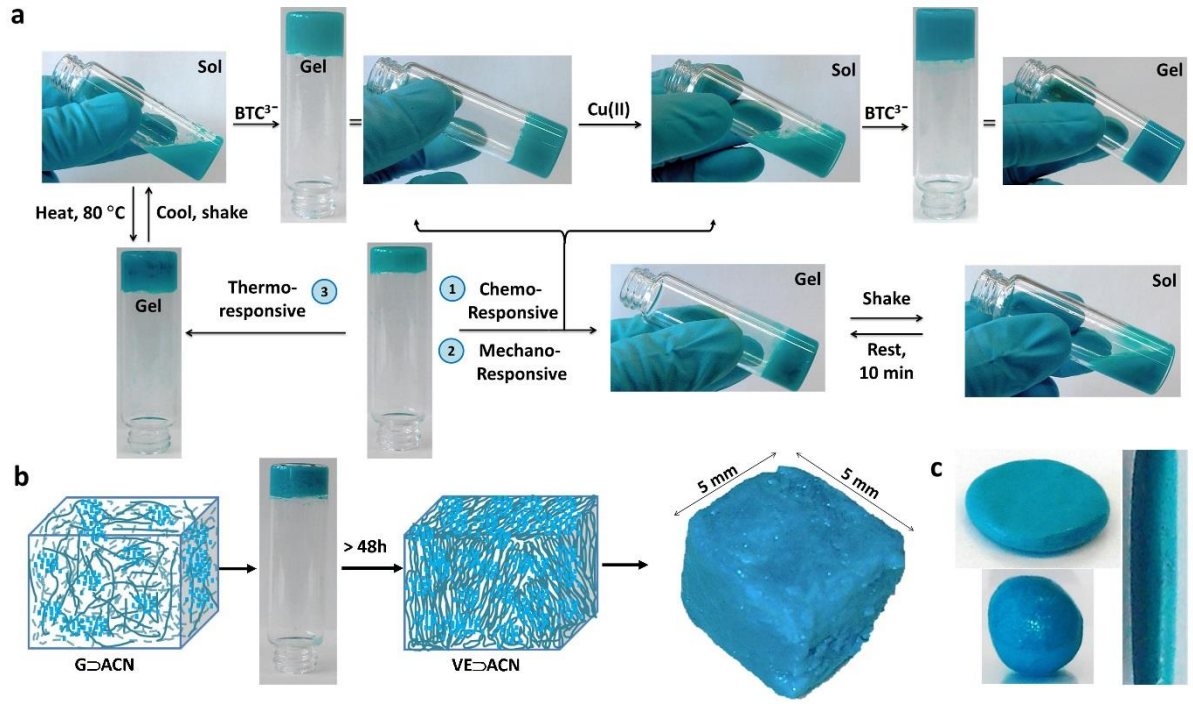

Figure 4.1 (a) Multi-stimuli chemo-mechano-thermo responsive behaviour enabled *via* sol-gel transformation of G⊃DMSO. (b) Schematic illustration showing phase transformation of G⊃ACN, after ~48 hours, forming the visco-elastic material, termed VE⊃ACN. Schematics: fibrous strands (dark green) represent the 3D network scaffolding, which is integrated with HKUST-1 NMOF particles (light blue). Right: a cuboid measuring 5×5×5 mm^3 moulded from a monolith of VE⊃ACN. (c) Examples of several 3D objects made from VE⊃ACN.

Second, mechanical stresses invoked by shaking could disrupt the structural integrity of the G⊃DMSO hybrid assembly, causing the gel to collapse into a viscous sol (Figure 4.1a). This gel phase, however, can be regained either by subjecting the sol to sonication for ~1-2 minutes, or simply by leaving it uninterrupted for ~10-15 minutes. The gel was found to be extremely sensitive to application of external forces, such that phase recovery (sol to gel) takes longer to occur when gel is mechanically agitated for

a longer period of time. Third, further to chemical and mechanical responses, this particular hybrid gel also demonstrates thermo-responsive behaviour; for instance, the sol of G⊃DMSO can be transformed back into a gel when heated at 80 °C for just ~1-2 minutes.

4.4.2 Gel to Viscoelastic Transition

I identified another striking phase change phenomenon conferred by the acetonitrile solvent (ACN), wherein the corresponding hybrid gel synthesised is designated as G⊃ACN. Initial observation of G⊃ACN gels transforming into a semi-solid-like material has prompted us to study this effect in detail. I established that, by allowing G⊃ACN sample (sealed in a vial) unperturbed for more than 48 hours would eventually transform the gel phase into a visco-elastic (VE) material (Figure 4.1b, c), which I termed VE⊃ACN (detailed visco-elastic mechanical behaviour presented in later sections). Its two major characteristics are: (1) if gentle mechanical stress is imposed onto G⊃ACN in the gel state (for instance, by shaking sample vial), this causes the fibrous gel scaffolding to break down to yield a sol; and (2) more vigorous mechanical agitation of the reactant mixture ultimately produces only precipitation, prohibiting any further gelation from occurring. Above findings support the notion that gel to visco-elastic phase change can be accomplished, only if, the underlying gel scaffolding (i.e. building skeleton) is kept stress-free and maintained stable with encapsulated solvent molecules. In the light of this, the foundation for constructing a rigid fibre network stems from the gel itself, acting as the 3D scaffold; but without which, phase change into the visco-elastic material cannot occur. An attractive physical property of the VE⊃ACN material lies in its shape-persistent capacity; it is mechanically robust enough to be

dissected, deformed, or moulded into a range of 3D shapes, a few examples of which illustrated in Figure 4.1b and 4.1c.

4.5 Microstructural Features of SupraMOF

Figure 2 shows microstructural characteristics of the supramolecular hybrid gel materials characterised by scanning electron microscopy (SEM), revealing exquisite fine-scale morphologies that correlate to their chemical structures and physical properties (Figure 4.2). Comparing Figures 4.2a to 4.2b, it was found that the visco-elastic material (VE⊃ACN) consists of fine fibrous filaments hierarchically packed within fibre bundles, which are reminiscent of fibrils present in structural biological materials[34-35]. Such a microstructure, however, is absent in the initial gel material (G⊃ACN) prior to its visco-elastic conversion. It can be seen that micrographs of the G⊃DMSO system that displays multi-stimuli response reveal relatively thicker rods of gel-like blocks; two examples of which shown in Figure 4.2c and 4.2d with dimensions of ~200 × 50 μm. In contrast, the remaining gel samples (Figure 4.2e-j) feature appreciably smaller bundles of microscopic fibres, growing unidirectionally in the form of strips, whose lengths may extend from several μm up to 100s of microns. It is worth noting that recent literature on MOF-based aerogels,[73, 133, 154] xerogels[155] and metal-organic gels (MOGs)[131, 156] exhibit substantially different fine-scale microstructures, compared with the distinctive fibre micro-architectures I reported here.

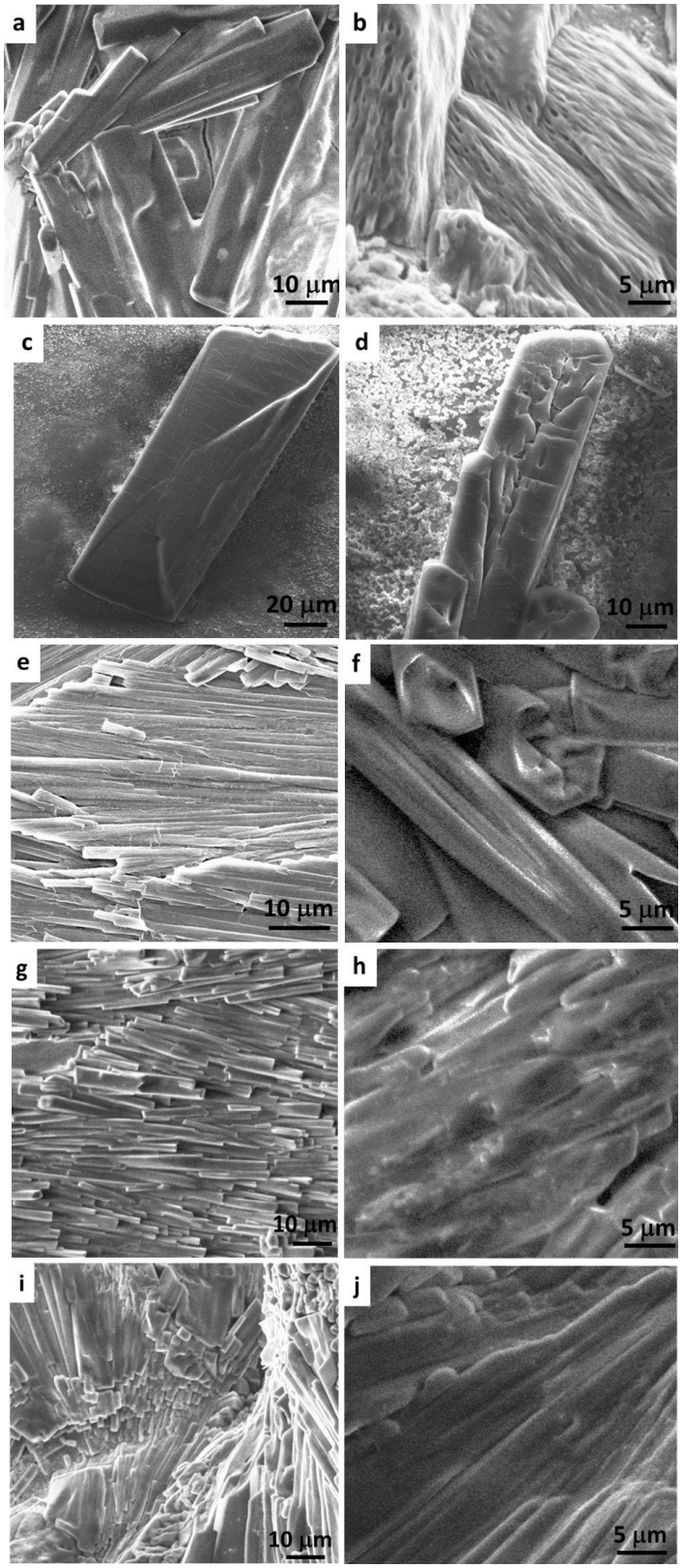

Figure 4.2 SEM micrographs of hierarchically self-assembled gel microstructures (dried samples) obtained from synthesis employing different solvents. (a) G⊃ACN and (b) its corresponding visco-elastic material VE⊃ACN, (c and d) G⊃DMSO, (e and f) G⊃MEH, (g and h) G⊃DMF, (i and j) G⊃ETH.

Given the identical chemical precursors employed in all the synthesis (Figure 3.1), apart from the choice of solvent, it is intriguing that sol-gel transformation was identified only in the case of G⊃DMSO, whereas visco-elastic conversion evidenced only in the case of G⊃ACN. This result underscores the critical role played by the specific solvent molecules, which in turn, affects the microstructures of the resultant fibre network assembly (Figure 4.2) and, henceforth its physico-chemical characteristics. Electron donor atoms, *viz*. O, N, S, which are present in certain solvent molecules enhance interaction with Cu(II) centres, and may extend the structural connectivity by means of hydrogen bonding. Especially in the DMSO solvent, for example, I propose that soft S and hard O donor atoms (at opposing ends of molecule) facilitate switchable connections for weak bond making-breaking process; this mechanism could accommodate supramolecular association-dissociation processes thus triggering sol-gel conversion of G⊃DMSO (Figure 4.1). Moreover, because S and O readily interact with soft and hard electrophiles, DMSO forms strong hydrogen bonding (Kamlet-Taft parameters: $\alpha = 0.00$, $\beta = 0.76$)[157] with BTC.[158] Of the systems I studied, G⊃DMSO requires the longest gelation time, suggesting that the reaction responsible for fibre formation is occurring at a relatively slower rate, due to effects of solvent interaction that may cage BTC^{3-} linkers approaching the Cu(II) cations. Although O donor is also present in other solvent molecules, I found that monodentate ligation property is inadequate to trigger microstructural re-integration fundamental to reversible sol-gel conversions. Turning to G⊃ACN, the linear molecular structure of acetonitrile (ACN) means that, not only its associated geometrical constraints should be weaker, but also it offers opportunity for coordination to the Cu(II) centres to further stabilize the overall supramolecular network assembly. Together, it is projected that such auxiliary effects, over time, perpetuate transformation of gel into the visco-elastic

material, which constitutes fine-scale fibrous architecture specific to VE⊃ACN (Figure 4.2b).

4.6 Mechanism Underpinning Hybrid Self-Assembly

By virtue of the rapid formation of G⊃MEH gels from methanol (~2 minutes), I probed this material to gain insights into the basic structural development mechanisms. During the reaction, I observed intense colour emerging from nanoparticles embedded in the fibres as time advances; these nanoparticles can be easily harvested from embedding fibrous matter by washing the gel thrice using excessive methanol.

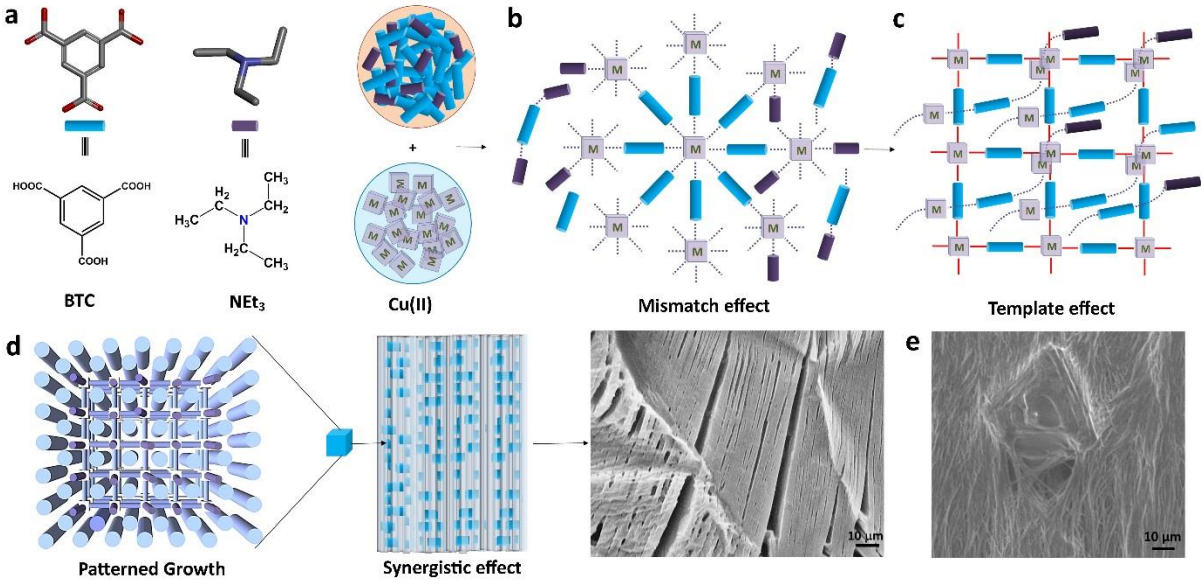

Figure 4.3 Schematic illustrating the proposed mechanism underpinning hierarchical growth of MOF hybrid network encompassing highly directional fibers. (a) Fundamental building blocks reacted to create (b) weak interaction with each other *via* the mismatch effect (c) template effect involving development of coordinating bonds between BTC^{3-} and Cu(II), facilitated by inter-penetration of one-dimensional networks bound by weak interactions. (d) Patterned growth by means of the synergistic effects between nanoparticles and self-assembled fibrous structure, informed from SEM image of G⊃MEH containing nano- HKUST-1 particles integrated in fibers (see Figure 4.4g). Note: black dotted lines represent weak inter-molecular interactions; red bold lines denote coordination bonding. (e) Formation of a defective crystal of HKUST-1 embedded in the fiber network of G⊃DMSO.

Bulk amount of nanoparticles collected this way have been examined by powder X-ray diffraction, scanning electron microscopy and atomic force microscopy, confirming that they are in fact nanometre-sized MOF (NMOF) particles of phase pure HKUST-1.

I rationalise that the mechanism underpinning the construction of supramolecular MOF hybrid progresses in accordance with Figure 4.3 (a-d), endorsed by experimental observations. At the beginning of the self-assembly process, organic and inorganic basic building blocks coalesce *via* weak interactions in a nascent network of gel material. This development is subsequently accompanied by stronger coordination bonds forming between Cu(II) and BTC^{3-}; despite overcoming weaker molecular interactions, it caused no collapse to the former assembly, therefore yielding HKUST-1 nanoparticles in the fibre network.

Recent reports on inter-convertible polymer-metal-organic framework (poly-MOF)[159] hybrid materials and conversion of MOFs into gel-like MOFs[160-161] are worth describing here for comparison. In the case of poly-MOFs, amorphous polymers bearing coordinating donor atoms (in repeating units) interact with metal ions to form MOF-containing hybrid material. Gel-like MOF material,[160-161] on the other hand, is thought to form by interconnection of Functionalised cross-linking organic linkers present in the MOF. In contrast, the supramolecular assembly of the current series of hybrid materials follows an entirely different mechanism. Distinctively, MOF nanoparticles evolved by overcoming the weakly interacting species present in the nascent assembly, which ultimately yields hierarchical architecture where NMOFs constitute the major crystalline phase of the overall soft matter. Abundance of HKUST-1 NMOF particles and unoccupied metal sites in HKUST-1 crystal lattice offers prospect to other molecules to either coordinate or penetrate the intrinsically hollow MOF channels (resembling templating effects, Figure 4.3c). It can be inferred that the

3-fold rotational symmetry of BTC molecules, paired with coordination to Cu(II) centres, may direct growth of fibrous network in a highly aligned fashion (patterning effect). Moreover, the use of NEt_3 for deprotonating BTC generates cationic NEt_3^+ species; it can be noted from literature [162-163] that the propensity of NEt_3 to coordinate with Cu(II) in the presence of coordinating organic ligands. Such a mechanism, termed the 'mismatching molecular effect',[133] creates competition between multiple coordinating molecular species alongside NMOF formation due to the resultant synergistic effects (Figure 4.3d).

To further understand the growth behaviour, in another experiment I have interrogated the effects of uneven dissemination of starting materials have on the self-assembly mechanism. A layer of BTC^{3-} solution in DMSO (solution viscosity 3.92×10^{-2} Pa·s) was first coated on the glass substrate by dip coating, on top of which was subsequently introduced several droplets of Cu(II) solution containing DMSO. This approach generates a concentration gradient attributed to the localised mixing of organic and inorganic reactants. Because DMSO is a high-boiling-point solvent, the wet sample of G⊃DMSO obtained was left to dry at room temperature; SEM images acquired from the dried sample revealed interesting microstructural attributes elucidating the synergistic self-assembly process, see Figure 4.3e. This finding reveals not only that, NMOF particles integrated in nanometre-sized fibres could behave as small seeds (nuclei) that lead to formation of larger HKUST-1 crystals, but also because of mismatching molecular interactions,[133] defective crystals featuring screw-like dislocations[164] have evolved on the hybrid gel fibre networks. Here it is worth emphasising that normal synthesis of hybrid materials (performed in glass vials with uniform mixing of reactants) will not result in the formation of such defective crystals.

4.7 Rheological Properties of SupraMOFs

4.7.1 Frequency Sweep Measurements

Dynamic rheological experiments were performed to study the structural integrity of the supramolecular hybrid MOFs, when subjected to shear deformation (γ) and corresponding shear stress (τ). The main results are summarised in Figure 4.4, where the storage modulus (*G'*) and loss modulus (*G"*) are measures of the recoverable elastic response and dissipative viscous behaviour, respectively. It follows that the shear modulus ($G = \tau / \gamma$), whose magnitude is, $\sqrt{(G')^2 + (G'')^2}$ thereby reflects the material's mechanical rigidity, *i.e.* its structural resistance (stiffness) against distortion caused by a shear deformation. From Figure 4.4a and 4.4b, it can be seen that the storage (*G'*) and loss (*G"*) moduli of the gel samples are distinct from one another, which indicate tuneable mechanical properties of this family of hybrid materials based on judicious choice of solvents. On one hand, higher storage moduli of the order of *G'*~15-25 kPa have been determined for G⊃ACN, G⊃DMF and G⊃ETH; on the other hand, significantly lower magnitudes were found for G⊃DMSO (~5 kPa) and G⊃MEH (~1 kPa) highlighting that an exceedingly low shear modulus is also attainable.

The loss tangent (tan δ = *G"*/*G'*) versus frequency plot in Figure 4.4c shows characteristic peaks appearing in G⊃ACN, G⊃MEH and G⊃ETH, corresponding to phase changes associated with higher angular frequencies between ~50-100 Hz. Particularly large deviation was observed in G⊃ACN, indicating that its hybrid network is relatively weaker against shear forces imposed at higher frequencies; conversely, G⊃DMSO demonstrates virtually negligible phase change implying good mechanical stability towards shear deformation.

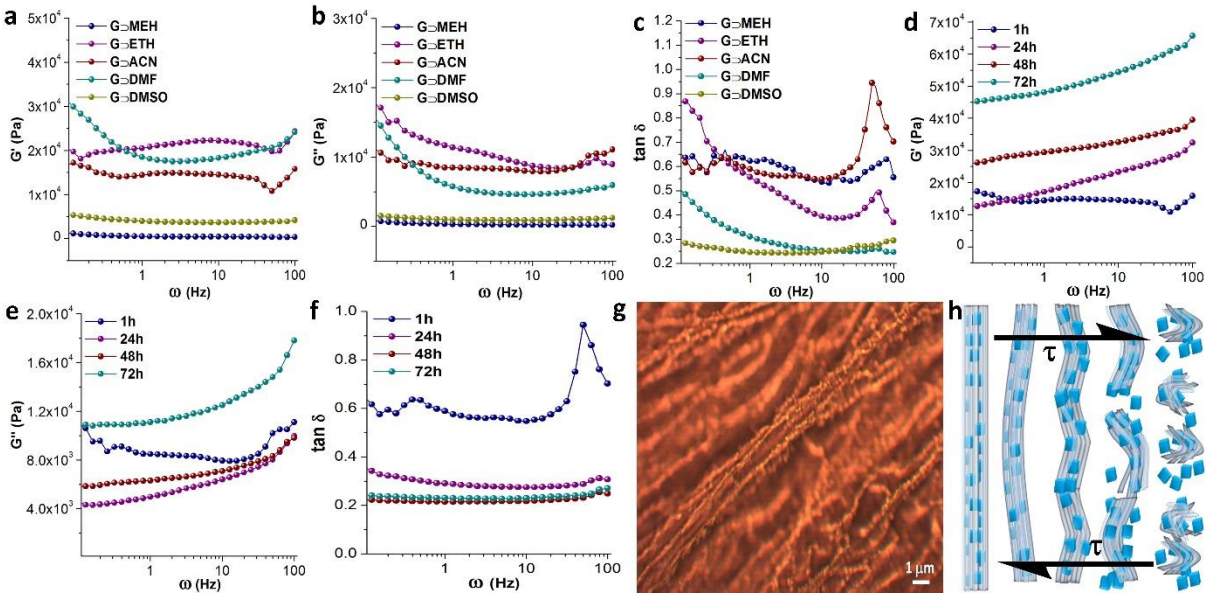

Figure 4.4 Frequency sweep rheological properties under shear deformation for all hybrid materials as a function of oscillatory angular frequency, ω = 0.1 to 100 Hz: strain = 1% (a) storage moduli *G'*, (b) loss moduli *G"*, and (c) loss tangent (tan δ = *G"/G'*). All samples were tested after 1 h from the point of material synthesis (because gelation time in different solvents varies). Evolution of the mechanical response of G⊃ACN measured at 1, 24, 48, 72 h after material synthesis, each of which acquired using a different fresh sample: (d) storage moduli, (e) loss moduli, and (f) loss tangent data, indicating phase stability of VE⊃ACN beyond ~48 h. (g) Optical microscopy image showing highly-ordered HKUST-1 nanoparticles embedded inside the fibers, and (h) schematic representing the proposed microstructural changes occurring over phase transition in the hybrid fiber bundles subjected to an opposing pair of shear stresses τ.

4.7.2 Dynamic Strain Sweep: Reversibility of Phase

Thixotropic nature[165] of the G⊃DMSO sample has been investigated by performing dynamic strain sweep measurements,[130] which confirmed the reversible recovery of the gel phase (within 15 minutes, over shear strain relaxation from 100% to 0.1% at 0.1 Hz angular frequency). Below I have studied the shear-induced disintegration of the supramolecular network assembly using the schematic proposed in Figure 4.4h, in accordance with the observed fibrous architecture integrating HKUST-1 nanoparticles, as exemplified in Figure 4.4g. Indeed the thixotropic timescales[165] of the order of minutes have been established in G⊃DMSO, for which could be linked to

the high concentration of nano-MOF particles affecting the nature of supramolecular hybrid breakdown and its subsequent reconstruction (i.e. recovery upon strain removal. Figure 4.5).

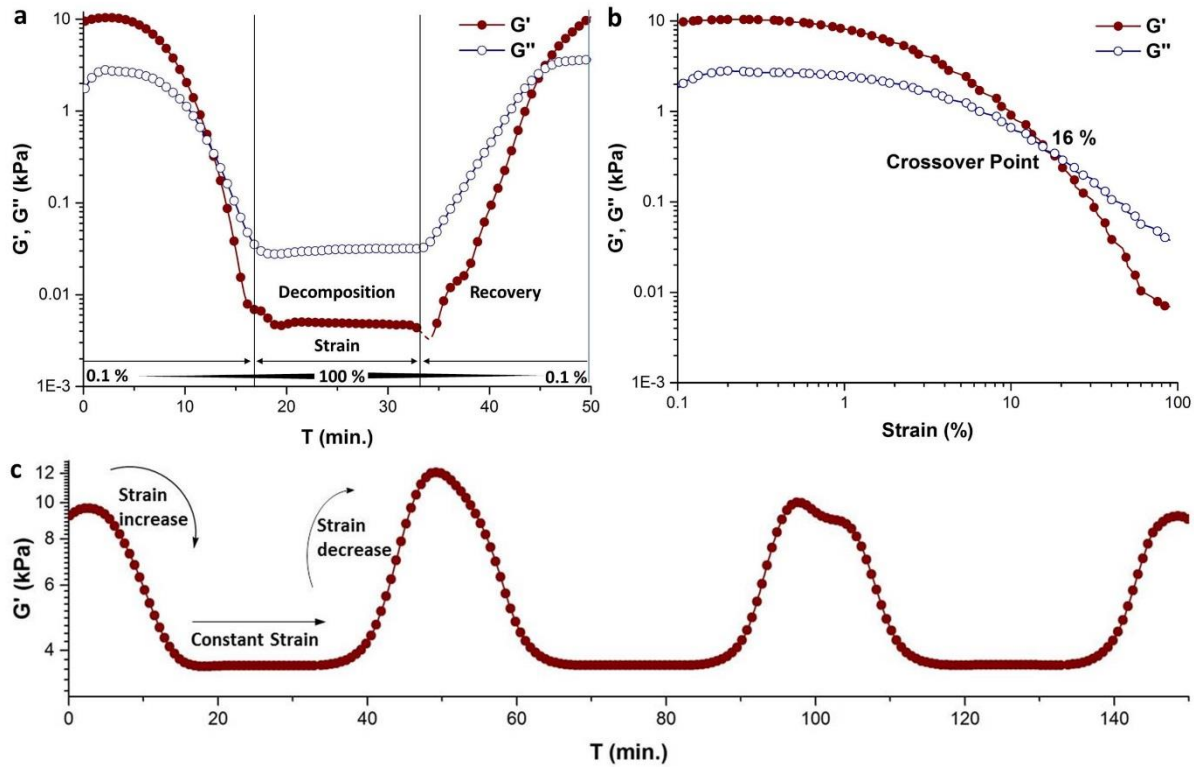

Figure 4.5 Dynamic strain sweep (DSS) measurement on stimuli-responsive G⊃DMSO to confirm its (a) thixotropic behaviour, and (b) to determine the maximum strain tolerance limit (ω = 0.1 Hz). Gel phase recovery in 15 minutes is in agreement with the observed sol to gel transition time lapse observed for mechanical stimulus (c) strain sweep measurement demonstrating the non-linear viscoelastic response of reversible gel phase for multiple consecutive strain cycles.

4.7.3 Creep Recovery Tests to Understand Visco-Elastic Response

By monitoring the structural transitions of G⊃ACN *via* rheology, I have established how the conversion into subsequent visco-elastic phase (VE⊃ACN) alters the overall network rigidity. Figures 4.4d and 4.4e present the storage and loss moduli data, corresponding to 1, 24, 48 and 72 hours, where dynamic structural variations were evidenced from substantial rise in storage moduli with time in a non-linear fashion. For instance at 0.1 Hz, the magnitude of *G'* was initially at 17 kPa (1 h), but increased to

26 kPa (48 h) and finally reached 45 kPa (72 h); likewise at higher frequencies (e.g. 100 Hz) I found *G'* exceeds a factor of three times higher than that of a freshly prepared sample. Significantly, the loss tangent plot in Figure 4.4f shows that, independent of frequency, there is no phase change detected beyond 48 h. This finding further substantiates the claim that, over time, weak supramolecular network in G⊃ACN gel has become more rigid (higher *G*) and thus mechanically strengthened against further shear-induced deformation, as it evolves into VE⊃ACN, constituting a vastly interwoven microstructure (Figure 4.2b).

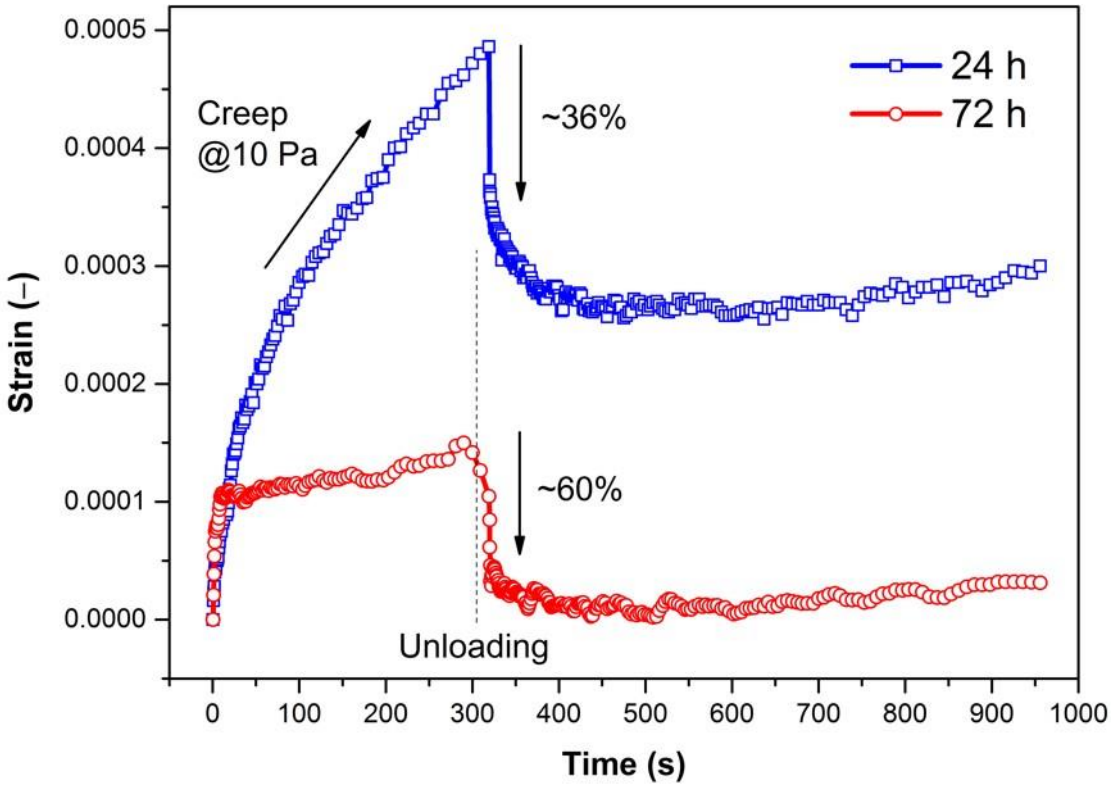

Figure 4.6 Creep-recovery tests at room tempeture performed under a constant shear stress τ = 10 Pa, and followed by complete unloading at 300 sec. The resulting strains as a function of time shows the visco-elastic nature of the G⊃ACN → VE⊃ACN compounds at 24 h and 72 h, with respectively experiencing ~36% and ~60% in strain recovery (w.r.t. maximum strain prior to unloading). This finding confirms that the transformation of 'weak' G⊃ACN gel network (suffers from substantial creep) to the VE⊃ACN semi-solid material confers major improvement in mechanical rigidity.

Dynamic strain sweep measurement on VE⊃ACN has established a strain tolerance of ~11%, which was determined from the crossover point between the storage and loss moduli (Figure 4.5b). Moreover, I performed constant-stress creep experiments comparing the strain recovery of samples at 24 h versus 72 h, in which the latter case corresponding to VE⊃ACN shows remarkably higher creep resistance and strain recovery response (Figure 4.6).

4.8 Electrical Conductivity Response of SupraMOF Hybrids

Electrical conductivity measurements were performed under direct current settings using a potential bias of ±10 V. The conductivity data presented in Figure 4.7 show tuneable electrical properties, for which the magnitude of charge mobility can be varied for samples synthesised from different solvents. Notably, the sample of G⊃MEH exhibits the highest electrical conductivity value at 9.44 S m^{-1}, whereas the lowest conductivity was determined for G⊃DMSO at 0.14 S m^{-1}, i.e. approaching two orders of magnitude below that of the former gel. The second highest conductivity was determined in G⊃ACN (2.51 S m^{-1}), which is followed by G⊃ETH (1.14 S m^{-1}). While a relatively low conductivity has been ascertained for G⊃ACN (2.51 S m^{-1}), surprisingly, the visco-elastic material (VE⊃ACN) derived from the same gel sample yields a markedly higher conductivity value of 9.86 S m^{-1}. Indeed the unique ability for tuning the electrical properties of MOF materials is currently of great interest.[166] Additionally given that VE⊃ACN is malleable, displaying good strain tolerance and it can be easily shaped or moulded into stable structures (Figure 4.1b), its improved electrical conduction property may potentially find utility in future device integration.[167]

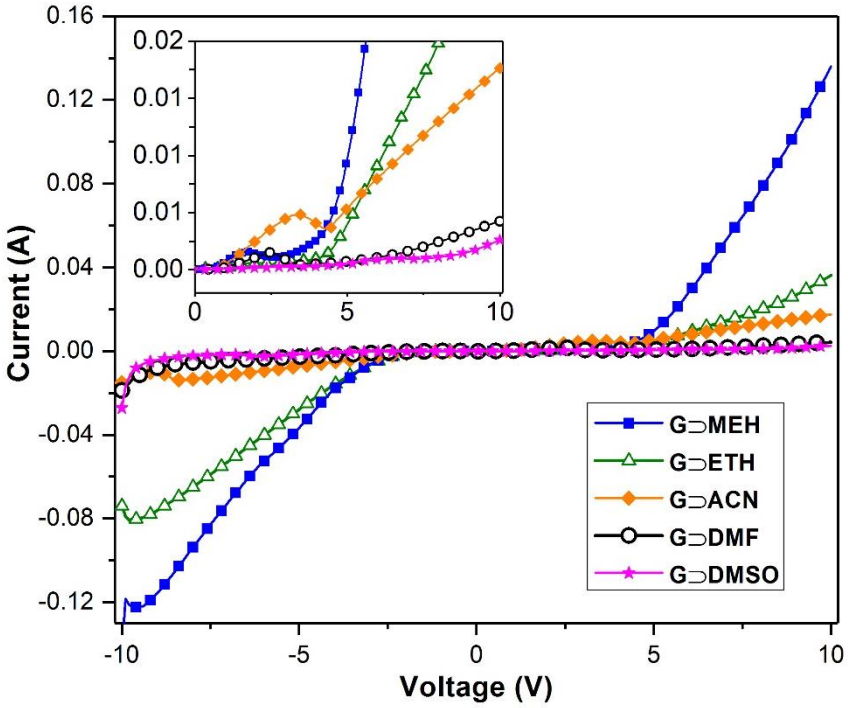

Figure 4.7 Current versus voltage (I-V) curves demonstrating tuneable electrical conductivities of supramolecular MOF-based hybrid materials synthesised by using different solvents. The inset shows the relatively flat sections between approximately ±5 V, which can be associated with the work function of the aluminium electrodes used in direct current conductivity measurements. This electrode surface effect is similar to other examples present in the literature.[168]

Hydrogen bonding and π—π interactions dominating the fiber network architecture could play an important role for integration of multiple charge carrier species, which are responsible for facile charge (ionic) transport in the current series of supramolecular MOF hybrids. *In situ* formation of nano- HKUST-1 particles in the supramolecular assembly also function as molecular anchors to adjacent fibrous network, in which MOF channels occupied with (guest) charge carrier species will facilitate additional charge transfer. Nevertheless, poorer electrical conductors in the case of, for example, G⊃DMF (0.23 S m^{-1}) and G⊃DMSO (0.14 S m^{-1}) could be explained by the "cage effect"[169] of charge carriers (weakly interacting ions), whose mobility is impeded by strongly-interacting solvent molecules surrounding the stable gel phase, thus suppressing its overall charge mobility.

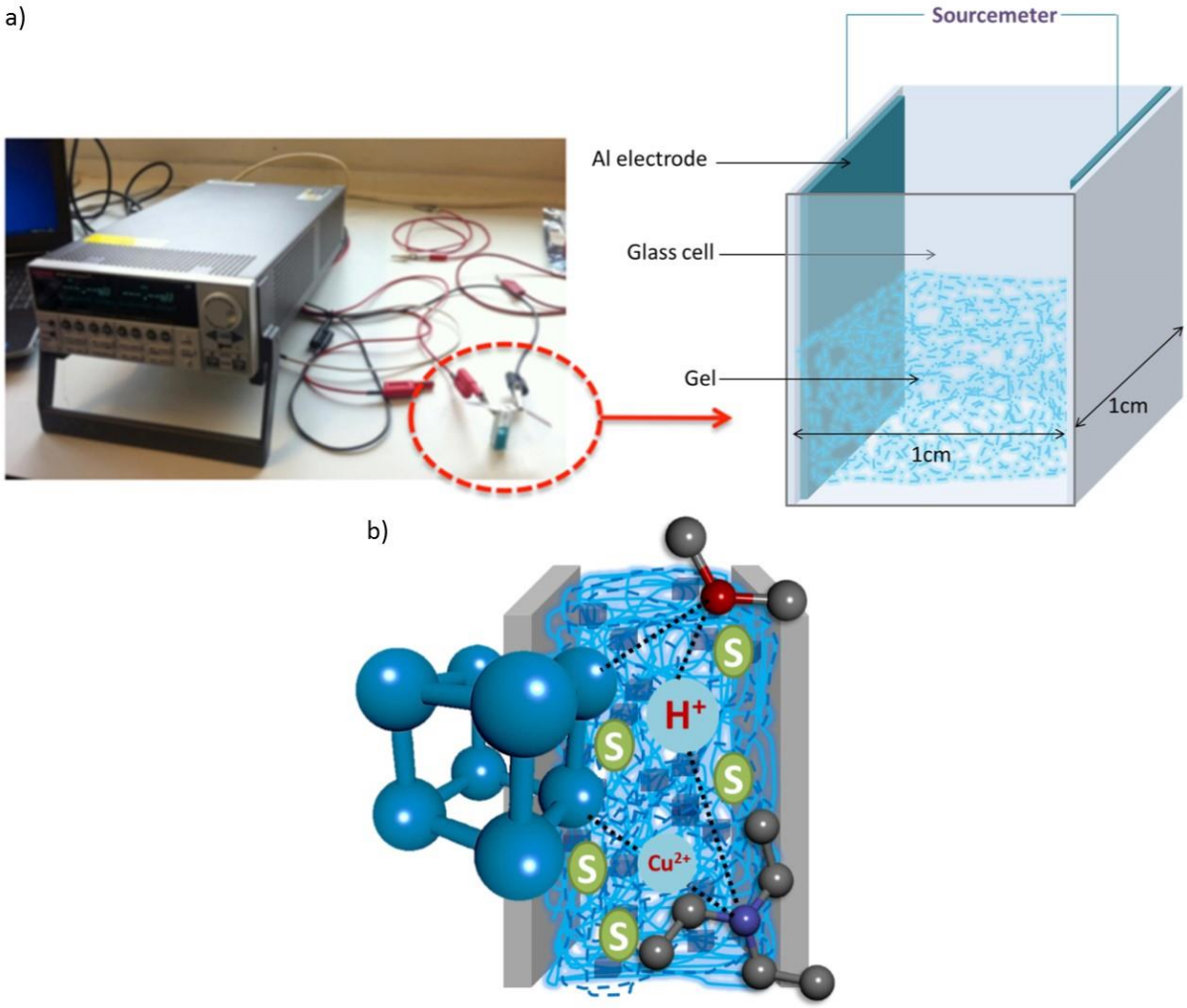

Figure 4.8 a) Experimental setup and geometry of test cell used in electrical conductivity measurements of gel samples, where gels are in direct contact with large surface of Aluminium electrode, b) illustration depicting potential charge carriers encompassing reactive Cu metal sites in MOF nanoparticles, weakly interacting Cu(II) cations and other ionic species present in fibrous network, in addition to H+ ions from occluded solvent.

Allendorf *et al.*[170] revealed that electrical conduction mechanism in HKUST-1 can be explained by the extrinsic guest doping mechanism, where tetracyanoquinodimethane (TCNQ) guest molecules interact with Cu(II) sites across the framework voids, forming an uninterrupted linear chain of Cu(paddle wheel)–TCNQ clusters enabling charge transport. Following this line of enquiry, here I propose that electrical conductivity witnessed in the current family of supramolecular fibre

networks may be attributed to the integrated effects of weakly-interacting charge carrying species, encompassing Cu(II), BTC^{3-}, NEt_3^+, NO_3^- and HKUST-1 nanoparticles (active metal sites) bearing charge carriers, all of which are abundant in the hybrid supramolecular assemblies (Figure 4.8). It is important to note that the conductivity observed in this case is contribution from ions present in gels and the conductivity observed in the case of HKUST-TCNQ compound is pure solid state electronic conduction due to electron hoping.

4.9 Use of SupraMOFs for Thin Film MOF Coatings

In addition to the unique physical properties of supramolecular MOF hybrids discussed above, another advantage of such sol-gel phases lies in the making of HKUST-1 NMOF thin films. By exploiting hybrid gels as precursors, I have established the applicability of three different techniques to fabricate HKUST-1 films, namely dip coating, doctor blade coating and spin coating. High uniformity in crystallite size contributes to the generation of compact and high-quality thin films, particularly without having to resort to the use of relatively costly self-assembled monolayer (SAM). For the exemplar in Figure 4.9, addition of solvent (here methanol) to G⊃MEH breaks down rapidly the gel fibrous network to yield pure HKUST-1 nanoparticles (NPs), whose sol suspension can be dip coated onto a glass substrate or a silicon wafer. Such NP suspension facilitates large-area thin film deposition operation, for instance, sol obtained from G⊃DMSO is especially effective for use with the doctor blade technique to produce films with controlled thicknesses, which have been characterised *via* infinite focus microscopy.

Coated films were air dried and then washed by careful immersion into methanol for ~15 minutes; this step removes unwanted soluble parts thus leaving behind pure HKUST-1 NMOF films. Unwashed coatings show green colour upon

heating to higher temperature while the washed version shows colour change expected of an activated HKUST-1 material, i.e. switching from turquoise to dark blue (Figure 4.9b) upon removal of coordinated water from the copper centres within the porous framework. Thin films produced by sol-gel approach display excellent uniformity with typical surface roughness of ~10-30 nm and a mean grain size of ~100 nm, as determined by AFM surface topography (Figure 4.9c and 4.9d). Furthermore, the high sensitivity of AFM is ideal for characterising fine-scale mechanical properties of thin film surfaces. In a first experiment, I attempted the combined AM-FM approach (amplitude modulated-frequency modulated)[171] using high-resolution amplitude tapping mode (topography by AM) and high-sensitivity frequency modulation mode (elasticity by FM) to interrogate the nano-mechanical behaviour of HKUST-1 coatings. Figure 4.8e shows the elastic stiffness map of HKUST-1 thin film, where the Young's modulus (E) was found to lie between ~3-6 GPa; this stiffness magnitude is broadly consistent with elastic constants measured for a wide range of porous MOF materials, where $E < 10$ GPa.[172] Herein I demonstrate that the AM-FM approach recently implemented in an AFM setup is promising for studying nanomechanical properties of MOF thin films, which otherwise will be inaccessible to other mechanical characterisation techniques.

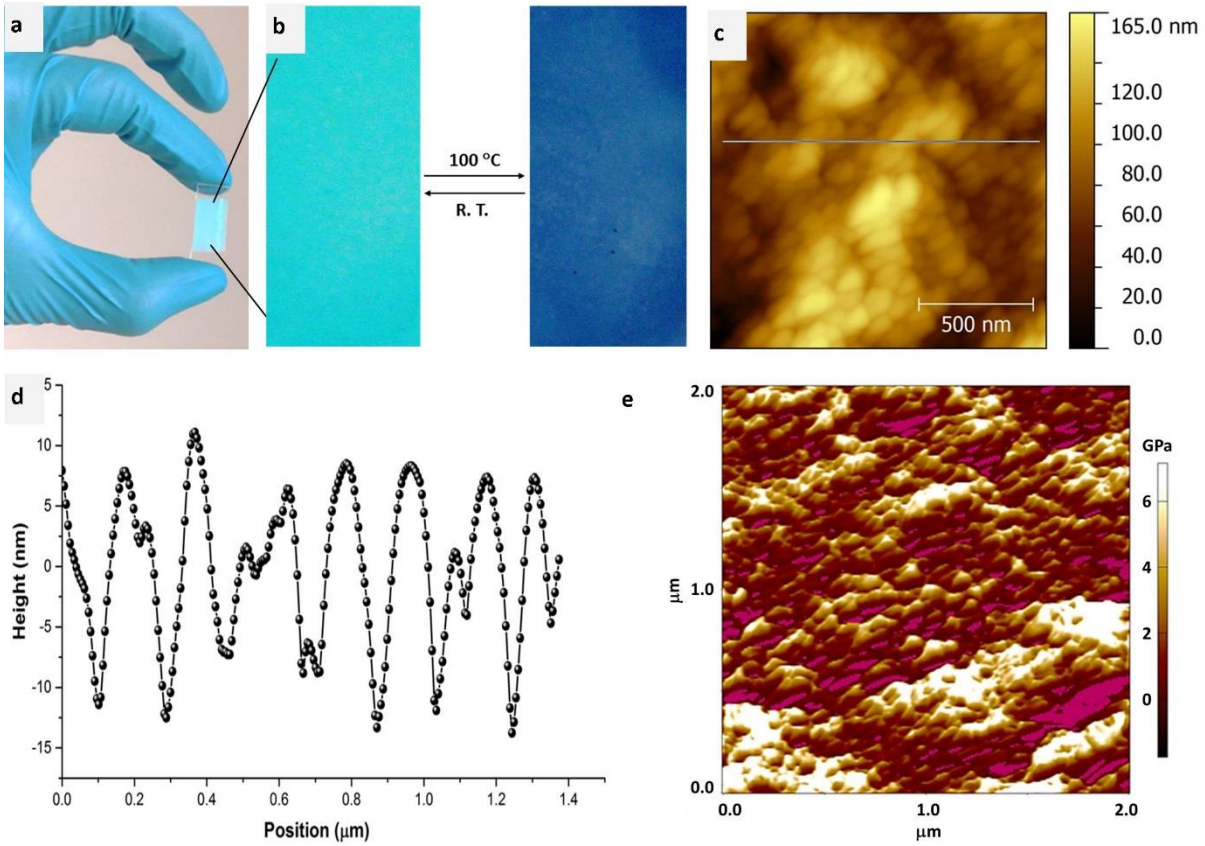

Figure 4.9 Thin films of HKUST-1 fabricated by dip coating using nanoparticle suspension (sol) of G⊃MEH: (a) on a glass substrate, (b) thin film demonstrating reversible color change upon heating, (c) AFM height topography, (d) surface roughness profile extracted from AFM line scan marked in (c). (e) Youn*G*'s modulus stiffness map of the thin film surface measured by AM-FM technique. The wide range of elastic moduli obtained (3-6 GPa) may be linked to elastic anisotropy,[172] suggesting that the external facets of HKUST-1 nanocrystals are oriented across a range of crystallographic directions.

4.10 Summary

In this chapter I demonstrated that, by employing a high concentration of standard reactants of HKUST-1 in a relatively small quantity of solvents, yields previously unreported gel-like hybrid materials that exhibit counterintuitive chemico-physical properties. Novel development of multifunctional materials is ultimately dictated by precise control over its fine-scale microstructural organisation, made possible only through the mechanism of molecular self-assembly. Indeed it is central to establish the collective effects underpinning complex structural evolution, specifically to gain

insights into structure-property relationships across the multiple temporal and length scales. In this work, I have illustrated an unconventional system comprising MOF-based supramolecular hybrid gels, termed ‘’SupraMOFs’’, can be created *via* hierarchically self-organising inorganic and organic basic building blocks. The highly tunable microstructural features reported in this study are distinctively different from the ‘traditional’ hybrid gels and soft matter.

Chapter Five

Towards Optically Active MOFs: Fluorescent MOF Crystals Using *in situ* Guest Encapsulation

5.1 Background

An exciting topic area in the field of light-emitting materials concerns the bottom-up fabrication of optoelectronic devices integrating materials with controlled architectures and ordered microstructures,[173-174] which are fundamentally important to effect unidirectional light production, inter-/intra-molecular electron transport, efficient light conversion and energy harvesting. One of the most promising contemporary materials featuring a highly-ordered crystalline network are the hybrid (inorganic-organic) coordination compounds,[1, 175] known as metal-organic frameworks (MOFs) or porous coordination polymers (PCPs).[3, 140, 176] MOFs or PCPs possess two active sites to tune their optoelectronic properties, *viz*. organic linkers and metal centers. In principle by varying these two basic building blocks, the optical and electronic properties of the compound can be manipulated.[5, 177] Furthermore, their nanoporous framework architectures offer active coordination voids (*via* long-range ordered nanocages) which could establish complex intermolecular interactions[6] and, by accommodating functional guest molecules to tune energy transfer and electronic conductivity.[178] There are many recent studies of luminescent MOFs[4, 179-181] that elaborated on a number of promising methodologies to afford encapsulation of light-emitting metal complexes either as a linker[182-183] or as a guest,[184] for instance: cationic dyes,[10, 185-186] quantum dots,[14, 187] nanoparticles,[188-189] or small luminous molecules[190] within MOFs for manipulating its light emission behaviour and photophysical properties. In fact the guest-induced properties of MOFs is an emerging area that could yield numerous novel device applications.[5, 178]

5.2 Why *In Situ* Guest Encapsulation?

At present, however, there are at least two major constraints encountered in this field of research. Firstly, conventional *ex situ* encapsulation methods usually require long processing times; guest infiltration or exchange processes can consume many hours[185] and this could extend into several days.[10, 191] Secondly, effective infiltration of MOFs is further limited to guest molecules whose size is typically smaller than that of the pore window aperture of the host framework material, after taking into account framework flexibility associated with lattice dynamics. To this end, identification of a suitable MOF structure with the propensity to self-organize spontaneously (*via* mixing of organic linker and metal ion solutions at ambient conditions) would be fundamental to accomplish *in situ* encapsulation of molecular guests inside its pores.

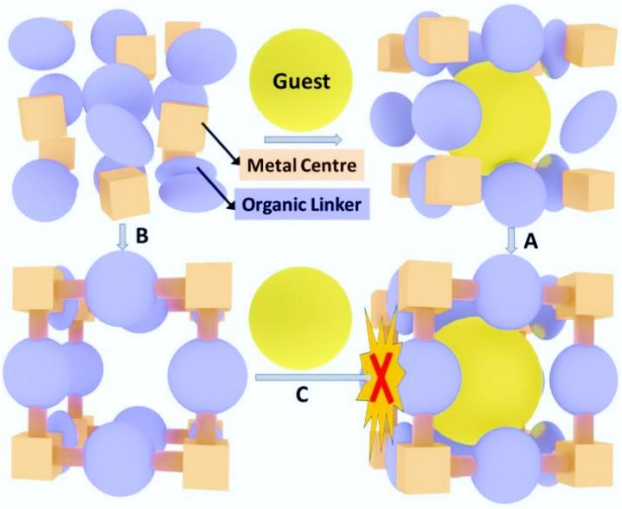

Scheme 5.1 Schematic diagram illustrating the concept of *in situ* confinement of a bulky guest in the nanocage of a MOF coordination space (A). Typically this nanoscale void space will become inaccessible to a bulkier molecule after the completion of MOF self-assembly process (B-C), because of steric hindrance imposed by narrow pore window apertures.

5.3 Host-Guest Selection

5.3.1. ZIF-8: Promising Zn(II) Based MOF Candidate For Optical Properties

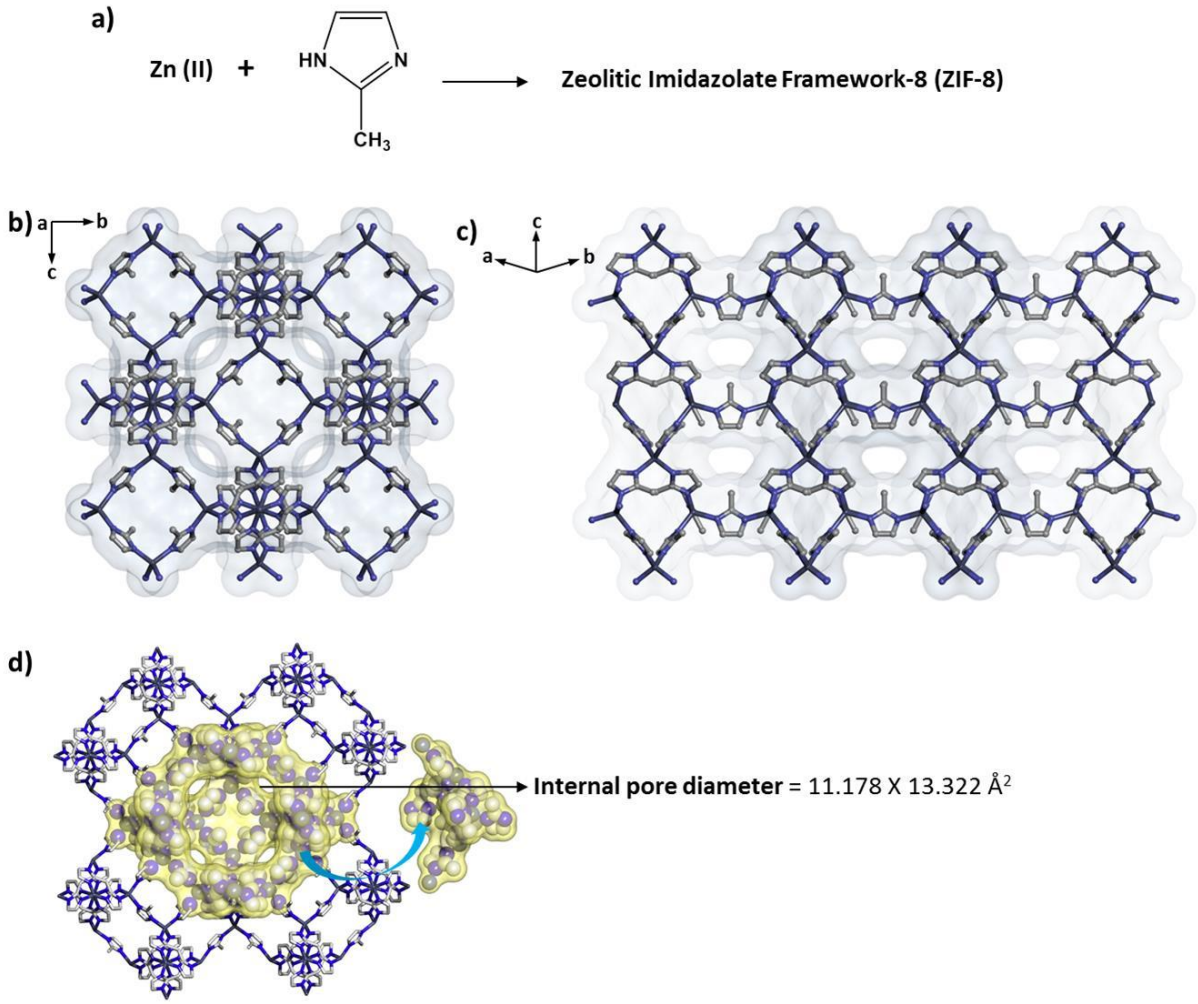

Figure 5.1 (a) Scheme showing synthesis of ZIF-8 MOF; b) packing diagram with solvent accessible surface showing very small pores along [100] axis and c) along [110] axis; (d) internal pore with more than 1 nm (excluding van der Waal radii) effective dimension.

Specifically, the advantage of facile MOF synthesis (e.g. ZIF-8 nanocrystals)[192] can be exploited to offer a straightforward route to confine a guest molecule bigger than the physical dimensions permitted by the MOF window opening. In this study, I selected the zeolitic imidazolate framework-8 (ZIF-8)[47] material to act as the nanoporous host structure, within which I encapsulate a luminescent molecular guest.

This strategy was motivated by the larger internal void size of ZIF-8 at 13.32 Å × 11.18 Å (excluding van der Waals surface) viewed along its cubic cell axis (see Figure 5.1b-d); noting that albeit its pore window aperture is much narrower with a diameter of ~3.4 Å. While ZIF-8 is a topical MOF material whose sodalite topology[37] is identical to that of inorganic zeolites, the former framework exhibits an appreciably lower elastic moduli[193-194] (of at least a factor of ten times lower).[195-196] Its intrinsically smaller window aperture may, however, hinder the true advantage of having a larger internal void space. Indeed recent studies showed that only small gas molecules could penetrate the internal void cavity of ZIF-8 upon application of a threshold pressure[197] and as facilitated by flexible gate-opening dynamics.[198] In this work, I have exploited the ease and rapidity of ZIF-8 nanocrystal formation (*via* simple mixing of 2-methylimidazole (mIm) and $Zn(NO_3)_2$ solutions in methanol)[199] in combination with the concept of *in situ* guest confinement (Scheme 5.1), to construct a new host-guest MOF hybrid composite (Figure 5.2) with tunable guest-induced electronic and optical emission properties.

5.3.2. ZnQ: Promising Zn(II) Based Small Emissive Metal Complex For Functionalisation

Herein the choice of a compatible guest molecule containing interaction sites for effective intermolecular interactions with host framework is key. By considering the structural dimensions of ZIF-8 (Figure 5.1), I identified the highly luminescent monomeric inorganic metal complex: Zn-(bis-8-hydroxyquinoline), termed ZnQ,[200] for encapsulation within the internal pores of ZIF-8 (Figure 5.2). Noteworthy, ZnQ is one of the relatively smaller and yet highly luminescent (quantum yield 36.6%)[201] metal complexes amongst the renowned Mq_n series (e.g. Alq_3, Gaq_3, Inq_3).[202]

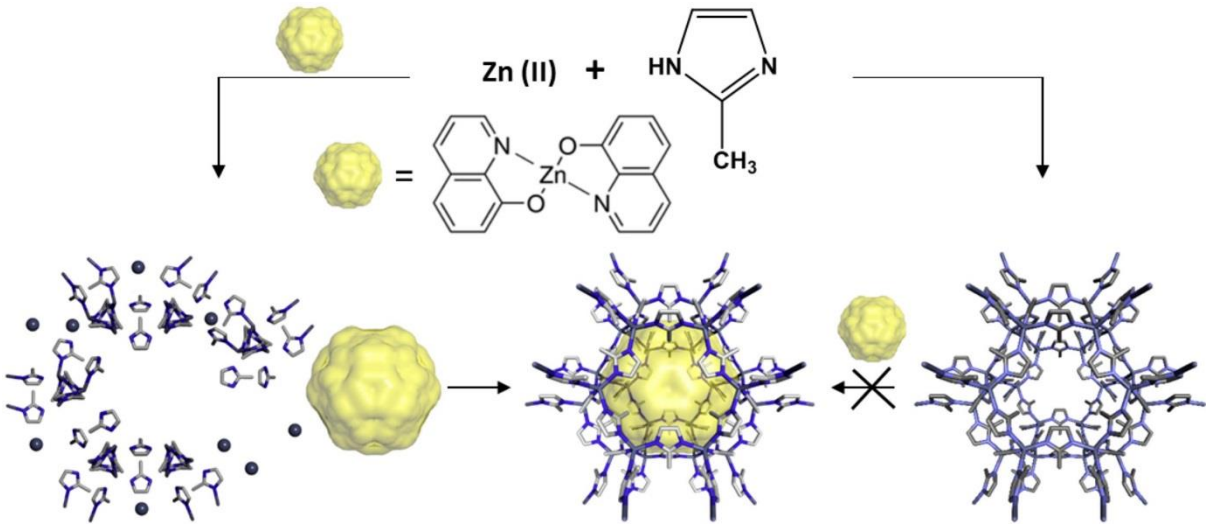

Figure 5.2 Scheme illustrating *in situ* encapsulation of supramolecular guest bis-(8-hydroxyquinoline)Zn^{II} inside the internal pore of ZIF-8.

Molecular dimensions of the ZnQ metal complex is approximately 11.74 × 6.49 $Å^2$ (with van der Waals radii), which is geometrically favorable for nanoconfinement within the pore of ZIF-8. Although many studies have been carried out for ZnQ complex alone, to the best of our knowledge this is the first demonstration of emission effect upon confinement of ZnQ within a porous MOF material.

5.4 Synthesis of Guest@MOF Material

5.4.1. One Step Synthesis Method

To obtain host-guest hybrid complexation of ZnQ@ZIF-8, I first attempted the material synthesis by direct addition of Zn^{2+} cations into a transparent solution containing an equal amount of 2-methylimidazole (mIm) and 8-hydroxyquinoline (8HQ) linkers. Nonetheless, I discovered that such an approach would only result in an instantaneous formation of ZnQ guests (confirmed by immediate intense yellow coloration of the solution), whereas the crystallisation of ZIF-8 was suppressed completely. Accordingly it became evident that since I am dealing with a common metal ion in both the host

and guest, the coordination tendency of 8HQ linker towards Zn^{2+} is considerably stronger than the mIm linker, due to the presence of the electron-rich naphthalene moiety (constituting O, N donors) in 8HQ compared to the 5-membered mIm ring (comprising one secondary and one tertiary amine sites). To overcome this obstacle for accomplishing reactions (1) and (2), I have designed a set of reactions by maintaining a constant molar ratio of Zn^{2+} : mIm (*i.e.* ZIF-8 formation) but systematically adjusting the concentrations of Zn^{2+} : 8HQ (*i.e.* ZnQ formation), in accordance to Table 5.1.

$$\mathrm{Zn^{2+} + 8HQ = ZnQ} \quad (1)$$

$$\mathrm{ZnQ + Zn^{2+} + mIm = ZnQ@ZIF-8} \quad (2)$$

Table 5.1 Solution-based chemical reactions designated as **I** to **IV**, conducted at 80 °C using different combinations of starting reactant concentrations in 25 ml of methanol (concentration mentioned in mmol).

Reaction no.	ZnQ guest		ZIF-8 host		Products
	Zn^{2+}	8HQ	Zn^{2+}	mIm	
I	3	6	4	16	Impure product mixtures
II	2	4	4	16	Impure product mixtures
III	1	2	4	16	No crystallisation
IV	0.5	1	4	16	Phase pure nanocrystals

5.4.2. Right Combination of Host to Guest Reactant Ratio

Results summarising different combinations of reactions (Table 5.1) provide important insights of the optimal concentration of ZnQ guest molecules required for successful confinement in the ZIF-8 host. For instance, the application of a high concentration of ZnQ in reactions **I** and **II** yielded non phase-pure products containing a mixture of crystalline stable forms of ZnQ complexes. This outcome can be explained by the

strong chelating effects of 8HQ forcing the oligomerisation of monomers into tetramers.[203] As a corollary, raising the concentration of ZnQ may encourage the formation of ZnQ stable species, instead of achieving guest encapsulation inside the MOF pores. Especially I found that reaction **IV** utilising a much lower concentration of ZnQ complex produced a purely crystalline phase; in contrast reaction **III** formed no crystalline products, implying that ZnQ converts into $(ZnQ_2)_n$ oligomers that remain stable in solution state. I pinpointed reaction **IV** as the optimal route for undertaking successful ZnQ@ZIF-8 encapsulation reaction, thereby properties of this sample are studied in detail below.

5.5 Material Characterisation

5.5.1. Morphological Study of Host-Guest System Using Optical Microscopy, Dynamic Light Scattering and Transmission Electron Microscopy (TEM)

Visual inspections indicated that the pure crystalline dried product obtained from reaction **IV** (Table 5.1) showed a pale ivory color, unlike the distinctively white color of pristine ZIF-8, or the yellow color characteristic of pristine ZnQ powder. Optical and TEM images of this sample confirmed a rhombic dodecahedral morphology (of twelve facets)[192] and, its crystal size in the range of 500 nm to 2 µm (Figure 5.3). Comprehensive information about the crystal size distribution was further determined by means of dynamic light scattering (DLS) experiments. It can be seen in Figure 5.3c that the pristine ZIF-8 nanocrystals exist in the range of 200-500 nm, as synthesised at room temperature using methanol. In contrast, I established from Figure 5.3d that the nanoconfinement process to afford encapsulation of ZnQ guest within ZIF-8 has resulted in a relatively larger crystal size distribution of between 800 nm to 2 µm.

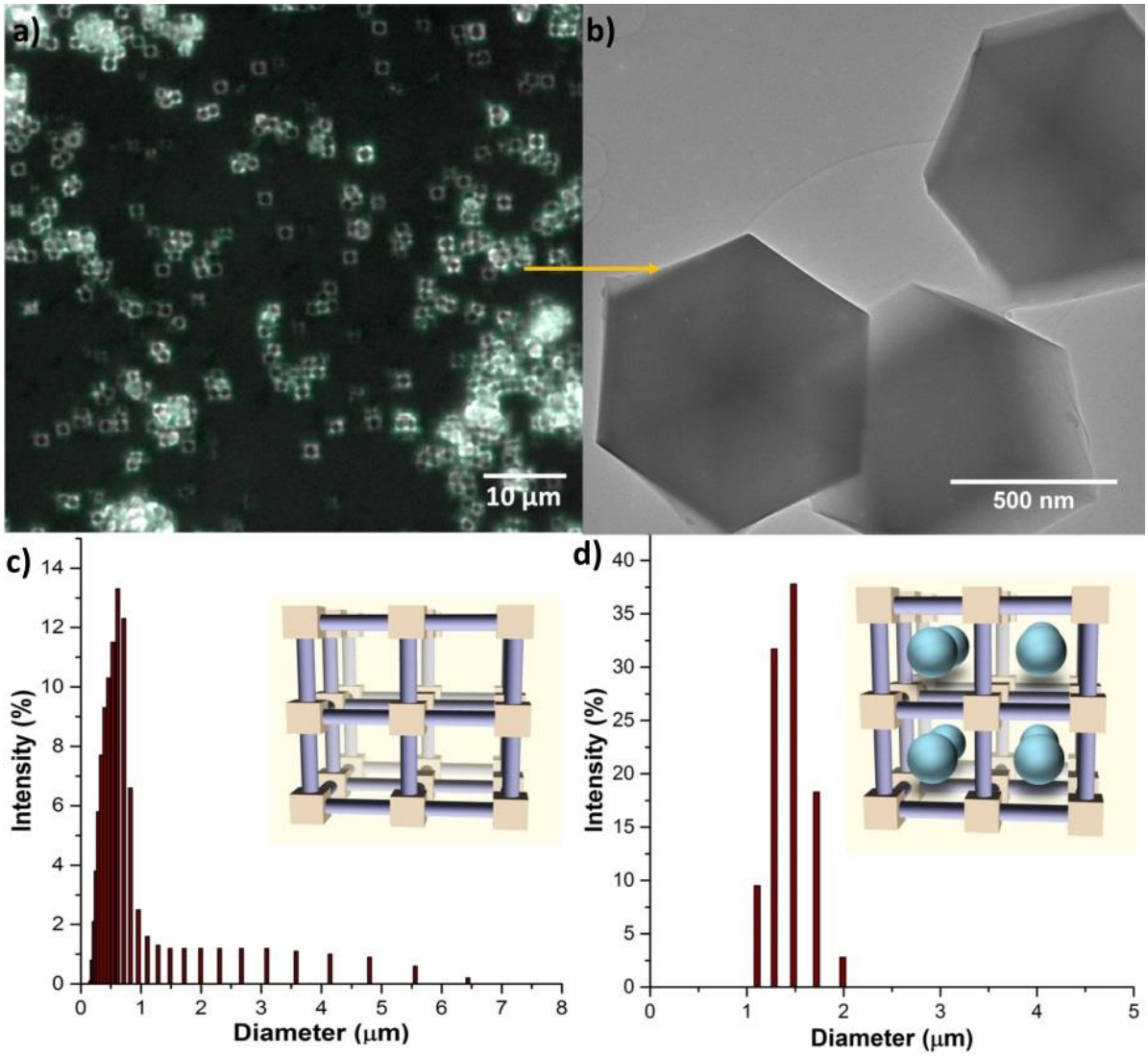

Figure 5.3 (a) Optical micrograph of ZnQ@ZIF-8 crystals and (b) the corresponding TEM image showing the single-crystal rhombic dodecahedral morphology. Dynamic light scattering spectra of (c) pristine ZIF-8 versus (d) encapsulated ZnQ@ZIF-8.

The DLS data suggest that the co-operative self-assembly route (Figure 5.2) responsible for guest species encapsulation could also stimulate the growth rate of ZIF-8 nanocrystals.

5.5.2. Powder X-Ray Diffraction, Raman and FT-IR Spectroscopy

Figure 5.4 presents the structural data of the pristine ZIF-8 material compared with its guest-encapsulated counterpart. Powder X-ray diffraction data (PXRD) in Figure 5.4a show the structural integrity of ZnQ@ZIF-8 evidenced from the sharp peaks and the

phase purity of the bulk sample, showing a good agreement to the simulated X-ray pattern of ZIF-8. Likewise, vibrational data measured by Raman and infrared (IR) spectroscopy further demonstrated matching signatures in agreement with the pristine ZIF-8 compound (Figure 5.4b-c). Together I found that the ZIF-8 host has retained its pristine structural form, upon confinement of the ZnQ guests, for which no major structural changes have been observed. This behaviour is similar to examples in literature which reported no change in structural X-ray diffraction pattern upon guest encapsulation in the ZIF-8[14] and ZIF-90[204] host compounds.

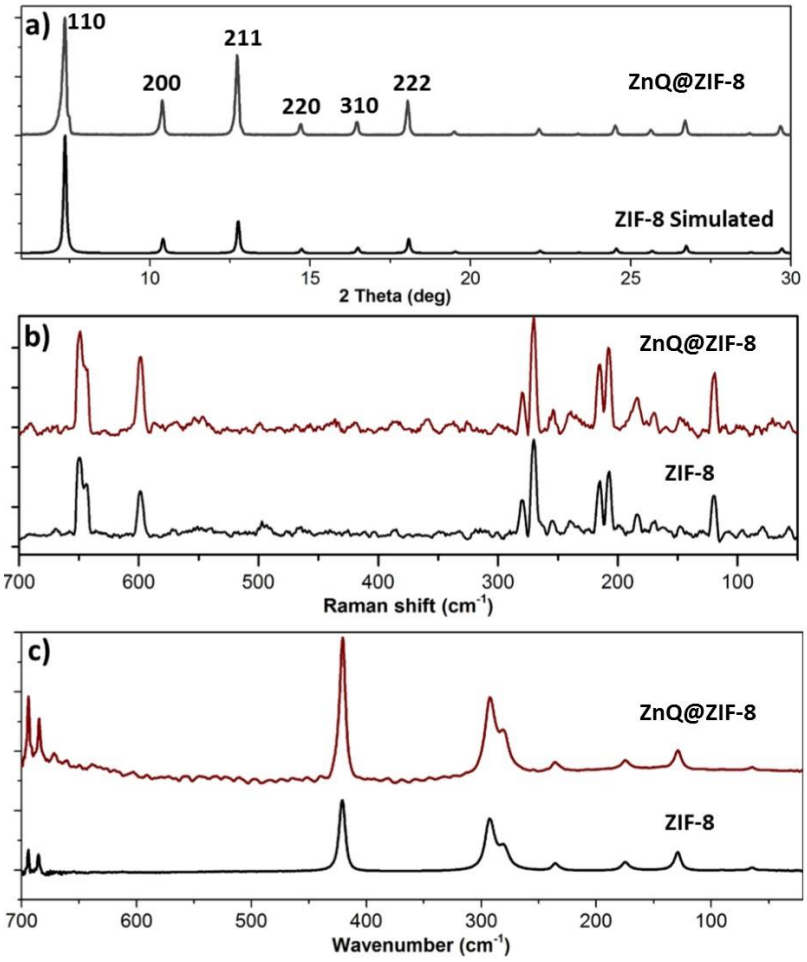

Figure 5.4 Structural characterisation of encapsulated ZnQ@ZIF-8 and pristine ZIF-8. (a) Powder X-ray diffraction pattern, (b) Raman vibrational spectra, and (c) infrared spectra. Note that the vertical axis represents intensity in arbitrary units.

5.5.3. Thermal Gravimetric Analysis

However, thermal gravimetric analysis (TGA) of hybrid and pure materials showed the indication of guest confinement and increased stability of guest upon confinement. Pure ZIF-8 exhibited thermal stability till 280°C however it showed two step loss for hybrid form i.e. with ZnQ encapsulated form (Figure 5.5). 4% sudden weight loss from 200°C to 235°C could be assigned to the coordinated water molecules of ZnQ molecule and further slow decomposition from 235 °C to 410 °C suggests the integrated slow decomposition of framework and guest, after 410 °C sudden decomposition was observed. TGA curves suggest that due to confinement effect coordinated water (loss at 180 °C for pure ZnQ and at 200 °C for confined form) and remained of guest molecule (slow decomposition from 200 °C for pure ZnQ and 235 °C for integrated form) decomposes at higher temperatures compared to their pure form.

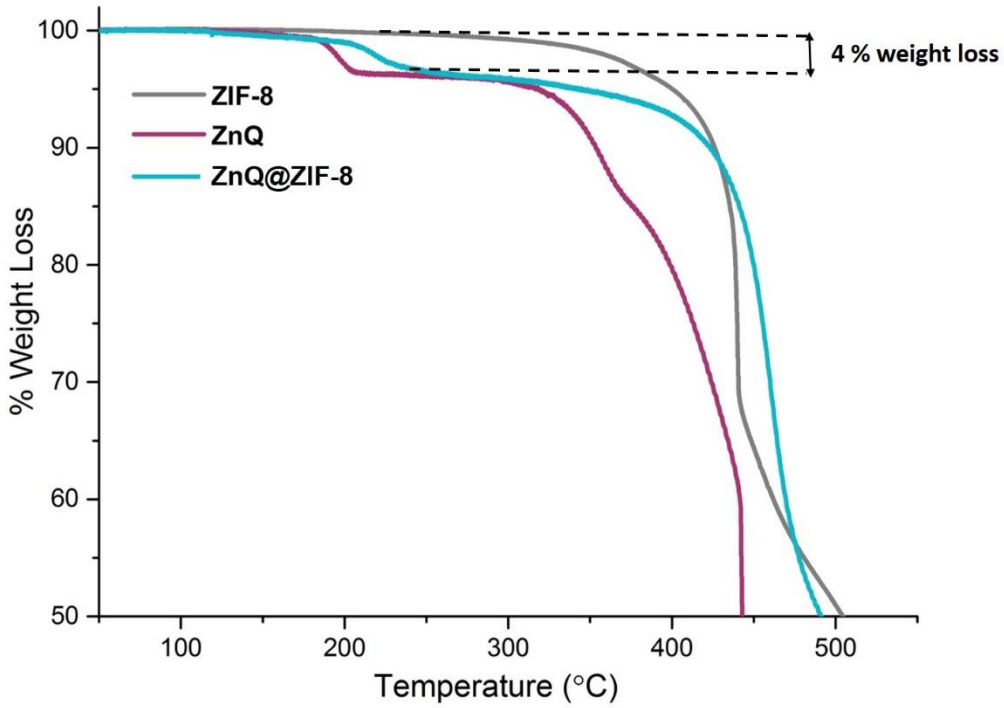

Figure 5.5 Thermal gravimetric analysis of compounds showing evidence of presence of guest within ZIF-8 framework by comparison with the curves of their pristine compounds.

5.5.4. Optical Properties

5.5.4.1. Absorption Properties

Absorption and emission optical spectra of the ZIF-8 host, ZnQ guest, and encapsulated ZnQ@ZIF-8 hybrid are presented in Figure 5.6 and 5.7, which elucidate the underlying host-guest interaction behaviours. Specifically, it can be seen in Figure 5.6a that pristine ZIF-8 exhibits a strong absorption peak at 221 nm, alongside two weaker absorption peaks at 304 nm and 370 nm (Figure 5.6b). On the other hand, the pure ZnQ metal complex has a broad absorption peak at 412 nm accompanied by a small distinctive hump at 261 nm (Figure 5.6b), which can be assigned to the intermolecular π—π interaction and the π—π* transition events, respectively. It is important to recognize that the characteristic absorption spectrum for the hybrid material, *i.e.* host-guest ZnQ@ZIF-8 in Figure 5.6, exhibits distinguishable identities of both the host and the guest species though with apparent deviations in peak profiles.

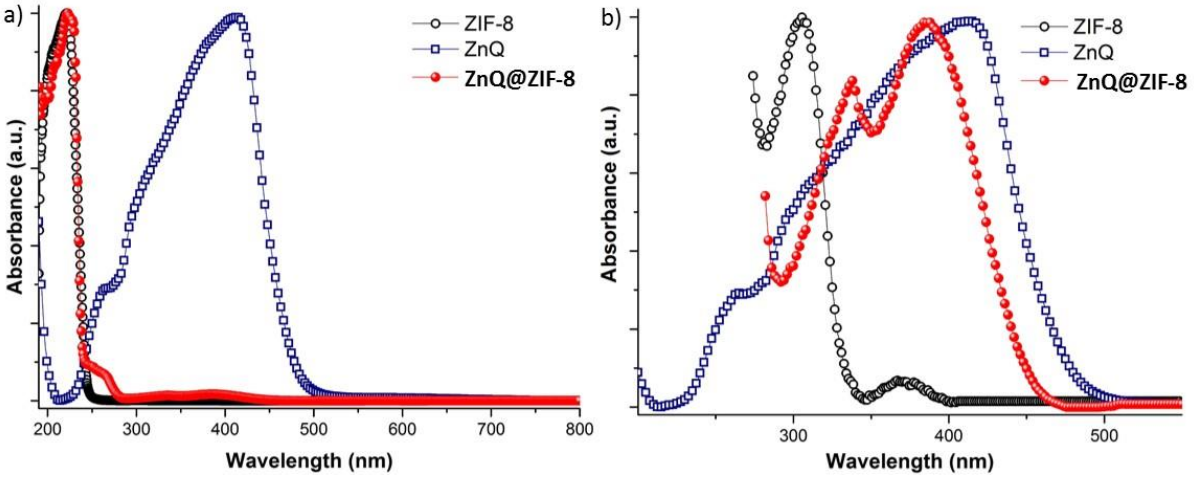

Figure 5.6 a) UV-Vis absorption spectra of the host and guest versus that of the encapsulated compound; b) normalised magnified spectra showing hidden weak absorption of confined guest.

More precisely, three main characteristics have been established: (i) the sharp peak of ZIF-8 at 221 nm was detected at the original position, but with an additional small hump at the base (266 nm) corresponding to the ZnQ guest. (ii) Absorption peaks reminiscent of ZnQ were recorded in the host-guest hybrid, but of a narrower peak area compared to the broader bands found in pristine ZnQ. (iii) Distinct shifts in peak positions were identified for ZnQ after guest encapsulation. Specifically, the red-shifted hump at 335 nm could be assigned to stabilisation of the excited state π—π* transition, while the blue-shifted main absorption peak at 384 nm can be attributed to spatial confinement (i.e. caging effect)[205] of guest molecule imposed by the sodalite cage of ZIF-8.

5.5.4.2. Photoluminescence Properties

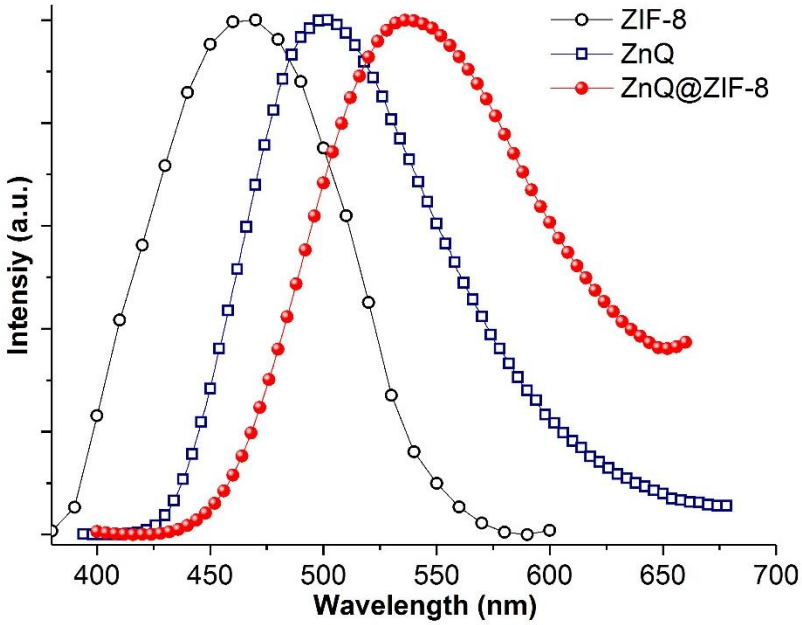

Figure 5.7 Fluorescence emission spectra of the three compounds excited at 350 nm.

Fluorescence spectra in Figure 5.7 provide evidence of co-operative host-guest intermolecular interactions responsible for the red-shifted emission spectrum

evidenced in ZnQ@ZIF-8. It can be seen that the maximum emission peak of ZnQ at ~500 nm has red-shifted by ~36 nm to a higher wavelength of λ_{em} ~536 nm, which occurred upon encapsulation of ZnQ guests inside the sodalite cage of ZIF-8 (pristine λ_{em} ~466 nm).

5.5.4.3. Photo-Stability: Shielding of Light Sensitive Guests by the Host Framework

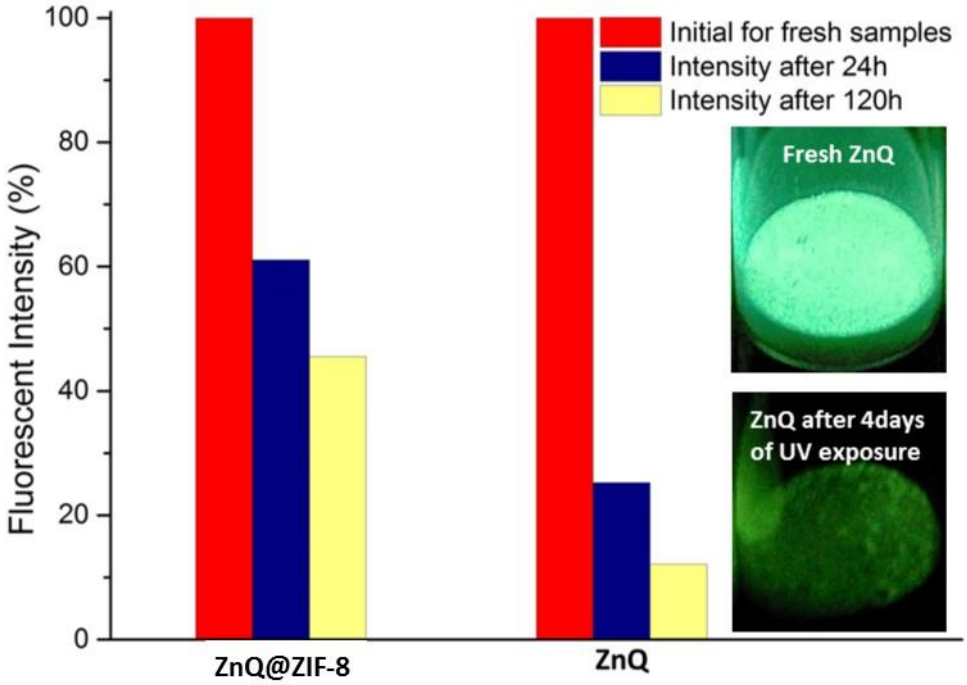

Figure 5.8 Emission intensity variation for the encapsulated form of ZnQ within ZIF-8 pores (ZnQ@ZIF-8 host-guest system) compared against the pure ZnQ species after exposure to sunlight irradiation for a period of 5 days. Note that the intensity for each thin film sample was normalised to 100% of its initial emission, and the change in photostability was determined by monitoring the same two thin film samples. It is evident that the photostability of the ZnQ emitter when shielded by the ZIF-8 pores are at least twice more stable than the unprotected ZnQ species. Inset: Emission of a freshly synthesised dry powder sample of ZnQ under exposure to UV light, and (e) its diminished luminescence after exposure to sunlight in under four days.

Another important observation concerns the preservation of the luminescence property of encapsulated-guest species by nanoconfinement in the MOF host.

Surprisingly, I discovered that ZnQ@ZIF-8 hybrid exhibits enhanced photostability, see Figure 5.8, whereas the 'unprotected' ZnQ complex is more susceptible to photochemical degradation upon exposure to sunlight irradiation (~4 days). Moreover, from the Raman experiments I observed that a laser power of 50 mW was adequate to instantaneously damage the ZnQ sample causing complete photochemical decomposition, however the encapsulated sample remained stable when tested in the same conditions. This provides additional evidence demonstrating the poor photostability of ZnQ against monochromatic laser lights (e.g. 532 nm, 12.5 to 50 mW), whereas I found that the encapsulated ZnQ could retain its optical properties after nanoconfinement in the ZIF-8 pore. The findings support the notion that trapping of light-sensitive guest molecules by caging them in the ordered porous architecture of MOFs may offer a simple method of shielding against swift photo-induced decay.

5.6 Theoretical Calculations: Effect of Guest on Host

5.6.1. HOMO-LUMO Orbitals

To understand the possible excitation mechanism behind such a host-guest interaction, I have studied the donor-acceptor type emission-absorption spectra, and also examined the HOMO-LUMO theoretical orbital energies of ZIF-8 against that of ZnQ (Figure 5.9). Interestingly, from the absorption spectrum of ZIF-8 (the anticipated acceptor) compared with the emission band of ZnQ (the anticipated electron-rich donor), I found no overlap between the isolated host and guest, suggesting that there is no energy transfer from ZnQ to ZIF-8.

On the basis of the HOMO and LUMO orbital alignments predicted by DFT calculations (Figure 5.9), I postulated that the higher-energy LUMO orbital of ZIF-8 could transfer its charge (harvested upon excitation) onto the low-lying LUMO orbital

of ZnQ, through an intermolecular weak interaction established by guest confinement. This energy transfer mechanism can shift the emission band to much higher wavelengths as witnessed in the experiments (Figure 5.7).

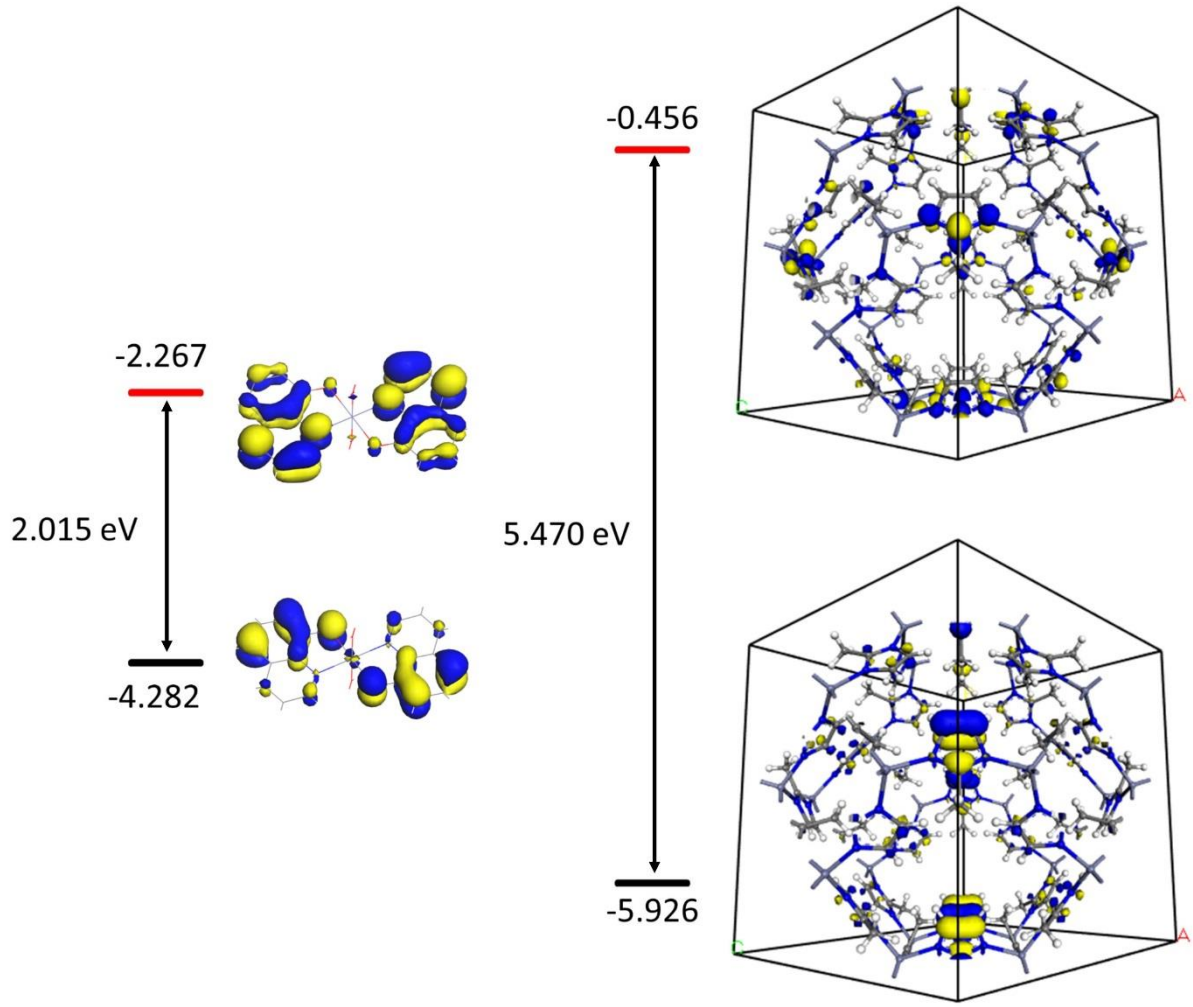

Figure 5.9 (a) HOMO-LUMO energy levels for ZnQ and ZIF-8 and their corresponding band gaps computed from DFT.

5.6.2. Band Gap Values: Comparison between Experiment and Theory

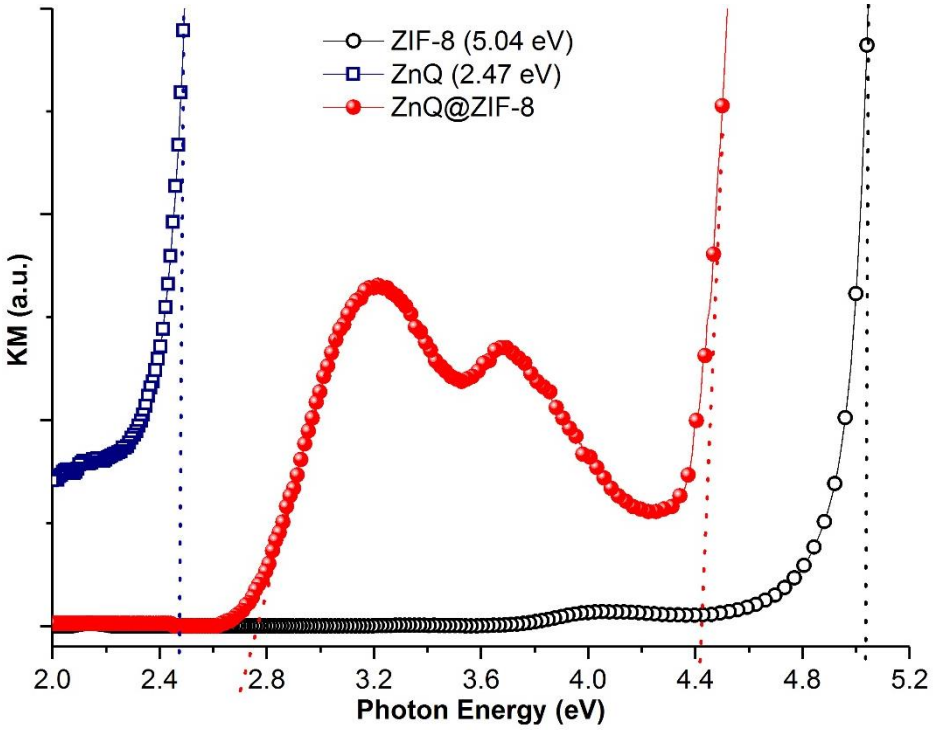

Figure 5.10 (b) Kubelka-Munk (KM) function to determine band gap values at the designated photon energy intercepts.

I have measured the change in band gap values of the ZnQ@ZIF-8 hybrid material compared to the pristine ZIF-8 or ZnQ by adopting the Kubelka-Munk (KM) function, whose results are shown in Figure 5.10. The band gap of pristine ZIF-8 (E_g = 5.04 eV) was found to decrease by 0.63 eV (to E_g = 4.41 eV) once the ZnQ guest has been encapsulated to form ZnQ@ZIF-8. On the contrary, encapsulated ZnQ shows a band gap of 2.74 eV, which is 0.27 eV higher than the isolated ZnQ complex (E_g = 2.47 eV). Additionally, I performed theoretical orbital energy calculations that predicted band gap values of 5.47 eV for ZIF-8 and 2.02 eV for ZnQ (Figure 5.9). It is worth highlighting that the experimental band gap of ZIF-8 as well as the theoretically calculated values obtained in this work are consistent with the experimental[206] and calculated[207] magnitudes from recent literature.

5.7 Structural Characteristics for Host-Guest Interaction

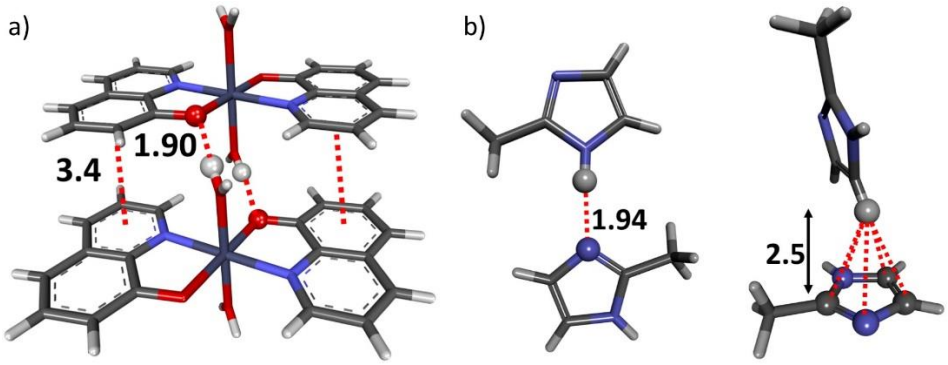

Figure 5.11 (a) Weak intermolecular interactions in ZnQ crystal packing showing π···π and O···H interactions.[103] (b) Hydrogen bonding and N-H···π interactions of the mIm packing.[208] [Red: oxygen; Dark blue: zinc; Light blue: nitrogen; Gray: carbon; White: hydrogen]

To further corroborate the photophysical phenomena presented above, I have examined detailed crystal structures of the mIm linker (2-methylimidazole) and the ZnQ complex from the perspective of their propensity to develop intermolecular bonding interactions. Figure 5.11a depicts the crystal-packing diagram of the ZnQ metal complex,[103] showing the parallel offset type π···π stacking interaction to a neighboring ZnQ molecule (whose spacing, *d* = 3.4 Å), together with the presence of a strong intermolecular hydrogen bonding (*d* = 1.906 Å) from its coordinated water to the other 'O'-site (of 8HQ) coordinated to the Zn center of an adjacent ZnQ molecule. Turning to the mIm organic molecule, Figure 5.11b shows the reported crystal configurations[208] revealing its ability to form strong N-H···π interactions with an adjacent mIm molecule (*d* = 2.5 Å), plus an intramolecular N···H bonding (*d* = 1.942 Å). Hence in the context of the ZnQ@ZIF-8 hybrid, its spatially confined host-guest intermolecular environment consists of: (i) π···π interactions established between the electron-rich aromatic moiety of ZnQ guest and the mIm linkages of ZIF-8 host, in conjunction with (ii) hydrogen bonding associated with the coordinated water

molecules in ZnQ guests to the N sites situated on the ZnN_4 tetrahedra of the sodalite ZIF-8 host.

5.8 Guest@Host Material asTuneable Emissive Coatings for LEDs

I have fabricated simple proof-of-principle LED-based lighting devices (Figure 5.12a) featuring a thin functional coating of active material made from ZnQ@ZIF-8. The improvement in luminescence intensity attributed to guest encapsulation was visibly detectable under the excitation of an ultraviolet (UV) LED source.

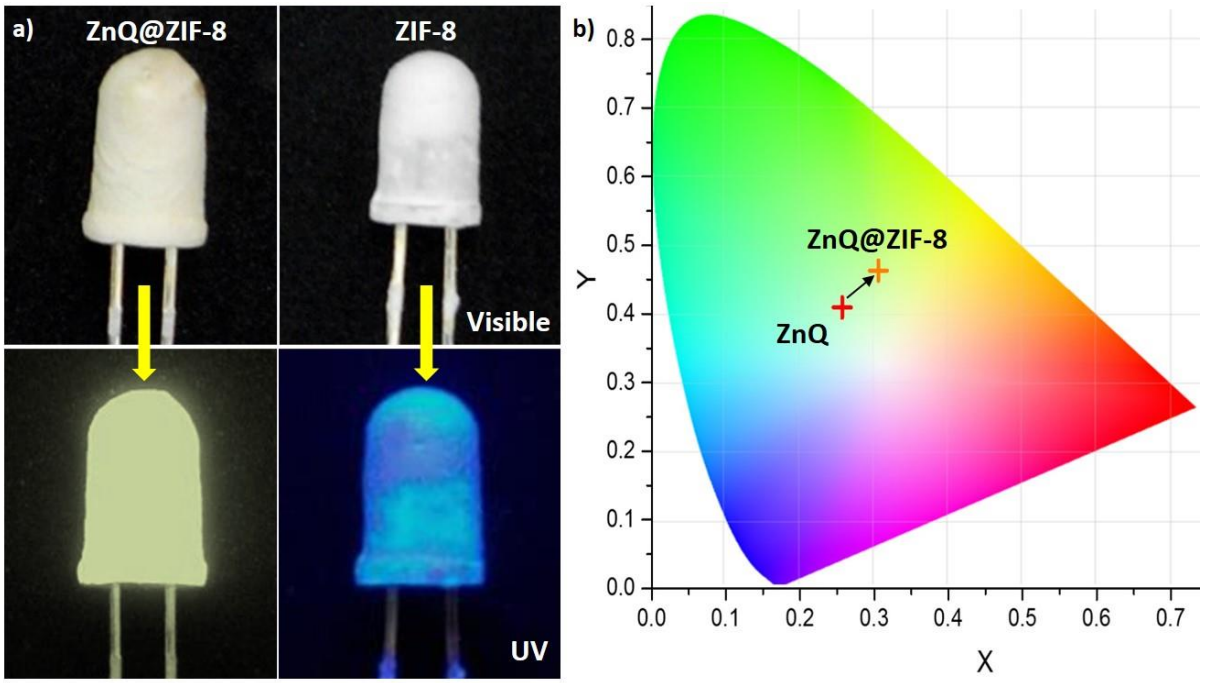

Figure 5.12 Visible light photographs showing UV LED (switched off) coated with a thin layer of encapsulated ZnQ@ZIF-8 versus pristine ZIF-8; bottom panel shows the corresponding devices taken in the dark with the UV LED switched on, showing ZnQ@ZIF-8 with light yellow emission and inactive ZIF-8 (blue intensity is from UV source). b) CIE 1931 color coordinates space of pure ZnQ (*x*: 0.2567, *y*: 0.4096) compared with the encapsulated ZnQ@ZIF-8 (*x*: 0.3055, *y*: 0.4630).

Significantly, it can be seen in Figure 5.12a that the ZnQ@ZIF-8 coating emits a light-yellow emission under UV excitation, whereas the pristine ZIF-8 coating in Figure 5.12a is essentially inactive (note that blue light is transmission from UV

source). Furthermore, I have evaluated the CIE chromaticity color coordinates shown in Figure 5.12b, and determined the correlated color temperature (CCT) of the samples. It is worth highlighting that the CCT of the pristine ZnQ is at ~8188 K (i.e. amongst cool colors), but this reduces to ~6196 K for ZnQ@ZIF-8 after nanoconfinement of ZnQ guest in the sodalite cage of ZIF-8, which translates into a perceptible red-shift towards a relatively warmer color rendering (Figure 5.12b).

5.9 Summary

I have demonstrated the efficacy of the concept of rapid *in situ* host-guest nanoconfinement, where encapsulation of a highly-emitting ZnQ guest molecule in the long-range ordered porosity of ZIF-8 yielded a hybrid nanomaterial with bespoke optoelectronic properties and enhanced photostability. In this study, I have discovered that there is a strong co-operative intermolecular interaction of the guest species with the framework host material, giving rise to a distinctive red-shifted emission measured in the ZnQ@ZIF-8 hybrid crystals. I have gathered evidence indicating the sodalite cage of ZIF-8 not only provides stabilisation of the guest *via* spatial nanoconfinement mechanism, but the host may function as a photon harvester transferring charge to the encapsulated guest *via* intimate host-guest electronic pathways. Furthermore, I have demonstrated that enhancement in photochemical stability can be accomplished through host-guest nanoconfinement within the protective molecular vessels of ZIF-8.

Chapter Six

Rapid and Easier Method towards Optically Active Host-Guest MOF Materials: HCR Approach

6.1 Background

Two-dimensional (2D) nanosheets are contemporary materials with exceptional physical and functional properties, derived from a broad class of low-dimensional solids containing atomically thin structures,[209-210] exfoliated 2D frameworks,[91, 211-212] and molecular membranes.[213-214] Considerable efforts are being devoted to 2D graphene-related materials[93] to yield improved mechanical, electronic and optical modulations, important for device integration and disruptive technologies. On the contrary, far less widespread are thin-layered materials derived from self-assembled supramolecular systems,[27, 215] whose weak interlayer non-covalent chemical interactions are van der Waals in nature. Such molecule-based 2D materials may provide significant benefits towards physical and chemical tunability, structural flexibility, and ease of exfoliation.[216] There is recent intensifying interest in an emergent class of 2D nanosheets constructed by *downsizing* 3D metal-organic frameworks (MOFs),[13, 33, 213, 217-220] which are inorganic-organic (hybrid) structures possessing an enormous physicochemical[140, 221-223] and structural versatility.[49, 151, 224] Furthermore, the nanoscale porosity of MOFs could function as a vessel to “host” a variety of functional “guest” molecules,[139, 225-227] imparting a unique combination of properties through intimate host-guest interactions.[178, 228] Yet, preparation of Functionalised MOF as 2D nanosheets exemplifying tunable host-guest sensing response is uncommon in literature, unlike its traditional counterparts.[4, 180].

6.2 SupraMOF for Functional Guest@Host Systems

6.2.1 One Step Rapid Synthesis

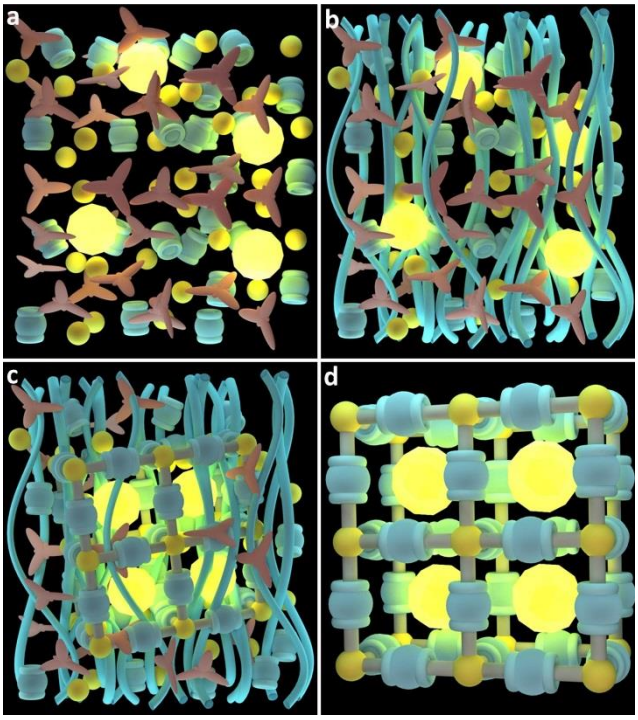

Scheme 6.1 Proposed supramolecular synthetic strategy for constructing an optochemically active Guest@MOF (Host) system. (a) *In situ* assembly began with a one-pot solution mixture of high-concentration reactants, combined with functional guest species (e.g. luminescent complexes represented by yellow spheres). (b) This solution mixture produces a fibrous supramolecular assembly, facilitating formation of (c) periodic MOF structures encapsulating functional guest molecules. (d) Disassembly of scaffolding fibers to harvest functionalised Guest@MOF composite systems.

In this work, I present a simple supramolecular self-assembly strategy to accomplish concomitant 2D nanosheet synthesis and functionalisation of a porous MOF system, and demonstrate its efficacy for application as a tunable optochemical sensor. I leverage our recently elucidated supramolecular “high-concentration reactions” (HCR) approach,[134] to realize one-pot synthesis of functionalised MOF nanosheets at ambient conditions; the basic concept is illustrated in Scheme 6.1. Here I describe a representative study employing 1,4-benzenedicarboxylic acid (BDC) as the organic

linker, because of its strong propensity to construct an extended chemical network upon coordination with metal centers; for instance, by utilising divalent Zn^{2+}. Triethylamine base (NEt_3) featuring a flexible tripodal geometry was used to trigger fast activation (deprotonation) of the BDC linkers.

6.2.2 Fibrous Morphology

It is striking to see that, a white gel-like fibrous soft matter was immediately obtained at room temperature (Figure 6.1a), arising from the high-concentration reaction (HCR) between Zn^{2+} and BDC^{2-}, augmented by the NEt_3^+ cations. I observed a discernible two-stage material transformation *via* optical microscopy (Figure 6.1b): initially witnessing development of highly oriented fibers, prior to formation of a visually *shiny* phase prevalent on the fiber surfaces. The gel fiber diameter was found to be ~1 to 10s μm by scanning electron microscopy (SEM), see Figure 6.1c.

6.3 2D Nanosheets from SupraMOF

6.3.1 Thin Sheet Morphology Characterised Using Microscopy

Intriguingly, SEM revealed those supramolecular fibers are, in fact, constituting densely packed crystalline nanosheets (Figure 6.1d), thus confirming the (shiny) faceted appearance detected under optical microscopy (Figure 6.1b). To establish the detailed 2D morphologies, I examined nanosheets harvested from the supramolecular gels using transmission electron microscopy (TEM) and SEM (Figure 6.1e-f), as well as by atomic force microscopy (AFM) with which I have estimated the nominal thickness of the exfoliated 2D sheets is of the order of 10s nm (Figure 6.1g). Additional microscopy images showing the 2D nanosheet morphologies are presented in Figure 6.2.

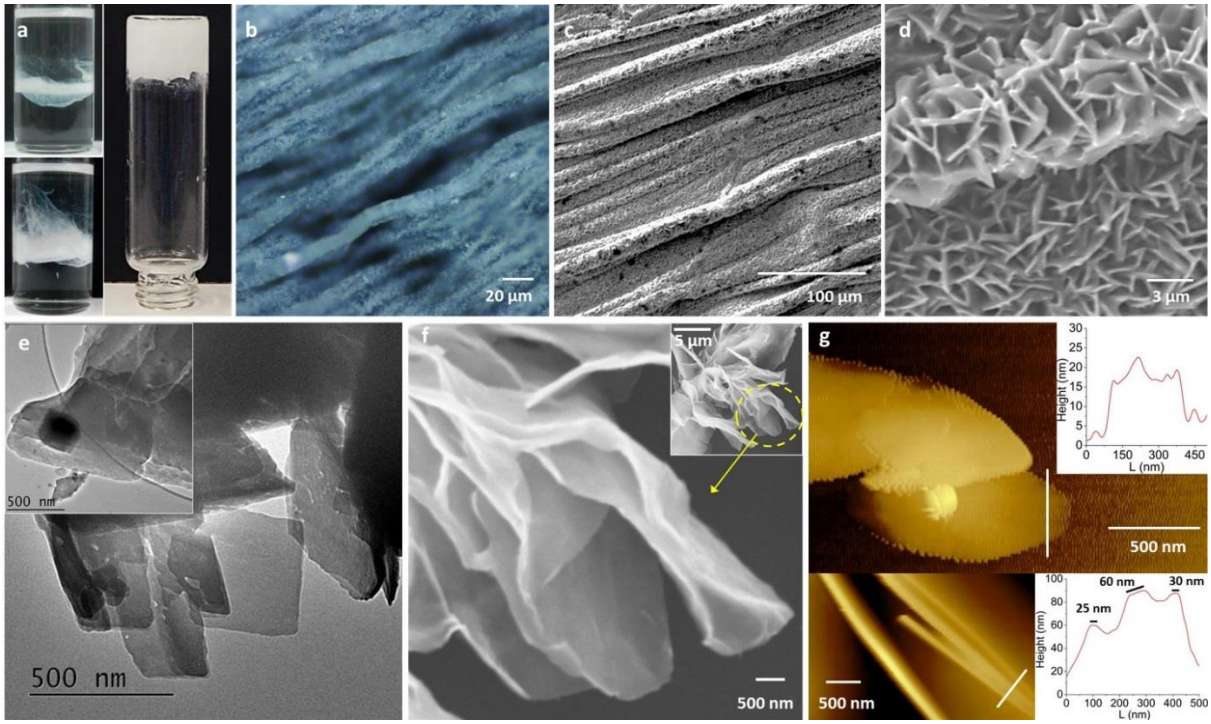

Figure 6.1 Two-dimensional nanosheets of self-assembled OX-1 MOF materials. (a) Supramolecular synthesis showing stepwise development of fibrous soft matter (left), forming a bulk of hybrid gel material (right: confirmed by vial inversion test). (b) Optical microscopy image of highly oriented fibrous material revealing shiny fiber surfaces. (c) SEM images of aligned fiber microstructures, and (d) densely packed nanosheets on gel fibers connected by weak intermolecular interactions. Samples (b-d) were synthesised by layering reactant solutions onto a flat glass substrate. (e) TEM images of thin 2D morphologies of the exfoliated OX-1 nanosheets; the inset shows similar morphology of functionalised (Guest@Host) nanosheets of ZnQ_{DMF}@OX-1. (f) SEM of ZnQ_{DMF}@OX-1 nanosheets revealing the dissociated 2D layers (this image is a magnified view of the inset micrograph) (g) AFM height topography showing the thickness of exfoliated layers.

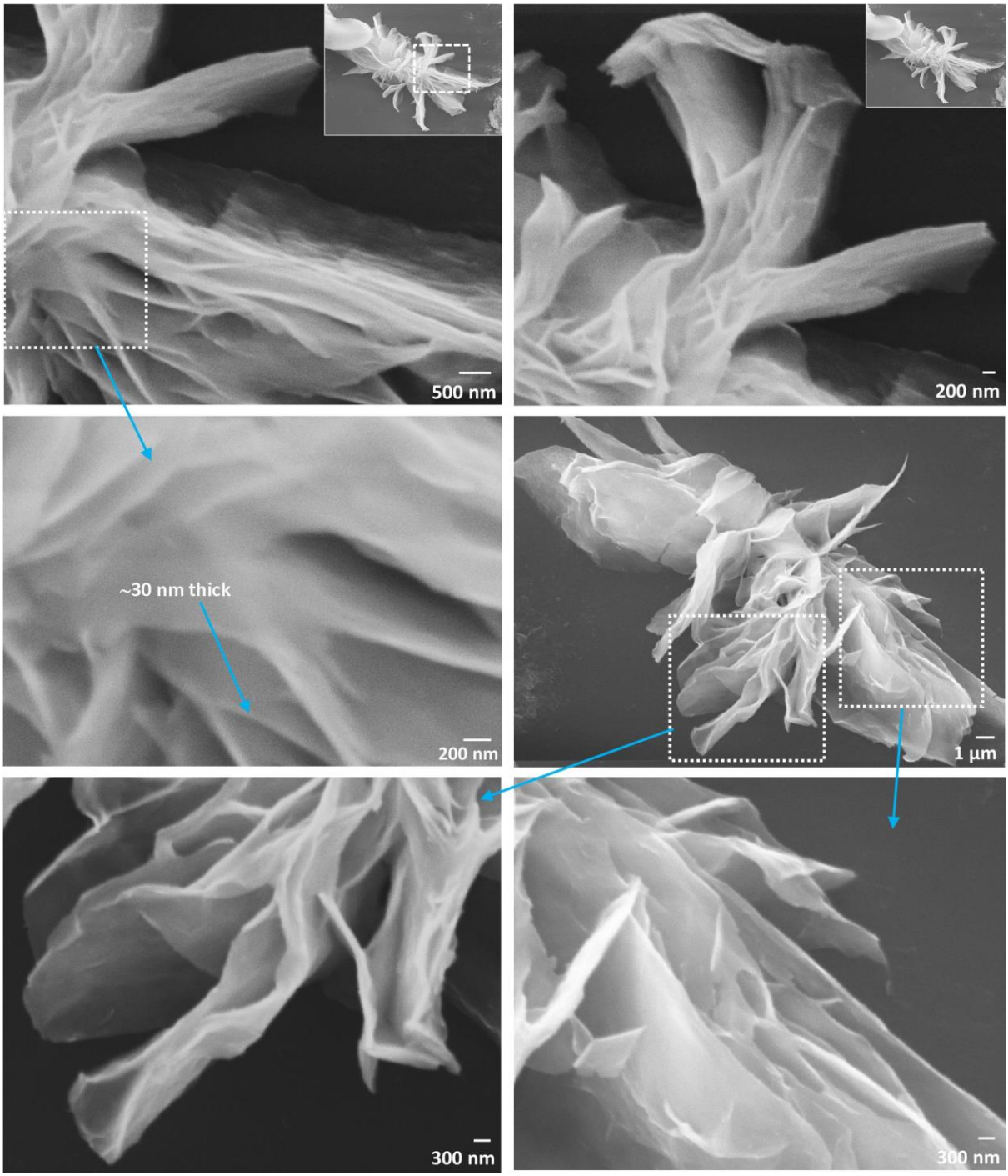

Figure 6.2 SEM images of functionalised nanosheet material i.e. ZnQ_{DMF}@OX-1 which clearly shows growth of thin extended sheets intertwined with each other as a result of HCR approach. Layered ZnQ_{DMF}@OX-1 material started to delaminate after thorough washing and 1 hour sonication. These images also give insights into how multiple layers of nanosheets are stacked together prior to the exfoliation step.

6.3.2 New 3D Framework Structure in 2D Morphology

6.3.2.1 Discovery of OX-1 (Oxford University-1) Framework Material: Pawley Refinement for Structural Elucidation

Powder X-ray diffraction studies (PXRD) (Figure 6.3) of nanosheets extracted from the supramolecular fibers (Figure 6.1e-f) showed crystallographic resemblance to a 3D MOF structure: $(H_2NEt_2)_2[Zn_3BDC_4]\cdot 3DEF$ reported by Burrows *et. al*[229] and Stock *et. al*[230]. However, there are important differences between the present MOF nanosheets and the materials mentioned earlier, from both the structural and the synthetic points of view. First, the diffraction data evidenced strong signature of peak shifts, especially of the diagonal (110) planes (Figure 6.3), which was solved by Pawley refinement (Figure 6.3a) revealing salient variations in the basic unit cell geometry (triclinic *vs*. monoclinic, see Table A3 in Appendix); and there are substantial peak broadening arising from the fine-scale nanosheet morphology (Figure 6.3). Crucially the crystal structure has predominantly unidirectional pores (Figure 6.3a inset), comprising 1D undulating channels down the *c*-axis. Second, neutralisation of the framework negative charges was previously mediated by diethylammonium cations ($H_2NEt_2^+$) liberated from hydrolysis of *N*, *N*-diethylformamide (DEF) solvent, accomplished either in a strong acidic solution (2M HNO_3) at high-temperature synthesis (120 °C, 1 day),[230] or in the presence of water molecules under protracted conditions (~weeks).[229] In contrast, MOF nanosheets prepared *via* the proposed rapid HCR method at room temperature (less than 1 min) incorporate charge-balancing cations NEt_3^+ (derived from its neutral form, when activating BDC linkers). Considered together our results show that, inclusion of NEt_3^+ cations inside MOF pores leads to deformation of host framework, where structural distortion by straining has reduced unit cell symmetry (see Table A3 in Appendix).

6.3.3 Powder X-ray Diffraction of the OX-1 Host

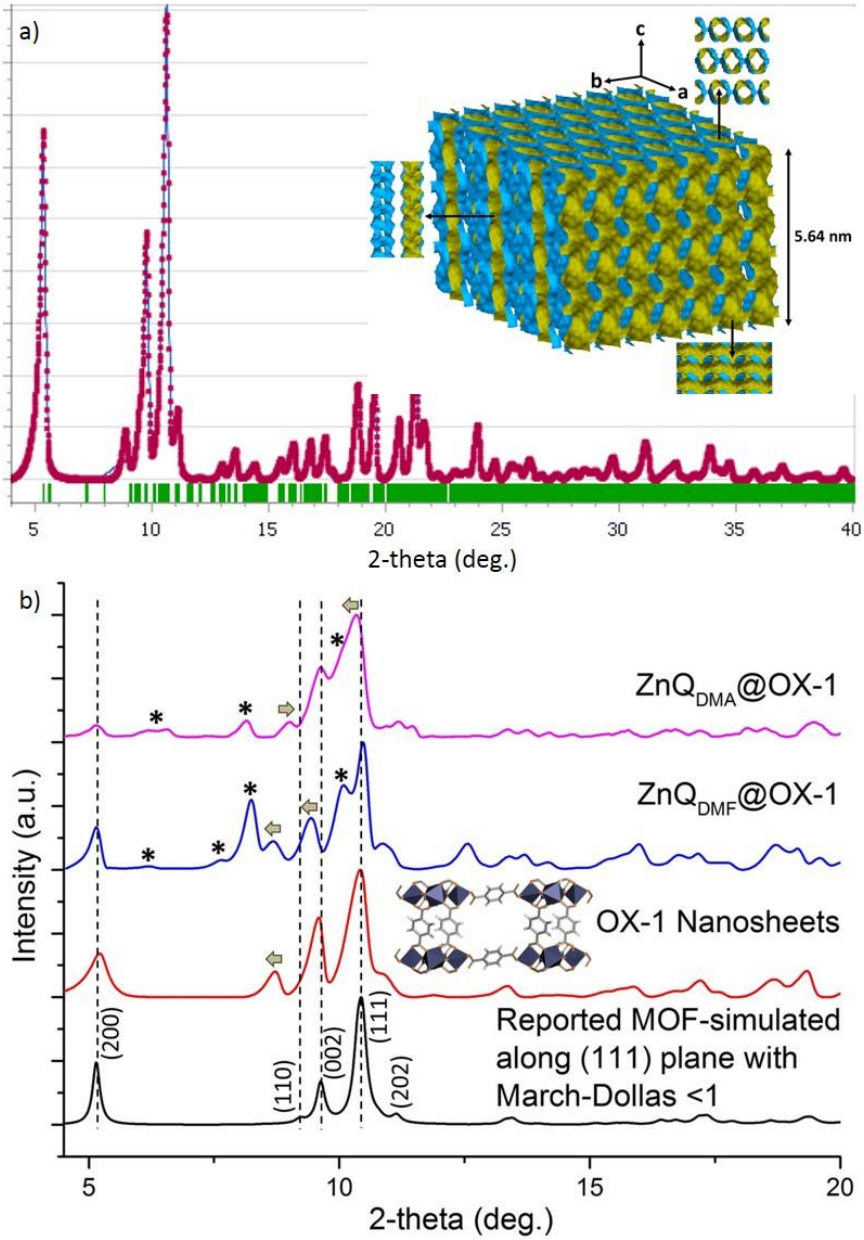

Figure 6.3 a) Pawley refinement of the OX-1 crystal structure incorporating NEt^{3+} charge-balancing cations (R_{wp} = 0.084). Color scheme: zinc in yellow, nitrogen in blue, oxygen in red, carbon in gray, hydrogen in white. The traces indicate data as follows; red: experimental data, blue: calculated from structural refinement, green: observed Bragg peak positions; inset : undulating pore architecture of 1D channels along *c* axis, solvent accessible volume is denoted by yellow surfaces. b) XRD patterns of MOF nanosheets with and without emissive ZnQ functional guests. Extra peaks are ascribed to the diffraction of ZnQ guest designated by the * symbol. Peak shift in OX-1 host in the case of ZnQ$_{DMA}$@OX-1 (marked by arrows on top of each peak at small angles) implies guest@host structural modification causing slight expansion in the cell dimensions.

6.3.3.1 Formula Determination from Thermal Gravimetric Analysis

I subsequently established the chemical formula of the present MOF structure to be: $(HNEt_3)_2[Zn_3BDC_4]\cdot solvent$ where *solvent* = DMF or DMA (*vide infra*), validated by thermogravimetric analysis (TGA) (Figure 6.4, 6.5). Hereafter the identified MOF nanosheet structure is designated as "OX-1" (*i.e.* Oxford University-1 material).

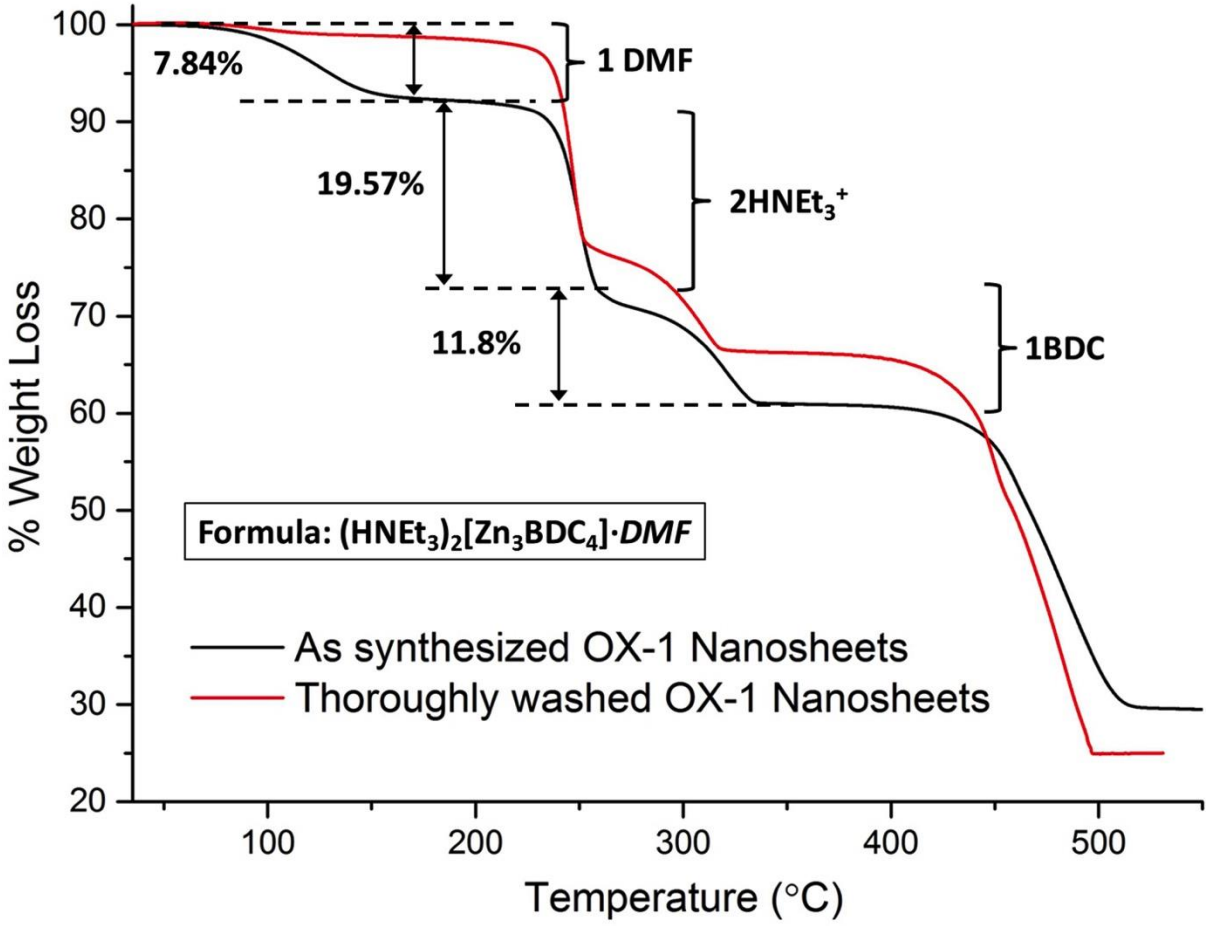

Figure 6.4 Thermogravimetric analysis (TGA) of OX-1·DMF nanosheet material synthesised in *N, N*-Dimethylformamide (DMF) revealing the formula for the material which is in close agreement to the expected weight loss of the components present in the material. Free solvent species occluded in the voids can be easily removed by thorough washing in low-boiling point solvents like acetone and evacuated by heating and vacuum treatment. This behaviour is very similar to the reported MOF structure[229] where they claimed removal of BDC linker achieved in the respective temperature range.

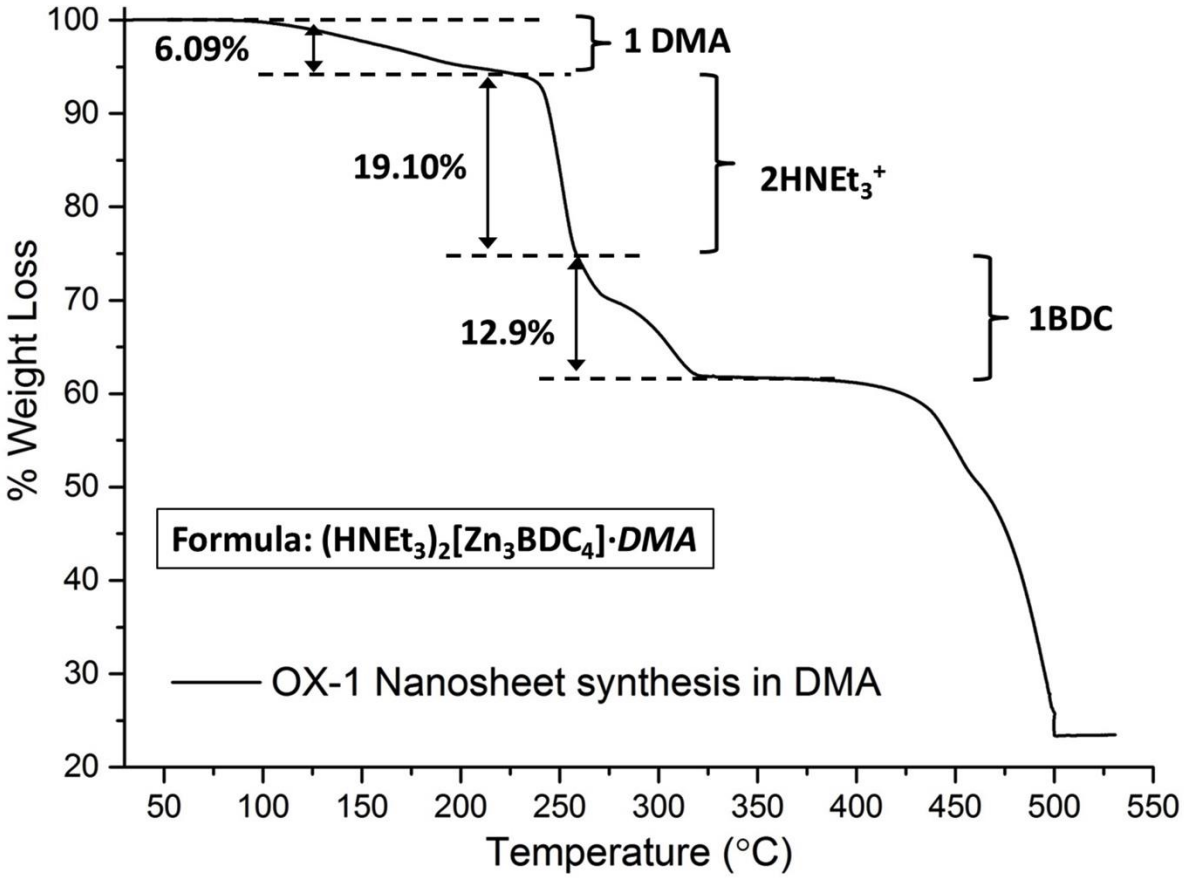

Figure 6.5 TGA of OX-1·DMA compound synthesised in *N,N*-Dimethylacetamide (DMA) with thorough washing and heat-vacuum treatment afterwards. Initial weight loss attributed to free solvent species that reveals entrapped solvent species cannot be removed by washing with low boiling solvent and heat-vacuum pre-treatments. (Washing step and pre-treatment conditions used were exactly the same for both compounds i.e. OX-1·DMF and OX-1·DMA, however, negligible initial weight loss for OX-1·DMF suggests removal of free solvents after pre-treatment. Conversely free solvents stay intact in OX-1·DMA even after pre-treatment).

6.4 Use of ZnQ Dynamics for Smart Luminescent Properties

6.4.1 Synthesis of ZnQ@OX-1 from DMF and DMA

Remarkably our HCR strategy can be adopted, to directly functionalise OX-1 nanosheets to derive new photoactive “Guest@Host” composite systems. To illustrate this, below I will demonstrate *in situ* nanoscale confinement of the luminescent metal complex “guest”

molecule: zinc(II) bis(8-hydroxyquinoline),[203] termed ZnQ, spatially confined inside the 1D pore channels of the OX-1 "host" framework employing one-pot supramolecular synthesis.

6.4.2 Same Guest, Same Host but Different Emission in Two Products

I discovered that, the coupled Guest@Host systems synthesised from *N*, *N*-dimethylformamide (DMF) and *N*, *N*-dimethylacetamide (DMA) solvents displayed significantly different luminescent behaviour, although identical synthetic conditions were applied, other than their solvent type. When subject to UV irradiation it can be seen that (Figure 6.6), nanosheets synthesised in DMF solvent emit an intense blue light (λ_{em} = 470 nm), whereas samples from DMA solvent display a green light emission (λ_{em} = 510 nm). Henceforth, these two new Guest@Host nanosheet systems were designated as: ZnQ_{DMF}@OX-1 and ZnQ_{DMA}@OX-1, respectively (subscript denotes solvent type used in synthesis). To understand their differential structure-property relationships, I performed spectroscopic measurements to study the detailed photophysical properties.

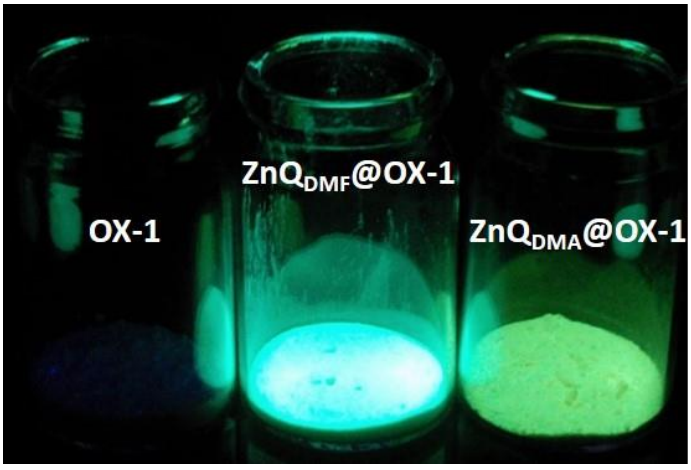

Figure 6.6 Photographs of emissive samples taken under 365 UV exposure.

6.4.3 Absorption Properties Elucidating ZnQ Dynamics under Confinement

Absorption UV-Vis spectroscopic measurements were used to elucidate the nature of the host-guest interactions and to identify spatial confinement effects due to nanoscale porosity. It can be seen in Figure 6.7a that, functionalised nanosheets of ZnQ_{DMF}@OX-1 and ZnQ_{DMA}@OX-1 exhibit an appreciably enhanced π—π^* electronic transition at 291 nm, confirming the successful encapsulation of luminous ZnQ guest emitter within the pores of the OX-1 host framework. This energy transfer phenomenon is caused by close-packing of host-guest aromatic moieties, characteristic of the caged guest molecules. Figure 6.7b shows the modification of band gaps as a consequence of intimate host-guest coupling. Through encapsulation of ZnQ in the OX-1 pores, a clear reduction in band gap of the OX-1 framework had been detected, which fell from greater than 4 eV to just below 2.8 eV. Interestingly, I found that ZnQ_{DMA}@OX-1 exhibits a maximum absorption corresponding to the ZnQ guest contribution at 371 nm, indicative of the confinement of *neat* ZnQ[231] inside OX-1 pores. Compared to DMF, because DMA is a relatively bulkier molecule, its coordination to the Zn center of ZnQ at two axial positions (Figure 6.7a inset) might be misplaced upon pore confinement, implicated by caging in the spatially constrained channels (Figure 6.3a inset). Neat ZnQ complex thus confers extra degrees of freedom to the coordinated bis-8-hydroxyquinoline (8HQ) aromatic moieties around the Zn^{2+} center of the guest emitter; this effect is illustrated in the inset of Figure 6.7a. In contrast, because Zn metal centers strongly prefer DMF over DMA,[232] coordinated DMF helps to stabilise the ZnQ structure. This is in agreement with the absorption data of ZnQ_{DMF}@OX-1 nanosheets, where λ_{max} was pinpointed at 387 nm indicating that the ZnQ has coordinated DMF.

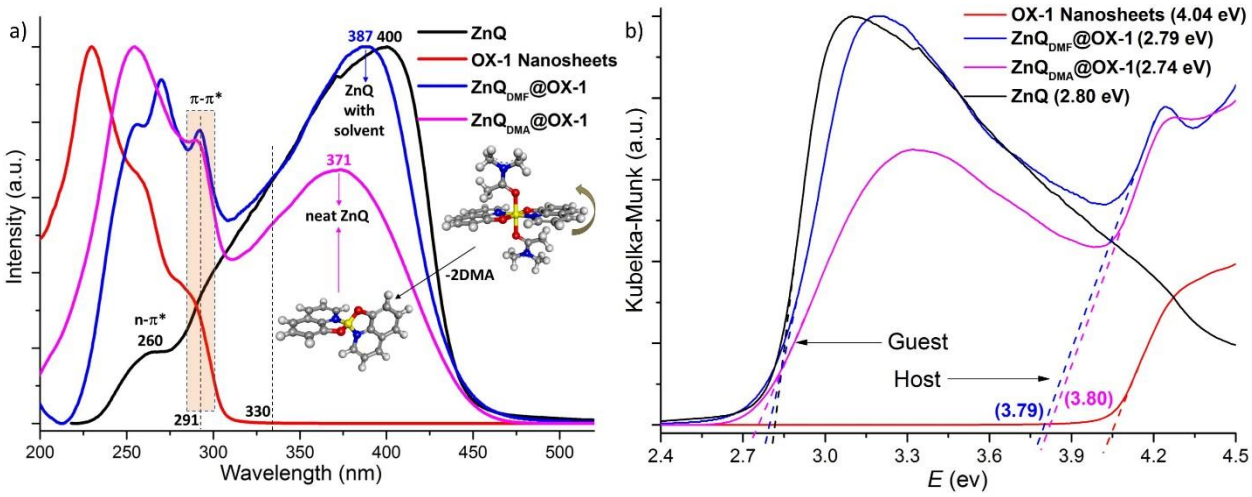

Figure 6.7 a) UV-Vis electronic absorption spectra of the OX-1 host framework, ZnQ guest emitter, and guest@OX-1 composite systems. Inset depicts conformational changes of the neat ZnQ guest emitter molecule, after losing two DMA coordinated solvent molecules from its axial positions. b) Band gap values determined from diffuse reflectance spectra and photon energy intercepts, signifying host-guest interactions.

6.4.4 Raman Spectroscopy to Study ZnQ Dynamics

Utilising Raman vibrational spectroscopy (Figure 6.8), I have achieved further insights into symmetry alterations of the ZnQ guest emitter due to pore confinement. For ZnQ_{DMA}@OX-1, the doubly-degenerate Raman modes at 503.8 cm^{-1} (assigned to skeletal in-plane bending vibrations[233]) and 514.04 cm^{-1} (Figure 6.8b) are pointing towards a reduction in molecular symmetry of the neat ZnQ (*i.e.* without DMA coordination, see Figure 6.7a inset); this phenomenon is prominent also in pure ZnQ. Interestingly for ZnQ_{DMF}@OX-1, only a single band was identified at 507.9 cm^{-1}, which meant that the confined ZnQ guest (with DMF) has higher structural symmetry. Relative mode intensities at 740.42 cm^{-1} associated with aromatic ring deformation is appreciably higher in ZnQ_{DMA}@OX-1 compared to ZnQ_{DMF}@OX-1, further supporting the notion that the former nanosheet confines neat ZnQ (higher degrees of freedom). The band at 862.5 cm^{-1}

corresponds to the out-of-plane γ(C-H) bending mode of BDC molecules[234] in the host framework. For ZnQ_{DMF}@OX-1, this mode is accompanied by a doubly-degenerate band identified at a lower frequency of 852.2 cm^{-1} (Figure 6.8b), implicated by strong intermolecular interactions of host-guest aromatic rings hence lessening structural symmetry.

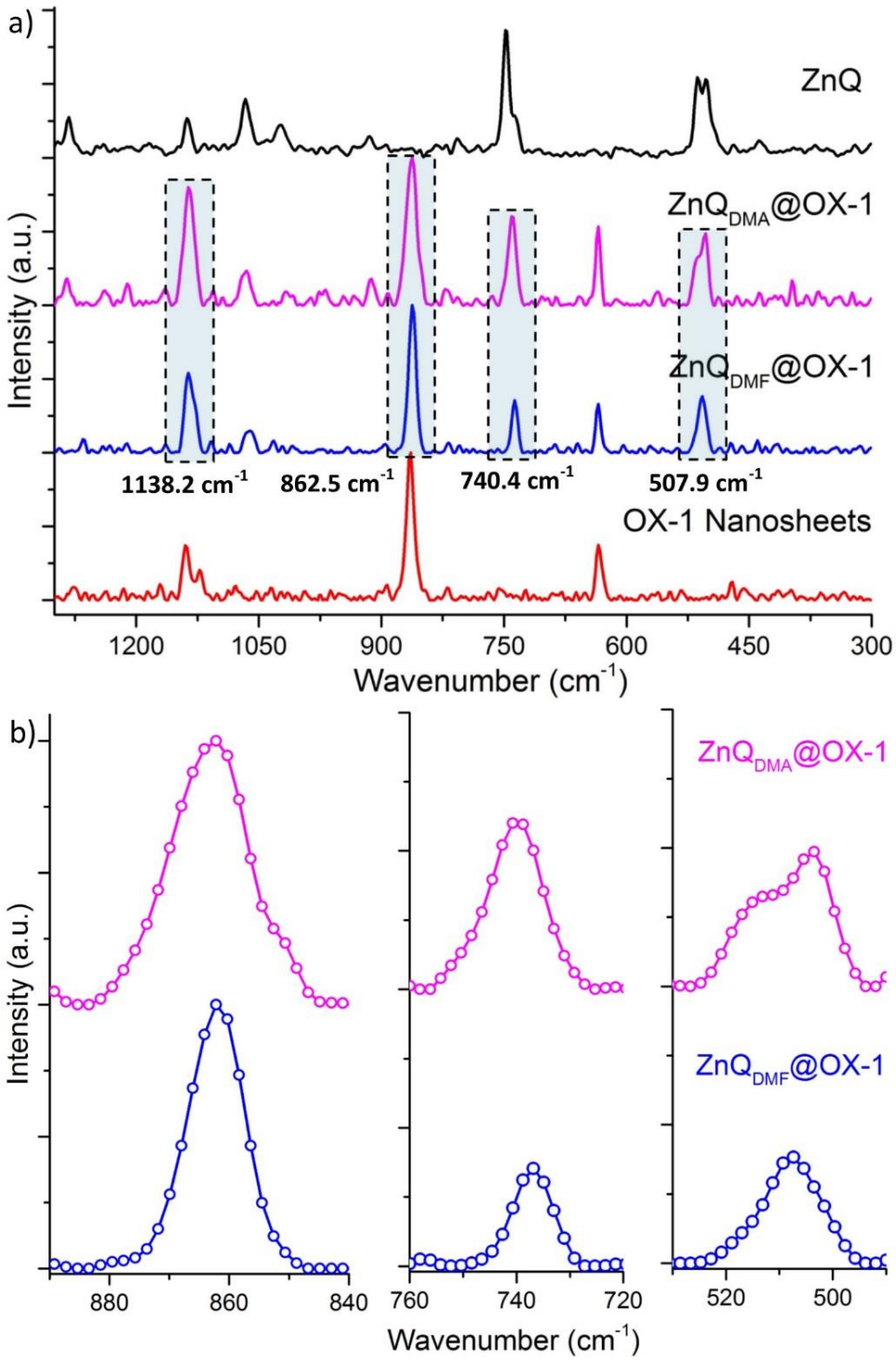

Figure 6.8 a) Raman spectra revealing intensity and peak alterations arising from the host-guest confinement effects. b) The doubly-degenerate bands at 852.2 cm^{-1} and 514.04 cm^{-1} arising from symmetry alterations of neat ZnQ guest emitter as affected by pore confinement.

6.4.5 Theoretical Calculations

6.4.5.1 Supporting Structural Dynamics

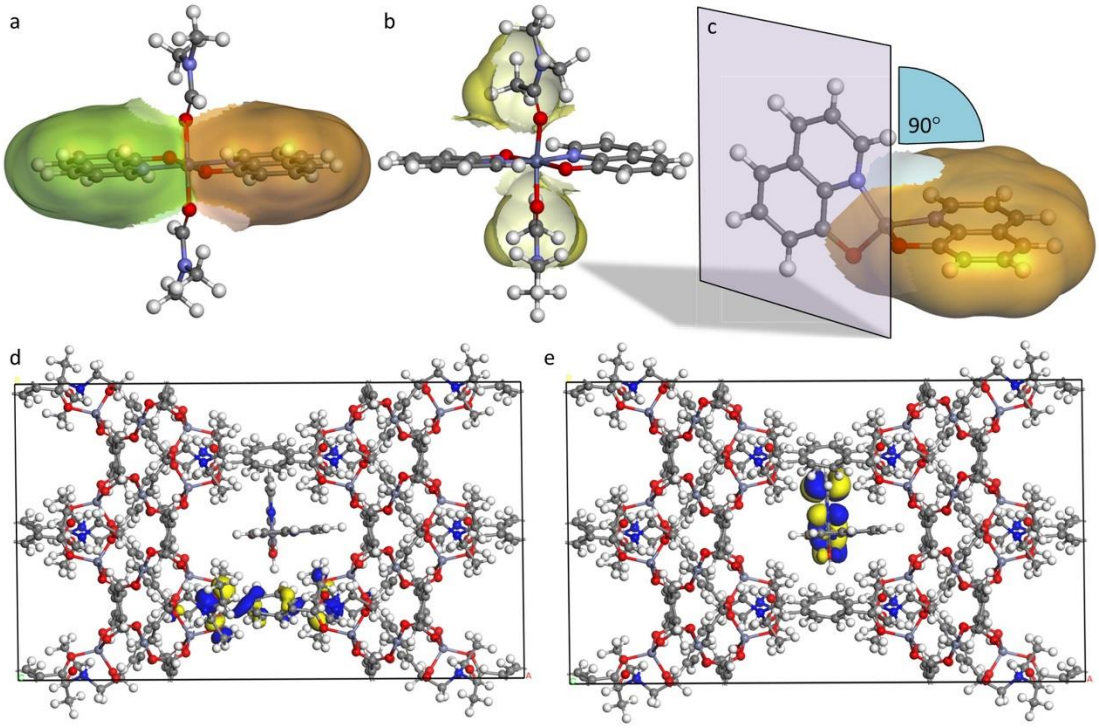

Figure 6.9 Optimised geometries of the ZnQ guest in three different structural configurations: (a) DMF solvent molecules coordinated axially to the Zn^{2+} octahedral center; less steric DMF molecule allowing planar spatial arrangement of the 8HQ aromatic rings (indicated by green and orange van der Waals surfaces). (b) Steric hindrance from axially coordinated DMA solvent molecules deforming the planarity of 8HQ aromatic rings; yellow surfaces represent CH_3 groups of the coordinated DMA. (c) Tetrahedral (Td) configuration achieved upon removal of the two axially coordinated DMA molecules, permitting a 90° rotation of one of the two 8HQ aromatic planes. ZnQ(Td)@OX-1 assembly in which (d) HOMO located on the BDC linker of the host framework, while (e) LUMO on the aromatic rings of ZnQ guest molecule confined within OX-1 pore. Blue and yellow isosurfaces are positive and negative charges respectively.

Our experimental results are further supported by theoretical calculations (see section 3.2.5.2 in chapter 3), elucidating that the ZnQ guest molecule could adopt different geometrical configurations under pore confinement. Figure 6.9a shows the optimised

structure of ZnQ with two DMF molecules coordinated to the Zn^{2+} axial positions, where the adjacent 8HQ aromatic rings are planar. However, these rings became non-planar when DMF was substituted by the bulkier DMA molecules (Figure 6.9b), leading to a significant geometrical distortion in confinement of the OX-1 framework; such a host-guest configuration is not favourable. In fact, the theoretical calculations revealed that ZnQ guest with tetrahedral center (Td) has the preferred geometry (Figure 6.9c: without coordinated DMA) formed by a 90° rotation of the 8HQ aromatic plane; this configuration also offers good interactions with the host framework *via* π-π and hydrogen bonding.

6.4.5.2 Transitions in Energy Gaps Due To ZnQ Dynamics inside OX-1: DFT Calculations

Density functional theory (DFT) band gap calculations show that, for example, when considering ZnQ(Td)@OX-1 pore confinement (Figure 6.9d,e) the highest occupied molecular orbital (HOMO) is localised on the BDC ring of the OX-1 host, whereas the lowest unoccupied molecular orbital (LUMO) is located on the aromatic rings of the ZnQ molecule. This HOMO-LUMO configuration suggests that host-guest energy transfer will be favorable during photoexcitation of the Guest@Host assembly. It can be seen that the hybrid orbitals of the ZnQ(Td)@OX-1 and ZnQ_{DMF}@OX-1 systems are exhibiting a notable reduction in bandgap energies, relative to the isolated OX-1 host and pure ZnQ guest molecule. Our results further support the recent literature where it has been proposed that: (i) mechanical deformation of flexible MOF structures could produce significant band gap changes[235] and, (ii) localised electronic density distribution of an encapsulated host-guest assembly could enable efficient energy transfer during excitation process.[236]

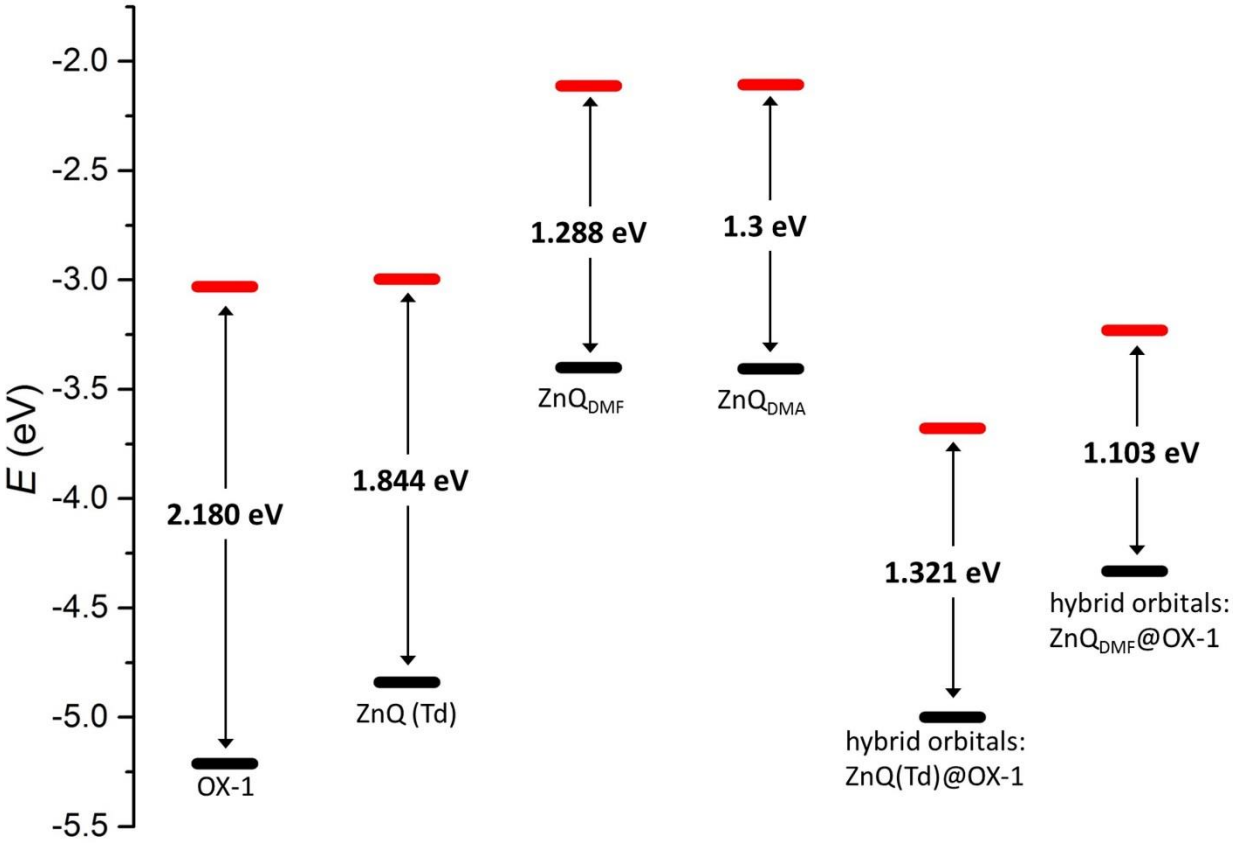

Figure 6.11 DFT calculated band gap energy values of the OX-1 host framework (1×2×1 supercell) and ZnQ guest emitter considering different possible host-guest configurations (DMF, DMA, Td). Formation of hybrid orbitals in Guest@OX-1 lowers the energy levels due to intimate host-guest interactions, shown on the right for the case of ZnQ(Td)@OX-1 and ZnQ_{DMF}@OX-1. Note that ZnQ_{DMA}@OX-1 is equivalent to ZnQ(Td)@OX-1, i.e. without DMA solvent coordination at its two axial positions.

6.4.6 Effect on Emission Behaviour of ZnQ Dynamics: Photoluminescence, Life Time and Quantum Yield

I measured the fluorescence quantum yield (QY%) of pure ZnQ guest emitter in DMF suspension (35%) and found that, it has risen to 43.8% upon nanoconfinement in the ZnQ_{DMF}@OX-1 system, which further resulting in an improved emission lifetime (Figure 6.10). Conversely, QY of the ZnQ_{DMA}@OX-1 system deteriorated to 23.3% (compared to

33% for pure ZnQ in a DMA suspension, see Figure 6.10). The findings are in line with the reported photophysical phenomena where ground and excited states of metal complexes can be modified by fine structural changes from pressure effects, which are manifested as decreasing non-radiative or increasing radiative rates.[237-239] My data suggest that ZnQ caged inside ZnQ_{DMF}@OX-1 is experiencing compressive strains enhancing its luminescence emission; but ZnQ_{DMA}@OX-1 is showing a reduction in luminescence due to higher intermolecular interactions between neat ZnQ aromatic rings and the host framework. This reasoning is consistent with the UV-Vis and Raman spectroscopic data discussed in sections 6.4.3 and 6.4.4.

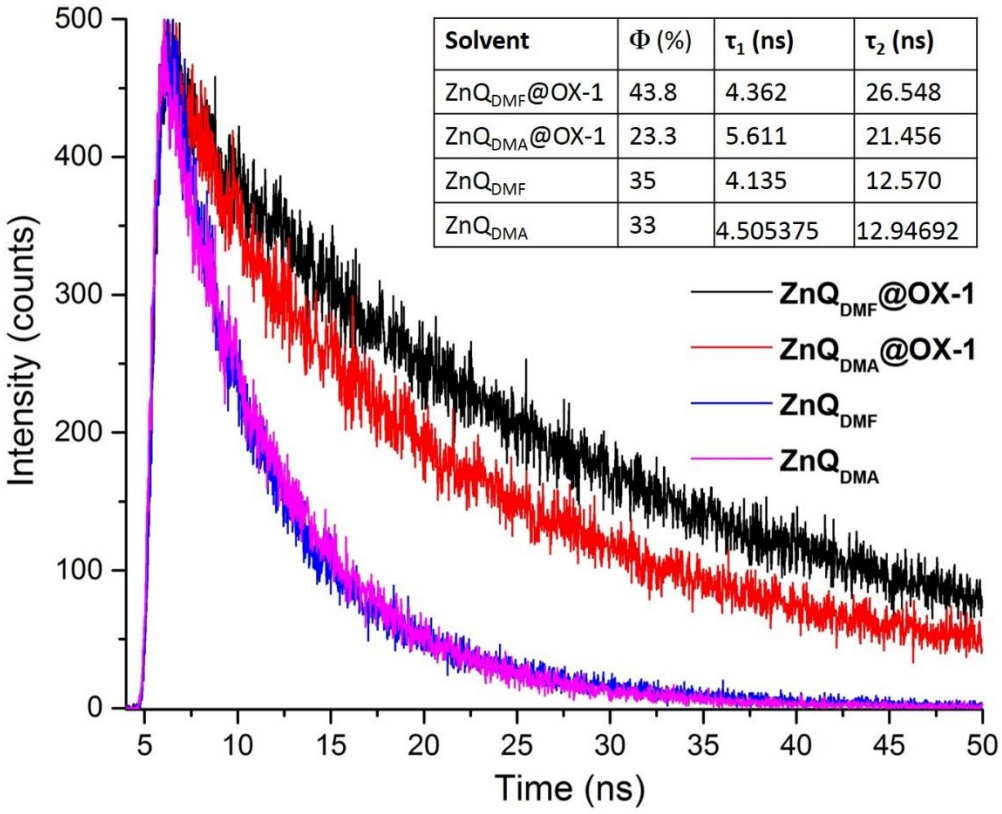

Figure 6.10 Fluorescence lifetime decay profiles for the ZnQ guest only, and the guest@host MOF materials revealing the nanoconfinement effects on the excited-state lifetime of fluorescent guest species. ϕ is quantum yield (%) and τ are time constants (ns).

6.5 Use of Confined ZnQ Dynamics for Opto-Chemical Sensing

6.5.1 Blue Emission of ZnQ_{DMF}@OX-1 for Sensing

I harnessed the tunable luminescent properties of the Functionalised Guest@OX-1 nanosheets as photactive materials, accomplishing optochemical sensing of volatile organic compounds (VOCs). Figures 6.12a and 6.13 show the luminescence data of ZnQ_{DMF}@OX-1 nanosheets as solution-state dispersions, upon perturbation by a series of main solvent species used as analytes. I discover major photophysical response not only in characteristic fluorescence wavelength and intensity (Figure 6.12b), but also in terms of colour chromaticity tuning behaviour (Figure 6.12c).

6.5.2 Intensity and Emission Wavelength Shifts of Solvent Dispersion

Between the small aliphatic alcohols being probed, methanol caused a fully diminished fluorescence intensity (quenching) after 3-4 minutes exposure, while nanosheets in isopropanol (IPA) retained majority of its intensity. In fact with rising alcohol polarity (Figure 6.13), I observed a sharper decline in emission intensity and a higher frequency red shift following the sequence of: methanol (510 nm) > ethanol (504 nm) > IPA (501 nm). Strongly polarisable protic solvent destabilises the ZnQ emitter guests, leading to fluorescence quenching *via* protonation of coordinated oxygen in 8HQ linkers.[240] The data indicate excited state proton-induced charge transfer of ZnQ guests in protic solvents,[241] where such a mechanism depresses luminescence.

Functionalised nanosheets exposed to non-polar aliphatic long-chain alkane (*n*-hexane) and cyclic alkane (cyclohexane) displayed interesting optochemical stimulation behaviours.

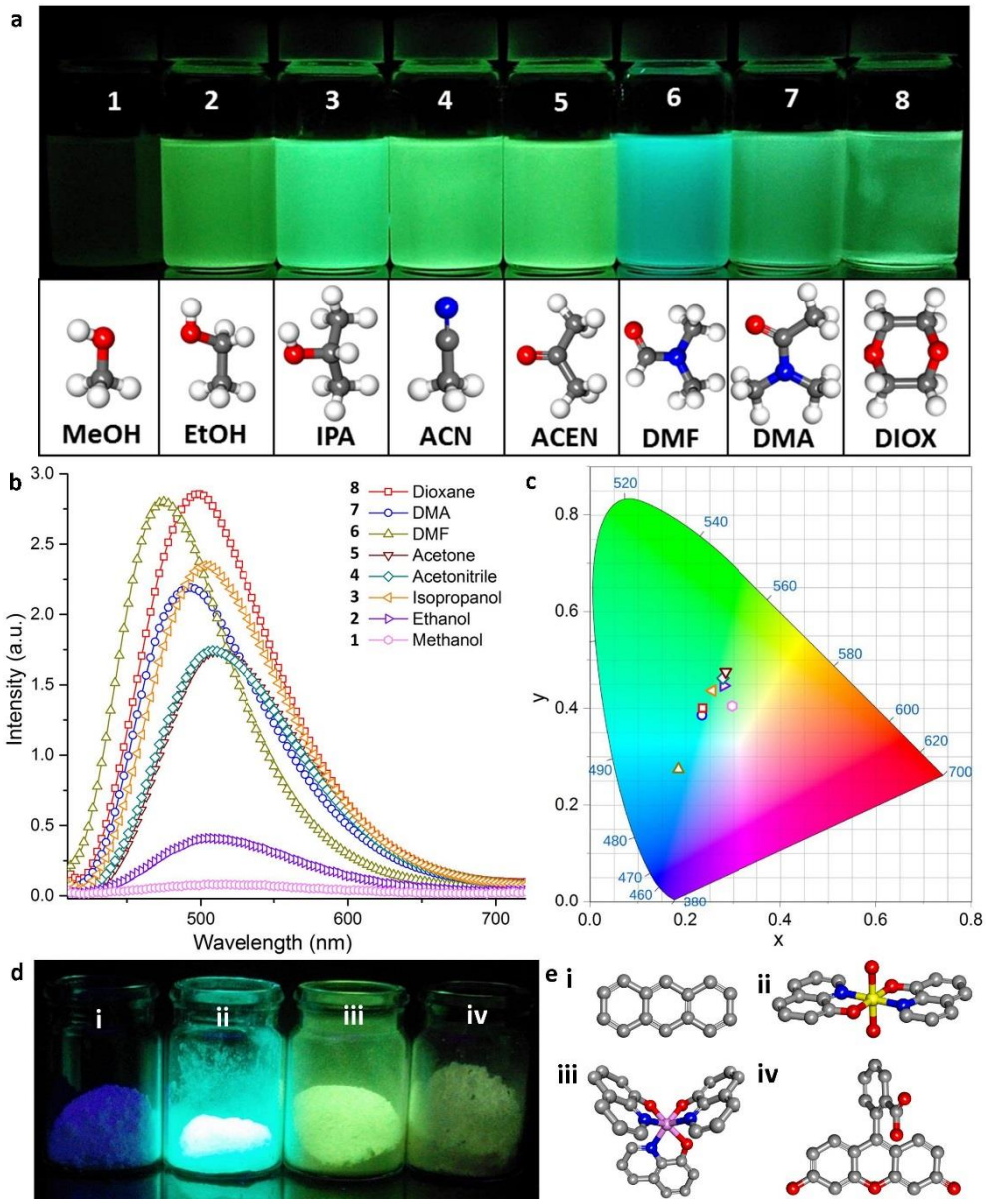

Figure 6.12 (a) Visible to naked eye are distinct modulations in emission properties of dispersions of functionalised nanosheets in a range of small-molecule solvents (each comprising 5 mg of active material in 15 mL solvent). (b) Emission profiles and emission intensities of respective dispersions showing different levels of blue (hypsochromic) or red (bathochromic) shifts. (c) Chromaticity plot (CIE 1931) indicating the emission color coordinates of the respective dispersions. (d) A family of luminescent host-guest materials synthesised by one-pot supramolecular method (Scheme 6.1), adopting the same OX-1 host framework but confining different light-emitting guest molecules (e): i - Anthracene, ii - ZnQ, iii - AlQ (Al-(tris-8-Hydroxyquinoline), iv - Fluoresceine. Color scheme: zinc in yellow, aluminum in pink, nitrogen in blue, oxygen in red, carbon in gray, hydrogen in white.

Samples of ZnQ_{DMF}@OX-1 (λ_{em} = 470 nm) dispersed in these aliphatic analytes produced similar fluorescence intensities, but peaked at very different characteristic wavelengths ($\lambda_{em(n\text{-hexane})}$ = 496 nm *vs*. $\lambda_{em(cyclohexane)}$ = 477 nm, see Figure 6.13).

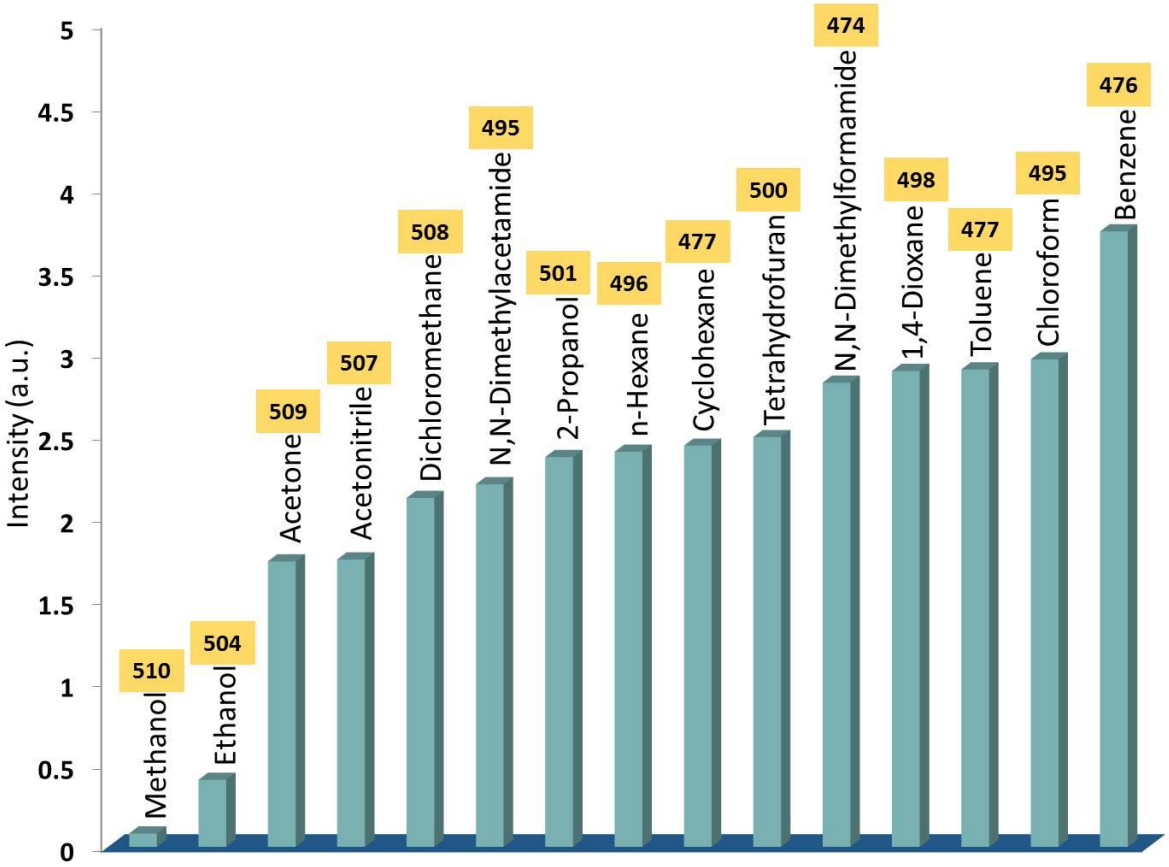

Figure 6.13 Small-molecule sensing ability of ZnQ_{DMF}@OX-1 nanosheets *via* changing emission intensity and shifting in wavelength due to optochemical perturbations in MOF pores. Numbers on top of each bar denotes the emission wavelength λ_{em} (nm).

This meant that higher molecular mobility of linear *n*-hexane in the OX-1 pores generates a stronger red shift, which can be used to distinguish against the bulkier cyclohexane analyte. Indeed molecular-size selectivity effect was best demonstrated for the aromatic pair — benzene *vs*. toluene (both of similar polarity), where nanosheets exposed to

bulkier toluene experienced only a minor intensity rise, however that caused by benzene was the most intense detected amongst all the analytes being tested (Figure 6.13). Significantly this result elucidates that by increasing π—π interaction within the ZnQ_{DMF}@OX-1 system, it strengthens fluorescence intensity without modifying the emission wavelength. Considering yet another pair of related analytes — dichloromethane (DCM) *vs*. chloroform, I established that the relatively smaller DCM molecules can readily infiltrate the tortuous 1D MOF channels yielding a major red shift (>30 nm), while diminishing fluorescence intensity due to its strong electron withdrawing nature. Collectively the above comprehensive perturbation data confirmed that, the functionalised nanosheets are extremely sensitive towards salient solvent parameters, encompassing polarity, molecular size, hydrogen bond donor and acceptor affinity, and non-covalent π—π interactions. Long-range crystallinity of the OX-1 host implies that there is a well-ordered arrangement of functional guests (e.g. ZnQ emitters), where its periodicity and accessible porosity offers direct interaction with incoming solvent analytes permitting fast chemical detection. In fact we must recognise that, analyte dependent sensing capability is absent when deploying pure ZnQ complexes alone, *i.e.* without the host-guest nanoconfinement environment imparted by the porous OX-1 nanosheets.

6.5.3 Paper Device for Quick Reversible Acetone Vapour Sensing

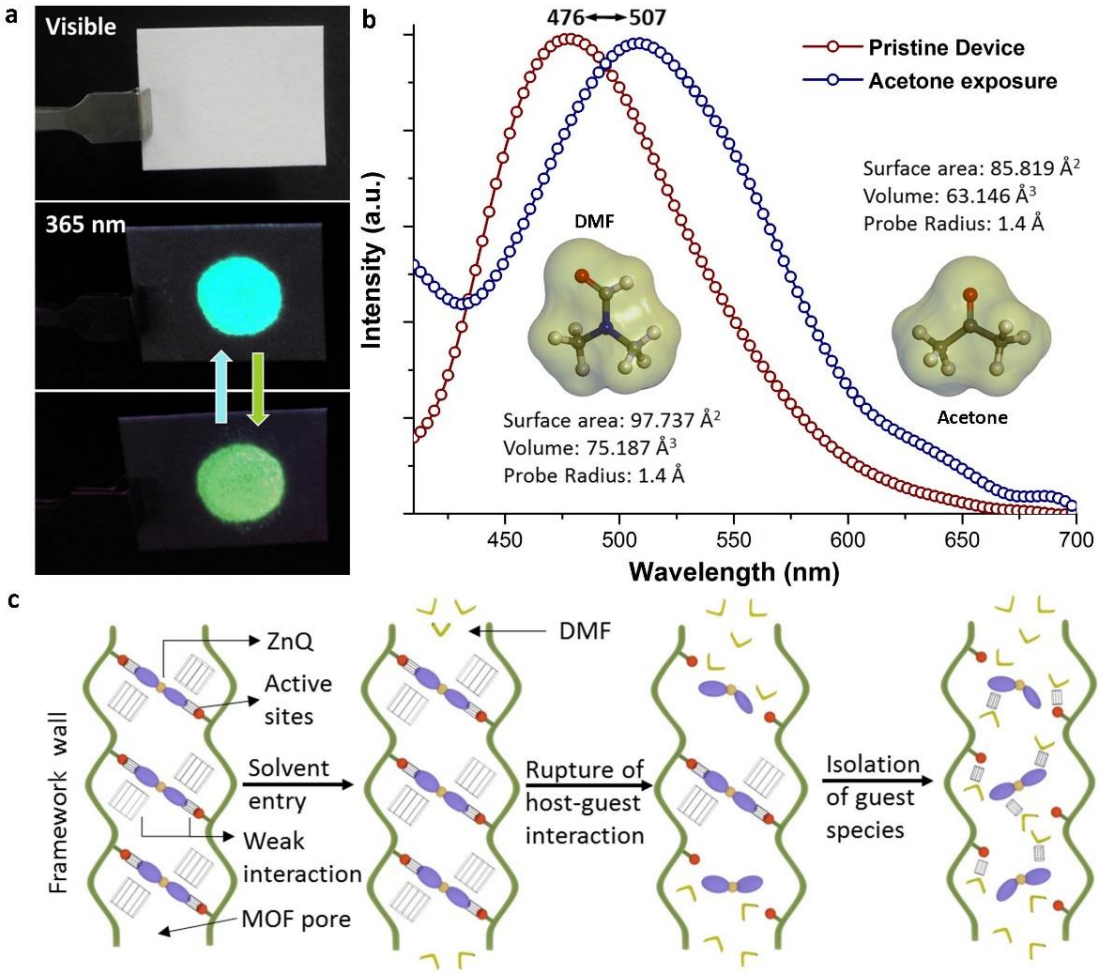

Figure 6.14 Optochemically active sensory materials comprising ZnQ_{DMF}@OX-1 nanosheets. (a) Paper-based optochemical sensor demonstrating reversible acetone sensing ability. (b) A 31-nm red shift upon acetone exposure and, recovery to its original emission wavelength upon DMF exposure. Inset shows chemical structures of DMF and acetone analytes and their differential molecular sizes. (c) Proposed mechanisms involving multiple host-guest interactions under the nanoscale confinement of 1D undulating (tortuous) channels of OX-1 host framework (vertical: *c*-axis, corresponding to 1D channels of OX-1), and upon the introduction of a DMF analyte triggering a blue shift transformation.

Motivated by the capacity exhibited by functionalised guest@OX-1 nanosheets in the detection of numerous solvent analytes and VOCs, I present a simple proof-of-

concept device demonstrating the efficacy of ZnQ_{DMF}@OX-1 as a reversible solid-state chemical sensor. A paper-based device (Figure 6.14a) was fabricated by drop coating a small amount of ZnQ_{DMF}@OX-1 (*e.g.* ~2 µL dispersion made from 5 mg nanosheets suspended in 1 mL hexane) onto a Whatman filter paper. I tested this paper device with a small concentration of analyte. For example, ~1 µL acetone applied to this paper device swiftly produced a substantial 31 nm red shift (under 365 nm UV), which is clearly perceptible to the naked eye (Figure 6.14a). Intriguingly this transition is reversible (507 ⇌ 476 nm, Figure 6.14b); the device is again reusable after ~10 sec drying time at room temperature as acetone is volatile (in contrast the ZnQ_{DMA}@OX-1 has an initial emission wavelength of λ_{em} = 510 nm, thus rendering it unsuitable for wavelength-shift based sensing of acetone). Nonetheless, repetitive exposures to acetone could retain the device emission at a higher wavelength of 507 nm.

6.5.4 Mechanism for Emission Change

The results presented above suggests that increased acetone occupancy in OX-1 pores is strengthening non-covalent interactions bridging the ZnQ emitter to the host framework. However, even such an effect is non-permanent in nature; it can be reverted to its initial 476 nm (blue) emission simply by exposing the device to DMF for several minutes. Key observations made in emission response upon DMF exposure elucidates the plausible host-guest interaction mechanisms, as depicted in Figure 6.14c. The moment the active material was exposed to DMF, it was observed that emission colour quickly turned greenish-yellow for fraction of a second before beginning to undergo blue shifting and eventually returning to its original 476 nm. On this basis, I hypothesise that weak interactions connecting the ZnQ guest and the host framework sites began to slowly

rupture upon infiltration of external DMF analyte. I reasoned that penetration of DMF molecules through the 1D tortuous pore channels of the OX-1 host is relatively sluggish, thereby isolating ZnQ from adjacent weak interactions in a stepwise fashion (Figure 6.14c); eventually this reaches a complete conversion evidenced by the (blue) 476 nm emission. Comparatively immediate response towards acetone exposure can be explained by contrasting the molecular size of the analytes concerned (Figure 6.14b inset): acetone molecule is approximately 16% smaller compared to DMF, so the former infiltrates the undulating pores much easier given its smaller size and weakly interacting nature.

6.6 Summary

In summary, this Chapter presents a new paradigm to prepare Guest@MOF porous nanosheets, resulting in tunable nanoscale material systems highly sensitive to coupled optoelectronic and chemical perturbations. The proposed high-concentration reaction (HCR) supramolecular strategy is very powerful, and it could be utilised to systematically engineer a variety of functionalised Guest@MOF composite systems. To show that this is an exciting possibility, I have implemented the HCR approach in conjunction with the Guest@OX-1 platform to integrate a number of topical guest emitters successfully (see Figures 6.12d-e), including anthracene, ZnQ, AlQ, naphthalene, and fluorescein.

Chapter Seven

Mechanochromic luminescent MOF Nanoplates: Spatial Molecular Isolation of Light-Emitting Guests in a Sodalite Framework Structure

7.1 Background

7.1.1 Concept of Mechanochromic luminescence

Functional nanomaterials with adjustable luminescent properties[88, 91, 242] are greatly sought after to achieve new generation photonics-based sensing and tunable optoelectronics applications.[15, 243-244] Indeed, a vast range of fluorescent materials, including conjugated organic molecules, metal complexes, liquid crystals, oligomers, polymers, metallogels, supramolecular assemblies and quantum dots have shown huge potential for use in many luminescent based devices and sensors.[36, 245-247] One of the most intriguing findings in this topic area is mechanochromic luminescence. Mechanochromic luminescent materials have gained increasing attention in recent years, where researchers seek to understand, control and tune luminescent properties with the help of exogenous mechanical stimuli, ranging from shearing, grinding and rubbing, to tension, compression and impact.

7.1.2 Uses, Challenges and New Direction for Mechanochromic luminescent Materials

It is envisaged that smart mechanochromic luminescent materials can be integrated into deformation-based detectors, security papers, optical memories, and photonic strain gauges.[248-249] Regarding material design, it is essential to control its intermolecular weak

interactions, which are dictating the optical behaviour as a function of mechanical stress and strain.[250-251] Outstanding challenges in the field include aggregation caused quenching (ACQ), solid-state phase change and amorphisation, limited structural resilience and difficulty in the precise control of molecular orientations needed for practical applications. Traditional approaches for making mechanochromic luminescent materials often require complicated molecular designs and will involve difficult multistep synthetic procedures.[252-255] To address the foregoing challenges, one possible solution is to combine chemical traits of existing fluorophoric molecules into ordered nanoscale host assemblies, by leveraging the host-guest spatial confinement strategy.[135, 139, 256-257]

7.2 MOF as a Host to Achieve Mechanochromic luminescence

To trigger switchable optical properties of guest molecules under the confinement of the nanoscale pores in MOF host, dynamic MOF systems is highly desirable owing to their structural versatility. In Chapter 5, I have demonstrated the efficacy of the sodalite cage of ZIF-8 for hosting bulky metal complexes to engineer luminescent material with improved photostability.[139] In this study, I combine our understanding of the dynamic behaviour of ZIF-8 framework and its use as a host for accommodating external guest species to contrive a new mechanoluminescent host-guest material. There are already a few examples of (host-only) mechanoluminescent MOFs reported in the literature (e.g. refs.[258-262]) in which mechanoluminescence originated typically from the N-donor based coordinating linkers. To the best of knowledge, the host-guest system reported herein is the first example of a mechanoluminescent material demonstrating spatially ordered fluorophoric guests constrained in a periodic MOF structure.

7.3 One Step Straightforward Synthesis for Guest@Host Assembly

7.3.1 Ease of Host Synthesis, Porosity and Potential Structure for Multifunctionality

Facile reaction of 2-methylimidazole (mIm) with Zn(II) cations yields the formation of ZIF-8 adopting the sodalite framework topology.[194] ZIF-8 is a highly topical MOF structure for encapsulation of functional guest molecules, for example see refs.[14, 97, 139, 188, 190, 225, 263-265], because it features long-range periodicity with a relatively large pore (~1 nm diameter) located in the middle of each sodalite cage. The ease of synthesis combined with the unique pore architecture and mechanical properties of ZIF-8 (elasticity[193] and dynamics),[198] could offer vast possibilities to engineer novel Guest@MOF systems exhibiting tunable functionalities. In this study, I have exploited the spherical voids of ZIF-8 as spatially arranged “host” spaces, allowing encapsulation of the polycyclic aromatic hydrocarbon: Perylene ($C_{20}H_{12}$), which is an efficient light-emitting “guest” molecule.

7.3.2 HCR Synthesis Approach for Guest Confinement in ZIF-8 Voids

I adopted the concept of high-concentration reaction (HCR) introduced in Chapter 6 to synthesize a new host-guest assembly termed: Perylene@ZIF-8, at ambient conditions. The detailed synthetic procedures are described in Chapter 2. In essence, the proposed self-assembly route enables us to achieve nanoscale spatial confinement of bulky Perylene guest molecules in the voids of the ZIF-8 host. Introduction of triethylamine (NEt_3) during HCR, not only accelerates the reaction process resulting in a high amount of Perylene@ZIF-8 product, but also it provides additional control over the morphology of

the product, specifically the downsizing of the 3-D framework architecture of the ZIF-8 material to derive two-dimensional (2-D) nanoplates (Figure 7.1).

7.4 Highly Controlled Morphology of Materials

7.4.1 2D Nanoplates of Host-Guest System

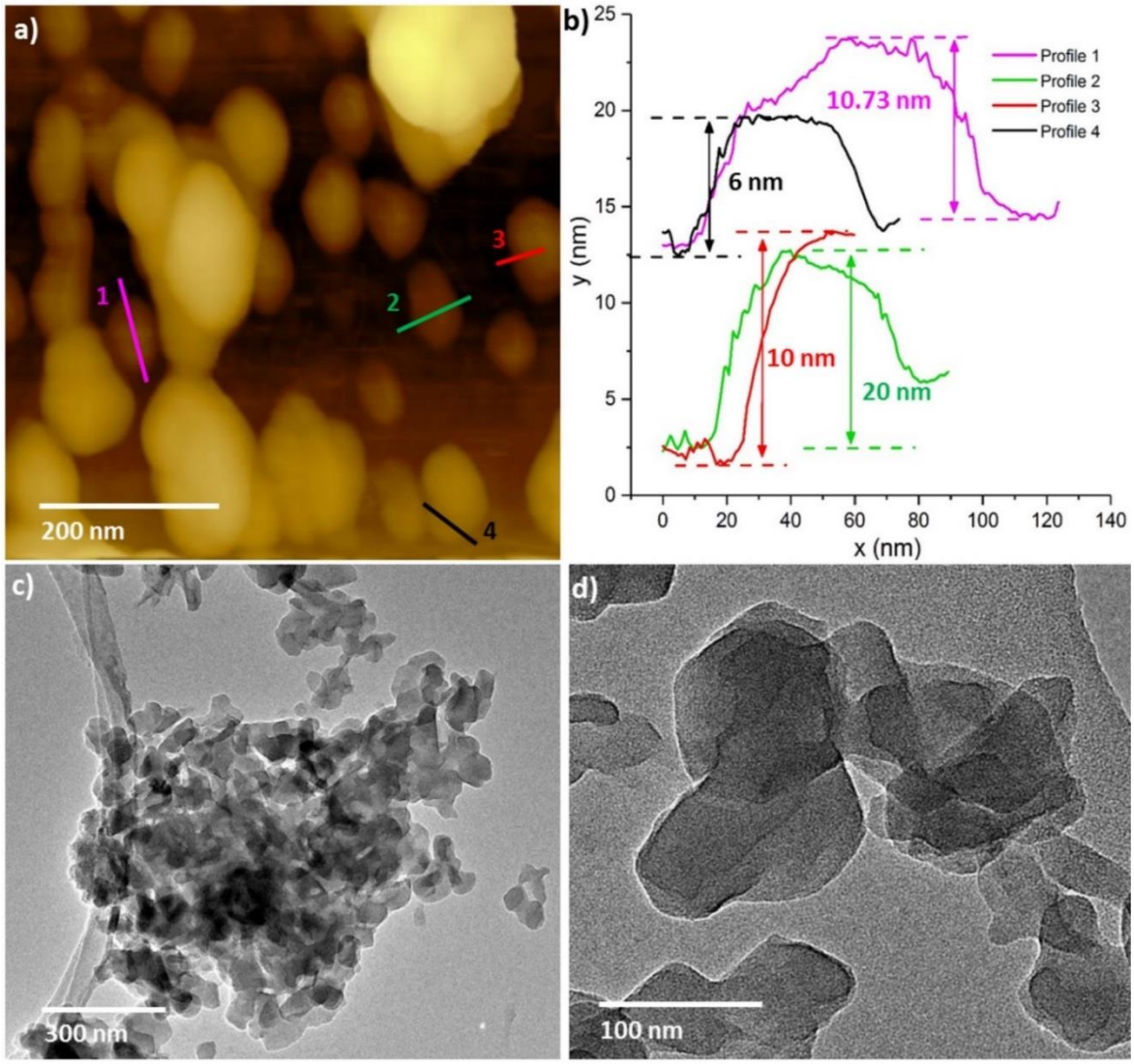

Figure 7.1 (a) AFM topography image of nanoplates of Perylene@ZIF-8. (b) Representative thickness profiles of nanoplates obtained from the AFM image in (a), indicating a typical thickness of the order of ~10s nm. (c) TEM micrograph showing the aggregated nature of the finer scale Perylene@ZIF-8 nanoplates. (d) A higher-magnification TEM image showing the intertwined 2-D microstructural features of the nanoplates.

Figure 7.1 shows the 2-D morphologies of the Perylene@ZIF-8 compound I obtained, where TEM and AFM were applied to characterize the microstructural features of the nanoplates. The lateral size of the nanoplates of Perylene@ZIF-8 varies from ~15 nm to ~150 nm, however, their thickness ranges from ~6 nm to ~20 nm (Figure 7.1a, b, more details in Appendix- Figure A1 and Table A1). The TEM micrographs (Figure 7.1c, d) revealed that, in fact the HCR product consists of an aggregation of intertwining finer scale nanoplates. Notably, the aggregated nanoplates will readily transform into a monolith simply by drying at 90 °C under vacuum for 6 hours (see Chapter 2 for details), which can be attributed to the densification of the intertwined 2-D nanoplates.

Interestingly, I discovered that the optical properties of the monolithic form of Perylene@ZIF-8 and its fine powder counterpart (*viz*. ground monolith), are distinctively different as summarised in Figure 7.2. It can be seen that the monolith material emits a light yellow-green emission, when excited under a 365 nm UV light (Figure 7.2a, b). But grinding of monolith into a fine powder resulted in a blue shift to emit in the lower wavelength. This drastic change in emission behaviour due to mechanical grinding effect has inspired us to investigate the phenomenon in detail. I found that, as depicted in Figure 7.2c, the fine powders experienced a red-shift (442 nm→502 nm) when being mechanically compressed into a pellet utilising a relatively low pressure of less than ~40 MPa. Conversely, I show that by breaking the pellet down into a fine powder produced a blue-shift (502 nm→442 nm) instead, as illustrated in Figure 7.2d.

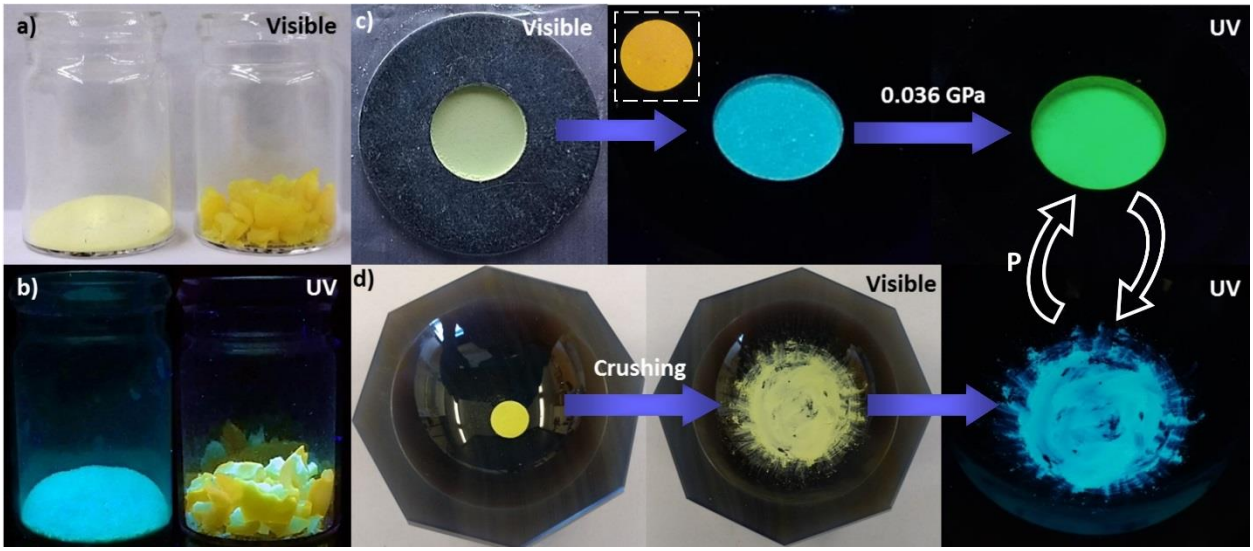

Figure 7.2 (a) Fine powder and monolithic form of Perylene@ZIF-8 seen in the visible light, and (b) their distinctively different emissions observed under the 365 nm UV excitation. (c) Reversible mechanoluminescent behaviour (442 ⇌ 502 nm) of Perylene@ZIF-8: a pale-yellow powder (hand pressed into a metallic mould Ø13 mm) seen under visible light and under 365 nm UV excitation, a red-shift in emission to green 502 nm can be seen upon application of 0.036 GPa pressure. Inset shows the deep-orange emission of a pristine Perylene pellet under UV, for comparison. (d) A dark-yellow pellet observed under visible light, showing the recovery of the light-blue 442 nm emission (under UV) after being crushed to recover a fine powder form.

This effect is reversible upon the application and removal of mechanical forces. In the sections below, I shall interrogate the mechanoluminescent mechanism underpinning Perylene@ZIF-8, using UV-Vis spectroscopy, theoretical band gap calculations, and X-ray diffraction techniques.

7.5 Photophysical Characterisation to Reveal Host-Guest Interactions and Energy Transfer

7.5.1 Absorption Spectroscopy

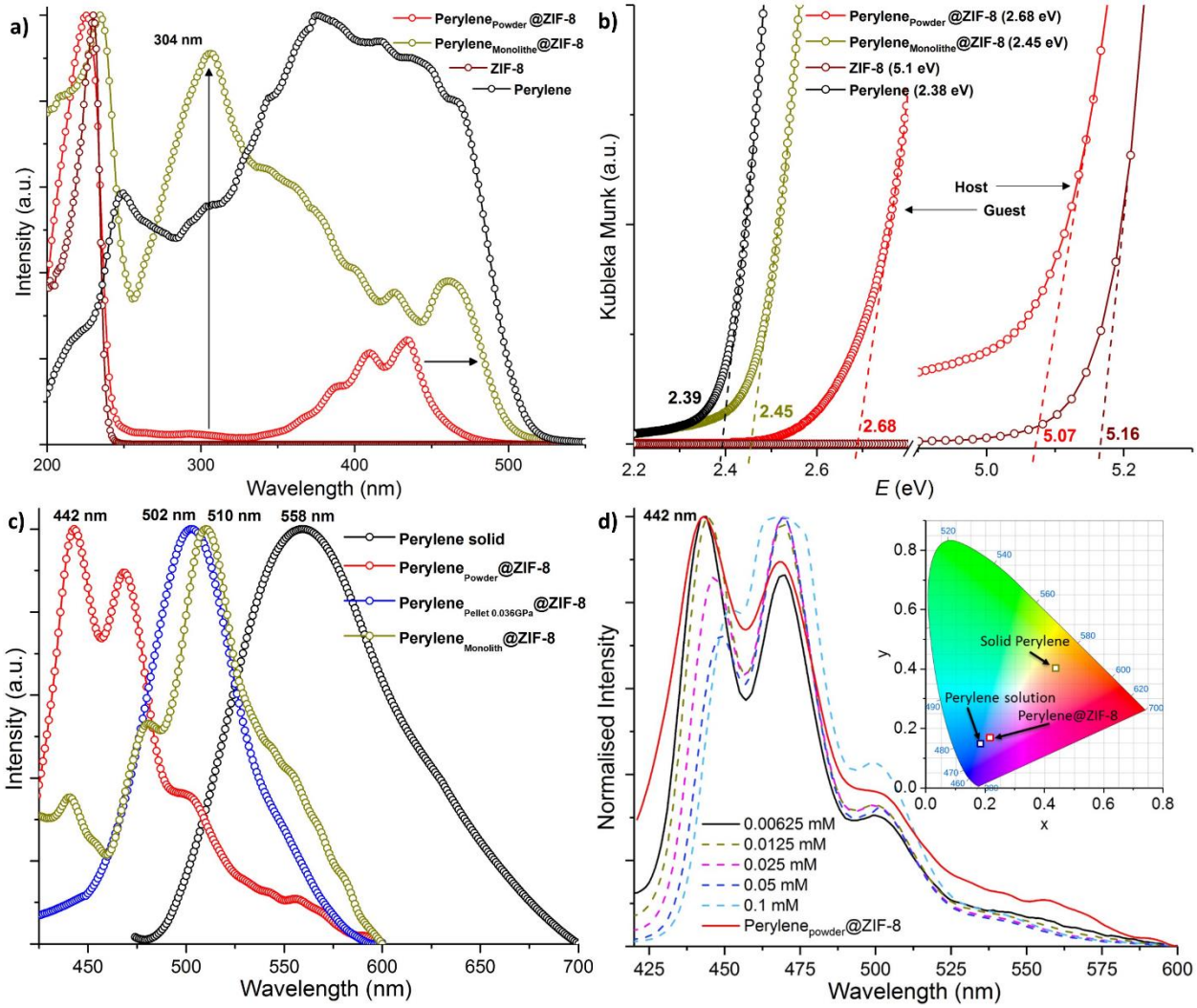

Figure 7.3 (a) Comparison of absorption behaviour obtained from diffuse reflectance of the pristine host (ZIF-8), pristine guest (solid Perylene), and host-guest system (Perylene@ZIF-8). (b) Kubelka-Munk (KM) function for determining the band gaps based on the photon energy intercepts. (c) Fluorescence emission spectra of the pristine Perylene compared with Perylene@ZIF-8 compounds when excited at 365 nm. (d) Emission spectra of different concentrations of Perylene solution (in dichloromethane) and solid-state Perylene$_{powder}$@ZIF-8. Inset: CIE 1931 color chromaticity diagram showing the drastic effect of Perylene confinement within ZIF-8 in solid state, and how this behaviour is resembling the dilution of Perylene solution at a very low concentration of 0.00625 mM.

I performed diffuse reflectance spectroscopy to correlate the mechanoluminescence behaviour to salient changes in the molecular structure of the host-guest assembly. Figure 7.3a shows a broad absorption peak detected between 255-510 nm for the Perylene@ZIF-8 monolith, which is completely absent in the pristine ZIF-8; this result confirms the successful confinement of Perylene (guest) within the spherical voids of ZIF-8 (host). Importantly, the spectra show significant changes observed in the absorption properties of Perylene@ZIF-8, when it was converted from a monolith into powder form (by grinding in mortar). More precisely, the distinct absorption band at 304 nm has experienced a sharp decline in its intensity when the monolith was crushed into a powder form. This finding indicates that the monolith has a pronounced $\pi-\pi^*$ transition because of the densely-packed arrangement of the nanoplate aggregates, which disappears after being converted into a loosely-packed powder form. This notion is further supported by: (i) The disappearance of the broad absorption band associated with the Perylene guest species, which transformed into multiple more well-defined peaks between 380-450 nm when the monolith was crushed into powder. (ii) The absorption peak observed at 225 nm corresponding to the pristine ZIF-8 structure has blue-shifted by ~10 nm when converting the monolith into powders, again signifying a decline in its nominal packing density.

7.5.2 Solution–Like Absorption of Solid Samples

Unlike the absorption spectra of pure Perylene in the solid-state, interestingly I found that spatially confined Perylene has absorption bands akin to the ones observed in the liquid solution.[266] Allendorf *et al*.[102] described the “solution-like” optical properties in the case of

organic linkers in solid-state as a result of isolation in space due to MOF formation. Similar effects are observed in the current host-guest system, but the difference here is that the guest molecules (not linkers) have been isolated in space through 3-D partitioning afforded by the MOF porosity. Weak intermolecular interactions, such as π−π interactions could modify the optical behaviour. Being structurally planar and aromatic in nature, the Perylene molecule may readily establish π−π stacking, therefore a deep-orange emission is observed for the solid Perylene powder (Figure 7.2c inset). Similar effects have been reported in organic molecules due to formation of the J (or H) type of aggregates.[267] Importantly, the ZIF-8 host environment offers tuning of the weak interactions of the confined Perylene guest emitters. In Chapter 5, I have described the ability of ZIF-8 for making weak interactions *via* the 2-methylimidazole (mIm) linkers.[139] Likewise, in this case the confined Perylene molecules could establish CH−π and/or π−π interactions with the adjacent imidazole rings. In fact, the resultant broad emission band of the monolith from 430 nm to 600 nm (Figure 7.3c) can be explained by the presence of weak host-guest interactions elucidated above.

7.5.3 Effect on Band Gap

Direct evidence of intermolecular weak interactions was witnessed from modifications to the band gap values, determined from the diffuse reflectance data. Figure 7.3b shows how the band gap increases from the monolith (2.45 eV) to a fine powder (2.68 eV). Electronic properties of the host framework (ZIF-8) was found to be affected by guest confinement, with its band gap decreasing from 5.16 eV to 5.07 eV. Conversely, the band gap of the Perylene guest molecule has increased due to spatial confinement, compared

to that of a pure Perylene solid. Figure 7.4 presents the theoretical band gap calculations confirming this outcome, where the calculated band gap of Perylene was found to rise from 1.313 eV to 1.793 eV when it is positioned in a confined pore environment. However, the calculated band gap of the distorted ZIF-8 host was found to be relatively lower (4.361 eV) compared with that of a cubic ZIF-8 structure (5.204 eV). A good qualitative agreement in terms of band gap values can be seen, between the experiments and theoretical trends associated with host-guest confinement effects. These new results illustrate the potential of accomplishing band gap engineering exploiting the Guest@MOF confinement strategy.

7.5.4 Solution-Like Emission

From the photograph of the monoliths in Figure 7.2b, interestingly one may observe that there are different regions displaying light green to dark yellow emissions when subjected to UV excitation. The edges of the monolith mainly emit a lighter green-blue colour which can be assigned to the emission of ‘loosely packed’ nanoplates of Perylene@ZIF-8; while a darker yellow-green emission can be assigned to regions containing ‘densely packed’ nanoplates. These varying color characteristics are detectable in the emission spectrum of the monolith shown in Figure 7.3c, corresponding to the spectral hump and shoulder located at 440 nm and 479 nm, respectively. I reasoned that additional small humps observed at, for instance 543, 554, 568 and 581 nm, could arise due to entrapped Perylene molecules between the aggregation of 2-D nanoplates (but not within ZIF-8 pores). Surprisingly, the maximum emission observed at 510 nm in the case of monolithic Perylene@ZIF-8 could not be attained by the reconstituted fine powders (mechanically

compressed into a pellet). Instead, an emission spectrum with only a single feature, λ_{max} = 502 nm, was observed for the pellet of Perylene@ZIF-8 pressed under 0.036 GPa. Like absorption, fluorescence of the finely ground powder obtained from the monolithic Perylene@ZIF-8 also shows a solution-like emission behaviour. Indeed, I have confirmed this phenomenon in Figure 7.3d, in which the emission spectra of different concentrations of Perylene solutions in dichloromethane revealed that the aggregation of molecules in a solution state causes merging of peaks at around 450 nm, but upon dilution the merged peaks became more and more separated to eventually give a maximum emission at 442 nm. This is in good agreement with the solid-state spectra of $Perylene_{powder}$@ZIF-8. Particularly, the heavily diluted Perylene with a concentration of 0.00625 mM shows less influence from its neighboring molecules, which is precisely the “solution-like” effect observed in the solid-state when the Perylene molecules have been spatially separated through nanoconfinement within the ZIF-8 host framework. Figure 7.3d clearly shows the transition of emission behaviour of concentrated and diluted solutions and how it finally overlaps (at 442 nm) with the solid-state emission spectrum of $Perylene_{powder}$@ZIF-8.

In Figure 7.3c, emission of the reconstituted pellet at 502 nm suggests that the dense packing achieved in the original monolith (obtained from drying a wet sample post synthesis), cannot be fully recovered upon strain relaxation after being ground into a powder form. Therefore, the emission of monolith observed at a relatively higher wavelength of 510 nm, can be attributed to the greater charge transfer between densely aggregated nanoplates. I propose a mechanism behind the mechanoluminescence of Perylene@ZIF-8 nanoplates, as illustrated in Figure 7.5. It is reasonable to expect some microscopic sized voids to be present between the randomly-oriented nanoplates in

powder form (Figure 7.5a). After application of an external pressure during the pelletisation process its packing will improve, offering better inter-nanoplate interaction to enhance electronic charge delocalisation between the adjacent nanoplates (Figure 7.5b), facilitated by the electron-rich Perylene guest entrapped in the pores of the sodalite cages of the ZIF-8 host.

7.5.5 Theoretical Calculations to Gain Insights of Optical Properties

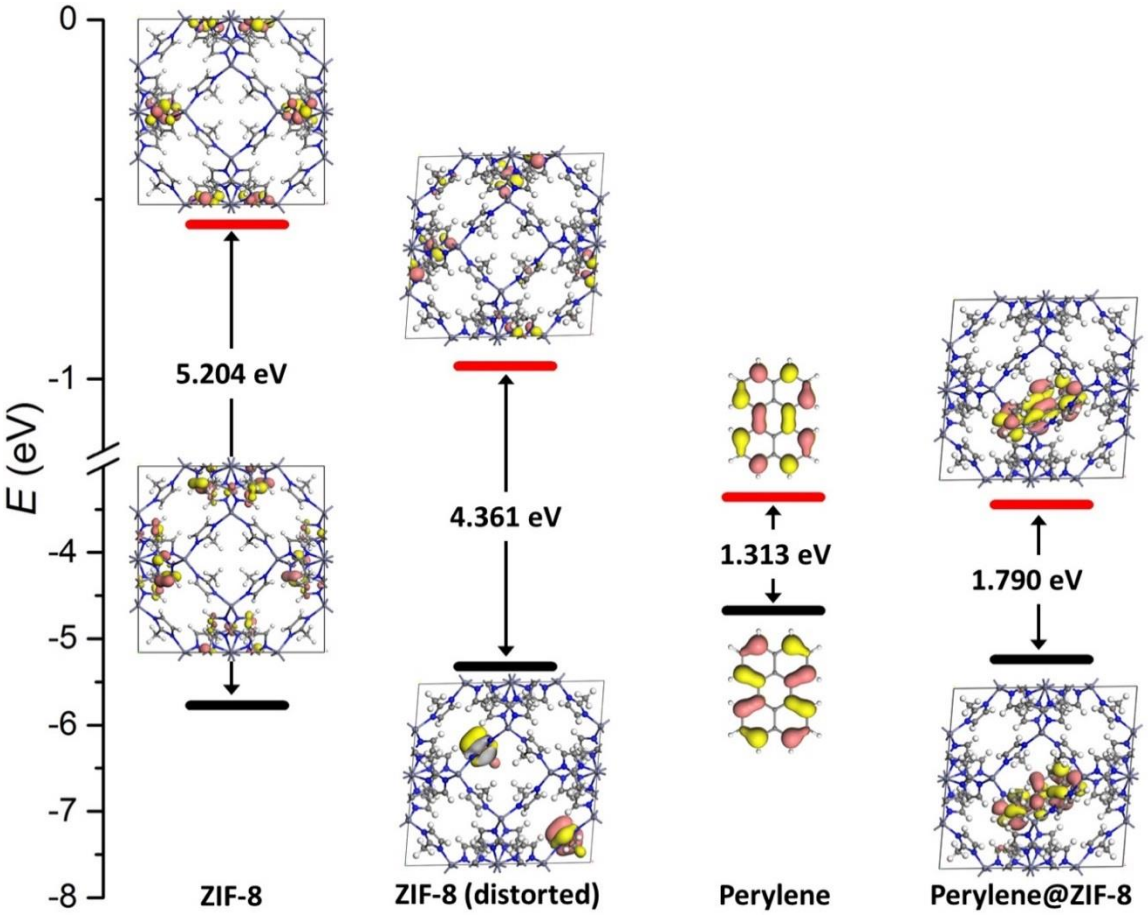

Figure 7.4 Effect of host-guest confinement on the band gap values of Perylene was calculated theoretically, which followed the trends observed experimentally in Figure 7.3b Symbols used: HOMO (black) − LUMO (red) for the energy levels; dark pink and yellow iso-surfaces representing the positive and negative charges of the molecular orbitals.

The modification of the electronic structure of the host-guest assembly is presented in Figure 7.4, calculated using DFT. Theoretical band gap energy levels give additional insights into the plausible energy transfer pathway, from the LUMO (lowest unoccupied molecular orbital) of ZIF-8 to the LUMO of Perylene upon photoexcitation. The HOMO (highest unoccupied molecular orbital) hybrid orbitals of Perylene@ZIF-8 show an electronic distribution that is highly localised on the Perylene molecules, with limited sharing with the C=C bonds in the imidazole moiety of the ZIF-8 host. The LUMO of Perylene@ZIF-8 is exclusively occupied by the Perylene molecule, indicating the propensity for energy transfer between the hybrid orbitals of the host-guest assembly and the guest species confined within. The role of the flexible nature of ZIF-8 framework can be seen in the reduction of band gap energy (~1 eV) upon shear distortion of the host structure,[193] which is again important in the context of host-guest assembly for establishing intermolecular interactions upon application of external pressure. It is well documented in literature that planarity of molecules will contribute to the reduction of band gaps by facilitating conjugation of adjacent molecules.[12] On this basis I suggest that, under pressure or mechanical stress the elasticity of ZIF-8[193] permits better planarity to be established between the local intermolecular alignment of mIm▪▪▪Perylene, yielding the “molecular wire effect”[268] (Figure 7.5b) that could account for the red shifts being observed in the absorption and emission spectra (Figure 7.3). However, apart from this possible mechanism another possibility that could also occur is discussed in section 7.6.2.

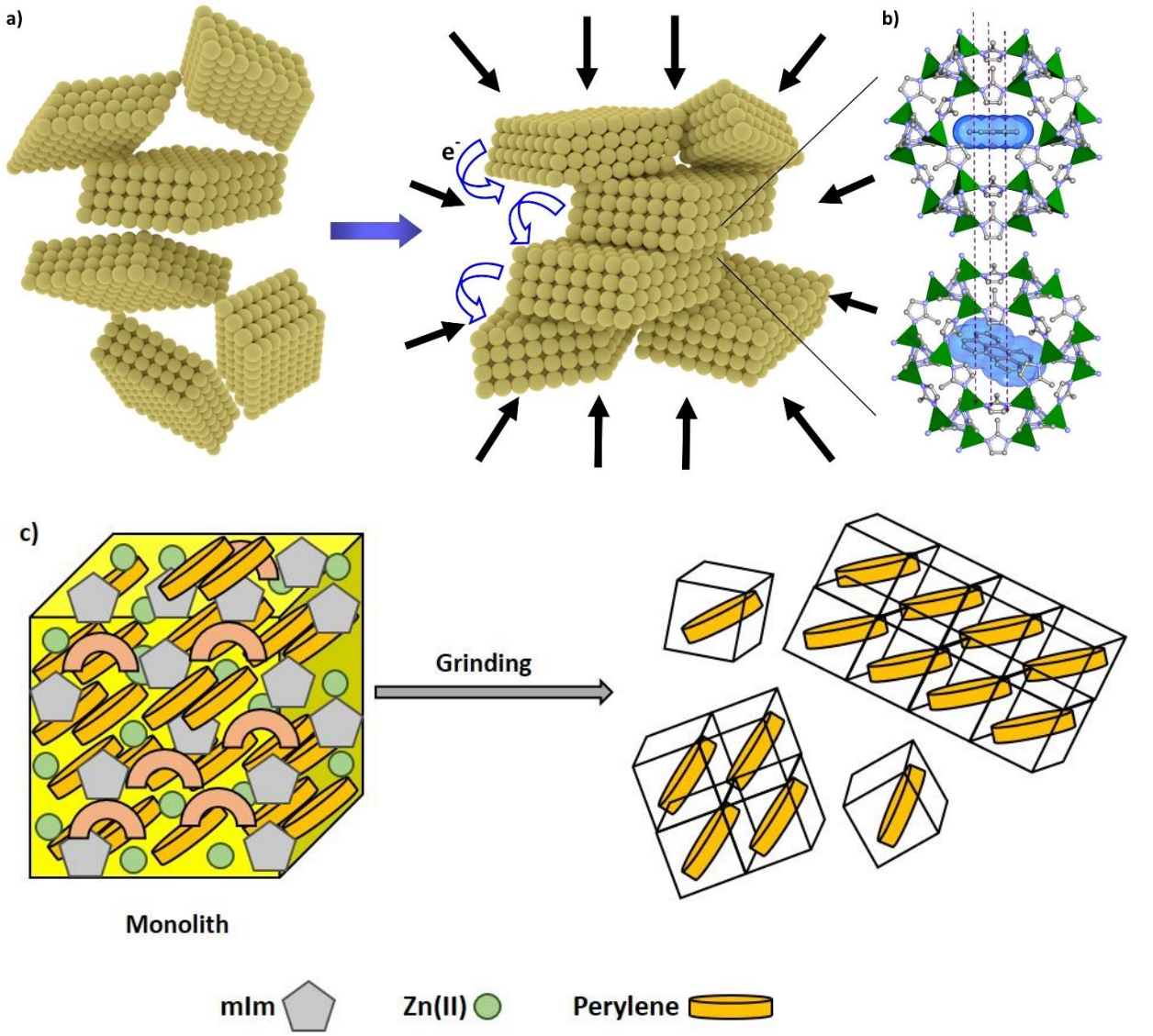

Figure 7.5 Schematic representing a) the randomly oriented nanoplates of Perylene@ZIF-8, with air gaps present in the powder form due to its loosely-packed configuration. Upon compaction by an externally applied hydrostatic pressure, the nanoplates rearrange themselves to become more densely aggregated together. b) Proposed energy transfer pathway of two adjacent nanoplates attributed to the "molecular wire effect", facilitated by the π−π interactions connecting the mIm▪▪▪Perylene▪▪▪mIm molecular pathways. c) Second possible mechanism that could occur due to grinding step, where grinding of monolithic sample can trigger the formation of ZIF-8 simultaneously separating and encapsulating Perylene molecules.

7.6 Structural Evolution as a Function of Compressive Stress

7.6.1 Structural Changes in Host Framework: Pawley Refinement

X-ray diffraction (XRD) technique was used to characterise structural changes in the ZIF-8 host. It can be seen in Figure 7.6a that, the XRD pattern of Perylene@ZIF-8 monolith showed its crystalline nature, but with the presence of relatively broad peaks. Upon grinding of the monolith for ~5 minutes (*via* mortar and pestle) to yield a 'powder' sample, sharper Bragg peaks were detected that are coinciding with the simulated pattern of the ideal ZIF-8 structure. However, in addition to all the matching primary peaks, the splitting and broadening of peaks were observed suggesting the reduction of ZIF-8's cubic cell symmetry.

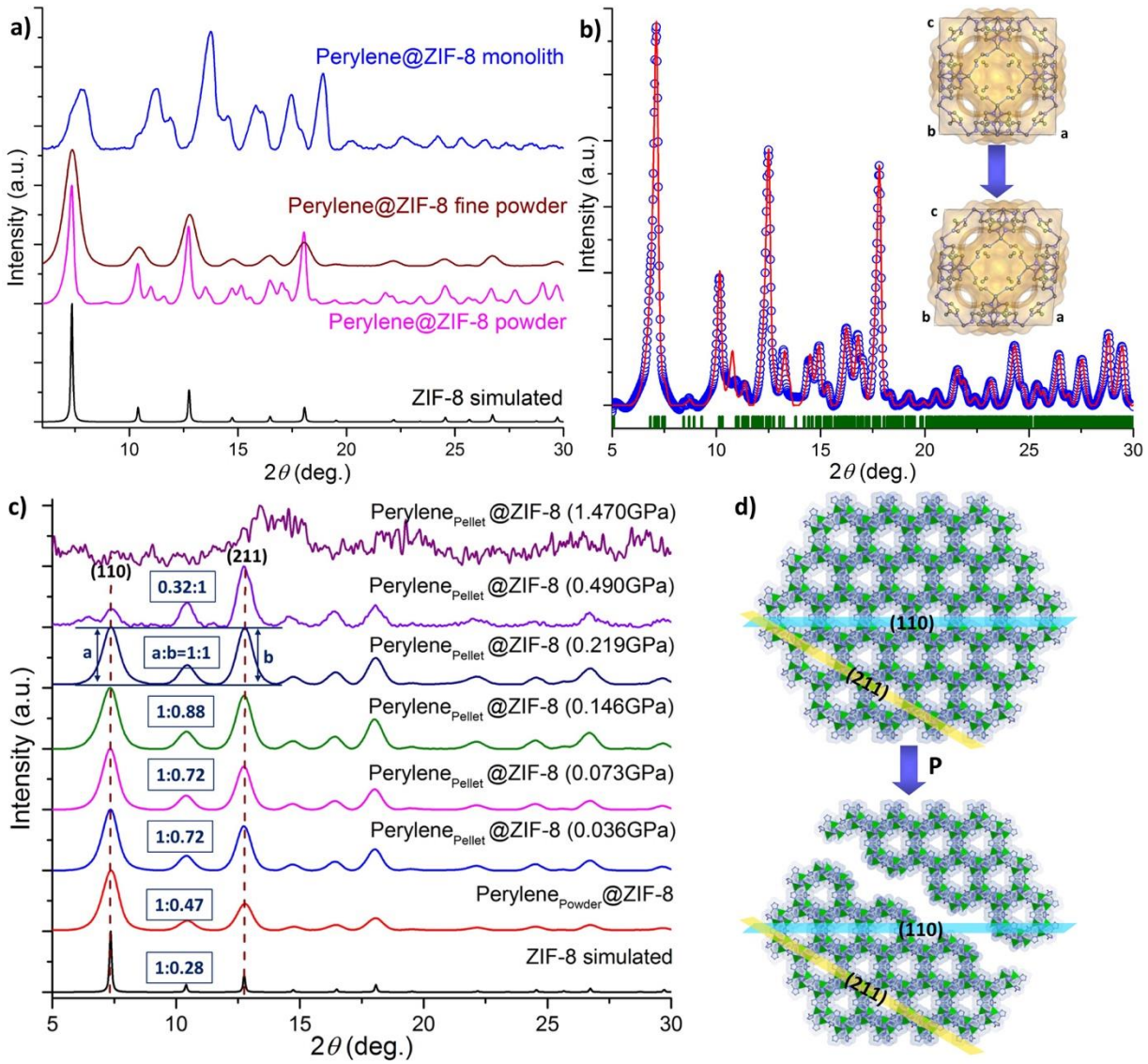

Figure 7.6 (a) Comparison of the XRD patterns of the monolithic, powder (~5 min grinding in mortar), and fine powder forms (~20 min grinding) of Perylene@ZIF-8. (b) Pawley structural refinement (R_{wp} = 8.2%) of an X-ray diffraction pattern of a powder sample of Perylene@ZIF-8. Symbols used: blue circles are experimental data; red line is the calculated pattern; green bars representing the observed Bragg reflections. The inset shows the structural distortions of ZIF-8 viewed along the *b*-axis. (c) Systematic XRD study to monitor changes in relative peak intensities of the {110}- and {211}-oriented crystallographic planes upon compression of the fine powdered Perylene@ZIF-8 sample using different pressures. (d) Proposed structural fracture mechanism endorsed by XRD data, suggesting the cleavage of Perylene@ZIF-8 nanoplates across the {211} planes due to shearing deformation attributed to compressive stress, eventually causing amorphisation of the compound at ~1.5 GPa.

Hence, I performed Pawley structure refinement on the experimental powder data, to establish the precise changes to the cell parameters of the host. The results in Figure 7.6b revealed that: $a = b = c = 16.992$ Å of the pristine ZIF-8 have increased to $a = 17.339$ Å, $b = 17.127$ Å, $c = 17.072$ Å, whereas, $\alpha = \beta = \gamma = 90°$ of its cubic cell have deformed to $\alpha = 87.073°$, $\beta = 90.321°$, and $\gamma = 84.677°$ (see details in Table A4 in Appendix). The cell expansion of the host framework can be attributed to the spatial confinement of the bulky Perylene guest molecules in the pore of ZIF-8. This is accompanied by reduction in the α and γ angles, which can be explained by shear deformation[193] (inset of Figure 7.6b) of the 2-D nanoplate morphology from aggregation-induced mechanical strains.

7.6.2 Grinding Effects on Structure Using Powder X-Ray Diffraction

Grinding (*via* mortar and pestle) of the Perylene@ZIF-8 'powder' for a further ~15-20 minutes yielded a 'fine powder' sample, exhibiting broadened Bragg peaks evidenced in Figure 7.6a. Here, the disappearance of peak splitting can be ascribed to the relaxation of strains in the aggregated nanoplates, while peak broadening observed is indicative of the formation of finer scale particles by crushing larger aggregates. To test the effect of grinding on emission, I have compared the emission spectra of samples ground for 5-minute (powder) vs. 20-minute (fine powder), but detected no further changes. Another possible molecular arrangement that could occur will be the actual ZIF-8 formation from the constituent elements present in the monolith upon grinding. During the grinding process non-confined or aggregated Peryelene molecules would be expected to separate from each other by ZIF-8 framework walls of each void. The emission arising from ground powder will be the blue emission from individual Perylene molecules separated from other

peryelene molecules, which otherwise will exhibit green yellow emission in aggregated form as seen from monolith form.

7.6.3 Pressure Effects on Structure Using Powder X-Ray Diffraction

To further investigate the ability of the reconstituted Perylene@ZIF-8 fine powder to exhibit red shift beyond 502 nm, I systematically prepared a series of pellets using an increasing pressure and monitored their structural evolution by XRD (Figure 7.6c) and emission spectroscopy. I found that the emission of the reconstituted pellets stayed unchanged at 502 nm, for all pellets prepared from as low as 0.036 GPa to a maximum stress of 1.47 GPa. Results above support the notion that the aggregated nanoplates in the monolithic form are very tightly packed together (yielding emission 510 nm), which cannot be regained in the reconstituted powder pellets (less dense, thus, lower emission at 502 nm).

Detailed analysis of the relative peak intensities from XRD data of different pellets made with ascending pressures can give us a deeper insight into structural changes of the material. Figure 7.6c shows a decreasing trend in the intensity of the (110) plane, accompanied by a gradual increase in the intensity of the (211) plane. The ratios of the changing relative peak intensities of (110):(211) planes are summarised in Figure 6c, where the initial ratio rises from 1:0.47 for a ground fine powder sample to attain 1:1 for the pellet pressurised at 0.219 GPa. Then by more than doubling the pelleting pressure to 0.49 GPa, a ratio of 0.32:1 was obtained alongside the appearance of extra diffraction peaks. Eventually at a significantly higher pressure of 1.47 GPa, this led to the disappearance of all the Bragg peaks associated with ZIF-8 because of framework amorphisation.[269] Figure 6d illustrates the proposed fracture mode of ZIF-8 that can

account for such a phenomenon, in which the cleavage planes oriented along the {211} facets rupturing by shear stresses. In fact, this failure mechanism is reminiscent to that reported for ZIF-8 subject to a high-rate impact mechanical deformation, which also led to formation of the preferred {211}-oriented planes.[270]

Significantly, all the pellets described above showed reversible mechanoluminescence behaviour. Surprisingly, the amorphised sample prepared at 1.47 GPa remains mechanoluminescent by retaining its emission at 502 nm; this finding is suggesting that the spatial confinement of Perylene within the pores of ZIF-8 remains effective despite the host framework losing its long-range periodicity *via* amorphisation.

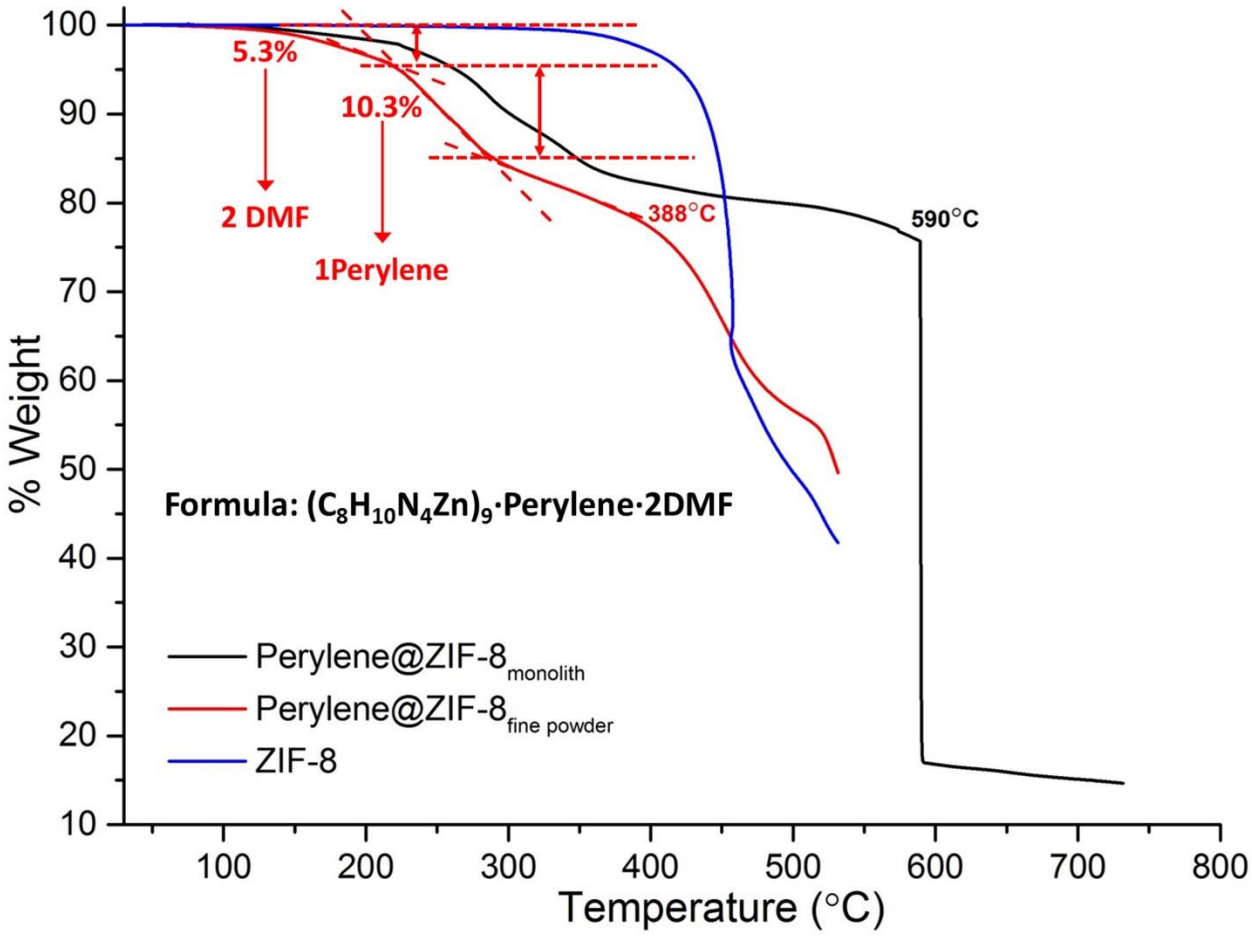

Figure 7.7 TGA of Perylene@ZIF-8 compound revealing its probable formula. Higher thermal stability of monolithic Perylene@ZIF-8 can be seen from the figure compared to the pristine ZIF-8 or powdered Perylene@ZIF-8 compound. Sharp decomposition at 590°C of the monolithic compound and higher thermal stability suggest dense packing of nanoplates of Perylene@ZIF-8 could enhance thermomechanical stability compared with the pristine ZIF-8 host.

Finally, thermogravimetric analysis (TGA) of the Perylene@ZIF-8 powder indicated that the thermal stability of the monolithic form is higher than its powder form by ~200°C (Figure 7.7). This finding is in support of denser arrangement of nanoplates in monolithic form possessing a greater thermal stability than its fine powder form.

7.7 Summary

In summary, I have shed new light on the use of orderly-arranged voids conferred by MOF compounds acting as 3-D nanoscale scaffolding, to spatially isolate emissive guest molecules for accomplishing a unique “solution-like” luminescent behaviour. In our materials design, I have employed an optically-inactive MOF host (sodalite cage of ZIF-8) for the spatial confinement of a bulky polycyclic fluorophore guest (Perylene), resulting in a novel Guest@MOF system — Perylene@ZIF-8 — with switchable emission properties (442 ⇌ 502 nm) when subject to a reversible mechanical stress or hydrostatic pressure. I have harnessed the high-concentration reaction (HCR) synthetic strategy for morphology control, yielding nanoplates of an inherently 3-D ZIF-8 structure co-assembled with the Perylene guests. Remarkably, such nanoscale 2-D configuration permits facile aggregation and separation of Perylene@ZIF-8 nanoplates under stress (~10s MPa), which is responsible for the reversible mechanoluminescence phenomenon being reported in this Chapter.

Chapter Eight

Mechano-Stimulus ZIF-8 gel: Promising Way for Development of Other Functional Materials

8.1 Background

In this chapter, I will show that HCR synthetic approach can be extended to hybrid molecular systems to obtain new smart SupraMOF materials. Here details of SupraMOF possessing reversible sol-gel transition will be described and supported with detailed rheological measurements.

8.2 Mechano-Stimulus Responsive SupraMOF

8.2.1 Rapid One Step Synthesis

Figure 8.1 Photograph showing tube inversion test for SupraMOF gel material containing ZIF-8.

The ZIF-8 supraMOF (Figure 8.1) was synthesised by adopting the 'high concentration reaction' (HCR) approach.[134] It involves high concentrations of mIm and $Zn(NO_3)_2$ (see Table 8.1, reaction A); but prior to mixing the mIm organic linkers to the Zn(II) metal ion solution, the former was first to be deprotonated by taking an equivalent molar concentration of trimethylamine base (NEt_3). Upon combining the above solution reactants, I observed that a white phase containing fibre-like morphologies formed immediately, which quickly converted into a gel phase within a few seconds. Sonication for a further 5 seconds resulted in the formation of a mechanically stable gel phase. After sonication, the sample container was inverted to test for gelation (by inversion test), and I found that similar to the conventional low-molecular-weight gels (LMWG),[32] this gel material can resist gravity by refusing to flow downwards.

8.2.2 Rapid Sol-Gel Conversion

Interestingly, this candidate of ZIF-8 supraMOF exhibited rapid sol-gel phase transition upon application of an external mechanical stimulus (stress).

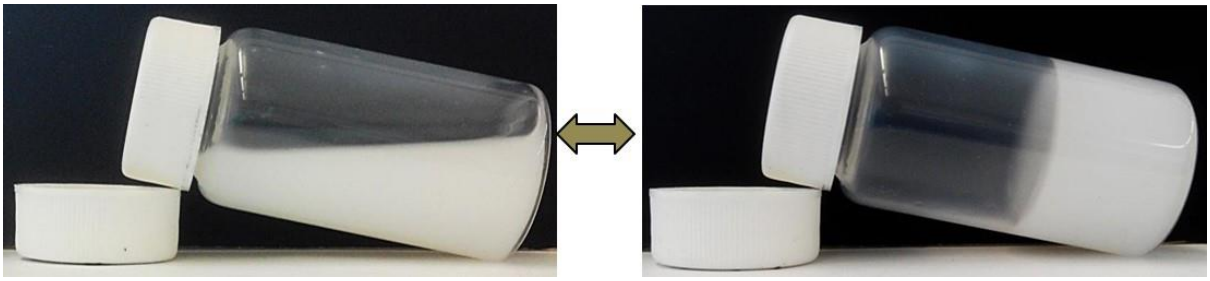

Figure 8.2 Photos show reversible sol-gel conversion of SupraMOF material containing ZIF-8.

Vigorous shaking of the sealed glass vial containing the gel material quickly transformed it into a sol phase, which could easily revert back to a stable gel phase simply by allowing the sol unperturbed for about 5 seconds (Figure 8.2). The real-time sol ⇌ gel recovery can be seen in the video clip[271], which demonstrates fast phase reversibility in a matter of seconds.

8.3 Rheological Studies

8.3.1 Frequency Sweep Measurements

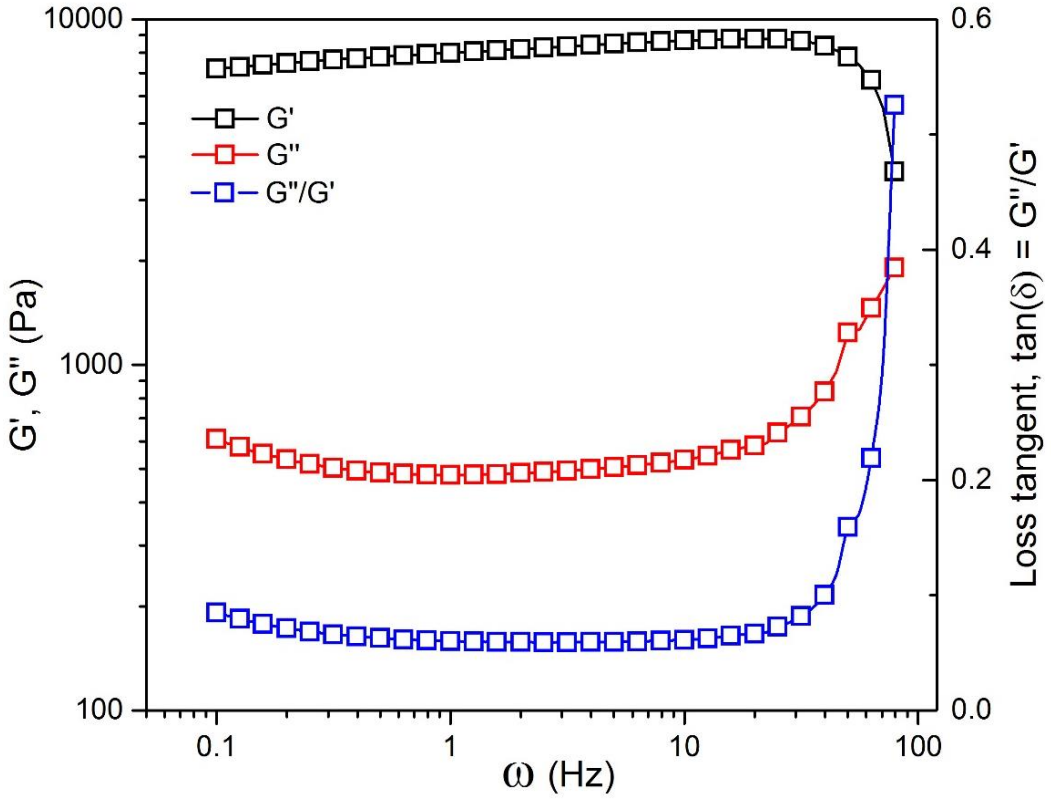

Figure 8.3 Oscillatory frequency-sweep rheological experiments for the ZIF-8 based supraMOF gel tested under a constant applied shear strain of 0.1%. *G'* and *G"* are the storage and loss moduli, respectively. Loss tangent, tan(δ) = *G"/G'* data indicating a phase change at above ~30 Hz.

To gain detailed insights into gel stability and sol-gel conversion phenomenon, dynamic rheological measurements were performed using controlled parameters as shown in

Figure 8.3. It can be seen in Figure 8.3 that oscillatory frequency sweep between 0.1 Hz to 100 Hz showed a relatively steady behaviour for the storage modulus (*G'*) and loss modulus (*G"*), without any strong dependence on the frequency until beyond ~30 Hz. After which, the magnitude of *G'* suddenly fell while *G"* began to increase, this behaviour signifies the collapse of an integrated network of the gel phase. Likewise, the distinct rise of the loss tangent ($\tan(\delta) = G''/G'$) versus frequency data above ~30 Hz is evident of an occurrence of the gel-to-sol phase transformation. *G'* is an order of magnitude higher than *G"*, indicating that the ZIF-8 supraMOF can be considered as a stable gel material unperturbed. Figure 8.4 shows the dynamic strain sweep measurements performed from 0.1 to 100% strain at 0.1 Hz, to characterise the stability of the gel against phase change under an incremental shear strain. Horizontal profiles of *G'* and *G"* between 0.1 to ~2% shear strain was found to start becoming strain dependent with an increase in strain. The *G'* and *G"* profiles coincided at ~4%, marking the yield point of the gel (more details in Figure A2 in Appendix). Subsequently, the magnitude of *G"* became much greater than *G'* for between shear strains of ~5 and 100%, clearly this meant that energy dissipation has exceeded energy storage because the stable gel phase has collapsed into a sol suspension (see Figure 8.4).

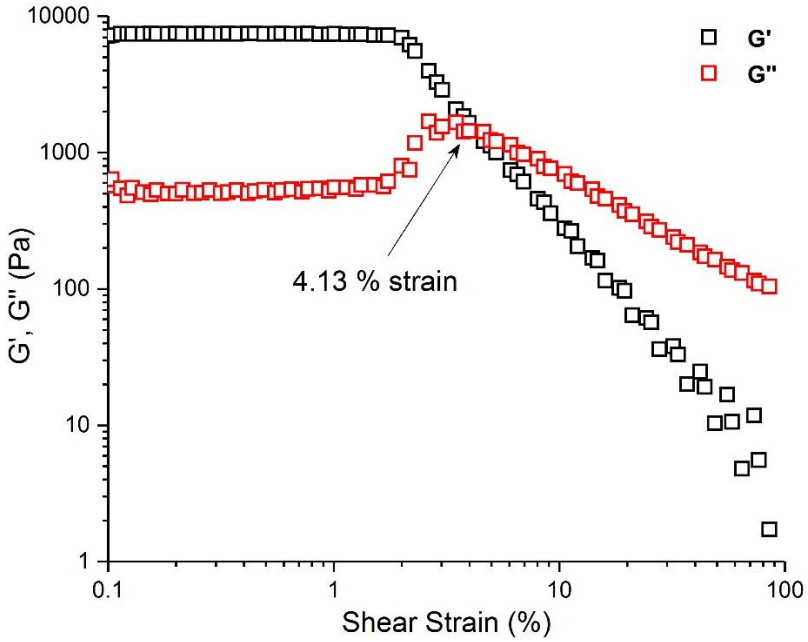

Figure 8.4 Dynamic strain sweep measurement established the yield point at ~4%, at which the gel converts to sol.

8.3.2 Sol-gel conversion: cyclic dynamic strain sweep measurements

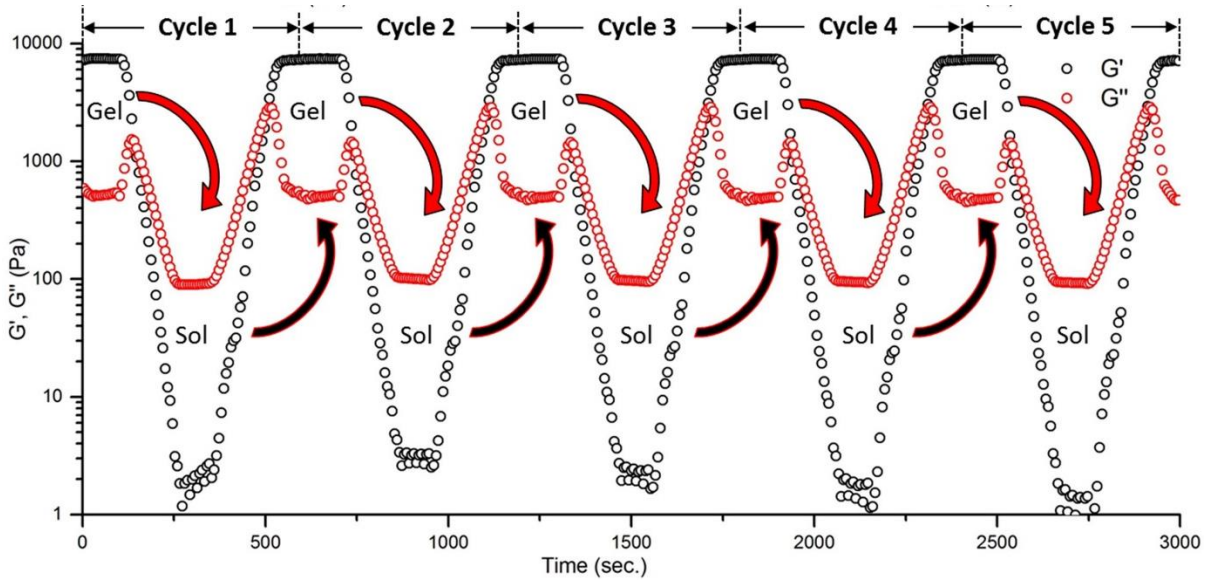

Figure 8.5 Mechano-stimulus response of the ZIF-8 supraMOF material tested by performing a cyclic dynamic strain-sweep experiment (consecutive 5 cycles are shown), demonstrating its capability to transform reversibly between gel ⇌ sol with highly reproducible mechanical properties.

By imposing a cyclic (load-unload) mechanical stimulus, I have characterised the phase reversibility of the ZIF-8 supraMOF material as shown in Figure 8.5, so as to establish its thixotropic nature under a cyclic shear strain set between 0.1% ⇌ 100%. I found that the results in Figure 8.4 are in fact reversible, that is upon removal of shear strain from 100% to 0.1% the sol recovered to the gel form evidenced by *G'>G"* (storage>loss).

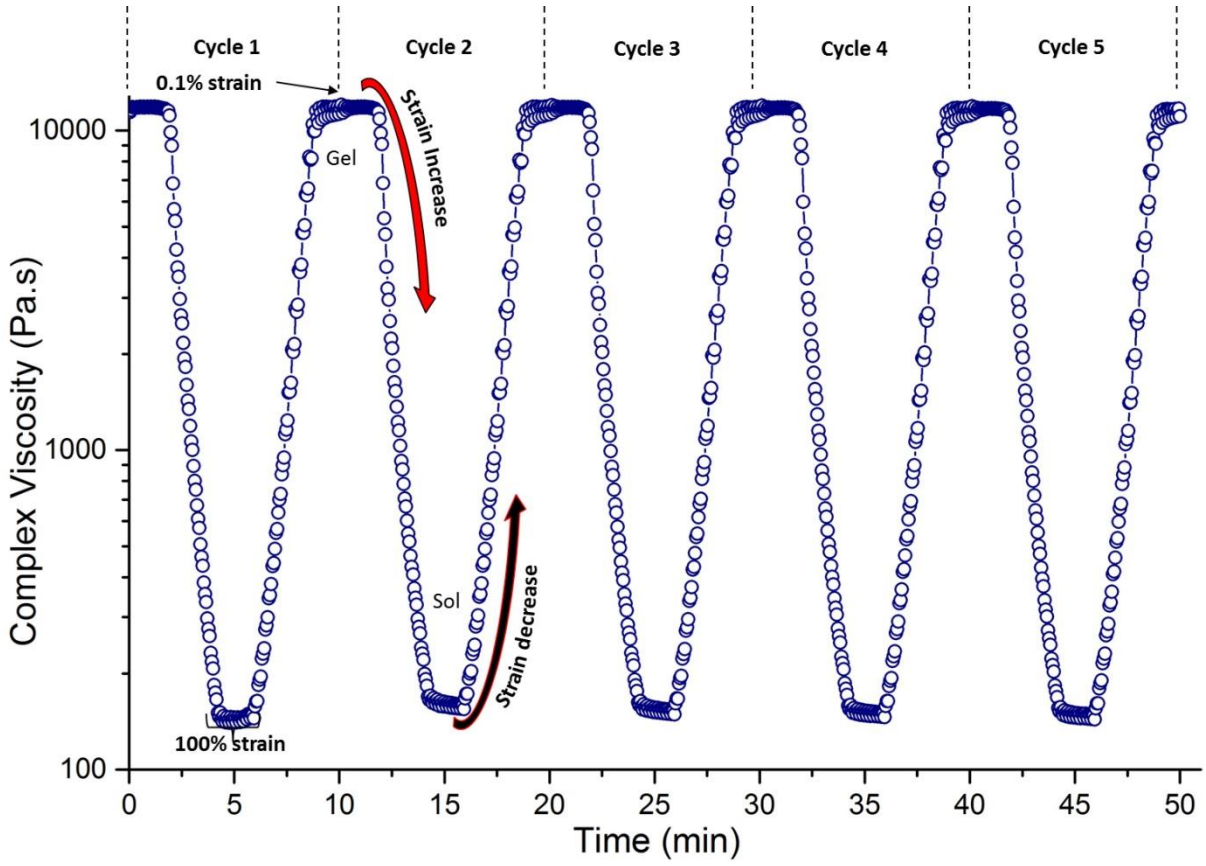

Figure 8.6 Complex viscosity measurement of ZIF-8 supraMOF gel sample for consecutive five cycles with dynamic strain sweep between a shear strain of 0.1% to 100%. Removal of strain recovers viscosity of gel sample confirming the reversible phase change of material switching between the sol ⇌ gel phases under cyclic mechanical deformation. Each cycle consists of: 250 sec from 0.1% to 100% strain causing gel → sol, hold for 100 sec, 250 sec from 100% to 0.1% strain causing sol → gel, hold for 100 sec, and then repeat.

Such gel ⇌ sol reversibility tests were performed for multiple consecutive cycles, for example, shown in Figure 8.5 are data representing the profiles obtained by allowing 150 seconds for the recovery of gel from a collapsed sol phase. Furthermore, the cyclic stress experiments revealed precisely how the complex viscosity can be very reversibly tuned, over a wide range of 10^2 - 10^4 Pa·s as effected by the recoverable sol-gel transformations (Figure 8.6).

8.4 Reasons behind Smart Response

8.4.1 Material Morphology

To study the origin of the mechano-responsive behaviour, I carried out a systematic materials characterisation study to correlate the observed property with its underlying material structure. Gel sample prepared on a piece of glass substrate by layering a thin layer of material was imaged under the scanning electron microscope (SEM) to characterise its microstructure. The SEM micrographs obtained are shown in Figure 8.7, where the gel material forms what appeared to be densely packed and continuous sheet-like phase, very unlike the typical fibrous network[131, 272] found in conventional gel materials.

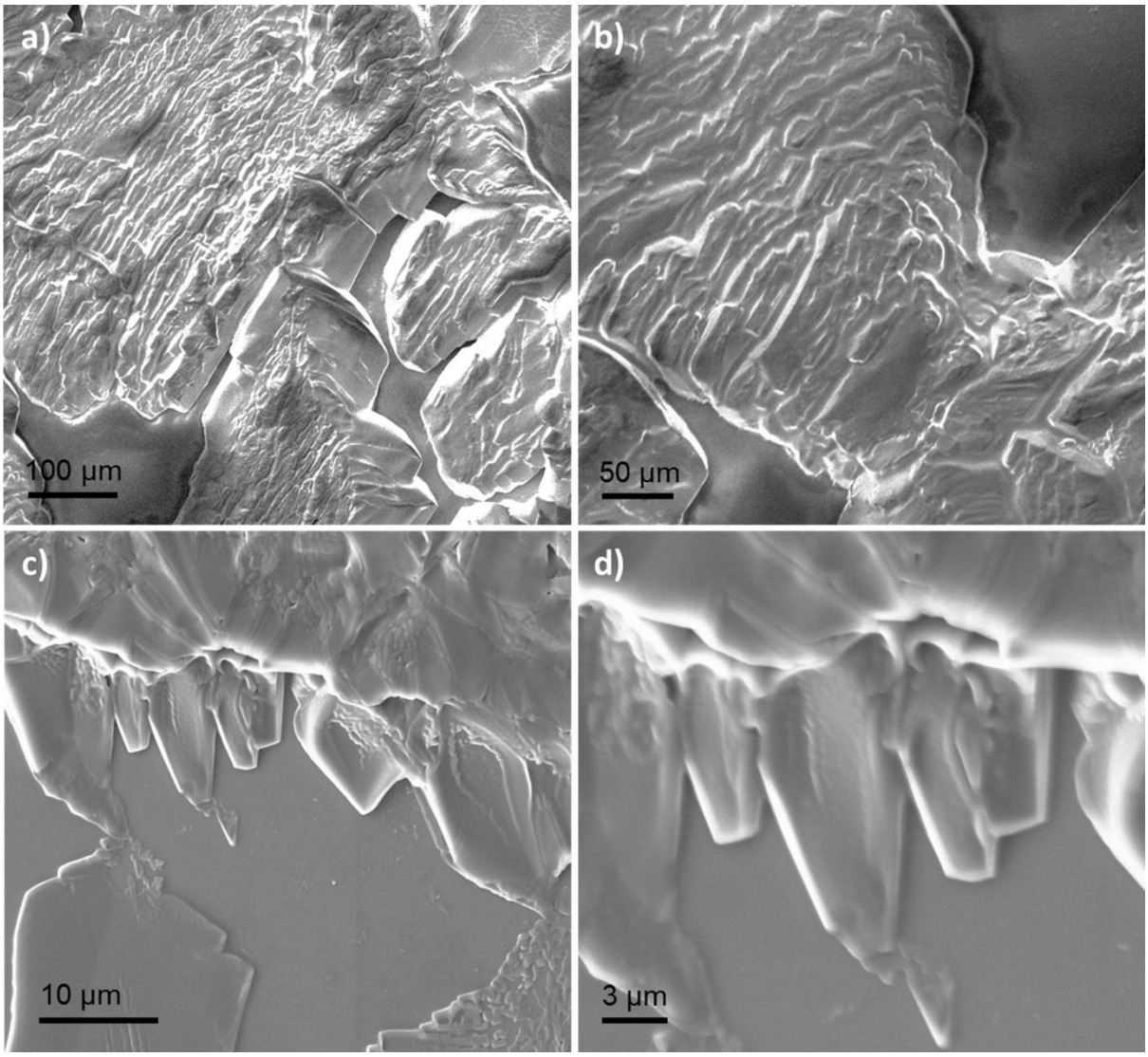

Figure 8.7 SEM images of the supraMOF gel sample coated onto glass substrates.

8.4.2 Inner Constituents of Gel: Nanoplates of Hybrid Framework Compound

To further understand the supraMOF gel constitution, I used copious amounts of DMF and methanol to break down (disintegrate) the gel phase, liberating an abundance of 'fine particles' that were then isolated by centrifugation (8000 rpm). Surprisingly, transmission electron microscopy (TEM) revealed that, the isolated particles are resembling the two-dimensional (2D) morphologies of nanoplates (Figure 8.8a,b). I confirmed the nanoplate

geometry *via* atomic force microscopy (AFM) as presented in Figure 8.8(c-d), where the averaged nanoplate thickness was found to be of the order of 10s nm and with an aspect ratio (i.e. width/thickness) of at least ~5 (more details in Appendix- see Figure A3-7 and Table A2).

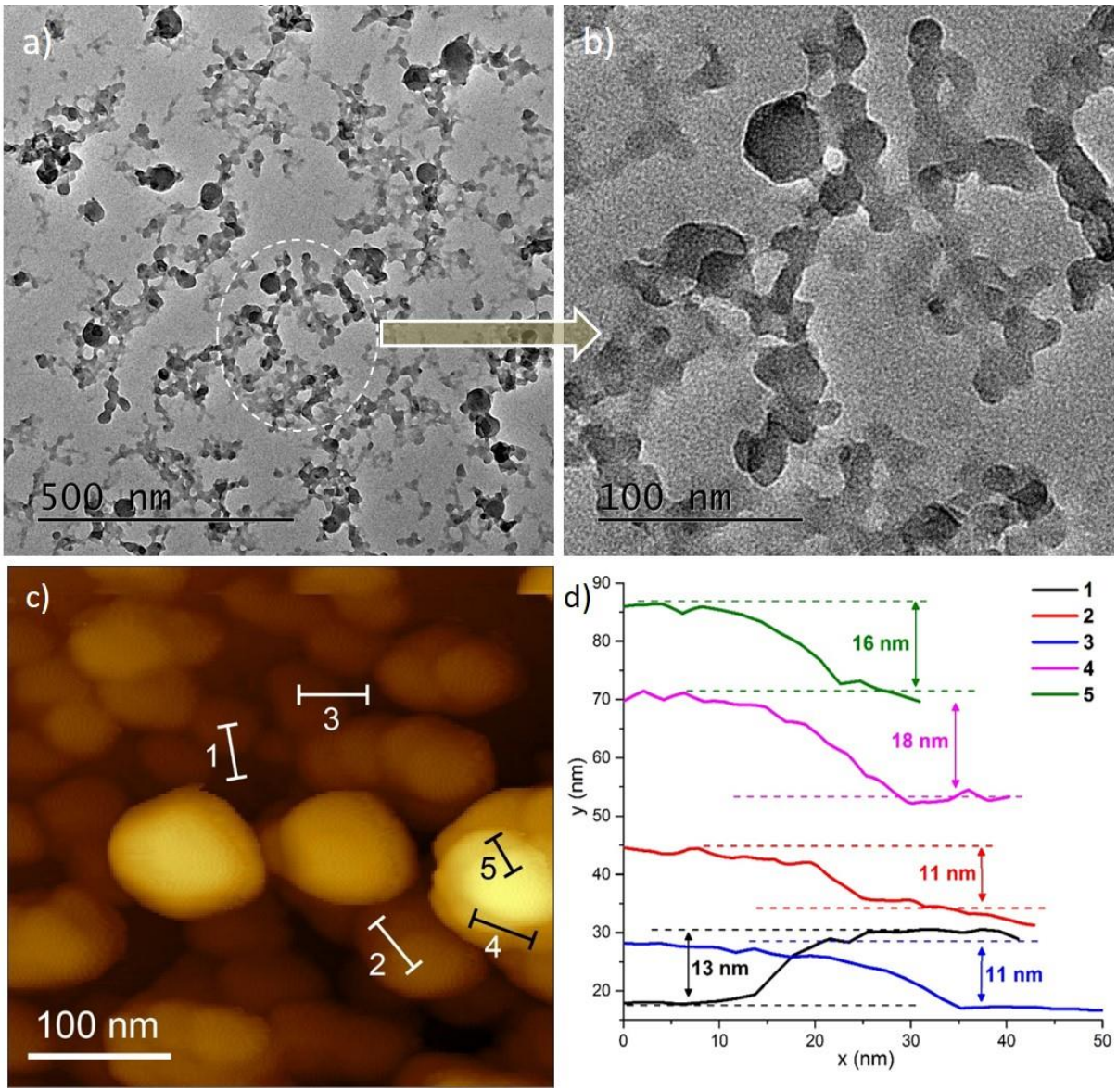

Figure 8.8 TEM image of the nanoplates obtained after breaking down the gel material into fine powder particles and b) the enlarged area from same image (c) AFM topography image revealing the 2D morphology of larger isolated nanoplates, and (d) their individual thickness profiles of *ca*. 10-20 nm corresponding to the specific regions marked in (c).

Intriguingly the mechano-responsive gel phase is comprising nanoplates of distorted ZIF-8, whose crystal structure will be elucidated below.

8.4.3 Molecular Structural Features of Nanoplate: ZIF-8 Structure

8.4.3.1 Dynamics of ZIF-8 from Molecular Crowding: Powder X-Ray Diffraction Study to Monitor Structural Changes

The bulk aggregates of nanoplates harvested from the supraMOF gel phase transformed into a monolith after drying at 110°C. This monolith was carefully ground into a fine powder and then characterised using powder X-ray diffraction (PXRD). Figure 8.9 shows that its PXRD pattern has sharp peaks matching the ideal simulated XRD pattern of ZIF-8, but with the appearance of a few broadened extra peaks suggesting the reduction of crystal symmetry. To investigate this effect, I have carried out a systematic study by varying the reactant concentrations in accordance with Table 8.1. Specifically, different reactions using mIm and Zn(II) were performed by maintaining the same synthetic parameters apart from the total volume of the DMF solvent used, which was varied from 6 mL (for highly concentrated reaction) to 500 mL (very diluted reaction condition). The products obtained from the five reactions were washed and dried prior to PXRD (Figure 8.9), showing a systematic reduction in intensity of the extra peaks as a function of rising solvent used. This result is supported by systematic colour change of the samples detectable by naked eye (Figure 8.9 inset), I reasoned that additional guest species (e.g. NEt_3, DMF) trapped in framework from concentrated reactions will decompose upon heating of compound producing a yellowish powder (vs. a whiter powder of ZIF-8).

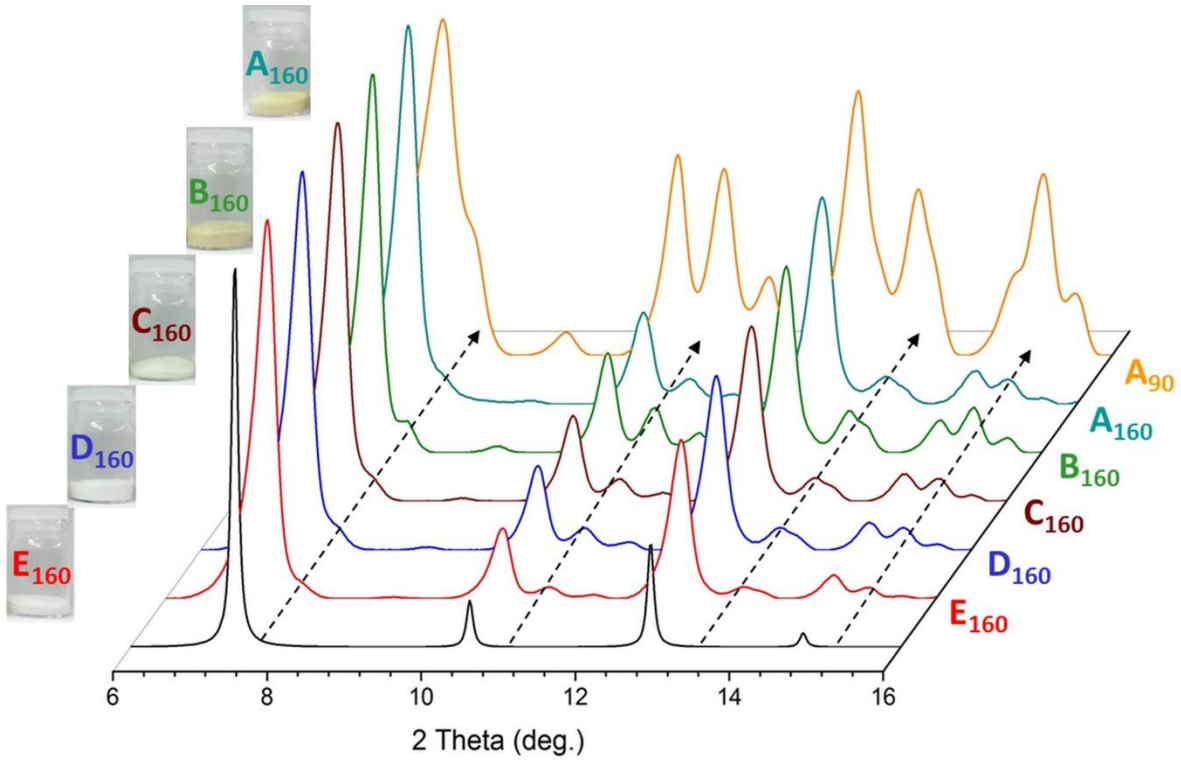

Figure 8.9 PXRD patterns of samples derived from the reactions labelled A-E in Table 1, where the subscripts denote the drying temperature of either 90°C or 160°C. Sample colours obtained (shown to the left of XRD spectra) revealed the apparent variations between the A to E reaction products. Dotted arrows designate the positions of the extra diffraction peaks due to occluded guests.

Table 8.1 Series of reactions A-E to investigate the effects of concentration on the framework structure of ZIF-8. Note: DMF volume was divided 50:50 between $Zn(NO_3)_2$ and mIM.

Reaction	DMF (total)	$Zn(NO_3)_2$	mIm	NEt_3
A (Gel)	6 mL	3 mmol	12 mmol	12 mmol
B	25 mL	3 mmol	12 mmol	12 mmol
C	100 mL	3 mmol	12 mmol	12 mmol
D	300 mL	3 mmol	12 mmol	12 mmol
E	500 mL	3 mmol	12 mmol	12 mmol

8.4.3.2 Distortion in ZIF-8 Investigated Using Pawley Refinement

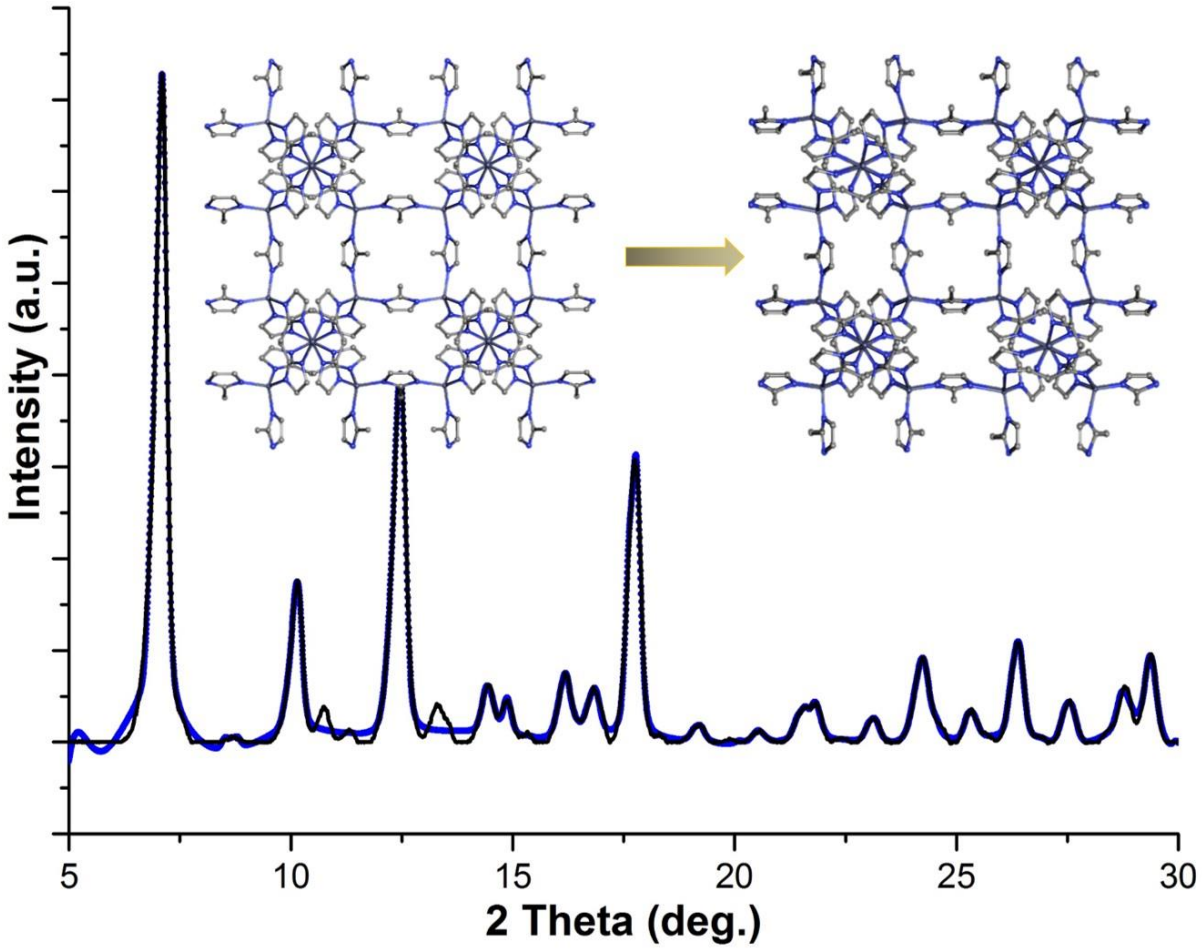

Figure 8.10 Pawley refinement method to determine the lattice geometry of the distorted ZIF-8 framework from the experimental PXRD data of sample A160. Inset: structural changes from the (standard) cubic cell of ZIF-8 to a tricilinic distorted structure of ZIF-8.

To determine the salient changes of the structural parameters of ZIF-8, the PXRD data from reaction A160 (gel) were utilised for Pawley structural refinement. Refinement results in Figure 8.10 show that the high-symmetry (cubic) structure of ZIF-8 has reduced to a low-symmetry (triclinic) crystal structure (R_{wp} = 6.42%) for the nanoplates extracted from the ZIF-8 supraMOF gel. Cell dimensions of the cubic ZIF-8 structure were found to have been modified from *a*, *b*, *c* = 17.086 Å to *a* = 17.46Å, *b* = 17.12Å, *c* = 16.95Å, and,

the unit cell angles changed from α, β, $\gamma = 90°$ to $\alpha = 89.01°$, $\beta = 89.50°$, $\gamma = 88.19°$ (see details in Table A5 in Appendix).

8.4.4 Thermal Stability

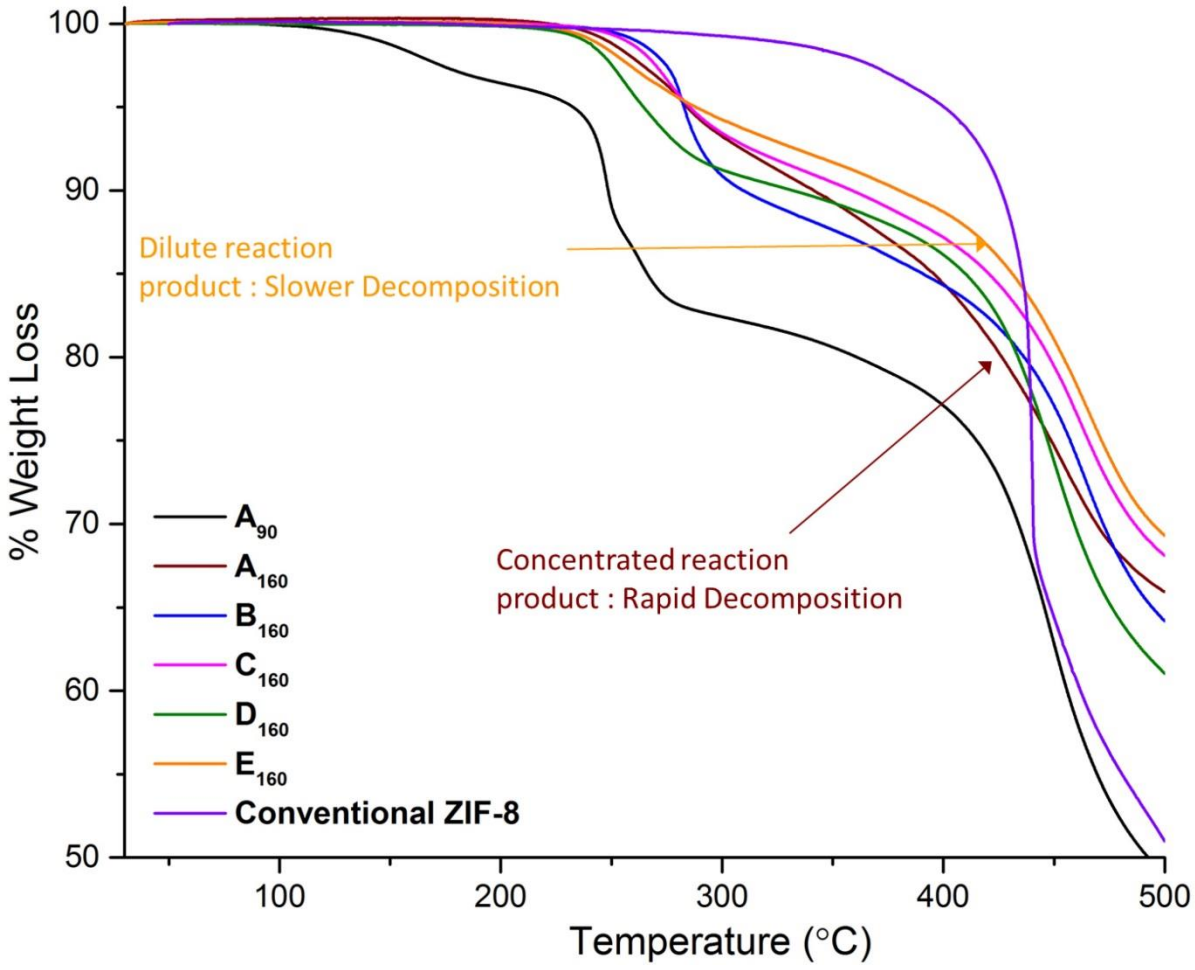

Figure 8.11 TGA of a series of compounds obtained ranging from concentrated to dilute reaction conditions (A→E), in accordance with Table 8.1. Comparing A_{90} to A_{160} (both extracted from SupraMOF gel), it can be seen that by simply drying the same product "A" at a higher temperature of 160°C prior to TGA could enhance its thermal stability up to ~250°C, suggesting the removal of occluded guests (e.g. NEt_3, DMF). Thus more concentrated reaction results in products that entrap more guest species leading to a faster decomposition upon heating. In contrast, the thermal stability of diluted reaction products (such as E_{160}) is approaching the thermal stability of conventional ZIF-8 compound.

Moreover, thermogravimetric analysis (TGA) of these compounds detected changes to the thermal stability of the framework material when being synthesised in concentrated conditions (Figure 8.11). Unlike thermal stability of conventional ZIF-8 powder till ~350°C, the nanoplates comprising reduced symmetry ZIF-8 (derived from supraMOF) have a relatively lower thermal stability up to ~250°C, which can be ascribed to the decomposition of entrapped guest species.

8.5 Summary

I have demonstrated the efficacy of the high-concentration reaction (HCR) strategy to derive a previously unreported ZIF-8-based supraMOF gel material. Surprisingly, this supraMOF gel contains an abundance of ZIF-8 nanoplates with only ~10s nm thickness, completely dissimilar to the conventional ZIF-8's rhombic dodecahedral crystals ubiquitous in the literature.[47] Exceptionally this ZIF-8 supraMOF gel is mechano-stimuli responsive, exhibiting fast sol-gel conversions and highly reversible mechanical properties subject to a multi-cyclic strain deformation.

Chapter Nine

Conclusions and Future Work

9.1 Smart SupraMOFs and Their Stimuli Responsive Properties

The HKUST-1 MOF-based supramolecular hybrid materials 'SupraMOFs' synthesised from unique solvent molecules could afford unconventional combination of chemico-physical properties, which are linked to their very distinctive micro-architectures generated from hierarchical self-organisation. To illustrate this, hybrid gels derived from dimethyl sulfoxide (termed G⊃DMSO) display remarkable multi-stimuli responsive sol-gel switching phenomena, which are reversible, when being subjected to chemical-mechanical-thermal stimuli. Another example concerns the even more striking phase change phenomenon, witnessed in the hybrid gel synthesised using acetonitrile (termed G⊃ACN), highlighting the radical structural conversion that eventually yields a 'rigid' viscoelastic hybrid material (termed VE⊃ACN). Intriguingly, the latter material not only is mechanically robust, but also is highly malleable and electrically conducting (~10 S m^{-1}). Other major findings encompass the demonstrations that, the entire family of MOF-based supramolecular hybrids (examples derived from polar-protic and -aprotic solvents) possess very promising potential to accommodate straightforwardly tuneable electrical and mechanical properties. Moreover, the uniformly-sized MOF nanoparticles (~100 nm) that have been synergistically created in the hybrid gel-like network, can indeed be easily harvested (*via* rapid sol-gel switching), and subsequently used as a sol-based precursor to fabricate high-quality MOF thin films with defined thicknesses. This exciting new approach opens up the possibility of combining supramolecular materials

science and low-cost sol-gel routes (thus avoiding the need to use costly self-assembled monolayers, SAMs) to engineer multifunctional MOF thin-film coatings, for targeting emergent technological device applications, such as next-generation sensors, actuators, supercapacitors and ultralow-*k* dielectrics.

9.2 *In Situ* Metal-Complex Guest Encapsulation for Improved Optical Properties

One attraction of the proposed in-situ guest encapsulation approach lies in its capacity to confine bulky guest molecules in certain MOF hosts, particularly ones featuring narrow window apertures that inevitably prevent conventional (*ex situ*) guest infiltration or ion-exchange strategies. It is envisioned that, this strategy can be extended to nano-caging and nano-manipulation of a wide variety of light-sensitive fluorophores combined with the diverse family of MOF hosts[141, 273] and porous structures[274] exist in literature. In the current study, well known ZnQ metal complex has been explored from completely new direction in order to obtain different emission behaviour compared to that of pure ZnQ complex. Indeed improving the photostability performance and overall long-term material durability through nanoporous host-guest encapsulation is important to the field of light-matter interactions science, with many exemplars already demonstrated for inorganic zeolites,[275] self-assembled cavitand-based capsules,[276] and molecular sieves;[277] the current study offers an attractive strategy whereby MOF can also be utilised to achieve such an effect.

9.3 Extension of High Concentration Reaction to Attain Functional Nanosheets of MOFs

My work has demonstrated that the synergistic effects of molecular crowding interaction and molecular self-assembly help to derive a supramolecular material incorporating MOF nanosheets. While the basic idea of supramolecular assembly is not new in the field of

materials science, this is its first creative implementation to accomplish a MOF nanosheet assembly within another supramolecular gel assembly. The one-pot synthetic approach developed is exceedingly fast, requiring less than 1-minute of reaction time to obtain nanosheets with a thickness of the order of 10s nanometers. In addition to morphological control, the process opens the door to novel materials functionalisation through the formation of host-guest systems, termed “Guest@MOF” nanosheets. Such Guest@MOF nanosheets are excellent photochemical sensors, exhibiting an extraordinary propensity for the detection of a vast range of harmful volatile organic compounds (VOCs), and small polar and non-polar molecules important for applications. This is possible thanks to the intimate nature of host-guest coupling bestowed by MOF nanoscale confinement, implicating substantial optochemical perturbations that are easily detectable by the naked eye (emission blue-to-red shifts, intensity modification or luminescence quenching). The promising results pave the way for the future development of photonics-based chemical sensors and tunable optoelectronics. In the light of this, I anticipate that the proposed methodology will open the door to a new family of low-dimensional MOF-based smart materials, whose bespoke physico-chemical properties will be of significant utility to the chemical sensors, photonics, and electronics material sectors.

9.4 High Concentration Reaction (HCR) for Host-Guest Dependent Mechanoluminescent MOF System.

I show that using the HCR synthetic approach, MOF host-guest system can be made exhibiting unusual emissive behaviour unlike normal emission seen in the pure form of the guest compound. From detailed experiments, I concluded that framework flexibility and weak interaction between guest and host are crucial parameters to obtain reversible mechano-triggered luminescent properties. I also discovered that the structural transition

from a crystalline to amorphous phase could retain its mechanoluminescence properties, thereby opening an exciting route for fabricating functional amorphous materials constituting fluorescent Guest@MOF nanocomposites. Together, the demonstrated new findings and innovative approach towards mechanoluminescence will be valuable in expanding the frontier of MOF science, especially in the pursuit of next-generation host-guest nanomaterials exhibiting tunable optoelectronic and sensing properties.

9.5 Creating Other Smart SupraMOF

I further demonstrated that the HCR strategy has tremendous potential for making supramolecular systems containing nanoMOFs (SupraMOF systems). For demonstration, I have shown the possibility of making SupraMOF gel using Zn(II) and mIm ligand, a combination of reactants that subsequently forms the hierarchical assembly enriched with ZIF-8 nanoplates. Fine scale thickness of only ~10s nm observed in the case of MOF nanoplates indicates the huge advantage of a new way of accomplishing 2D self-assembly. Remarkably this supraMOF gel is receptive to the exertion of an external mechanical force, displaying rapid sol-gel transformations and reversible mechanical response for multiple strain cycles. The current study not only presents the first discovery of a ZIF-type gel material, but also describes the simple synthetic methodology that may be widened to explore its applicability for other well-studied MOFs to yield supramolecular stimuli-responsive systems and to achieve rare 2D morphologies.

9.6 Future Work

9.6.1 Pre-Functionlisation of SupraMOFs

From above study it is clear that prior to the assembling of metal ions, organic linkers and solvents together into SupraMOF assembly, one can functionalise SupraMOFs by simply

mixing functional organic molecules, metal-complexes, dye molecules into the reactant solutions. For examples ZnQ@ZIF-8, ZnQ@OX-1, Perylene@ZIF-8 are the direct demonstrations of this concept. In future work, study can be extended to other guest species and other MOF host structures to tailor the optical properties.

9.6.2 Post-Doping of SupraMOFs

Sol-gel transitions are useful phase changes that allow mixing of external molecular species into the assembly. Already formed gel phase of SupraMOF can be functionalised by simply mixing fluorescent molecules like fluorescein in sol phase. Other molecular engineering processes like metal exchange or metal ion insertion into the final framework product may be attempted by introducing metal ion solution into the sol phase of SupraMOF. Further study can be directed at post-functionalised SupraMOFs and such materials can be studied for their possible optoelectronic, ionic conduction, and sensing properties.

9.6.3 Precise Morphological Control of MOF Nanostructures

Current work also has potential to create highly controlled morphologies of MOF structures from the bottom up to yield nanosheets, nanoplates, nanoparticles etc. Reported synthetic strategies in the current thesis hold a lot of promise for making other exotic nano scale MOF systems that otherwise will only form in large size. In addition to morphological control significant changes in structural arrangement can be achieved, which could allow tuning of the band gap values of material either by structural changes in MOF or by close packing of framework hosts with confined guest species.

9.6.4 Thin Film Fabrication for Optoelectronic Properties

As above listed points i.e. functionalisation, emission, conduction, band gap engineering, structural control, morphological control in nano regime etc. are essential for engineering smart devices. SupraMOF systems and HCR synthetic approach will enable facile processing of thin film MOF based devices for various applications falls under optoelectronics.

Appendices

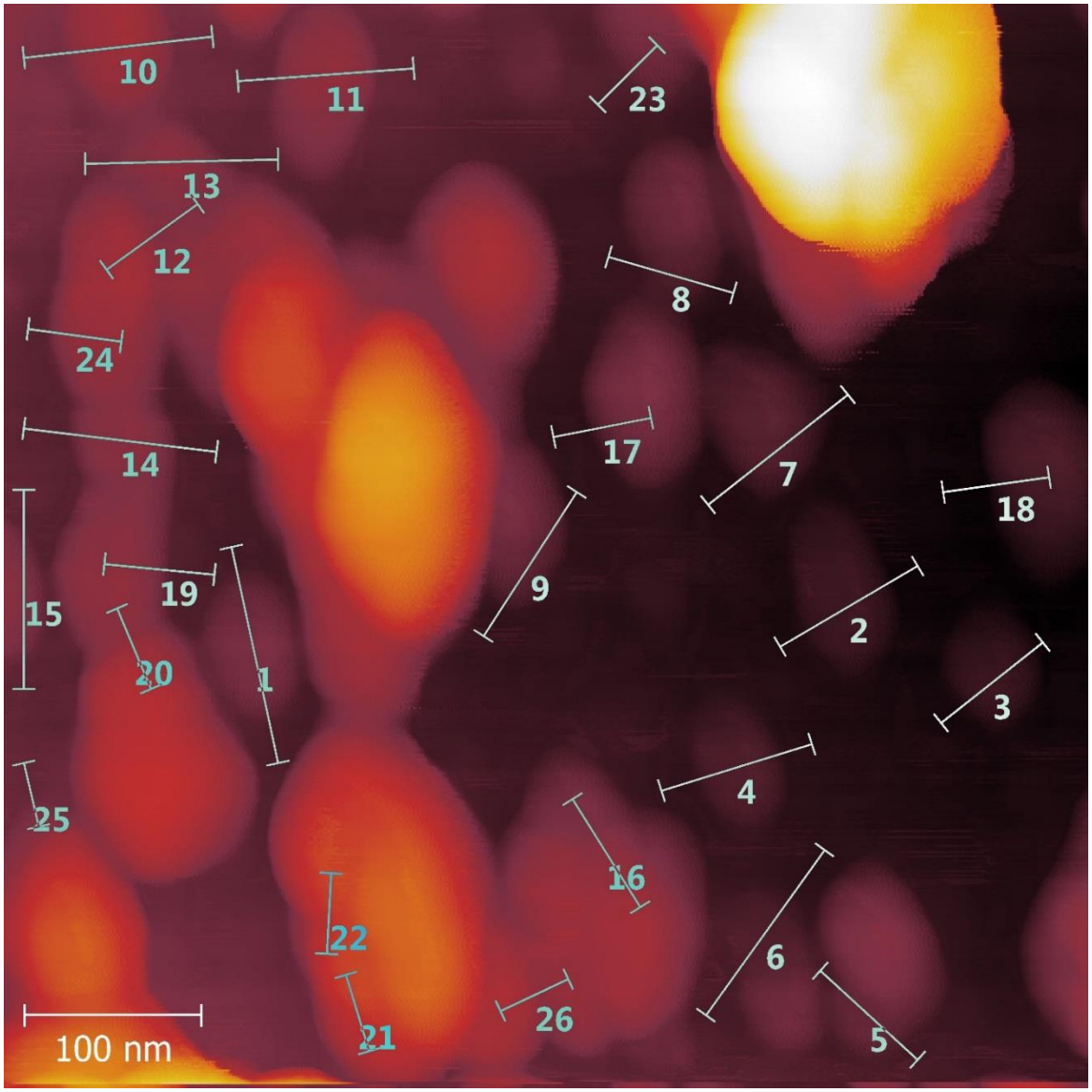

Figure A1 Atomic force microscopy image showing nanoplate morphology of Perylene@ZIF-8 material. Twenty-six different nanoplates were selected in above image for elucidating their thickness profile, which are plotted separately on following page and tabulated in Table A1.

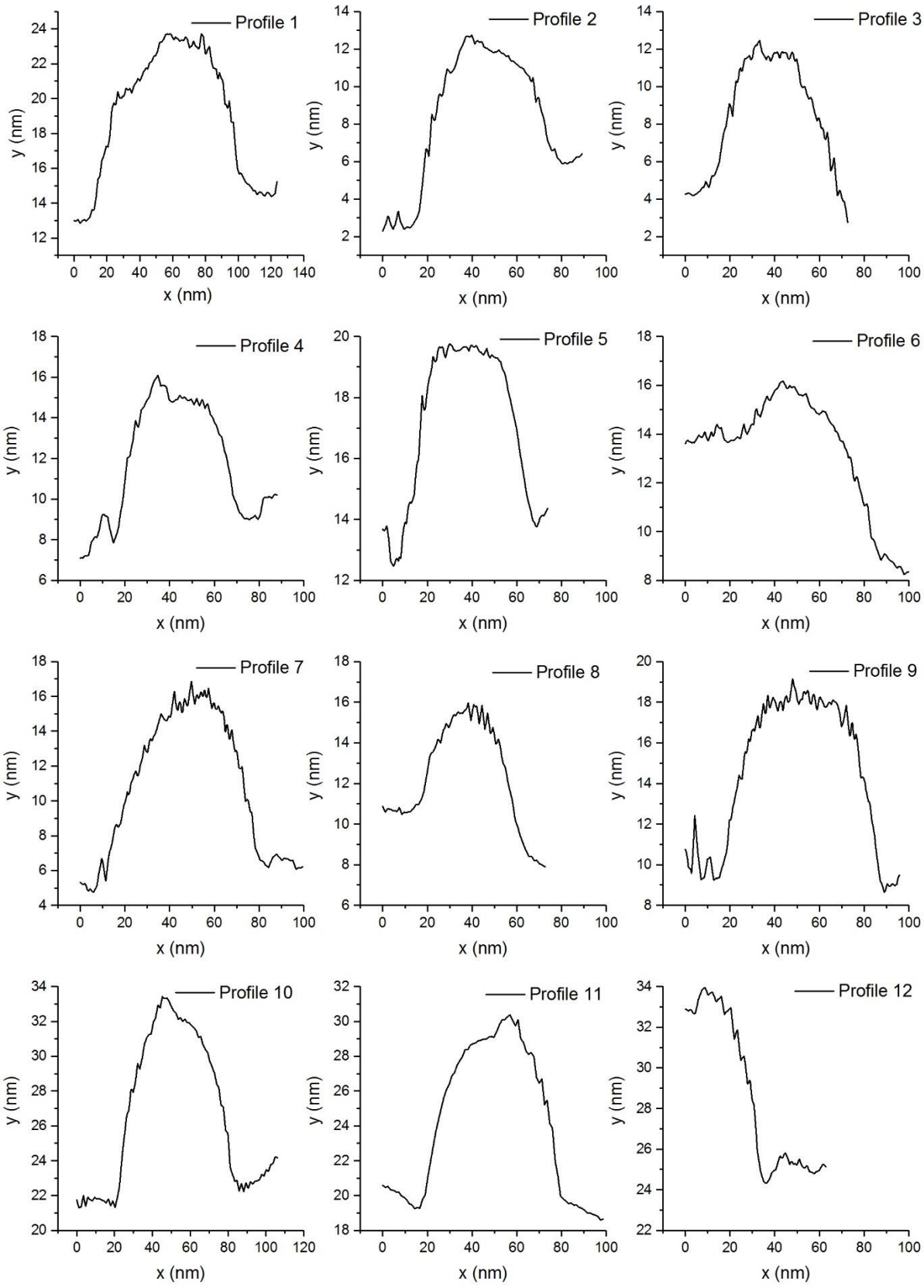
Profile 1
Profile 2
Profile 3
Profile 4
Profile 5
Profile 6
Profile 7
Profile 8
Profile 9
Profile 10
Profile 11
Profile 12
y (nm)
x (nm)

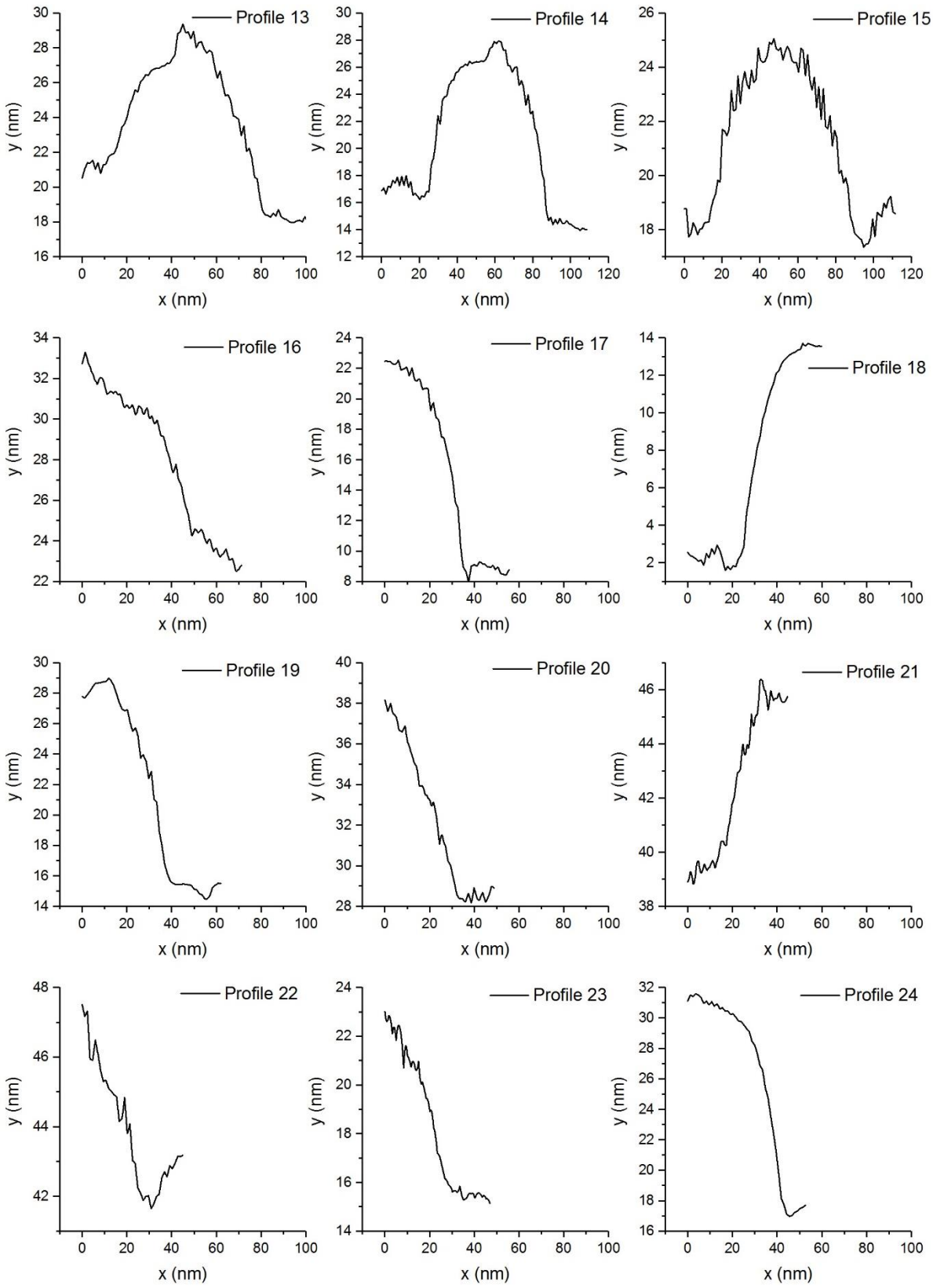
Profile 13
Profile 14
Profile 15
Profile 16
Profile 17
Profile 18
Profile 19
Profile 20
Profile 21
Profile 22
Profile 23
Profile 24
y (nm)
x (nm)

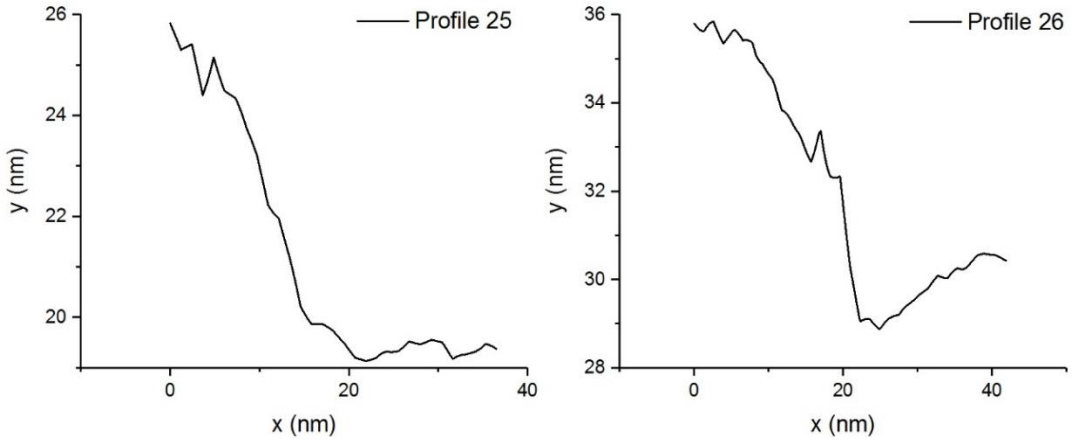

Table A1. Nanoplate dimension analysis from AFM image shown in Figure A1.

Profile	Height/Thickness h (nm)	Mean with Standard Deviation	Width w (nm)	Breadth b (nm)	Aspect Ratio 1 w/h	Aspect ratio 2 b/h
1	10.73	9.28 ± 2.56 nm	77	54	7.17	5.03
2	10.28		93	48	9.07	4.66
3	8.22		53	41	6.44	4.98
4	7.1		69	48	9.71	6.76
5	6.4		NA	NA	—	—
6	7.11		NA	NA	—	—
7	10.05		81	59	8.05	5.87
8	6.32		86	52	13.6	8.22
9	9.51		NA	NA	—	—
10	11.67		NA	NA	—	—
11	11.01		95	57	8.62	5.17
12	9.1		NA	NA	—	—
13	11.3		NA	NA	—	—
14	12.19		NA	NA	—	—
15	7.27		NA	NA	—	—
16	7.54		NA	NA	—	—
17	13.67		100	65	7.31	4.75
18	12		NA	NA	—	—
19	13.77		NA	NA	—	—
20	9.53		NA	NA	—	—
21	6.52		NA	NA	—	—
22	5.64		NA	NA	—	—
23	7.32		NA	NA	—	—
24	13.79		NA	NA	—	—
25	6.62		NA	NA	—	—
26	6.79		NA	NA	—	—

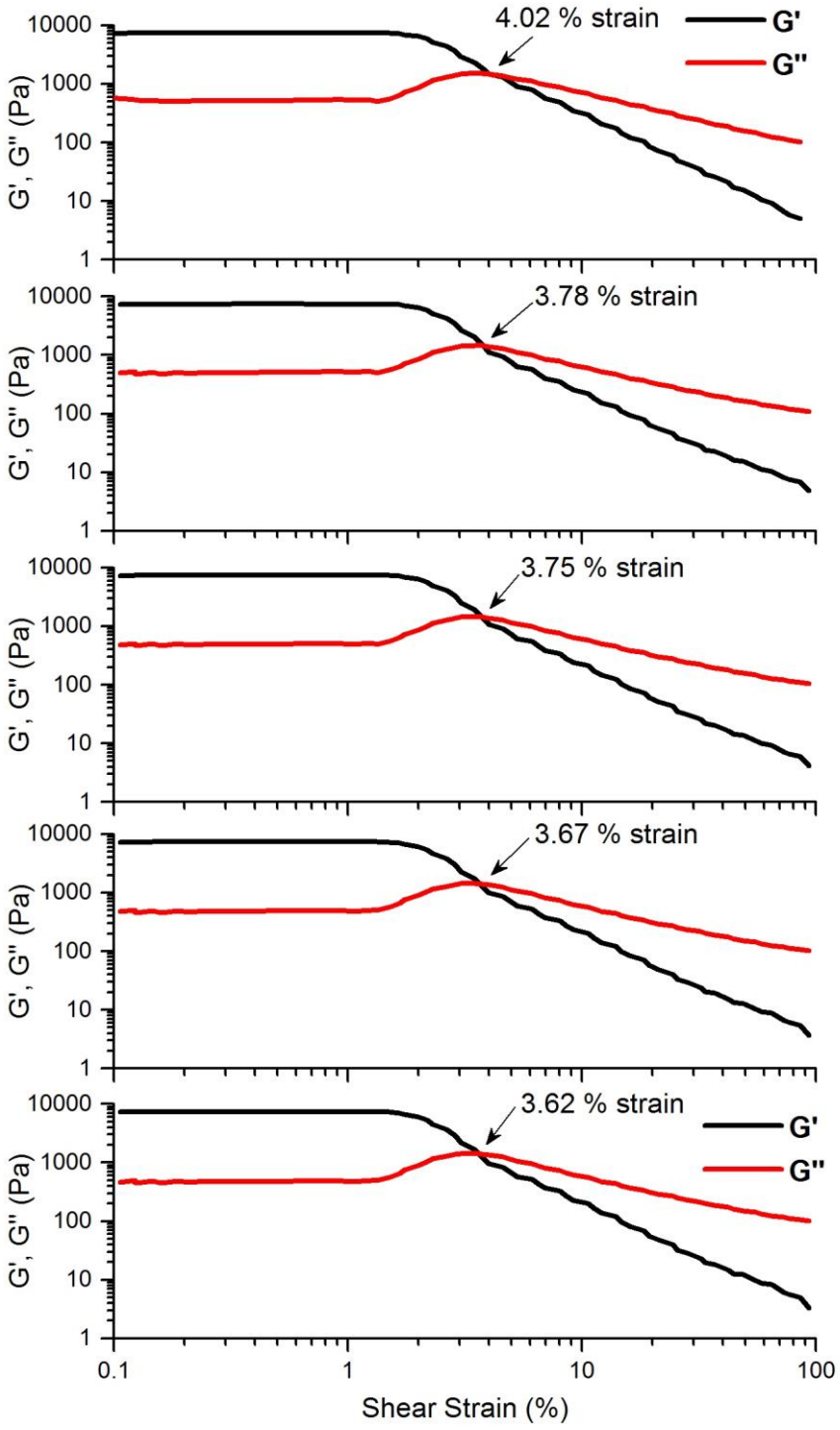

Figure A2. Dynamic strain sweep measurements for five consecutive shear strain cycles of 0.1% to 100%, corresponding to the data in Figure 8.5. The yield points (in %) were established at the intercepts of the *G'* and *G"* data.

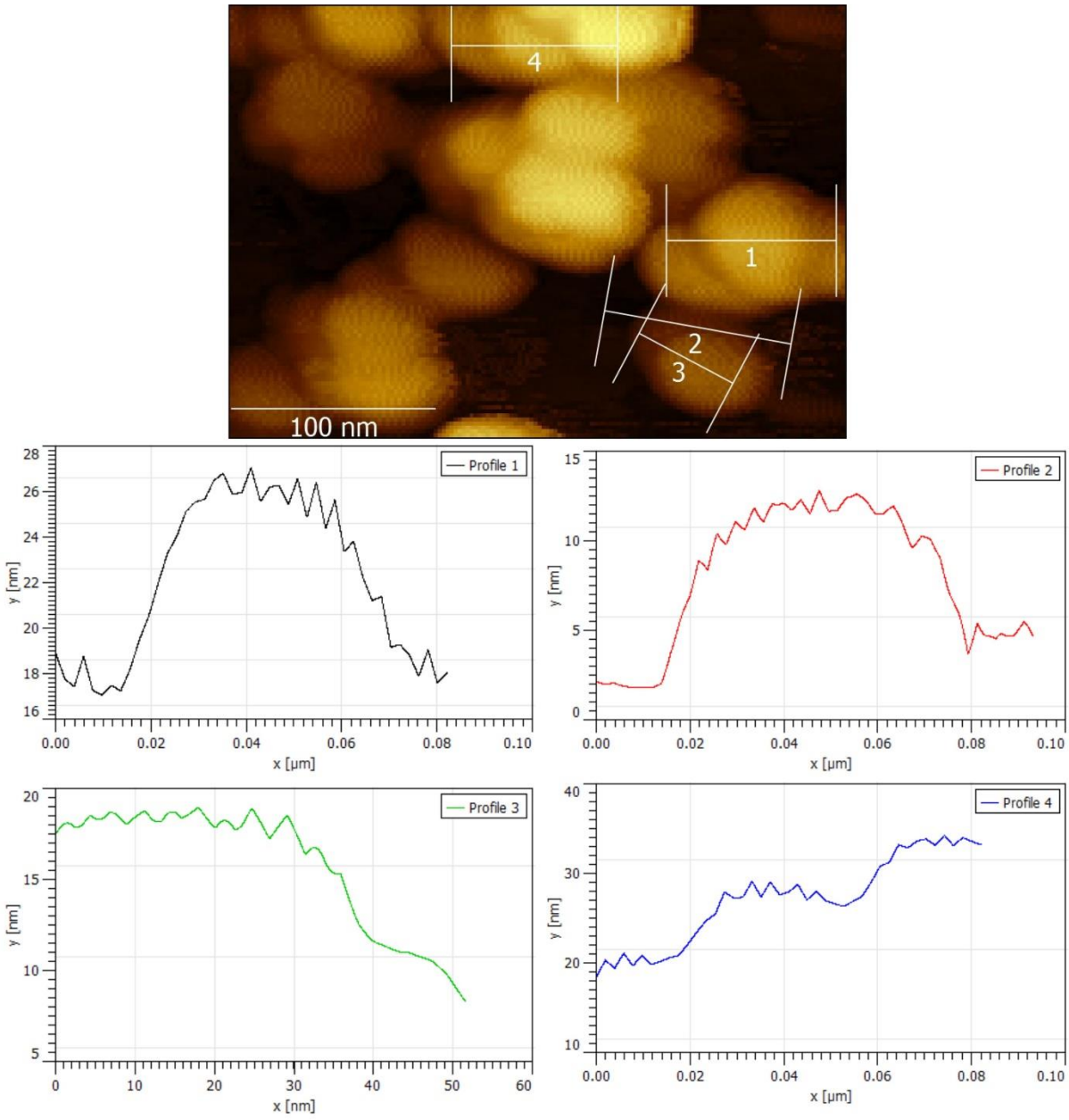

Figure A3. Atomic force microscopy (AFM) images for determining the nanoplate thickness of distorted ZIF-8 (Table A2). The thickness profiles correspond to the locations marked in the height topography image at the top.

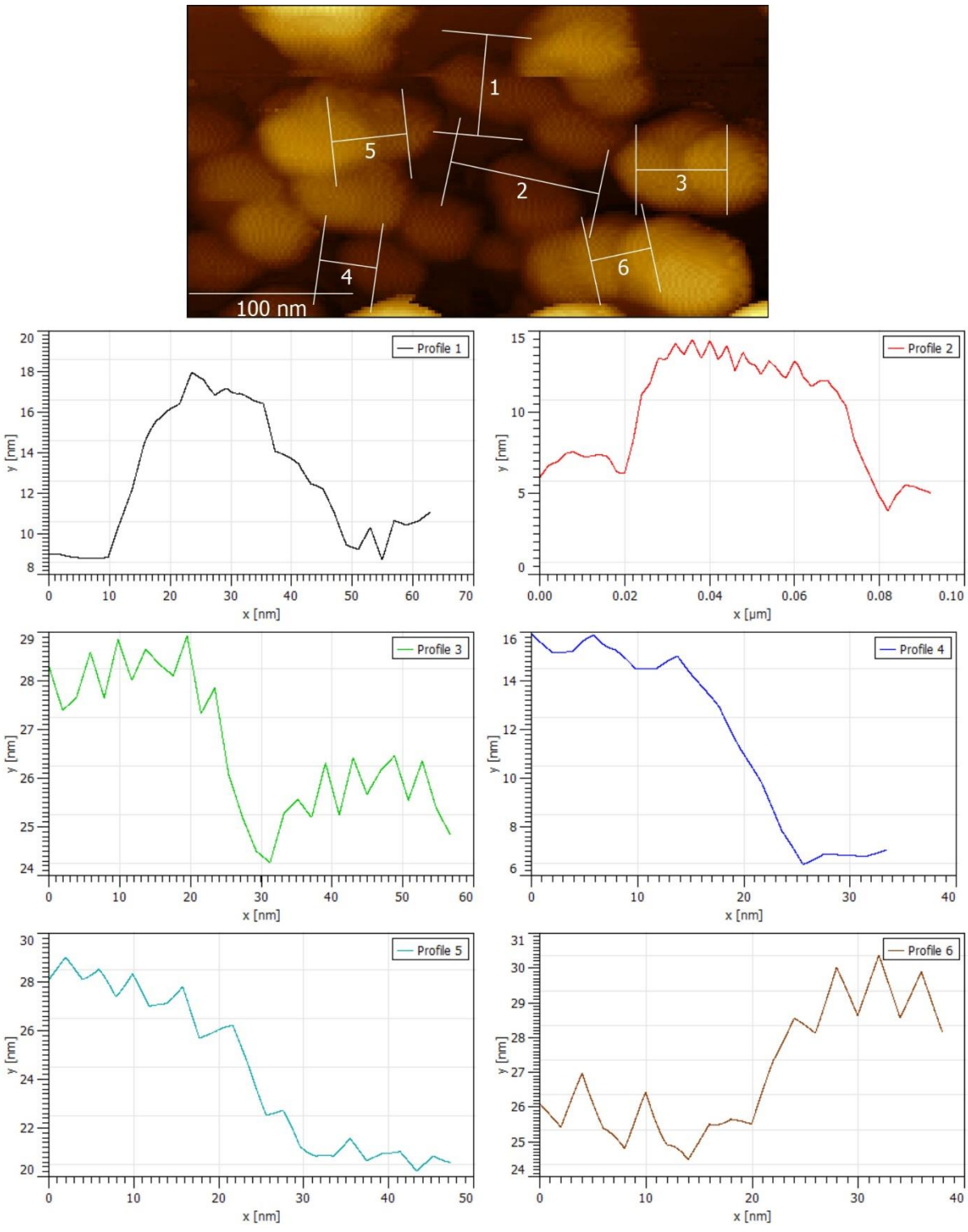

Figure A4. Nanoplate thickness profiles of distorted ZIF-8 using AFM.

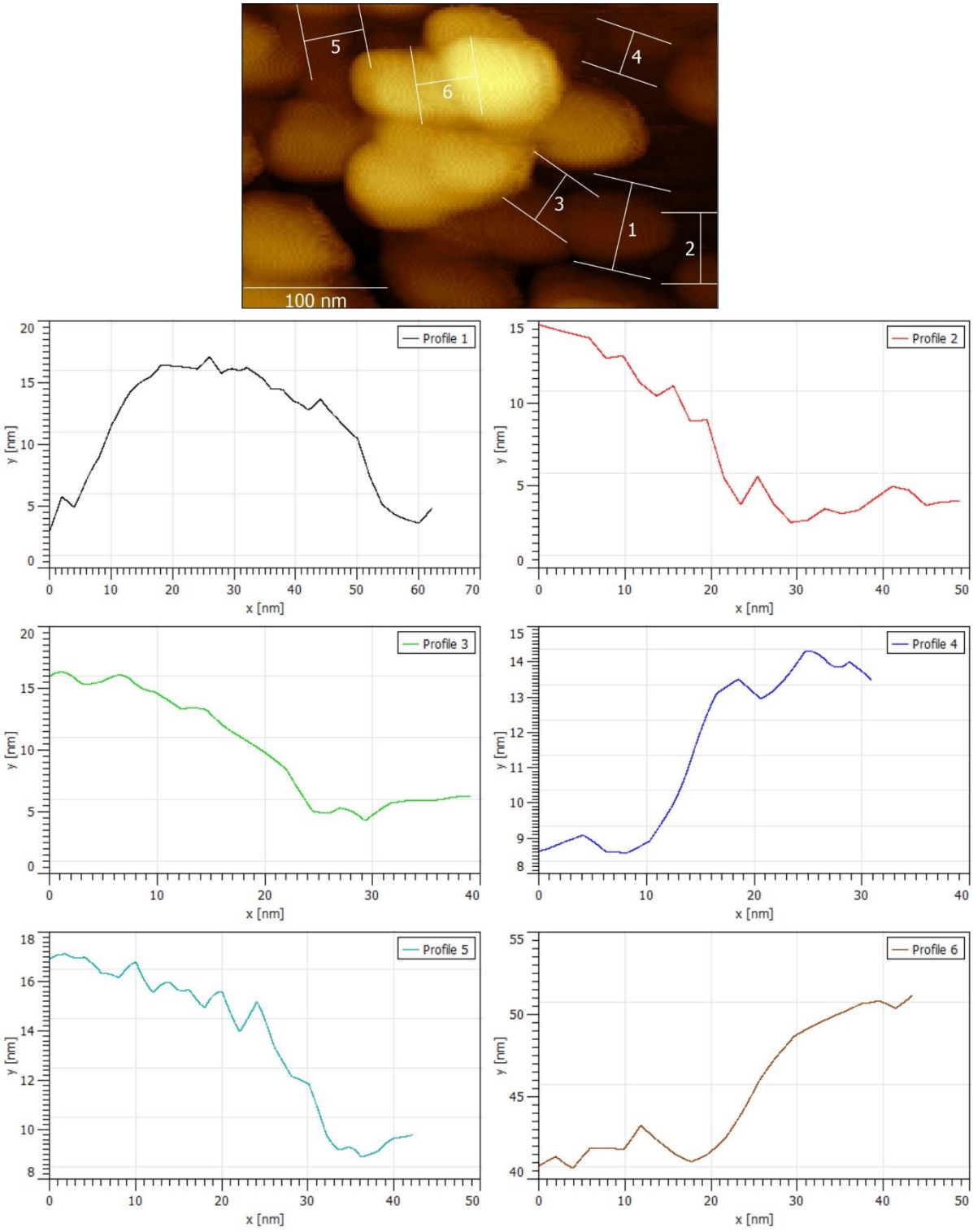

Figure A5. Nanoplate thickness profiles of distorted ZIF-8 using AFM.

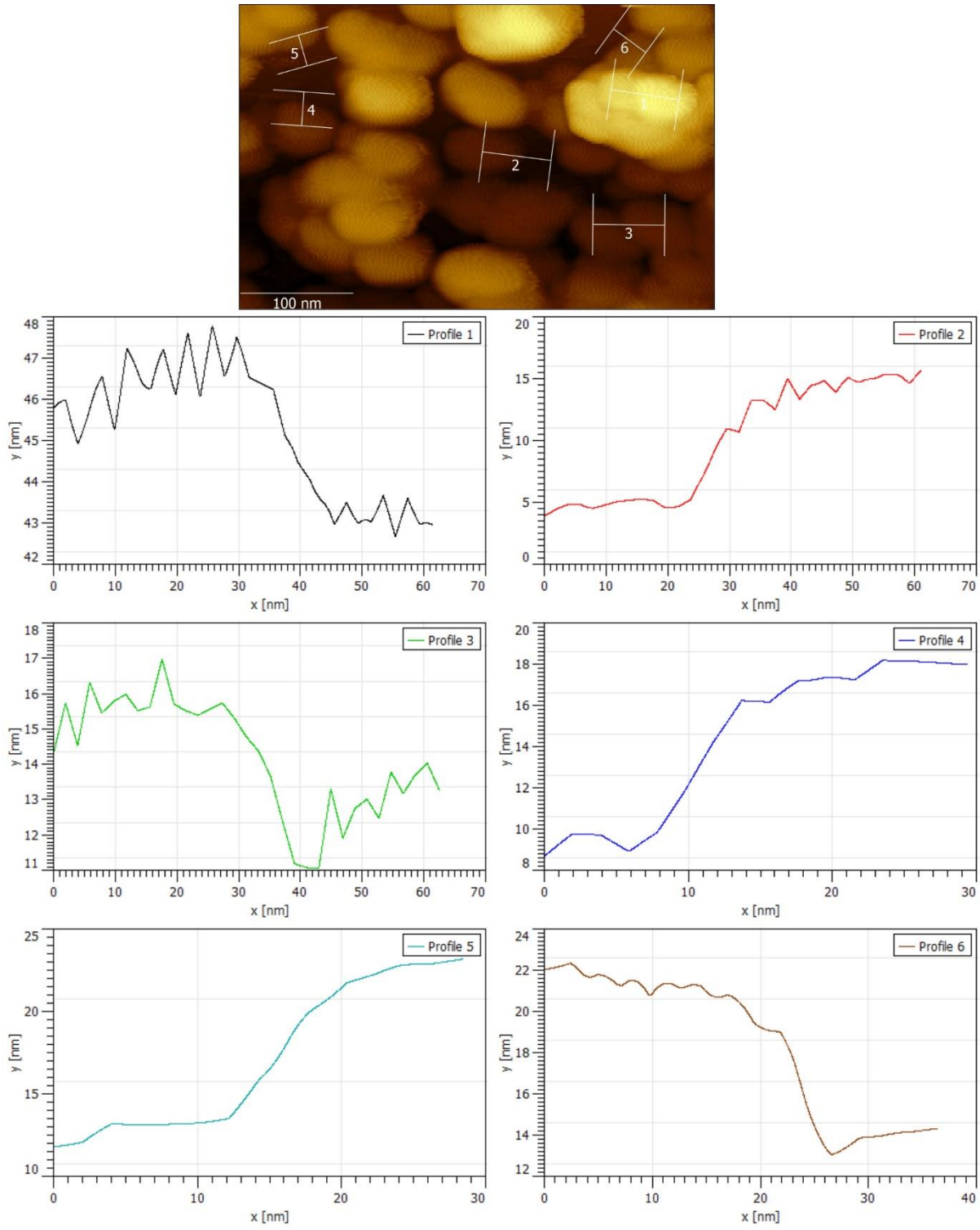

Figure A6. Nanoplate thickness profiles of distorted ZIF-8 using AFM.

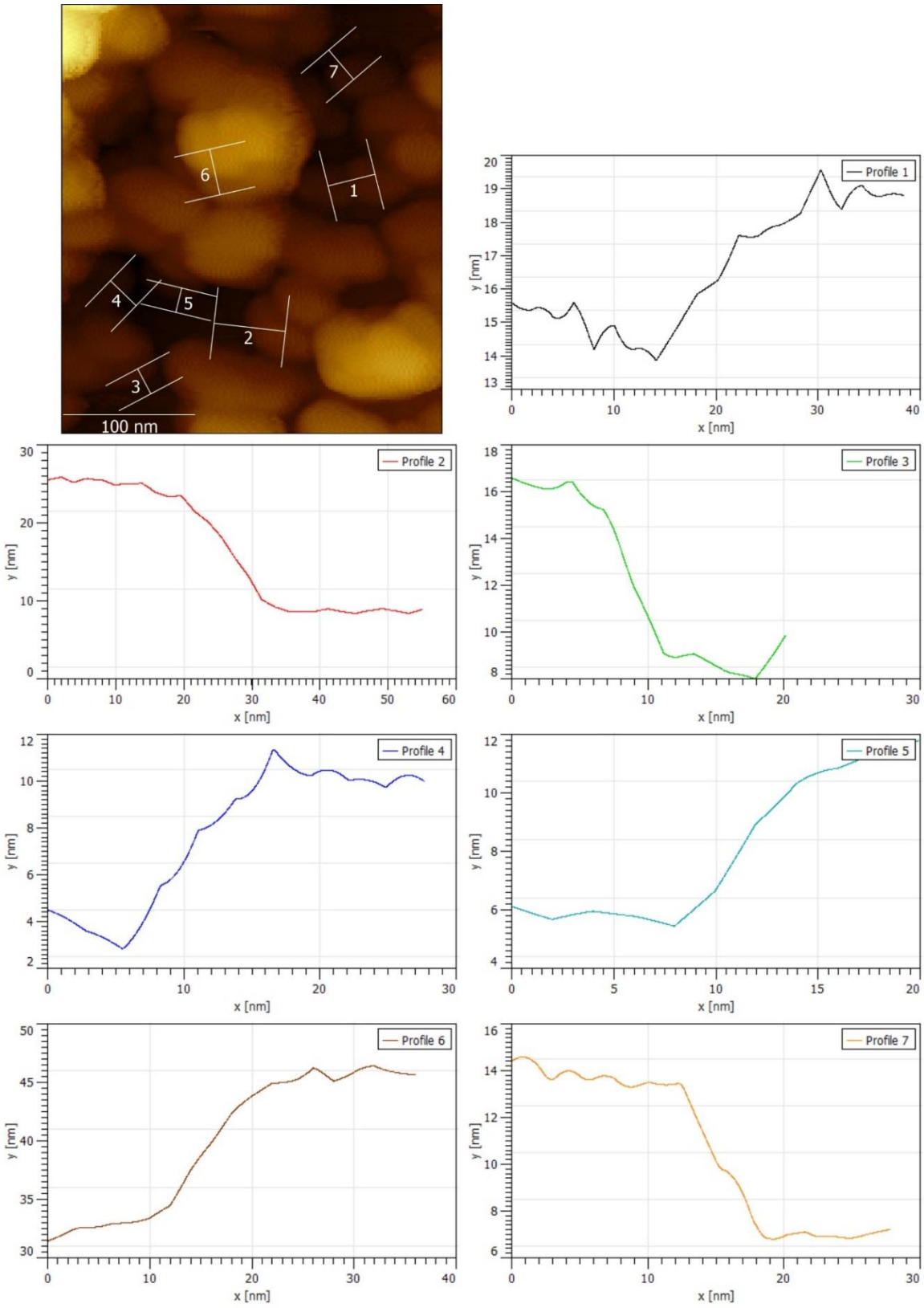

Figure A7. Nanoplate thickness profiles of distorted ZIF-8 using AFM.

Table A2: Quantification of the nanoplate thickness using the AFM height topography data. Based on 35 sampling points, the thickness was determined to be 9.3 ± 3.8 nm.

Figure No.	Profile #	Thickness (nm)	Mean ± standard deviation (nm) calculated from 35 samples
A3	1	25.6-17.2=8.4	9.26 ± 3.77 nm
	2	14-4=10	
	3	18-11=7	
	4	1)= 28-20=8	
		2)= 34-28=6	
A4	1	17-9=8	
	2	13-6=7	
	3	28.4-24.3=4.1	
	4	15.4-6.8=8.6	
	5	28-20.4=7.6	
	6	29.5-25.8=3.7	
A5	1	16-3=13	
	2	15-3=12	
	3	16-4=12	
	4	14-8.5=5.5	
	5	17-8.6=8.4	
	6	52-40=12	
A6	1	47-43=4	
	2	15-4=11	
	3	16-11=5	
	4	18-9=9	
	5	23-13=10	
	6	22-14=8	
A7	1	19-14=5	
	2	26-8=18	
	3	16.6-8=8.6	
	4	10.6-3=7.6	
	5	11-5.6=5.4	
	6	46-32=14	
	7	14-6.8=7.2	
Figure 8.8 (c-d) (in chapter 8)	1	13	
	2	11	
	3	11	
	4	18	
	5	16	

Table A3 Structural parameters for OX-1 determined by Pawley refinement of the X-ray diffraction data (performed in Reflex module in Accelrys Material Studio v.8), compared with reported MOF structures with a higher symmetry.

Compound	OX-1 Nanosheets	MOF reported by Burrows *et al* [229]	MOF reported by Stock *et al* [230]
Crystal System	Triclinic	Monoclinic	Monoclinic
Space Group	P1	C2/c	C2/c
X-ray Source	CuKα	not mentioned	MoKα
λ [Å]	1.5418	-	0.71073
Refined Range [°]	4 to 40	-	-
a [Å]	33.576	33.6075	33.3724
b [Å]	9.8147	9.8727	9.8317
c [Å]	18.2668	18.1642	18.1967
α [°]	90.1257	90.00	90.00
β [°]	90.5996	92.226	92.4550
γ [°]	90.4146	90.00	90.00
Volume [Å^3]	6019.11	6022.27	5964.99
Step Size	0.02	-	-
Peak Profile	Pseudo-Voigt	-	-
R factors	0.084 (R_{wp})	0.0510 (R_1)	0.0395 (R_1)
	0.09 (R_p)	0.1458 (wR_2)	0.0843 (wR_2)

Table A4 Changes in the unit cell parameters of the (distorted) ZIF-8 structure due to high concentration reaction and encapsulation of the Perylene guest within the pore of ZIF-8.

Compound	ZIF-8 reported by Yaghi *et al*.[47]	Nanoplates of ZIF-8
Crystal System	Cubic	Triclinic
Space Group	I-4 3 m	P1
X-ray Source	MoKα	CuKα
λ [Å]	0.71073	1.5418
Refinement Range of 2θ [°]	-	5 to 30
a [Å]	16.9910(12)	17.339
b (Å]	16.9910(12)	17.127
c [Å]	16.9910(12)	17.072
α [°]	90	87.073
β [°]	90	90.321
γ [°]	90	84.677
Volume [Å^3]	4905.2	5041.48
Peak Profile	-	Pseudo-Voigt
R factor	0.0314 (R_1)	0.0818 (R_{wp})
Structure Solution Method	Single Crystal	Powder Refinement
Software	SHELXTL' 97	Reflex (Material Studio)

Table A5 Changes in the unit cell parameters of the (distorted) ZIF-8 structure due to high concentration reaction.

Compound	ZIF-8 reported by Yaghi *et al*. [47]	Nanoplates of ZIF-8
Crystal System	Cubic	Triclinic
Space Group	I-4 3 m	P1
X-ray Source	MoKα	CuKα
λ [Å]	0.71073	1.5418
Refinement Range of 2θ [°]	-	5 to 30
a [Å]	16.9910(12)	17.46
b (Å]	16.9910(12)	17.12
c [Å]	16.9910(12)	16.95
α [°]	90	89.01
β [°]	90	89.50
γ [°]	90	88.19
Peak Profile	-	Pseudo-Voigt
R factor	0.0314 (R_1)	0.0642 (R_{wp})
Structure Solution Method	Single Crystal	Powder Refinement
Software	SHELXTL' 97	Reflex (Material Studio)

Table A6 Theoretical parameters used for calculation of band gap values.

Task parameters for ZIF-8 and ZnQ used for calculation of band gap values reported in Chapter 5	
Scf_density_convergence :	1.000000e-006
Scf_charge_mixing :	2.000000e-001
Scf_spin_mixing :	5.000000e-001
Scf_diis :	6 pulay
Scf_iterations :	50
Electronic parameters	
Spin_polarisation:	unrestricted
Charge:	0
Basis:	dnp
Pseudopotential:	none
Functional:	gga(p91)
Aux_density :	octupole
Integration_grid :	fine
Occupation :	fermi
Cutoff_Global :	4.4000 angstrom
Calculated properties	
Print_eigval_window :	-1.d9
Plot :	homo
Plot :	lumo
Grid msbox	3 0.2500 0.2500 0.2500 3.0000
Task parameters for compounds reported in Chapter 6	
Task parameters for ZnQ_{DMF}	
Calculate	energy
Symmetry	on
Max_memory	15000
File_usage	smart
Scf_density_convergence	1.000000e-006
Scf_charge_mixing	2.000000e-001
Scf_spin_mixing	5.000000e-001
Scf_diis	6 pulay
Scf_iterations	50
Electronic parameters	
Spin_polarisation	unrestricted
Charge	0
Basis	dnp

Pseudopotential	none
Functional	gga(p91)
Aux_density	octupole
Integration_grid	fine
Occupation	fermi
Cutoff_Global	4.4000 angstrom
Task parameters for ZnQ_{DMA}	
Calculate	energy
Symmetry	on
Max_memory	15000
File_usage	smart
Scf_density_convergence	1.000000e-006
Scf_charge_mixing	2.000000e-001
Scf_spin_mixing	5.000000e-001
Scf_diis	6 pulay
Scf_iterations	50
Electronic parameters	
Spin_polarisation	unrestricted
Charge	0
Basis	dnp
Pseudopotential	none
Functional	gga(p91)
Aux_density	octupole
Integration_grid	fine
Occupation	fermi
Cutoff_Global	4.4000 angstrom
Task parameters for ZnQ(Td)	
Calculate	energy
Symmetry	on
Max_memory	15000
File_usage	smart
Scf_density_convergence	1.000000e-006
Scf_charge_mixing	2.000000e-001
Scf_spin_mixing	5.000000e-001
Scf_diis	6 pulay
Scf_iterations	50
Electronic parameters	

Spin_polarisation	unrestricted
Charge	0
Basis	dnp
Pseudopotential	none
Functional	gga(p91)
Aux_density	octupole
Integration_grid	fine
Occupation	fermi
Cutoff_Global	4.4000 angstrom
Task parameters for OX-1	
Electronic parameters	
Spin_polarisation	unrestricted
Charge	0
Basis	dnp
Pseudopotential	none
Functional	gga(p91)
Aux_density	octupole
Integration_grid	medium
Occupation	fermi
Cutoff_Global	4.4000 angstrom
Kpoints	off
Task parameters for ZnQ_{DMF}@OX-1	
Symmetry	on
Max_memory	15000
File_usage	smart
Scf_density_convergence	1.000000e-006
Scf_charge_mixing	2.000000e-001
Scf_spin_mixing	5.000000e-001
Scf_diis	6 pulay
Scf_iterations	50
# Electronic parameters	
Spin_polarisation	unrestricted
Charge	0
Basis	dnp
Pseudopotential	none
Functional	gga(p91)
Aux_density	octupole

Integration_grid	medium
Occupation	fermi
Cutoff_Global	4.4000 angstrom
Kpoints	off
Task parameters for ZnQ(Td)@OX-1	
Symmetry	on
Max_memory	15000
File_usage	smart
Scf_density_convergence	1.000000e-005
Scf_charge_mixing	2.000000e-001
Scf_spin_mixing	5.000000e-001
Scf_diis	6 pulay
Scf_iterations	50
Electronic parameters	
Spin_polarisation	unrestricted
Charge	0
Basis	dnp
Pseudopotential	none
Functional	gga(p91)
Aux_density	octupole
Integration_grid	medium
Occupation	fermi
Cutoff_Global	3.9000 angstrom
Kpoints	off
Task parameters for compounds reported in Chapter 7.	
Task parameters for Perylene@ZIF-8	
Calculate	energy
Symmetry	on
Max_memory	15000
File_usage	smart
Scf_density_convergence	1.000000e-006
Scf_charge_mixing	2.000000e-001
Scf_spin_mixing	5.000000e-001
Scf_diis	6 pulay
Scf_iterations	50
Electronic parameters	

Spin_polarisation	unrestricted
Charge	0
Basis	dnp
Pseudopotential	none
Functional	gga(p91)
Aux_density	octupole
Integration_grid	fine
Occupation	fermi
Cutoff_Global	4.4000 angstrom
Kpoints	off
Calculated properties	
Print_eigval_window	-1.d9
Plot	homo
Plot	lumo
Grid	msbox 3 0.2500 0.2500 0.2500 3.0000
Task parameters for ZIF-8 & distorted ZIF-8	
Calculate	energy
Symmetry	on
Max_memory	15000
File_usage	smart
Scf_density_convergence	1.000000e-006
Scf_charge_mixing	2.000000e-001
Scf_spin_mixing	5.000000e-001
Scf_diis	6 pulay
Scf_iterations	50
Electronic parameters	
Spin_polarisation	unrestricted
Charge	0
Basis	dnp
Pseudopotential	none
Functional	gga(p91)
Aux_density	octupole
Integration_grid	fine
Occupation	fermi
Cutoff_Global	3.9000 angstrom
Kpoints	off
Calculated properties	
Print_eigval_window	-1.d9

Plot	homo
Plot	lumo
Grid	msbox 3 0.2500 0.2500 0.2500 3.0000
Task parameters for Perylene	
Calculate	energy
Symmetry	on
Max_memory	15000
File_usage	smart
Scf_density_convergence	1.000000e-006
Scf_charge_mixing	2.000000e-001
Scf_spin_mixing	5.000000e-001
Scf_diis	6 pulay
Scf_iterations	50
Electronic parameters	
Spin_polarisation	unrestricted
Charge	0
Basis	dnp
Pseudopotential	none
Functional	gga(p91)
Aux_density	octupole
Integration_grid	fine
Occupation	fermi
Cutoff_Global	3.7000 angstrom
Calculated properties	
Print_eigval_window	-1.d9
Plot	homo
Plot	lumo
Grid	msbox 3 0.2500 0.2500 0.2500 3.0000

Publications

1. A. K. Chaudhari, I. Han, J. C. Tan, Multifunctional supramolecular hybrid materials constructed from hierarchical self-ordering of *in situ* generated metal-organic framework (mof) nanoparticles. Adv. Mater. 27, 4438-4446 (2015), (selected for the back inside cover).

2. A. K. Chaudhari, M. R. Ryder, J. C. Tan, Photonic hybrid crystals constructed from in situ host-guest nanoconfinement of a light-emitting complex in metal-organic framework pores. Nanoscale 8, 6851-6859 (2016).

3. E. M. Mahdi, A. K. Chaudhari, J. C. Tan, Capture and immobilisation of iodine (I_2) utilising polymer-based ZIF-8 nanocomposite membranes. Molecular Systems Design & Engineering 1, 122-131 (2016).

4. A. K. Chaudhari, H. J. Kim, I. Han, J. C. Tan, Optochemically responsive 2D nanosheets of a 3D metal-organic framework material. Adv. Mater. 29, (2017), 1701463 (selected for the front inside cover).

5. A. K. Chaudhari, J. C. Tan, Mechano-responsive supramolecular metal-organic framework (supraMOF) gel material rich in ZIF‑8 nanoplates. Chem. Commun. Article in press, (2017), DOI: 10.1039/C7CC03478D (selected for the front cover of the issue).

6. A. K. Chaudhari, J. C. Tan, Mechanoluminescent Nanoplates: Spatial Isolation of Highly Emissive Guests in a Metal-Organic Framework for Stress-Induced Reversible Optical Switching, (2017), Under Review.

References

1. Hoskins, B. F.; Robson, R., Infinite Polymeric Frameworks Consisting of 3 Dimensionally Linked Rod-Like Segments. *J. Am. Chem. Soc.* **1989,** *111*, 5962-5964.

2. Yaghi, O. M.; Li, G. M.; Li, H. L., Selective Binding and Removal of Guests in a Microporous Metal-Organic Framework. *Nature* **1995,** *378*, 703-706.

3. Kitagawa, S.; Kitaura, R.; Noro, S., Functional porous coordination polymers. *Angew. Chem. Int. Ed.* **2004,** *43*, 2334-2375.

4. Kreno, L. E.; Leong, K.; Farha, O. K.; Allendorf, M.; Van Duyne, R. P.; Hupp, J. T., Metal-organic framework materials as chemical sensors. *Chem. Rev.* **2012,** *112*, 1105-1125.

5. Stavila, V.; Talin, A. A.; Allendorf, M. D., MOF-based electronic and opto-electronic devices. *Chem. Soc. Rev.* **2014,** *43*, 5994-6010.

6. Horike, S.; Shimomura, S.; Kitagawa, S., Soft porous crystals. *Nat. Chem.* **2009,** *1*, 695-704.

7. Demessence, A.; D'Alessandro, D. M.; Foo, M. L.; Long, J. R., Strong CO_2 Binding in a Water-Stable, Triazolate-Bridged Metal−Organic Framework Functionalized with Ethylenediamine. *J. Am. Chem. Soc.* **2009,** *131*, 8784-8786.

8. Kepert, C. J.; Prior, T. J.; Rosseinsky, M. J., A versatile family of interconvertible microporous chiral molecular frameworks: The first example of ligand control of network chirality. *J. Am. Chem. Soc.* **2000,** *122*, 5158-5168.

9. Ogborn, J. M.; Collings, I. E.; Moggach, S. A.; Thompson, A. L.; Goodwin, A. L., Supramolecular mechanics in a metal-organic framework. *Chem. Sci.* **2012,** *3*, 3011-3017.

10. Yu, J.; Cui, Y.; Xu, H.; Yang, Y.; Wang, Z.; Chen, B.; Qian, G., Confinement of pyridinium hemicyanine dye within an anionic metal-organic framework for two-photon-pumped lasing. *Nat. Commun.* **2013,** *4*, 2719.

11. Mahdi, E. M.; Chaudhuri, A. K.; Tan, J.-C., Capture and immobilisation of iodine (I_2) utilising polymer-based ZIF-8 nanocomposite membranes. *Mol. Syst. Des. Eng.* **2016,** *1*, 122-131.

12. Holder, E.; Tessler, N.; Rogach, A. L., Hybrid nanocomposite materials with organic and inorganic components for opto-electronic devices. *J. Mater. Chem.* **2008,** *18*, 1064-1078.

13. Rodenas, T.; Luz, I.; Prieto, G.; Seoane, B.; Miro, H.; Corma, A.; Kapteijn, F.; Llabres i Xamena, F. X.; Gascon, J., Metal-organic framework nanosheets in polymer composite materials for gas separation. *Nat. Mater.* **2015,** *14*, 48-55.

14. Biswal, B. P.; Shinde, D. B.; Pillai, V. K.; Banerjee, R., Stabilization of graphene quantum dots (GQDs) by encapsulation inside zeolitic imidazolate framework nanocrystals for photoluminescence tuning. *Nanoscale* **2013,** *5*, 10556-10561.

15. Stassen, I.; Burtch, N.; Talin, A.; Falcaro, P.; Allendorf, M.; Ameloot, R., An updated roadmap for the integration of metal-organic frameworks with electronic devices and chemical sensors. *Chem. Soc. Rev.* **2017,** *46*, 3185-3241.

16. Chui, S. S., A Chemically Functionalizable Nanoporous Material [Cu3(TMA)2(H2O)3]n. *Science* **1999,** *283*, 1148-1150.

17. Spokoyny, A. M.; Kim, D.; Sumrein, A.; Mirkin, C. A., Infinite coordination polymer nano- and microparticle structures. *Chem. Soc. Rev.* **2009,** *38*, 1218-1227.

18. Huxford, R. C.; Della Rocca, J.; Lin, W. B., Metal-organic frameworks as potential drug carriers. *Curr. Opin. Chem. Biol.* **2010,** *14*, 262-268.

19. Jiang, D. M.; Burrows, A. D.; Edler, K. J., Size-controlled synthesis of MIL-101(Cr) nanoparticles with enhanced selectivity for CO2 over N-2. *CrystEngComm* **2011,** *13*, 6916-6919.

20. Jiang, D. M.; Mallat, T.; Krumeich, F.; Baiker, A., Polymer-assisted synthesis of nanocrystalline copper-based metal-organic framework for amine oxidation. *Catal. Commun.* **2011,** *12*, 602-605.

21. Shekhah, O.; Wang, H.; Paradinas, M.; Ocal, C.; Schupbach, B.; Terfort, A.; Zacher, D.; Fischer, R. A.; Woll, C., Controlling interpenetration in metal-organic frameworks by liquid-phase epitaxy. *Nature Materials* **2009,** *8*, 481-484.

22. Stassen, I.; Burtch, N.; Talin, A.; Falcaro, P.; Allendorf, M.; Ameloot, R., An updated roadmap for the integration of metal-organic frameworks with electronic devices and chemical sensors. *Chem. Soc. Rev.* **2017**.

23. Fujita, D.; Suzuki, K.; Sato, S.; Yagi-Utsumi, M.; Yamaguchi, Y.; Mizuno, N.; Kumasaka, T.; Takata, M.; Noda, M.; Uchiyama, S.; Kato, K.; Fujita, M., Protein encapsulation within synthetic molecular hosts. *Nat. Commun.* **2012,** *3*, 1093.

24. Lyu, F.; Zhang, Y.; Zare, R. N.; Ge, J.; Liu, Z., One-Pot Synthesis of Protein-Embedded Metal–Organic Frameworks with Enhanced Biological Activities. *Nano Lett.* **2014,** *14*, 5761-5765.

25. Chen, B.; Yang, Y.; Zapata, F.; Lin, G.; Qian, G.; Lobkovsky, E. B., Luminescent open metal sites within a metal-organic framework for sensing small molecules. *Adv. Mater.* **2007,** *19*, 1693-+.

26. Wei, Z.; Gu, Z. Y.; Arvapally, R. K.; Chen, Y. P.; McDougald, R. N., Jr.; Ivy, J. F.; Yakovenko, A. A.; Feng, D.; Omary, M. A.; Zhou, H. C., Rigidifying fluorescent linkers by

metal-organic framework formation for fluorescence blue shift and quantum yield enhancement. *J. Am. Chem. Soc.* **2014,** *136*, 8269-8276.

27. Lehn, J. M., Toward complex matter: supramolecular chemistry and self-organization. *Proc. Natl. Acad. Sci. USA* **2002,** *99*, 4763-4768.

28. Stuart, M. A.; Huck, W. T.; Genzer, J.; Muller, M.; Ober, C.; Stamm, M.; Sukhorukov, G. B.; Szleifer, I.; Tsukruk, V. V.; Urban, M.; Winnik, F.; Zauscher, S.; Luzinov, I.; Minko, S., Emerging applications of stimuli-responsive polymer materials. *Nat. Mater.* **2010,** *9*, 101-113.

29. Stupp, S. I.; LeBonheur, V. V.; Walker, K.; Li, L. S.; Huggins, K. E.; Keser, M.; Amstutz, A., Supramolecular Materials: Self-Organized Nanostructures. *Science* **1997,** *276*, 384-389.

30. Nakahata, M.; Takashima, Y.; Yamaguchi, H.; Harada, A., Redox-responsive self-healing materials formed from host-guest polymers. *Nat. Commun.* **2011,** *2*, 511.

31. Cordier, P.; Tournilhac, F.; Soulie-Ziakovic, C.; Leibler, L., Self-healing and thermoreversible rubber from supramolecular assembly. *Nature* **2008,** *451*, 977-980.

32. Foster, J. A.; Piepenbrock, M. O.; Lloyd, G. O.; Clarke, N.; Howard, J. A.; Steed, J. W., Anion-switchable supramolecular gels for controlling pharmaceutical crystal growth. *Nat. Chem.* **2010,** *2*, 1037-1043.

33. Xu, G.; Yamada, T.; Otsubo, K.; Sakaida, S.; Kitagawa, H., Facile "modular assembly" for fast construction of a highly oriented crystalline MOF nanofilm. *J. Am. Chem. Soc.* **2012,** *134*, 16524-16527.

34. Weiner, S.; Wagner, H. D., The material bone: Structure mechanical function relations. *Annu. Rev. Mater. Sci.* **1998,** *28*, 271-298.

35. Meyers, M. A.; McKittrick, J.; Chen, P. Y., Structural biological materials: critical mechanics-materials connections. *Science* **2013,** *339*, 773-779.

36. Aida, T.; Meijer, E. W.; Stupp, S. I., Functional supramolecular polymers. *Science* **2012,** *335*, 813-817.

37. Huang, X. C.; Lin, Y. Y.; Zhang, J. P.; Chen, X. M., Ligand-directed strategy for zeolite-type metal-organic frameworks: zinc(II) imidazolates with unusual zeolitic topologies. *Angew. Chem. Int. Ed.* **2006,** *45*, 1557-1559.

38. An, J.; Shade, C. M.; Chengelis-Czegan, D. A.; Petoud, S.; Rosi, N. L., Zinc-adeninate metal-organic framework for aqueous encapsulation and sensitization of near-infrared and visible emitting lanthanide cations. *J. Am. Chem. Soc.* **2011,** *133*, 1220-1223.

39. Hoskins, B. F.; Robson, R., Design and Construction of a New Class of Scaffolding-Like Materials Comprising Infinite Polymeric Frameworks of 3-D-Linked Molecular Rods

- a Reappraisal of the $Zn(CN)_2$ and $Cd(CN)_2$ Structures and the Synthesis and Structure of the Diamond-Related Frameworks $[N(CH_3)_4][Cuiznii(CN)_4]$ and Cui[4,4',4'',4'''-Tetracyanotetraphenylmethane]$BF_4.xC_6H_5NO_2$. *J. Am. Chem. Soc.* **1990,** *112*, 1546-1554.

40. Gardner, G. B.; Venkataraman, D.; Moore, J. S.; Lee, S., Spontaneous Assembly of a Hinged Coordination Network. *Nature* **1995,** *374*, 792-795.

41. Subramanian, S.; Zaworotko, M. J., Porous Solids by Design:$[Zn(4,4'-bpy)_2(SiF_6)]n\cdot xDMF$, a Single Framework Octahedral Coordination Polymer with Large Square Channels. *Angew. Chem. Int. Ed.* **1995,** *34*, 2127-2129.

42. Abrahams, B. F.; Hoskins, B. F.; Michail, D. M.; Robson, R., Assembly of Porphyrin Building-Blocks into Network Structures with Large Channels. *Nature* **1994,** *369*, 727-729.

43. Yaghi, O. M.; Li, H. L.; Davis, C.; Richardson, D.; Groy, T. L., Synthetic strategies, structure patterns, and emerging properties in the chemistry of modular porous solids. *Acc. Chem. Res.* **1998,** *31*, 474-484.

44. Chen, B.; Eddaoudi, M.; Hyde, S. T.; O'Keeffe, M.; Yaghi, O. M., Interwoven metal-organic framework on a periodic minimal surface with extra-large pores. *Science* **2001,** *291*, 1021-1023.

45. Eddaoudi, M.; Kim, J.; Rosi, N.; Vodak, D.; Wachter, J.; O'Keeffe, M.; Yaghi, O. M., Systematic design of pore size and functionality in isoreticular MOFs and their application in methane storage. *Science* **2002,** *295*, 469-472.

46. Banerjee, R.; Phan, A.; Wang, B.; Knobler, C.; Furukawa, H.; O'Keeffe, M.; Yaghi, O. M., High-throughput synthesis of zeolitic imidazolate frameworks and application to CO_2 capture. *Science* **2008,** *319*, 939-943.

47. Park, K. S.; Ni, Z.; Cote, A. P.; Choi, J. Y.; Huang, R.; Uribe-Romo, F. J.; Chae, H. K.; O'Keeffe, M.; Yaghi, O. M., Exceptional chemical and thermal stability of zeolitic imidazolate frameworks. *Proc. Natl. Acad. Sci. USA* **2006,** *103*, 10186-10191.

48. Tian, Y. Q.; Cai, C. X.; Ren, X. M.; Duan, C. Y.; Xu, Y.; Gao, S.; You, X. Z., The silica-like extended polymorphism of cobalt(II) imidazolate three-dimensional frameworks: X-ray single-crystal structures and magnetic properties. *Chem. Eur. J.* **2003,** *9*, 5673-5685.

49. O'Keeffe, M.; Yaghi, O. M., Deconstructing the crystal structures of metal-organic frameworks and related materials into their underlying nets. *Chem. Rev.* **2012,** *112*, 675-702.

50. Goldberg, I., Metalloporphyrin molecular sieves. *Chem. Eur. J.* **2000,** *6*, 3863-3870.

51. Yu, P.; Kahn, O.; Sletten, J.; Renard, J. P.; Georges, R.; Gianduzzo, J. C.; Curely, J.; Qiang, X., Structure and Magnetism of the 1st Alternating Bimetallic Chain Compound $MnCu(OPB)(H_2O)_3.H_2O$ (OPB = Oxamidobis(Propionato)). *Inorg. Chem.* **1988,** *27*, 47-53.

52. Tamaki, H.; Zhong, Z. J.; Matsumoto, N.; Kida, S.; Koikawa, M.; Achiwa, N.; Hashimoto, Y.; Okawa, H., Design of metal-complex magnets. Syntheses and magnetic properties of mixed-metal assemblies $\{NBu_4[MCr(ox)_3]\}x$ (NBu_4+ = tetra(n-butyl)ammonium ion; ox^{2-} = oxalate ion; M = Mn^{2+}, Fe^{2+}, Co^{2+}, Ni^{2+}, Cu^{2+}, Zn^{2+}). *J. Am. Chem. Soc.* **1992,** *114*, 6974-6979.

53. Carling, S. G.; Mathoniere, C.; Day, P.; Malik, K. M. A.; Coles, S. J.; Hursthouse, M. B., Crystal structure and magnetic properties of the layer ferrimagnet $N(n\text{-}C_5H_{11})_4Mn^{II}Fe^{III}(C_2O_4)_3$. *J. Chem. Soc., Dalton Trans.* **1996**, 1839-1843.

54. Larionova, J.; Mombelli, B.; Sanchiz, J.; Kahn, O., Magnetic Properties of the Two-Dimensional Bimetallic Compounds $(NBu_4)[M^{II}Ru^{III}(ox)_3]$ (NBu_4 = Tetra-n-butylammonium; M = Mn, Fe, Cu; ox = Oxalate). *Inorg. Chem.* **1998,** *37*, 679-684.

55. Noro, S.; Kitagawa, S.; Yamashita, M.; Wada, T., New microporous coordination polymer affording guest-coordination sites at channel walls. *Chem. Commun.* **2002**, 222-223.

56. Kitaura, R.; Onoyama, G.; Sakamoto, H.; Matsuda, R.; Noro, S.; Kitagawa, S., Immobilization of a metallo Schiff base into a microporous coordination polymer. *Angew. Chem. Int. Ed.* **2004,** *43*, 2684-2687.

57. Kawata, S.; Kitagawa, S.; Kumagai, H.; Kudo, C.; Kamesaki, H.; Ishiyama, T.; Suzuki, R.; Kondo, M.; Katada, M., Rational Design of a Novel Intercalation System. Layer-Gap Control of Crystalline Coordination Polymers, $\{[Cu(ca)(H_2O)_m]G\}_n$(m= 2, G = 2,5-Dimethylpyrazine and Phenazine;m= 1, G = 1,2,3,4,6,7,8,9-Octahydrophenazine). *Inorg. Chem.* **1996,** *35*, 4449-4461.

58. Kitaura, R.; Fujimoto, K.; Noro, S.; Kondo, M.; Kitagawa, S., A pillared-layer coordination polymer network displaying hysteretic sorption: [Cu(2)(pzdc)(2)(dpyg)](n) (pzdc= pyrazine-2,3-dicarboxylate; dpyg=1,2-Di(4-pyridyl)glycol). *Angew. Chem. Int. Ed.* **2002,** *41*, 133-135.

59. Beauvais, L. G.; Shores, M. P.; Long, J. R., Cyano-Bridged Re_6Q_8(Q = S, Se) Cluster-Cobalt(II) Framework Materials: Versatile Solid Chemical Sensors. *J. Am. Chem. Soc.* **2000,** *122*, 2763-2772.

60. Dubbeldam, D.; Krishna, R.; Snurr, R. Q., Method for Analyzing Structural Changes of Flexible Metal-Organic Frameworks Induced by Adsorbates. *J. Phys. Chem. C* **2009,** *113*, 19317-19327.

61. Jones, C. L.; Tansell, A. J.; Easun, T. L., The lighter side of MOFs: structurally photoresponsive metal-organic frameworks. *J. Mater. Chem. A* **2016,** *4*, 6714-6723.

62. Kumari, G.; Patil, N. R.; Bhadram, V. S.; Haldar, R.; Bonakala, S.; Maji, T. K.; Narayana, C., Understanding guest and pressure-induced porosity through structural transition in flexible interpenetrated MOF by Raman spectroscopy. *Journal of Raman Spectroscopy* **2016,** *47*, 149-155.

63. Mazaj, M.; Mali, G.; Rangus, M.; Zunkovic, E.; Kaucic, V.; Logar, N. Z., Spectroscopic Studies of Structural Dynamics Induced by Heating and Hydration: A Case of Calcium-Terephthalate Metal-Organic Framework. *J. Phys. Chem. C* **2013,** *117*, 7552-7564.

64. Qiao, C.; Sun, L.; Zhang, S.; Liu, P.; Chang, L.; Zhou, C.; Wei, Q.; Chen, S.; Gao, S., Pore-size-tuned host–guest interactions in Co-MOFs via in situ microcalorimetry: adsorption and magnetism. *J. Mater. Chem. C* **2017,** *5*, 1064-1073.

65. Chaudhari, A. K.; Nagarkar, S. S.; Joarder, B.; Mukherjee, S.; Ghosh, S. K., Structural dynamism and controlled chemical blocking/unblocking of active coordination space of a soft porous crystal. *Inorg. Chem.* **2013,** *52*, 12784-12789.

66. Yanai, N.; Uemura, T.; Inoue, M.; Matsuda, R.; Fukushima, T.; Tsujimoto, M.; Isoda, S.; Kitagawa, S., Guest-to-host transmission of structural changes for stimuli-responsive adsorption property. *J. Am. Chem. Soc.* **2012,** *134*, 4501-4504.

67. Bureekaew, S.; Horike, S.; Higuchi, M.; Mizuno, M.; Kawamura, T.; Tanaka, D.; Yanai, N.; Kitagawa, S., One-dimensional imidazole aggregate in aluminium porous coordination polymers with high proton conductivity. *Nat. Mater.* **2009,** *8*, 831-836.

68. Hurd, J. A.; Vaidhyanathan, R.; Thangadurai, V.; Ratcliffe, C. I.; Moudrakovski, I. L.; Shimizu, G. K., Anhydrous proton conduction at 150 deg. C in a crystalline metal-organic framework. *Nat. Chem.* **2009,** *1*, 705-710.

69. Sadakiyo, M.; Yamada, T.; Kitagawa, H., Proton conductivity control by ion substitution in a highly proton-conductive metal-organic framework. *J. Am. Chem. Soc.* **2014,** *136*, 13166-13169.

70. Sadakiyo, M.; Okawa, H.; Shigematsu, A.; Ohba, M.; Yamada, T.; Kitagawa, H., Promotion of low-humidity proton conduction by controlling hydrophilicity in layered metal-organic frameworks. *J. Am. Chem. Soc.* **2012,** *134*, 5472-5475.

71. Jeong, N. C.; Samanta, B.; Lee, C. Y.; Farha, O. K.; Hupp, J. T., Coordination-chemistry control of proton conductivity in the iconic metal-organic framework material HKUST-1. *J. Am. Chem. Soc.* **2012,** *134*, 51-54.

72. Wei, Q.; James, S. L., A metal-organic gel used as a template for a porous organic polymer. *Chem. Commun.* **2005**, 1555-1556.

73. Lohe, M. R.; Rose, M.; Kaskel, S., Metal-organic framework (MOF) aerogels with high micro- and macroporosity. *Chem. Commun.* **2009**, 6056-6058.

74. Li, L.; Xiang, S.; Cao, S.; Zhang, J.; Ouyang, G.; Chen, L.; Su, C. Y., A synthetic route to ultralight hierarchically micro/mesoporous Al(III)-carboxylate metal-organic aerogels. *Nat. Commun.* **2013,** *4*, 1774.

75. Bueken, B.; Van Velthoven, N.; Willhammar, T.; Stassin, T.; Stassen, I.; Keen, D. A.; Baron, G. V.; Denayer, J. F. M.; Ameloot, R.; Bals, S.; De Vos, D.; Bennett, T. D., Gel-based morphological design of zirconium metal-organic frameworks. *Chem. Sci.* **2017,** *8*, 3939-3948.

76. Tian, T.; Velazquez-Garcia, J.; Bennett, T. D.; Fairen-Jimenez, D., Mechanically and chemically robust ZIF-8 monoliths with high volumetric adsorption capacity. *J. Mater. Chem. A* **2015,** *3*, 2999-3005.

77. Hosseini, P.; Wright, C. D.; Bhaskaran, H., An optoelectronic framework enabled by low-dimensional phase-change films. *Nature* **2014,** *511*, 206-211.

78. Yan, X.; Cook, T. R.; Wang, P.; Huang, F.; Stang, P. J., Highly emissive platinum(II) metallacages. *Nat. Chem.* **2015,** *7*, 342-348.

79. Babu, S. S.; Praveen, V. K.; Ajayaghosh, A., Functional pi-Gelators and Their Applications. *Chem. Rev.* **2014,** *114*, 1973-2129.

80. Chung, J. W.; Yoon, S. J.; Lim, S. J.; An, B. K.; Park, S. Y., Dual-mode switching in highly fluorescent organogels: binary logic gates with optical/thermal inputs. *Angew. Chem. Int. Ed.* **2009,** *48*, 7030-7034.

81. Srinivasan, S.; Babu, P. A.; Mahesh, S.; Ajayaghosh, A., Reversible self-assembly of entrapped fluorescent gelators in polymerized styrene gel matrix: erasable thermal imaging via recreation of supramolecular architectures. *J. Am. Chem. Soc.* **2009,** *131*, 15122-15123.

82. Sugiyasu, K.; Fujita, N.; Takeuchi, M.; Yamada, S.; Shinkai, S., Proton-sensitive fluorescent organogels. *Org. Biomol. Chem.* **2003,** *1*, 895-899.

83. Jang, H. S.; Yang, H.; Kim, S. W.; Han, J. Y.; Lee, S. G.; Jeon, D. Y., White light-emitting diodes with excellent color rendering based on organically capped CdSe quantum dots and Sr_3SiO_5 : Ce^{3+}, Li^+ phosphors. *Adv. Mater.* **2008,** *20*, 2696-.

84. Hu, J.; Li, C.; Liu, S., Hg2+-reactive double hydrophilic block copolymer assemblies as novel multifunctional fluorescent probes with improved performance. *Langmuir* **2010,** *26*, 724-729.

85. Li, N. J.; Xu, Q. F.; Xia, X. W.; Wang, L. H.; Lu, J. M.; Wen, X. W., A polymeric chemosensor for Fe^{3+} based on fluorescence quenching of polymer with quinoline derivative in the side chain. *Mater. Chem. Phys.* **2009,** *114*, 339-343.

86. Hyakutake, T.; Okura, I.; Asai, K.; Nishide, H., Dual-mode oxygen-sensing based on oxygen-adduct formation at cobaltporphyrin-polymer and luminescence quenching of

pyrene: an optical oxygen sensor for a practical atmospheric pressure. *J. Mater. Chem.* **2008,** *18*, 917-922.

87. Yu, X.; Marks, T. J.; Facchetti, A., Metal oxides for optoelectronic applications. *Nat. Mater.* **2016,** *15*, 383-396.

88. Xu, H.; Chen, R.; Sun, Q.; Lai, W.; Su, Q.; Huang, W.; Liu, X., Recent progress in metal-organic complexes for optoelectronic applications. *Chem. Soc. Rev.* **2014,** *43*, 3259-3302.

89. Britnell, L.; Ribeiro, R. M.; Eckmann, A.; Jalil, R.; Belle, B. D.; Mishchenko, A.; Kim, Y. J.; Gorbachev, R. V.; Georgiou, T.; Morozov, S. V.; Grigorenko, A. N.; Geim, A. K.; Casiraghi, C.; Castro Neto, A. H.; Novoselov, K. S., Strong light-matter interactions in heterostructures of atomically thin films. *Science* **2013,** *340*, 1311-1314.

90. Jiao, Y.; Zhou, L.; Ma, F.; Gao, G.; Kou, L.; Bell, J.; Sanvito, S.; Du, A., Predicting Single-Layer Technetium Dichalcogenides (TcX_2), X = S, Se) with Promising Applications in Photovoltaics and Photocatalysis. *Acs Appl. Mater. Inter.* **2016,** *8*, 5385-5392.

91. Choi, J.; Zhang, H.; Choi, J. H., Modulating Optoelectronic Properties of Two-Dimensional Transition Metal Dichalcogenide Semiconductors by Photoinduced Charge Transfer. *Acs Nano* **2016,** *10*, 1671-1680.

92. Li, S. L.; Tsukagoshi, K.; Orgiu, E.; Samori, P., Charge transport and mobility engineering in two-dimensional transition metal chalcogenide semiconductors. *Chem. Soc. Rev.* **2016,** *45*, 118-151.

93. Ferrari, A. C.; Bonaccorso, F.; Fal'ko, V.; Novoselov, K. S.; Roche, S.; Boggild, P.; Borini, S.; Koppens, F. H.; Palermo, V.; Pugno, N.; Garrido, J. A.; Sordan, R.; Bianco, A.; Ballerini, L.; Prato, M.; Lidorikis, E.; Kivioja, J.; Marinelli, C.; Ryhanen, T.; Morpurgo, A.; Coleman, J. N.; Nicolosi, V.; Colombo, L.; Fert, A.; Garcia-Hernandez, M.; Bachtold, A.; Schneider, G. F.; Guinea, F.; Dekker, C.; Barbone, M.; Sun, Z.; Galiotis, C.; Grigorenko, A. N.; Konstantatos, G.; Kis, A.; Katsnelson, M.; Vandersypen, L.; Loiseau, A.; Morandi, V.; Neumaier, D.; Treossi, E.; Pellegrini, V.; Polini, M.; Tredicucci, A.; Williams, G. M.; Hong, B. H.; Ahn, J. H.; Kim, J. M.; Zirath, H.; van Wees, B. J.; van der Zant, H.; Occhipinti, L.; Di Matteo, A.; Kinloch, I. A.; Seyller, T.; Quesnel, E.; Feng, X.; Teo, K.; Rupesinghe, N.; Hakonen, P.; Neil, S. R.; Tannock, Q.; Lofwander, T.; Kinaret, J., Science and technology roadmap for graphene, related two-dimensional crystals, and hybrid systems. *Nanoscale* **2015,** *7*, 4598-4810.

94. Carne, A.; Carbonell, C.; Imaz, I.; Maspoch, D., Nanoscale metal-organic materials. *Chem. Soc. Rev.* **2011,** *40*, 291-305.

95. Stassen, I.; Styles, M.; Grenci, G.; Gorp, H. V.; Vanderlinden, W.; Feyter, S. D.; Falcaro, P.; Vos, D. D.; Vereecken, P.; Ameloot, R., Chemical vapour deposition of zeolitic imidazolate framework thin films. *Nat. Mater.* **2016,** *15*, 304-310.

96. Jin, S.; Son, H. J.; Farha, O. K.; Wiederrecht, G. P.; Hupp, J. T., Energy transfer from quantum dots to metal-organic frameworks for enhanced light harvesting. *J. Am. Chem. Soc.* **2013,** *135*, 955-958.

97. Lin, X.; Gao, G.; Zheng, L.; Chi, Y.; Chen, G., Encapsulation of strongly fluorescent carbon quantum dots in metal-organic frameworks for enhancing chemical sensing. *Anal. Chem.* **2014,** *86*, 1223-1228.

98. Son, H. J.; Jin, S.; Patwardhan, S.; Wezenberg, S. J.; Jeong, N. C.; So, M.; Wilmer, C. E.; Sarjeant, A. A.; Schatz, G. C.; Snurr, R. Q.; Farha, O. K.; Wiederrecht, G. P.; Hupp, J. T., Light-harvesting and ultrafast energy migration in porphyrin-based metal-organic frameworks. *J. Am. Chem. Soc.* **2013,** *135*, 862-869.

99. Chen, B. L.; Yang, Y.; Zapata, F.; Lin, G. N.; Qian, G. D.; Lobkovsky, E. B., Luminescent open metal sites within a metal-organic framework for sensing small molecules. *Adv. Mater.* **2007,** *19*, 1693-1696.

100. Lan, A.; Li, K.; Wu, H.; Olson, D. H.; Emge, T. J.; Ki, W.; Hong, M.; Li, J., A luminescent microporous metal-organic framework for the fast and reversible detection of high explosives. *Angew. Chem. Int. Ed.* **2009,** *48*, 2334-2338.

101. Nagarkar, S. S.; Joarder, B.; Chaudhari, A. K.; Mukherjee, S.; Ghosh, S. K., Highly selective detection of nitro explosives by a luminescent metal-organic framework. *Angew. Chem. Int. Ed.* **2013,** *52*, 2881-2885.

102. Allendorf, M. D.; Bauer, C. A.; Bhakta, R. K.; Houk, R. J., Luminescent metal-organic frameworks. *Chem. Soc. Rev.* **2009,** *38*, 1330-1352.

103. Sun, Y. Q.; Lei, Y. L.; Gao, J.; Sun, X. H.; Lin, S. H.; Bao, Q. L.; Liao, Q.; Lee, S. T.; Liao, L. S., Two-dimensional optical waveguiding and luminescence vapochromic properties of 8-hydroxyquinoline zinc (Znq_2) hexagonal microsheets. *Chem. Commun.* **2014,** *50*, 10812-10814.

104. Pawley, G. S., Unit-Cell Refinement from Powder Diffraction Scans. *J. Appl. Crystallogr.* **1981,** *14*, 357-361.

105. Delley, B., Time dependent density functional theory with DMol3. *J Phys Condens Matter* **2010,** *22*, 384208.

106. Patey, M. D.; Dessent, C. E. H., A PW91 Density Functional Study of Conformational Choice in 2-Phenylethanol,n-Butylbenzene, and Their Cations: Problems for Density Functional Theory? *The Journal of Physical Chemistry A* **2002,** *106*, 4623-4631.

107. Lehn, J. M., Perspectives in Supramolecular Chemistry - from Molecular Recognition Towards Molecular Information-Processing and Self-Organization. *Angew. Chem. Int. Ed.* **1990,** *29*, 1304-1319.

108. Menger, F. M., Supramolecular chemistry and self-assembly. *Proc. Natl. Acad. Sci. USA* **2002,** *99*, 4818-4822.

109. Prins, L. J.; Huskens, J.; de Jong, F.; Timmerman, P.; Reinhoudt, D. N., Complete asymmetric induction of supramolecular chirality in a hydrogen-bonded assembly. *Nature* **1999,** *398*, 498-502.

110. Scherman, O. A., Supramolecular chemistry: form leading to function. *Nat. Chem.* **2009,** *1*, 524-525.

111. Hansell, C., Self-assembly: Sound and vision. *Nat. Chem.* **2014,** *6*, 459-459.

112. Tam, A. Y.; Yam, V. W., Recent advances in metallogels. *Chem. Soc. Rev.* **2013,** *42*, 1540-1567.

113. Lin, Q.; Sun, B.; Yang, Q. P.; Fu, Y. P.; Zhu, X.; Zhang, Y. M.; Wei, T. B., A novel strategy for the design of smart supramolecular gels: controlling stimuli-response properties through competitive coordination of two different metal ions. *Chem. Commun.* **2014,** *50*, 10669-10671.

114. Dong, S. Y.; Yuan, J. Y.; Huang, F. H., A pillar[5]arene/imidazolium [2]rotaxane: solvent-and thermo-driven molecular motions and supramolecular gel formation. *Chem. Sci.* **2014,** *5*, 247-252.

115. Buerkle, L. E.; Rowan, S. J., Supramolecular gels formed from multi-component low molecular weight species. *Chem. Soc. Rev.* **2012,** *41*, 6089-6102.

116. Byrne, M. E.; Park, K.; Peppas, N. A., Molecular imprinting within hydrogels. *Adv. Drug. Deliver. Rev.* **2002,** *54*, 149-161.

117. Wu, J. H.; Lan, Z.; Lin, J. M.; Huang, M. L.; Hao, S. C.; Sato, T.; Yin, S., A novel thermosetting gel electrolyte for stable quasi-solid-state dye-sensitized solar cells. *Adv. Mater.* **2007,** *19*, 4006-4011.

118. Kim, Y.; Kathaperumal, M.; Chen, V. W.; Park, Y.; Fuentes-Hernandez, C.; Pan, M. J.; Kippelen, B.; Perry, J. W., Bilayer Structure with Ultrahigh Energy/Power Density Using Hybrid Sol-Gel Dielectric and Charge-Blocking Monolayer. *Adv. Energy. Mater.* **2015,** *5*.

119. Mohan, D.; Pittman, C. U., Jr., Arsenic removal from water/wastewater using adsorbents-A critical review. *J. Hazard. Mater.* **2007,** *142*, 1-53.

120. Murata, K.; Aoki, M.; Nishi, T.; Ikeda, A.; Shinkai, S., New Cholesterol-Based Gelators with Light-Responsive and Metal-Responsive Functions. *J. Chem. Soc., Chem. Commun.* **1991**, 1715-1718.

121. Bengang, X. M.-F., C.; Bing, Xu, Design of Coordination Polymer Gels as Stable Catalytic Systems. *Chem. Eur. J.* **2002,** *8*, 5028-5032.

122. Tam, A. Y.; Wong, K. M.; Wang, G.; Yam, V. W., Luminescent metallogels of platinum(II) terpyridyl complexes: interplay of metal...metal, pi-pi and hydrophobic-hydrophobic interactions on gel formation. *Chem. Commun.* **2007**, 2028-2030.

123. Tu, T.; Fang, W.; Bao, X.; Li, X.; Dotz, K. H., Visual chiral recognition through enantioselective metallogel collapsing: synthesis, characterization, and application of platinum-steroid low-molecular-mass gelators. *Angew. Chem. Int. Ed.* **2011,** *50*, 6601-6605.

124. Piepenbrock, M. O.; Clarke, N.; Steed, J. W., Metal ion and anion-based "tuning" of a supramolecular metallogel. *Langmuir* **2009,** *25*, 8451-8456.

125. Miao, W.; Zhang, L.; Wang, X.; Cao, H.; Jin, Q.; Liu, M., A dual-functional metallogel of amphiphilic copper(II) quinolinol: redox responsiveness and enantioselectivity. *Chem. Eur. J.* **2013,** *19*, 3029-3036.

126. Gee, W. J.; Batten, S. R., Instantaneous gelation of a new copper(II) metallogel amenable to encapsulation of a luminescent lanthanide cluster. *Chem. Commun.* **2012,** *48*, 4830-4832.

127. Wei, Q.; James, S. L., A metal-organic gel used as a template for a porous organic polymer. *Chem. Commun.* **2005**, 1555-1556.

128. Nune, S. K.; Thallapally, P. K.; McGrail, B. P., Metal organic gels (MOGs): a new class of sorbents for CO_2 separation applications. *J. Mater. Chem.* **2010,** *20*, 7623-7625.

129. Yang, F.; Lin, Z.; He, X.; Chen, L.; Zhang, Y., Synthesis and application of a macroporous boronate affinity monolithic column using a metal-organic gel as a porogenic template for the specific capture of glycoproteins. *J. Chromatogr. A* **2011,** *1218*, 9194-9201.

130. Saha, S.; Das, G.; Thote, J.; Banerjee, R., Photocatalytic metal-organic framework from CdS quantum dot incubated luminescent metallohydrogel. *J. Am. Chem. Soc.* **2014,** *136*, 14845-14851.

131. Samai, S.; Biradha, K., Chemical and Mechano Responsive Metal-Organic Gels of Bis(benzimidazole)-Based Ligands with Cd(II) and Cu(II) Halide Salts: Self Sustainability and Gas and Dye Sorptions. *Chem. Mater.* **2012,** *24*, 1165-1173.

132. Zhang, J. Y.; Su, C. Y., Metal-organic gels: From discrete metallogelators to coordination polymers. *Coord. Chem. Rev.* **2013,** *257*, 1373-1408.

133. Zhang, Y.-M.; You, X.-M.; Yao, H.; Guo, Y.; Zhang, P.; Shi, B.-B.; Liu, J.; Lin, Q.; Wei, T.-B., A silver-induced metal-organic gel based on biscarboxyl-functionalised benzimidazole derivative: stimuli responsive and dye sorption. *Supramol. Chem.* **2013,** *26*, 39-47.

134. Chaudhari, A. K.; Han, I.; Tan, J. C., Multifunctional Supramolecular Hybrid Materials Constructed from Hierarchical Self-Ordering of In Situ Generated Metal-Organic Framework (MOF) Nanoparticles. *Adv. Mater.* **2015,** *27*, 4438-4446.

135. Chaudhari, A. K.; Kim, H. J.; Han, I.; Tan, J. C., Optochemically Responsive 2D Nanosheets of a 3D Metal-Organic Framework Material. *Adv. Mater.* **2017,** *29*, 1701463.

136. Tan, J. C.; Civalleri, B., Metal-Organic Frameworks and Hybrid Materials: From Fundamentals to Applications. *CrystEngComm* **2015,** *17*, 197-198.

137. Campbell, M. G.; Sheberla, D.; Liu, S. F.; Swager, T. M.; Dinca, M., Cu(3)(hexaiminotriphenylene)(2): an electrically conductive 2D metal-organic framework for chemiresistive sensing. *Angew. Chem. Int. Ed.* **2015,** *54*, 4349-4352.

138. Ferey, G., Hybrid porous solids: past, present, future. *Chem. Soc. Rev.* **2008,** *37*, 191-214.

139. Chaudhari, A. K.; Ryder, M. R.; Tan, J. C., Photonic hybrid crystals constructed from in situ host-guest nanoconfinement of a light-emitting complex in metal-organic framework pores. *Nanoscale* **2016,** *8*, 6851-6859.

140. Ryder, M. R.; Tan, J. C., Nanoporous metal organic framework materials for smart applications. *Mater. Sci. Technol.* **2014,** *30*, 1598-1612.

141. Furukawa, H.; Cordova, K. E.; O'Keeffe, M.; Yaghi, O. M., The chemistry and applications of metal-organic frameworks. *Science* **2013,** *341*, 1230444.

142. Furukawa, S.; Reboul, J.; Diring, S.; Sumida, K.; Kitagawa, S., Structuring of metal-organic frameworks at the mesoscopic/macroscopic scale. *Chem. Soc. Rev.* **2014,** *43*, 5700-5734.

143. Heeres, A.; van der Pol, C.; Stuart, M.; Friggeri, A.; Feringa, B. L.; van Esch, J., Orthogonal self-assembly of low molecular weight hydrogelators and surfactants. *J. Am. Chem. Soc.* **2003,** *125*, 14252-14253.

144. Hofmeier, H.; Schubert, U. S., Combination of orthogonal supramolecular interactions in polymeric architectures. *Chem. Commun.* **2005**, 2423-2432.

145. Chui, S. S.; Lo, S. M.; Charmant, J. P.; Orpen, A. G.; Williams, I. D., A chemically functionalizable nanoporous material. *Science* **1999,** *283*, 1148-1150.

146. Bhunia, M. K.; Hughes, J. T.; Fettinger, J. C.; Navrotsky, A., Thermochemistry of paddle wheel MOFs: Cu-HKUST-1 and Zn-HKUST-1. *Langmuir* **2013,** *29*, 8140-8145.

147. Wang, F. L.; Guo, H. L.; Chai, Y. M.; Li, Y. P.; Liu, C. G., The controlled regulation of morphology and size of HKUST-1 by "coordination modulation method". *Micropor. Mesopor. Mat.* **2013,** *173*, 181-188.

148. Ranft, A.; Betzler, S. B.; Haase, F.; Lotsch, B. V., Additive-mediated size control of MOF nanoparticles. *CrystEngComm* **2013,** *15*, 9296-9300.

149. Kim, K. J.; Li, Y. J.; Kreider, P. B.; Chang, C. H.; Wannenmacher, N.; Thallapally, P. K.; Ahn, H. G., High-rate synthesis of Cu-BTC metal-organic frameworks. *Chem. Commun.* **2013,** *49*, 11518-11520.

150. Huo, J.; Brightwell, M.; El Hankari, S.; Garai, A.; Bradshaw, D., A versatile, industrially relevant, aqueous room temperature synthesis of HKUST-1 with high space-time yield. *J. Mater. Chem. A* **2013,** *1*, 15220-15223.

151. Ameloot, R.; Vermoortele, F.; Vanhove, W.; Roeffaers, M. B.; Sels, B. F.; De Vos, D. E., Interfacial synthesis of hollow metal-organic framework capsules demonstrating selective permeability. *Nat. Chem.* **2011,** *3*, 382-387.

152. Carne-Sanchez, A.; Imaz, I.; Cano-Sarabia, M.; Maspoch, D., A spray-drying strategy for synthesis of nanoscale metal-organic frameworks and their assembly into hollow superstructures. *Nat. Chem.* **2013,** *5*, 203-211.

153. Jeremias, F.; Henninger, S. K.; Janiak, C., High performance metal-organic-framework coatings obtained via thermal gradient synthesis. *Chem. Commun.* **2012,** *48*, 9708-9710.

154. Xiang, S. L.; Li, L.; Zhang, J. Y.; Tan, X.; Cui, H. N.; Shi, J. Y.; Hu, Y. L.; Chen, L. P.; Su, C. Y.; James, S. L., Porous organic-inorganic hybrid aerogels based on Cr3+/Fe3+ and rigid bridging carboxylates. *J. Mater. Chem.* **2012,** *22*, 1862-1867.

155. Xia, W.; Zhang, X. M.; Xu, L.; Wang, Y. X.; Lin, J. H.; Zou, R. Q., Facile and economical synthesis of metal-organic framework MIL-100(Al) gels for high efficiency removal of microcystin-LR. *RSC Adv.* **2013,** *3*, 11007-11013.

156. Wei, S. C.; Pan, M.; Li, K.; Wang, S.; Zhang, J.; Su, C. Y., A multistimuli-responsive photochromic metal-organic gel. *Adv. Mater.* **2014,** *26*, 2072-2077.

157. Kamlet, M. J.; Abboud, J. L. M.; Abraham, M. H.; Taft, R. W., Linear solvation energy relationships. 23. A comprehensive collection of the solvatochromic parameters, .pi.*, .alpha., and .beta., and some methods for simplifying the generalized solvatochromic equation. *J. Org. Chem.* **1983,** *48*, 2877-2887.

158. Davey, R. J.; Brychczynska, M.; Sadiq, G.; Dent, G.; Pritchard, R. G., Crystallising trimesic acid from DMSO solutions – can crystallography teach us anything about the process of crystal nucleation? *CrystEngComm* **2013,** *15*, 856-859.

159. Zhang, Z.; Nguyen, H. T.; Miller, S. A.; Cohen, S. M., polyMOFs: A Class of Interconvertible Polymer-Metal-Organic-Framework Hybrid Materials. *Angew. Chem. Int. Ed.* **2015,** *54*, 6152-6157.

160. Tsotsalas, M.; Liu, J.; Tettmann, B.; Grosjean, S.; Shahnas, A.; Wang, Z.; Azucena, C.; Addicoat, M.; Heine, T.; Lahann, J.; Overhage, J.; Brase, S.; Gliemann, H.; Woll, C., Fabrication of highly uniform gel coatings by the conversion of surface-anchored metal-organic frameworks. *J. Am. Chem. Soc.* **2014,** *136*, 8-11.

161. Allen, C. A.; Cohen, S. M., Exploration of chemically cross-linked metal-organic frameworks. *Inorg. Chem.* **2014,** *53*, 7014-7019.

162. Mikuriya, M.; Azuma, H.; Nukada, R.; Handa, M., Synthesis, X-ray structures, and magnetic properties of $[Cu_2(piv)_4(Et_3N)_2]$ and $[Cu_6(piv)_6(EtO)_6]$ (Hpiv = pivalic acid): Role of base for dinuclear adduct and oligonuclear formation. *Chem. Lett.* **1999**, 57-58.

163. Chaudhuri, P.; Hess, M.; Weyhermuller, T.; Wieghardt, K., Aerobic oxidation of primary alcohols by a new mononuclear Cu-II-radical catalyst. *Angew. Chem. Int. Ed.* **1999,** *38*, 1095-1098.

164. Shoaee, M.; Anderson, M. W.; Attfield, M. P., Crystal growth of the nanoporous metal-organic framework HKUST-1 revealed by in situ atomic force microscopy. *Angew. Chem. Int. Ed.* **2008,** *47*, 8525-8528.

165. Barnes, H. A., Thixotropy - A review. *J. Non-Newton. Fluid Mechan.* **1997,** *70*, 1-33.

166. Park, S. S.; Hontz, E. R.; Sun, L.; Hendon, C. H.; Walsh, A.; Van Voorhis, T.; Dinca, M., Cation-dependent intrinsic electrical conductivity in isostructural tetrathiafulvalene-based microporous metal-organic frameworks. *J. Am. Chem. Soc.* **2015,** *137*, 1774-1777.

167. Pan, L.; Yu, G.; Zhai, D.; Lee, H. R.; Zhao, W.; Liu, N.; Wang, H.; Tee, B. C.; Shi, Y.; Cui, Y.; Bao, Z., Hierarchical nanostructured conducting polymer hydrogel with high electrochemical activity. *Proc. Natl. Acad. Sci. USA* **2012,** *109*, 9287-9292.

168. Gale, E.; Pearson, D.; Kitson, S.; Adamatzky, A.; Costello, B. D. L., The effect of changing electrode metal on solution-processed flexible titanium dioxide memristors. *arXiv:1106.6293v2* **2011**.

169. Del Pópolo, M. G.; Voth, G. A., On the Structure and Dynamics of Ionic Liquids. *J. Phys. Chem. B* **2004,** *108*, 1744-1752.

170. Talin, A. A.; Centrone, A.; Ford, A. C.; Foster, M. E.; Stavila, V.; Haney, P.; Kinney, R. A.; Szalai, V.; El Gabaly, F.; Yoon, H. P.; Leonard, F.; Allendorf, M. D., Tunable electrical conductivity in metal-organic framework thin-film devices. *Science* **2014,** *343*, 66-69.

171. *Oxford Instruments Asylum Research Inc., AM-FM Viscoelastic Mapping Mode Application Note*; 2013.

172. Tan, J. C.; Cheetham, A. K., Mechanical properties of hybrid inorganic-organic framework materials: establishing fundamental structure-property relationships. *Chem. Soc. Rev.* **2011,** *40*, 1059-1080.

173. Bisi, O.; Ossicini, S.; Pavesi, L., Porous silicon: a quantum sponge structure for silicon based optoelectronics. *Surf. Sci. Rep.* **2000,** *38*, 1-126.

174. Kamat, P. V., Meeting the clean energy demand: Nanostructure architectures for solar energy conversion. *J. Phys. Chem. C* **2007,** *111*, 2834-2860.

175. Rao, C. N. R.; Cheetham, A. K.; Thirumurugan, A., Hybrid inorganic-organic materials: a new family in condensed matter physics. *J. Phys.-Condes. Matter* **2008,** *20*, 083202.

176. Zhou, H. C.; Long, J. R.; Yaghi, O. M., Introduction to metal-organic frameworks. *Chem. Rev.* **2012,** *112*, 673-674.

177. Lee, J. H.; Jaworski, J.; Jung, J. H., Luminescent metal-organic framework-functionalized graphene oxide nanocomposites and the reversible detection of high explosives. *Nanoscale* **2013,** *5*, 8533-8540.

178. Allendorf, M. D.; Foster, M. E.; Leonard, F.; Stavila, V.; Feng, P. L.; Doty, F. P.; Leong, K.; Ma, E. Y.; Johnston, S. R.; Talin, A. A., Guest-Induced Emergent Properties in Metal-Organic Frameworks. *J. Phys. Chem. Lett.* **2015,** *6*, 1182-1195.

179. Cui, Y.; Yue, Y.; Qian, G.; Chen, B., Luminescent functional metal-organic frameworks. *Chem. Rev.* **2012,** *112*, 1126-1162.

180. Hu, Z.; Deibert, B. J.; Li, J., Luminescent metal-organic frameworks for chemical sensing and explosive detection. *Chem. Soc. Rev.* **2014,** *43*, 5815-5840.

181. Khajavi, H.; Gascon, J.; Schins, J. M.; Siebbeles, L. D. A.; Kapteijn, F., Unraveling the Optoelectronic and Photochemical Behavior of Zn4O-Based Metal Organic Frameworks. *J. Phys. Chem. C* **2011,** *115*, 12487-12493.

182. Wang, C.; Xie, Z.; deKrafft, K. E.; Lin, W., Doping metal-organic frameworks for water oxidation, carbon dioxide reduction, and organic photocatalysis. *J. Am. Chem. Soc.* **2011,** *133*, 13445-13454.

183. Maza, W. A.; Padilla, R.; Morris, A. J., Concentration Dependent Dimensionality of Resonance Energy Transfer in a Postsynthetically Doped Morphologically Homologous Analogue of UiO-67 MOF with a Ruthenium(II) Polypyridyl Complex. *J. Am. Chem. Soc.* **2015,** *137*, 8161-8168.

184. Sun, C. Y.; Wang, X. L.; Zhang, X.; Qin, C.; Li, P.; Su, Z. M.; Zhu, D. X.; Shan, G. G.; Shao, K. Z.; Wu, H.; Li, J., Efficient and tunable white-light emission of metal-organic frameworks by iridium-complex encapsulation. *Nat. Commun.* **2013,** *4*, 2717.

185. Cui, Y. J.; Song, T.; Yu, J. C.; Yang, Y.; Wang, Z. Y.; Qian, G. D., Dye Encapsulated Metal-Organic Framework for Warm-White LED with High Color-Rendering Index. *Adv. Funct. Mater.* **2015,** *25*, 4796-4802.

186. Shekhah, O.; Cadiau, A.; Eddaoudi, M., Fabrication and non-covalent modification of highly oriented thin films of a zeolite-like metal–organic framework (ZMOF) with rho topology. *CrystEngComm* **2014**.

187. Buso, D.; Jasieniak, J.; Lay, M. D.; Schiavuta, P.; Scopece, P.; Laird, J.; Amenitsch, H.; Hill, A. J.; Falcaro, P., Highly luminescent metal-organic frameworks through quantum dot doping. *Small* **2012,** *8*, 80-88.

188. Lu, G.; Li, S.; Guo, Z.; Farha, O. K.; Hauser, B. G.; Qi, X.; Wang, Y.; Wang, X.; Han, S.; Liu, X.; DuChene, J. S.; Zhang, H.; Zhang, Q.; Chen, X.; Ma, J.; Loo, S. C.; Wei, W. D.; Yang, Y.; Hupp, J. T.; Huo, F., Imparting functionality to a metal-organic framework material by controlled nanoparticle encapsulation. *Nat. Chem.* **2012,** *4*, 310-316.

189. Shen, L.; Wu, W.; Liang, R.; Lin, R.; Wu, L., Highly dispersed palladium nanoparticles anchored on UiO-66(NH(2)) metal-organic framework as a reusable and dual functional visible-light-driven photocatalyst. *Nanoscale* **2013,** *5*, 9374-9382.

190. Zhuang, J.; Kuo, C. H.; Chou, L. Y.; Liu, D. Y.; Weerapana, E.; Tsung, C. K., Optimized metal-organic-framework nanospheres for drug delivery: evaluation of small-molecule encapsulation. *ACS Nano* **2014,** *8*, 2812-2819.

191. An, J.; Rosi, N. L., Tuning MOF CO_2 adsorption properties via cation exchange. *J. Am. Chem. Soc.* **2010,** *132*, 5578-5579.

192. Cravillon, J.; Nayuk, R.; Springer, S.; Feldhoff, A.; Huber, K.; Wiebcke, M., Controlling Zeolitic Imidazolate Framework Nano- and Microcrystal Formation: Insight into Crystal Growth by Time-Resolved In Situ Static Light Scattering. *Chem. Mater.* **2011,** *23*, 2130-2141.

193. Tan, J. C.; Civalleri, B.; Lin, C. C.; Valenzano, L.; Galvelis, R.; Chen, P. F.; Bennett, T. D.; Mellot-Draznieks, C.; Zicovich-Wilson, C. M.; Cheetham, A. K., Exceptionally low shear modulus in a prototypical imidazole-based metal-organic framework. *Phys. Rev. Lett.* **2012,** *108*, 095502.

194. Tan, J. C.; Bennett, T. D.; Cheetham, A. K., Chemical structure, network topology, and porosity effects on the mechanical properties of Zeolitic Imidazolate Frameworks. *Proc. Natl. Acad. Sci. USA* **2010,** *107*, 9938-9943.

195. Tan, J. C.; Civalleri, B.; Erba, A.; Albanese, E., Quantum mechanical predictions to elucidate the anisotropic elastic properties of zeolitic imidazolate frameworks: ZIF-4 vs. ZIF-zni. *CrystEngComm* **2015,** *17*, 375-382.

196. Ryder, M. R.; Tan, J. C., Explaining the mechanical mechanisms of zeolitic metal-organic frameworks: revealing auxeticity and anomalous elasticity. *Dalton. Trans.* **2016,** *45*, 4154-4161.

197. Fairen-Jimenez, D.; Moggach, S. A.; Wharmby, M. T.; Wright, P. A.; Parsons, S.; Duren, T., Opening the gate: framework flexibility in ZIF-8 explored by experiments and simulations. *J. Am. Chem. Soc.* **2011,** *133*, 8900-8902.

198. Ryder, M. R.; Civalleri, B.; Bennett, T. D.; Henke, S.; Rudic, S.; Cinque, G.; Fernandez-Alonso, F.; Tan, J. C., Identifying the role of terahertz vibrations in metal-organic frameworks: from gate-opening phenomenon to shear-driven structural destabilization. *Phys. Rev. Lett.* **2014,** *113*, 215502.

199. Pan, Y.; Liu, Y.; Zeng, G.; Zhao, L.; Lai, Z., Rapid synthesis of zeolitic imidazolate framework-8 (ZIF-8) nanocrystals in an aqueous system. *Chem. Commun.* **2011,** *47*, 2071-2073.

200. Chen, Z.-F.; Zhang, M.; Shi, S.-M.; Huang, L.; Liang, H.; Zhou, Z.-Y., Diaquabis(8-quinolinolato-κ_2N,O)zinc^{II}. *Acta Crystallogr. Sect. Sect. E: Struct. Rep. Online* **2003,** *59*, m814-m815.

201. Wang, R. F.; Cao, Y. L.; Jia, D. Z.; Liu, L.; Li, F., New approach to synthesize 8-hydroxyquinoline-based complexes with Zn^{2+} and their luminescent properties. *Opt. Mater.* **2013,** *36*, 232-237.

202. Burrows, P. E.; Sapochak, L. S.; Mccarty, D. M.; Forrest, S. R.; Thompson, M. E., Metal-Ion Dependent Luminescence Effects in Metal Tris-Quinolate Organic Heterojunction Light-Emitting Devices. *Appl. Phys. Lett.* **1994,** *64*, 2718-2720.

203. Sapochak, L. S.; Benincasa, F. E.; Schofield, R. S.; Baker, J. L.; Riccio, K. K.; Fogarty, D.; Kohlmann, H.; Ferris, K. F.; Burrows, P. E., Electroluminescent zinc(II) bis(8-hydroxyquinoline): structural effects on electronic states and device performance. *J. Am. Chem. Soc.* **2002,** *124*, 6119-6125.

204. Morabito, J. V.; Chou, L. Y.; Li, Z.; Manna, C. M.; Petroff, C. A.; Kyada, R. J.; Palomba, J. M.; Byers, J. A.; Tsung, C. K., Molecular encapsulation beyond the aperture size limit through dissociative linker exchange in metal-organic framework crystals. *J. Am. Chem. Soc.* **2014,** *136*, 12540-12543.

205. Shameema, O.; Ramachandran, C. N.; Sathyamurthy, N., Blue shift in X-H stretching frequency of molecules due to confinement. *J. Phys. Chem. A* **2006,** *110*, 2-4.

206. Wang, F.; Liu, Z. S.; Yang, H.; Tan, Y. X.; Zhang, J., Hybrid zeolitic imidazolate frameworks with catalytically active TO4 building blocks. *Angew. Chem. Int. Ed.* **2011,** *50*, 450-453.

207. Butler, K. T.; Hendon, C. H.; Walsh, A., Electronic structure modulation of metal-organic frameworks for hybrid devices. *ACS Appl. Mater. Inter.* **2014,** *6*, 22044-22050.

208. Hachula, B.; Nowak, M.; Kusz, J., Crystal and Molecular Structure Analysis of 2-Methylimidazole. *J. Chem. Crystallogr.* **2010,** *40*, 201-206.

209. Peng, H.; Dang, W.; Cao, J.; Chen, Y.; Wu, D.; Zheng, W.; Li, H.; Shen, Z. X.; Liu, Z., Topological insulator nanostructures for near-infrared transparent flexible electrodes. *Nat. Chem.* **2012,** *4*, 281-286.

210. Osada, M.; Sasaki, T., Two-dimensional dielectric nanosheets: novel nanoelectronics from nanocrystal building blocks. *Adv. Mater.* **2012,** *24*, 210-228.

211. Coleman, J. N.; Lotya, M.; O'Neill, A.; Bergin, S. D.; King, P. J.; Khan, U.; Young, K.; Gaucher, A.; De, S.; Smith, R. J.; Shvets, I. V.; Arora, S. K.; Stanton, G.; Kim, H. Y.; Lee, K.; Kim, G. T.; Duesberg, G. S.; Hallam, T.; Boland, J. J.; Wang, J. J.; Donegan, J. F.; Grunlan, J. C.; Moriarty, G.; Shmeliov, A.; Nicholls, R. J.; Perkins, J. M.; Grieveson, E. M.; Theuwissen, K.; McComb, D. W.; Nellist, P. D.; Nicolosi, V., Two-dimensional nanosheets produced by liquid exfoliation of layered materials. *Science* **2011,** *331*, 568-571.

212. Tan, J. C.; Saines, P. J.; Bithell, E. G.; Cheetham, A. K., Hybrid nanosheets of an inorganic-organic framework material: facile synthesis, structure, and elastic properties. *ACS Nano* **2012,** *6*, 615-621.

213. Peng, Y.; Li, Y. S.; Ban, Y. J.; Jin, H.; Jiao, W. M.; Liu, X. L.; Yang, W. S., Metal-organic framework nanosheets as building blocks for molecular sieving membranes. *Science* **2014,** *346*, 1356-1359.

214. Varoon, K.; Zhang, X.; Elyassi, B.; Brewer, D. D.; Gettel, M.; Kumar, S.; Lee, J. A.; Maheshwari, S.; Mittal, A.; Sung, C. Y.; Cococcioni, M.; Francis, L. F.; McCormick, A. V.; Mkhoyan, K. A.; Tsapatsis, M., Dispersible exfoliated zeolite nanosheets and their application as a selective membrane. *Science* **2011,** *334*, 72-75.

215. Draper, E. R.; Eden, E. G.; McDonald, T. O.; Adams, D. J., Spatially resolved multicomponent gels. *Nat. Chem.* **2015,** *7*, 848-852.

216. Choi, B.; Yu, J.; Paley, D. W.; Trinh, M. T.; Paley, M. V.; Karch, J. M.; Crowther, A. C.; Lee, C. H.; Lalancette, R. A.; Zhu, X.; Kim, P.; Steigerwald, M. L.; Nuckolls, C.; Roy, X., van der Waals Solids from Self-Assembled Nanoscale Building Blocks. *Nano Lett.* **2016,** *16*, 1445-1449.

217. Sakata, Y.; Furukawa, S.; Kondo, M.; Hirai, K.; Horike, N.; Takashima, Y.; Uehara, H.; Louvain, N.; Meilikhov, M.; Tsuruoka, T.; Isoda, S.; Kosaka, W.; Sakata, O.; Kitagawa, S., Shape-memory nanopores induced in coordination frameworks by crystal downsizing. *Science* **2013,** *339*, 193-196.

218. Zhao, M.; Wang, Y.; Ma, Q.; Huang, Y.; Zhang, X.; Ping, J.; Zhang, Z.; Lu, Q.; Yu, Y.; Xu, H.; Zhao, Y.; Zhang, H., Ultrathin 2D Metal-Organic Framework Nanosheets. *Adv. Mater.* **2015,** *27*, 7372-7378.

219. Hermosa, C.; Horrocks, B. R.; Martinez, J. I.; Liscio, F.; Gomez-Herrero, J.; Zamora, F., Mechanical and optical properties of ultralarge flakes of a metal-organic framework with molecular thickness. *Chem. Sci.* **2015,** *6*, 2553-2558.

220. Cliffe, M. J.; Castillo-Martinez, E.; Wu, Y.; Lee, J.; Forse, A. C.; Firth, F. C. N.; Moghadam, P. Z.; Fairen-Jimenez, D.; Gaultois, M. W.; Hill, J. A.; Magdysyuk, O. V.; Slater, B.; Goodwin, A. L.; Grey, C. P., Metal-Organic Nanosheets Formed via Defect-Mediated Transformation of a Hafnium Metal-Organic Framework. *J. Am. Chem. Soc.* **2017,** *139*, 5397-5404.

221. Howarth, A. J.; Liu, Y. Y.; Li, P.; Li, Z. Y.; Wang, T. C.; Hupp, J.; Farha, O. K., Chemical, thermal and mechanical stabilities of metal-organic frameworks. *Nat. Rev. Mater.* **2016,** *1*, 15018.

222. Garai, B.; Mallick, A.; Banerjee, R., Photochromic metal-organic frameworks for inkless and erasable printing. *Chem. Sci.* **2016,** *7*, 2195-2200.

223. Yao, M. S.; Tang, W. X.; Wang, G. E.; Nath, B.; Xu, G., MOF Thin Film-Coated Metal Oxide Nanowire Array: Significantly Improved Chemiresistor Sensor Performance. *Adv. Mater.* **2016,** *28*, 5229-5234.

224. Ryder, M. R.; Civalleri, B.; Cinque, G.; Tan, J. C., Discovering connections between terahertz vibrations and elasticity underpinning the collective dynamics of the HKUST-1 metal-organic framework. *CrystEngComm* **2016,** *18*, 4303-4312.

225. Liedana, N.; Galve, A.; Rubio, C.; Tellez, C.; Coronas, J., CAF@ZIF-8: one-step encapsulation of caffeine in MOF. *ACS Appl. Mater. Inter.* **2012,** *4*, 5016-5021.

226. Anand, R.; Borghi, F.; Manoli, F.; Manet, I.; Agostoni, V.; Reschiglian, P.; Gref, R.; Monti, S., Host-guest interactions in Fe(III)-trimesate MOF nanoparticles loaded with doxorubicin. *J. Phys. Chem. B* **2014,** *118*, 8532-8539.

227. Xie, W.; He, W. W.; Du, D. Y.; Li, S. L.; Qin, J. S.; Su, Z. M.; Sun, C. Y.; Lan, Y. Q., A stable Alq3@MOF composite for white-light emission. *Chem. Commun.* **2016,** *52*, 3288-3291.

228. Aguilera-Sigalat, J.; Bradshaw, D., Synthesis and applications of metal-organic framework-quantum dot (QD@MOF) composites. *Coordin. Chem. Rev.* **2016,** *307*, 267-291.

229. Burrows, A. D.; Cassar, K.; Friend, R. M. W.; Mahon, M. F.; Rigby, S. P.; Warren, J. E., Solvent hydrolysis and templating effects in the synthesis of metal-organic frameworks. *CrystEngComm* **2005,** *7*, 548-550.

230. Biemmi, E.; Bein, T.; Stock, N., Synthesis and characterization of a new metal organic framework structure with a 2D porous system: $(H_2NEt_2)_2[Zn_3(BDC)_4]\cdot 3DEF$. *Sol. State Sci.* **2006,** *8*, 363-370.

231. Khaorapapong, N.; Ogawa, M., In situ formation of bis(8-hydroxyquinoline) zinc(II) complex in the interlayer spaces of smectites by solid-solid reactions. *J. Phys. Chem. Solids* **2008,** *69*, 941-948.

232. Ishiguro, S.; Umebayashi, Y.; Kanzaki, R., Characterization of metal ions in coordinating solvent mixtures by means of Raman spectroscopy. *Anal. Sci.* **2004,** *20*, 415-421.

233. Krishnakumar, V.; Ramasamy, R., DFT studies and vibrational spectra of isoquinoline and 8-hydroxyquinoline. *Spectrochim. Acta A Mol. Biomol. Spectrosc.* **2005,** *61*, 673-683.

234. Lee, M. W.; Kim, M. S.; Kim, K., Infrared and Raman spectroscopic study of terephthalic acid adsorbed on silver surfaces. *J. Mol. Struct.* **1997,** *415*, 93-100.

235. Ling, S. L.; Slater, B., Unusually Large Band Gap Changes in Breathing Metal-Organic Framework Materials. *J. Phys. Chem. C* **2015,** *119*, 16667-16677.

236. Yan, D.; Tang, Y.; Lin, H.; Wang, D., Tunable two-color luminescence and host-guest energy transfer of fluorescent chromophores encapsulated in metal-organic frameworks. *Sci Rep* **2014,** *4*, 4337.

237. Parsons, R. W.; Drickamer, H. G., Effect of Pressure on the Spectra of Certain Transition Metal Complexes. *J. Chem. Phys.* **1958,** *29*, 930-937.

238. Grey, J. K.; Butler, I. S., Effects of high external pressures on the electronic spectra of coordination compounds. *Coordin. Chem. Rev.* **2001,** *219*, 713-759.

239. Reber, C., Absorption and luminescence spectroscopy of transition metal compounds: from coordination geometries to excited-state properties. *Can. J. Anal. Sci. Spectros.* **2008,** *53*, 91-101.

240. Valeur, B.; Leray, I., Design principles of fluorescent molecular sensors for cation recognition. *Coord. Chem. Rev.* **2000,** *205*, 3-40.

241. Bardez, E.; Devol, I.; Larrey, B.; Valeur, B., Excited-state processes in 8-hydroxyquinoline: Photoinduced tautomerization and solvation effects. *J. Phys. Chem. B* **1997,** *101*, 7786-7793.

242. Zhao, Y. S.; Fu, H. B.; Peng, A. D.; Ma, Y.; Xiao, D. B.; Yao, J. N., Low-dimensional nanomaterials based on small organic molecules: Preparation and optoelectronic properties. *Adv. Mater.* **2008,** *20*, 2859-2876.

243. Dolgopolova, E. A.; Shustova, N. B., Metal-organic framework photophysics: Optoelectronic devices, photoswitches, sensors, and photocatalysts. *MRS Bull.* **2016,** *41*, 890-895.

244. Serpe, M. J.; Kang, Y.; Zhang, Q. M., *Photonic Materials for Sensing, Biosensing and Display Devices Preface*. Springer: 2016; Vol. 229.

245. Suri, J. T.; Cordes, D. B.; Cappuccio, F. E.; Wessling, R. A.; Singaram, B., Continuous glucose sensing with a fluorescent thin-film hydrogel. *Angew. Chem. Int. Ed.* **2003,** *42*, 5857-5859.

246. Ward, M. D., Photo-induced electron and energy transfer in non-covalently bonded supramolecular assemblies. *Chem. Soc. Rev.* **1997,** *26*, 365-375.

247. Yildiz, I.; Tomasulo, M.; Raymo, F. M., A mechanism to signal receptor-substrate interactions with luminescent quantum dots. *Proc. Natl. Acad. Sci. USA* **2006,** *103*, 11457-11460.

248. Hou, X.; Ke, C.; Bruns, C. J.; McGonigal, P. R.; Pettman, R. B.; Stoddart, J. F., Tunable solid-state fluorescent materials for supramolecular encryption. *Nat. Commun.* **2015,** *6*, 6884.

249. Wang, Y.; Tan, X.; Zhang, Y. M.; Zhu, S.; Zhang, I.; Yu, B.; Wang, K.; Yang, B.; Li, M.; Zou, B.; Zhang, S. X., Dynamic behavior of molecular switches in crystal under pressure and its reflection on tactile sensing. *J. Am. Chem. Soc.* **2015,** *137*, 931-939.

250. Boldyreva, E., Mechanochemistry of inorganic and organic systems: what is similar, what is different? *Chem. Soc. Rev.* **2013,** *42*, 7719-7738.

251. Kaupp, G., Mechanochemistry: the varied applications of mechanical bond-breaking. *CrystEngComm* **2009,** *11*, 388-403.

252. He, Z. K.; Zhang, L. Q.; Mei, J.; Zhang, T.; Lam, J. W. Y.; Shuai, Z. G.; Dong, Y. Q.; Tang, B. Z., Polymorphism-Dependent and Switchable Emission of Butterfly-Like Bis(diarylmethylene)dihydroanthracenes. *Chem. Mater.* **2015,** *27*, 6601-6607.

253. Chen, Z.; Zhang, J.; Song, M.; Yin, J.; Yu, G. A.; Liu, S. H., A novel fluorene-based aggregation-induced emission (AIE)-active gold(i) complex with crystallization-induced emission enhancement (CIEE) and reversible mechanochromism characteristics. *Chem. Commun.* **2015,** *51*, 326-329.

254. Misra, R.; Jadhav, T.; Dhokale, B.; Mobin, S. M., Reversible mechanochromism and enhanced AIE in tetraphenylethene substituted phenanthroimidazoles. *Chem. Commun.* **2014,** *50*, 9076-9078.

255. Benito, Q.; Le Goff, X. F.; Maron, S.; Fargues, A.; Garcia, A.; Martineau, C.; Taulelle, F.; Kahlal, S.; Gacoin, T.; Boilot, J. P.; Perruchas, S., Polymorphic copper iodide clusters: insights into the mechanochromic luminescence properties. *J. Am. Chem. Soc.* **2014,** *136*, 11311-11320.

256. Allendorf, M. D.; Medishetty, R.; Fischer, R. A., Guest molecules as a design element for metal-organic frameworks. *MRS Bull.* **2016,** *41*, 865-869.

257. Mieno, H.; Kabe, R.; Notsuka, N.; Allendorf, M. D.; Adachi, C., Long-Lived Room-Temperature Phosphorescence of Coronene in Zeolitic Imidazolate Framework ZIF-8. *Adv. Opt. Mater.* **2016,** *4*, 1015-1021.

258. Tzeng, B. C.; Chang, T. Y.; Sheu, H. S., Reversible phase transformation and luminescent mechanochromism of Zn(II)-Based coordination frameworks containing a dipyridylamide ligand. *Chem. Eur. J.* **2010,** *16*, 9990-9993.

259. Wen, T.; Zhou, X. P.; Zhang, D. X.; Li, D., Luminescent mechanochromic porous coordination polymers. *Chem. Eur. J.* **2014,** *20*, 644-648.

260. Sun, J. K.; Chen, C.; Cai, L. X.; Ren, C. X.; Tan, B.; Zhang, J., Mechanical grinding of a single-crystalline metal-organic framework triggered emission with tunable violet-to-orange luminescence. *Chem. Commun.* **2014,** *50*, 15956-15959.

261. Deshmukh, M. S.; Yadav, A.; Pant, R.; Boomishankar, R., Thermochromic and mechanochromic luminescence umpolung in isostructural metal-organic frameworks based on Cu_6I_6 clusters. *Inorg. Chem.* **2015,** *54*, 1337-1345.

262. Zhang, Q.; Su, J.; Feng, D.; Wei, Z.; Zou, X.; Zhou, H. C., Piezofluorochromic Metal-Organic Framework: A Microscissor Lift. *J. Am. Chem. Soc.* **2015,** *137*, 10064-10067.

263. Esken, D.; Turner, S.; Wiktor, C.; Kalidindi, S. B.; Van Tendeloo, G.; Fischer, R. A., GaN@ZIF-8: selective formation of gallium nitride quantum dots inside a zinc methylimidazolate framework. *J. Am. Chem. Soc.* **2011,** *133*, 16370-16373.

264. Lyu, F.; Zhang, Y.; Zare, R. N.; Ge, J.; Liu, Z., One-pot synthesis of protein-embedded metal-organic frameworks with enhanced biological activities. *Nano Lett.* **2014,** *14*, 5761-5765.

265. Song, Y.; Hu, D.; Liu, F.; Chen, S.; Wang, L., Fabrication of fluorescent SiO_2@zeolitic imidazolate framework-8 nanosensor for Cu^{2+} detection. *Analyst* **2015,** *140*, 623-629.

266. Ferguson, J., Absorption and Emission Spectra of the Perylene Dimer. *J. Chem. Phys.* **1966,** *44*, 2677-2683.

267. Spano, F. C.; Silva, C., H- and J-aggregate behavior in polymeric semiconductors. *Annu. Rev. Phys. Chem.* **2014,** *65*, 477-500.

268. Zhou, Q.; Swager, T. M., Fluorescent chemosensors based on energy migration in conjugated polymers: The molecular wire approach to increased sensitivity. *J. Am. Chem. Soc.* **1995,** *117*, 12593-12602.

269. Cao, S.; Bennett, T. D.; Keen, D. A.; Goodwin, A. L.; Cheetham, A. K., Amorphization of the prototypical zeolitic imidazolate framework ZIF-8 by ball-milling. *Chem. Commun.* **2012,** *48*, 7805-7807.

270. Kim, D. Y.; Joshi, B. N.; Lee, J. G.; Lee, J. H.; Lee, J. S.; Hwang, Y. K.; Chang, J. S.; Al-Deyab, S.; Tan, J. C.; Yoon, S. S., Supersonic cold spraying for zeolitic metal-organic framework films. *Chem. Eng. J.* **2016,** *295*, 49-56.

271. Chaudhari, A. K.; Tan, J. C., A mechano-responsive supramolecular metal-organic framework (supraMOF) gel material rich in ZIF-8 nanoplates. *Chem. Commun.* **2017,** *53*, 8502-8505.

272. Jayaramulu, K.; Geyer, F.; Petr, M.; Zboril, R.; Vollmer, D.; Fischer, R. A., Shape Controlled Hierarchical Porous Hydrophobic/Oleophilic Metal-Organic Nanofibrous Gel Composites for Oil Adsorption. *Adv. Mater.* **2017,** *29*, 1605307.

273. Silva, P.; Vilela, S. M.; Tome, J. P.; Almeida Paz, F. A., Multifunctional metal-organic frameworks: from academia to industrial applications. *Chem. Soc. Rev.* **2015,** *44*, 6774-6803.

274. Slater, A. G.; Cooper, A. I., Porous materials. Function-led design of new porous materials. *Science* **2015,** *348*, aaa8075.

275. Chretien, M. N.; Heafey, E.; Scaiano, J. C., Reducing adverse effects from UV sunscreens by zeolite encapsulation: comparison of oxybenzone in solution and in zeolites. *Photochem. Photobiol.* **2010,** *86*, 153-161.

276. Mitsui, M.; Higashi, K.; Takahashi, R.; Hirumi, Y.; Kobayashi, K., Enhanced photostability of an anthracene-based dye due to supramolecular encapsulation: a new type of photostable fluorophore for single-molecule study. *Photochem. Photobiol. Sci.* **2014,** *13*, 1130-1136.

277. Yao, Y. F.; Zhang, M. S.; Shi, J. X.; Gong, M. L.; Zhang, H. J.; Yang, Y. S., Encapsulation of fluorescein into MCM-41 mesoporous molecular sieve by a sol-gel method. *Mater. Lett.* **2001,** *48*, 44-48.